University of Nottingham
UK | CHINA | MALAYSIA

Exciton Dynamics and Structure-Property Relationships in Organic Semiconductors Containing Diketopyrrolopyrrole and Thiophene

Ling Jiang

Thesis submitted to the University of Nottingham
for the degree of Doctor of Philosophy

20 May 2022

To my family and friends

Contents

Acknowledgements

I want to thank my supervisors, Dr. Hainam Do, Prof. George Z. Chen and Prof. Jonathan D. Hirst, for their patience, guidance and support. It has been a great pleasure to work with them. They have enlightened me at first glance about research. I would also like to thank our collaborator Dr. David Rogers for helpful discussions. I thank Prof. David B. Amabilino for his valuable comments.

I am grateful for access to the University of Nottingham High-Performance Computing Facility in Ningbo China, and Nottingham UK. I thank the Faculty of Science and Engineering at University of Nottingham Ningbo China for a PhD scholarship.

In Nottingham, I thank Pilar for her accompany and her optimistic personality. She influenced me positively and helped me to be a happier person today than I was yesterday. I thank Tamara and Edward for their delicious Christmas dinner. I thank Chunyu Xiang and Dr. Samuel Dimitri Widijatmoko for all the fun we had. When I doubted myself, they enthusiastically encouraged me and told me I was invincible. I would also like to thank Jiamu Jiang and Adam Gajtkowski, who provided accommodation and greatly assisted me during my hard time. I thank Dr. Selma Farah Boudali for bringing unforgettable summertime memories when she visited Nottingham. I want to thank all the members of the Nottingham computational chemistry groups. In particular, Dr. Ellen Guest, Alexe Haywood, Abigail Miller, Dr. Adam Fouda, Dr. Meilani Wibowo, Dr. Tom Irons, Dr. Gregoire David, Dr. Joshua Baptiste, Ross Amory, Gosia Stankiewicz, Jennifer Coughlan, Dr. Steven Oatley, Dr. Ivan Derbenev and Isabel Cooley.

In Ningbo, I am grateful to Mingkai Li and Rui Zhao for their support and friendship. They cared for me for one week when I got carditis in the hospi-

tal. They deserve a big thanks. I had a fantastic experience working closely with Xiwen Guan, whose work attitude inspires me. I also thank Junxiao Zhang for forwarding this PhD opportunity. He gave helpful advice and encouraged me to apply to this PhD program. I would also like to thank my friend Jingxuan Huang, Yuhong Wang, Nengjia Ren and Yumeng Yang for being so supportive in my PhD journey. An immense thank you to my friends at University of Nottingham Ningbo China for showing confidence in my work and for their patience and help: Lei Li, Dr. Jiadi Yin, Dr. Manxuan Xiao, Jiayuan Xu, Wentong Xie, Ying Jiang, Zu Wang, Dr. Shuai Liu, Dr. Jorge Mendez Astudillo, Xinan Chen, Zhipeng Lin, Dr. Xiaoping Jiang, Dr. Francis M. Enjujekwu, Yuanli Ma, Dr. Jiahui Yu, Yanfei Xiong and Zeping Wang.

Last but not least, I would like to thank my family, especially my parents and grandparents, for spiritually supporting me throughout my life. They are always proud of me regardless of the decision or the path that I take.

Words fall far too short for these acknowledgements, and none of these lists is complete. All of you have made the last three and a half years precisely what they needed to be.

Thank you.

List of Publications

The following peer-reviewed journal articles have either been published or are in preparation to be published as a result of the work undertaken as part of this thesis:

1. **Jiang, L.**, Rogers, D. M., Hirst, J. D. & Do, H. (2020), 'Force fields for macromolecular assemblies containing diketopyrrolopyrrole and thiophene', *Journal of Chemical Theory and Computation* **16**(8), 5150–5162.
2. **Jiang, L.**, Hirst, J. D. & Do, H. (2022), 'Structure-property relationships in amorphous thieno[3,2-*b*]thiophene-diketopyrrolopyrrole-thiophene-containing polymers', *Journal of Physical Chemistry C* **126**(26), 10842–10854.
3. **Jiang, L.**, Hirst, J. D. & Do, H. (2022), 'Dynamic disorder drives exciton dynamics in molecular crystals', *Journal of Physical Chemistry C* **Under Review**.

The following peer-reviewed journal articles have either been published or are in preparation to be published, but not as part of this thesis:

4. Guan, X., **Jiang, L.**, Fan, D., Hernandez, A.G., Li, B. & Do, H. (2022), 'Molecular simulations of the structure-property relationships of N-A-S-H gels', *Construction and Building Materials*, **329**, 127166.
5. Peng, M., Li, H., Qin, Z., Li, J., Sun, Y., Zhang, X., **Jiang, L.**, Do, H. & An, J. (2022), 'Pentafluorophenyl group as activating group: Synthesis of α-deuterio carboxylic acid derivatives via Et_3N catalyzed H/D exchange', *Advanced Synthesis & Catalysis*, **364**, 2184–2189.

List of Figures

List of Tables

List of Abbreviations

ADMP	Atom Centred Density Matrix Propagation
ATC	Atomic Transition Charges
CCDC	Cambridge Crystallographic Data Centre
CGTO	Contracted Gaussian-type Orbital
CT	Charge Transfer
D-A	Doner-acceptor
DFT	Density Functional Theory
DOS	Density of State
DPP	1,4-diketopyrrolo[3-4-*c*]pyrroles
DPPTT	Thienothiophene-flanked Diketopyrrolopyrrole
DTPP	1,4-dithioketo-3,6-diphenyl-pyrrolo-[3,4-*c*]-pyrrole
e-h	Electron-hole
FET	Field-effect Transistor
FM	Force-matching
FRET	Förster Resonant Energy Transfer
GGA	Generalised Gradient Approximation
GTO	Gaussian-type Orbital
HOMO	Highest Occupied Molecular Orbitals
IR	Infrared
LCAO	Linear Combination of Atomic Orbitals
LDA	Local Density Approximation
LED	Light-emitting Diode
LEGS	Local Exciton Ground State

LH	Light-harvesting
LUMO	Lowest Unoccupied Molecular Orbitals
MC	Monte Carlo
MD	Molecular Dynamics
MEH-PPV	Poly[2-methoxy-5-(2'-ethylhexyloxy)-1,4-phenylene Vinylene]
MM	Molecular Mechanics
MO	Molecular Orbitals
MSD	Mean Square Displacement
NAMD	Nanoscale Molecular Dynamics
NTO	Natural Transition Orbital
OFET	Organic Field-effect Transistor
OLED	Organic Light-emitting Diode
OPLS	Optimised Potentials for Liquid Simulations
OPV	Organic Photovoltaic
OSC	Organic Semiconductor
P3HT	Poly(3-hexylthiophene-2,5-diyl
PBE	Perdew–Burke–Ernzerhof Functional
PBTTT	Poly(2,5-bis(3-hexadecylthiophen-2-yl)thieno[3,2-*b*]thiophene
PCDTBT	Poly[*N*-9"-hepta-decanyl-2,7-carbazole-*alt*-5,5-(4',7'-di-2-thienyl-2',1',3'-benzothiadiazole)]:[6,6]-phenyl
PCE	Power Conversion Efficiency
PDPPTT-T-10	Poly[[2,5-bis(2-octyldodecyl)-2,3,5,6-tetrahydro-3,6-dioxopyrrolo[3,4-*c*]pyrrole-1,4-diyl]-*alt*–[[2,2'-(2,5-thiophene)bis-thieno[3,2-b]thiophen]-5,5'-diyl]]
PhEtTh	Poly-2,5-bis(phenylethynyl)-1,3,4-thiadiazole
PI	Participation Index
PPV	Poly(phenylenevinylene)

PTPPTT-T	Poly(thieno[3,2*b*]thiophene-diketopyrrolopyrrole-*co*-thiophene
PV	Photovoltaic
PW91	Perdew–Wang Functional
QM	Quantum Mechanics
QuTiP	Quantum Toolbox in Python
RDF	Radial Distribution Function
RESP	Restrained Electrostatic Potential
RMSD	Root Mean Square Deviation
STO	Slater-type Orbital
T	Thiophene
TB	Tight-binding
TD-DFT	Time-dependent Density-functional Theory
TDM	Transition Density Matrix
TDPP	1,4-diketo-3,6-dithienylpyrrolo[3-4-*c*]pyrrole
TDSE	Time-dependent Schrödinger Equation
TPSS	Tao–Perdew–Staroverov–Scuseria
TT	Thieno[3,2-*b*]thiophene
UBEQOK	Diethyl 2,2'-(1,4-dioxo-3,6-bis(2-thienyl)pyrrolo[3,4-*c*]pyrrole-2,5(1H,4H)-diyl)diacetate
UBEQUQ	Ethyl (1,4-dioxo-3,6-bis(2-thienyl)-4,5-dihydropyrrolo[3,4-*c*]pyrrol-2(1H)-yl)acetate
VAF	Velocity Autocorrelation Function
vdW	van der Waals

Abstract

Despite significant efforts in the past few decades, charge transport efficiency in organic semiconducting materials remains much lower than its inorganic counterparts. There are various ways to improve the performance of organic electronics, such as updating device architecture, considering different electrodes and encapsulation materials, and the ease of processing. Nevertheless, the most challenging part is to obtain a clear picture of the exciton and charge transport properties of the active materials.

This thesis explores some fundamental aspects of exciton transport and the structure-property relationships in organic semiconductors from a theoretical point of view. After a brief review and bringing out the challenge of the field of organic electronics (Chapter 1), the theoretical methods most commonly used to describe excitation energy transfer and charge transport are summarised, emphasising the specific methods employed in this thesis (Chapter 2).

It is challenging to find accurate force fields for all applications where molecular dynamics simulation is a preliminary step toward studying electronic structure properties. All single molecules, biological chromophores, and semiconducting polymers of interest display a complex chemical structure with extended π-conjugation that prevents the use of standard force fields. Moreover, when one uses classical simulation methods as inputs for electronic structure calculations, the equilibrium structure of the classical simulation and the electronic structure calculations should be as close as possible. This challenge is addressed in Chapter 3, in which we utilise a force matching procedure to parameterise new force fields systematically for large conjugated systems. These force fields are subsequently employed to propagate the nuclear dynamics for systems studied in Chapters 4 and 5.

The ability to control dynamic disorder in molecular aggregates will provide valuable tools for the design and development of efficient organic semiconductors. Therefore, identifying key parameters that correlate with the efficiency of the transport of the excitation energy is highly desirable. Chapter 4 investigates the effects of the dynamic disorder on the exciton transport in molecular crystals of mono- and di-alkylated 1,4-diketo-3,6-dithiophenylpyrrolo[3-4-c]pyrrole derivatives. The exciton dynamics are studied using a Frenkel–Holstein like Hamiltonian, in which the thermal fluctuations of the excitonic coupling as well as the non-local exciton-phonon couplings have been appropriately taken into account. The contrasting views of the dependence of high charge mobility and exciton transport on morphology indicate the need for robust quantitative models of how (dis)order influences excitation energy transfer in organic semiconducting materials. Investigating the relationship between structure and electronic properties of materials requires constructing atomistic models of the systems and calculating their electronic structure properties. Chapter 5 provides insights into the electronic excited states of polymers and their connections to the dynamical disorder of the nuclei. Finally, Chapter 6 summarises the research efforts and contributions made by the thesis to the field of optoelectronics.

Chapter 1

Introduction

1.1 Synopsis

This chapter begins with the background introduction to organic electronics and emphasises its applications in sustainable energy and flexible electronic devices. It also gives an overview of the physical basis of organic semiconductors for a better understanding of the processes that affect the exciton dynamics and structure-property relationships in molecular aggregates. The chapter then introduces a particular type of organic semiconductors containing 1,4-diketopyrrolo[3-4-*c*]pyrroles, thiophene and thieno[3,2-*b*]thiophene, which have demonstrated remarkable improvements in the performance of both thin-film transistors and solar cell devices. It indicates that a thorough understanding of the relationship between the structure-property relationship and the exciton dynamics in these classes of materials is crucial for the design and development of high-performance organic electronic devices. Next, the chapter gives an overview of the excitation energy transfer in molecular aggregates, emphasising the importance of the short-range contributions to the excitonic couplings. After this, it highlights the current challenges for organic semiconductors and provides the aims and objectives of the research. Finally, the chapter ends with an outline of the thesis.

1.2 Organic Electronics

Energy is indispensable to human existence, and the continued high-growing demand for energy consumption prompts a transition from traditional to renewable and sustainable energy sources. Despite significant efforts in utilising alternative energy sources, most energy supply still comes from fossil fuels, including coal, oil, petroleum and natural gas. These natural resources are limited and rapidly depleted. In addition, fossil fuels suffer several disadvantages, including environmental hazards, rising prices, acid rain, and effects on human health. Thus, continued reliance on them may have significant environmental and social consequences.

Solar energy is attractive among several renewable energy sources since it is abundant and environmentally friendly. Among the different technologies to convert solar energy into electricity, photovoltaic (PV) technology, also referred to as the solar cell, is one of the most popular approaches. The PV technology could make the transition from fossil fuels to renewable energy possible (Archer & Green 2014).

A breakthrough in solar energy harvesting is the third generation PV technology - organic photovoltaic (OPV) cells, which combines the advantages of the first (silicon wafer-based technology) and second generation PV (thin films-based technology). OPV cells are also known as excitonic solar cells due to their charge generation mechanism based on the formation of excitons. Organic cells are powerful absorbents of light, being able to harness more significant amounts of sunlight than other solar cells. The power conversion efficiency of OPV cells has increased from around 1% to over 12% in the past 20 years (Zhu et al. 2022). Furthermore, organic solar cells offer the possibility of low–cost, lightweight, flexible and portable solar cells.

Besides the search for green and sustainable energy technology, the present generation also witnesses a big wave of transformation in electronic technologies. Smartphones that can be folded to fit in our pockets and video displays that roll up and down like a window blind are among current cutting edge technologies. These are made possible by the invention of organic light-emitting diode (OLED), a great success story of using organic materials in electronic devices. OLEDs are effectively a sandwich of one or more organic semiconducting materials in between layers that allow different electrical charges into the semiconductor. As charges meet in the middle of the sandwich, they combine to give out light. In addition, flexible displays rely upon electronic switches known as transistors. These organic field-effect transistors (OFETs) are also made from organic semiconducting materials. Behind each OLED pixel in the display is an OFET, ready to turn it on and off as required. OFETs work by having three electrical connections: the gate, source and drain. A voltage applied to the gate makes the semiconductor either more or less conductive. This either allows or prevents electrical current from flowing between the source and drain.

The potential for future applications of organic devices extends far beyond today's mobile phone and display technology. Organic materials also present the possibility of devices that can interface with biological systems, promising future healthcare applications. Smartphones that fold like a map and artificial skin with tactile sensitivity that could be used to treat burns, or add functionality to prosthetic limbs, are among the numerous potential applications for these new materials.

Nowadays, the study and utilisation of organic semiconducting materials in electronic applications is known as the field of "organic electronics". This is a platform for low cost and high performance optoelectronic and electronic devices that cover large areas, are lightweight, and can be flexible and conformable to irregularly shaped surfaces. The idea of organic semiconductors was initially proposed several years after the development of inorganic electronics. However, it was only speculatively linked to their advanced performance, living in the shadow of their inorganic counterpart for half a century.

Organic semiconductors have attracted the interest of the electronics industry due to several reasons. Notable properties are the solubility in organic solvents and light emission colour, which can be finely tuned via chemical synthesis. The tunability facilitates the engineering of molecules to fit specific requirements. Another attractive feature involves the ease of processing. Polymer coatings can be easily applied over large areas and to various substrates, including mechanically flexible ones. Associated with the ease of processing is the potential for low-cost fabrication. Progress in organic electronics is likely to closely follow advances in our understanding of the fundamental properties of organic materials. Furthermore, the availability of an unlimited number of different molecules represents the ultimate degree of freedom for researchers and the best reason for using organics to study semiconductor physics.

Despite offering many advantages, low charge mobility compared to single crystalline silicon is the critical factor that limits the range of applications envisioned for organics. Other drawbacks, such as the lack of analytical tools to characterise how the materials are assembled and integrated into devices and a thorough understanding of how organic electronic materials can be assembled to ensure reproducibility, are among those that prevent the full deployment of organic electronics. In terms of applications, OPV cells currently do not match the required industrial efficiency and long–term stability of first and second generation solar cells. On the other hand, OLED seems to be the perfect technology for all displays but suffers from a short lifetime, is expensive to produce, and is easily damaged by water. Thus, research is still needed to realise the full potential of organic semiconducting materials.

1.3 Organic Semiconducting Materials

Organic semiconductors are a class of carbon-based materials, classified into polymers and small molecules. Polymers are macromolecules made of chemically bonded repeating units (monomers), while small molecules are used as a broader term, including oligomers (up to a few tens of repeating units), dendrimers and smaller molecules. There are two major classes of materials that have been considered somewhat separately in the field of organic electronics. Crystalline molecular semiconductors, which have been studied in bulk and thin film with various techniques, offer the advantages of a well-defined structure and, in principle, a simple identification of the structure-property relation. On the other hand, polymeric semiconductors are potentially simpler to process and appear to be more suitable for "printed" electronics (Cheung & Troisi 2008).

The common feature which makes these materials semiconducting is conjugation, i.e., the presence of π orbitals delocalised over the molecule or the polymer backbone. The energy difference between the highest occupied molecular orbitals (HOMO) and lowest unoccupied molecular orbitals (LUMO) (HOMO-LUMO gap) is usually in the visible range and gives conjugated molecules photoactive properties such as the ability to absorb or emit light. The term "organic" distinguishes these predominantly carbon-based materials from conventional semiconductors based on inorganic materials such as silicon and germanium.

Conjugation is a common structural property of organic semiconductors, i.e., alternating single and double bonds between carbon atoms. The covalent bond of conjugation in this zigzag backbone results in a planar structure. It contains three sp^2 hybridised orbitals where the orbitals form a triangle within a plane, and one unhybridised p$_z$ orbital pointed out of the molecular plane. The overlap of one sp^2 hybridised orbital with that of another carbon atom along the internuclear axis is called the σ bond. The π bond is formed by overlapping one p_z orbital with the other p_z orbital of neighbouring carbon in a sidewise manner. Due to the energy gap between the occupied bonding orbitals and unoccupied anti-bonding orbitals in the σ bond being larger than that in the π bond, charge carriers are localised in σ bonds and show insulating properties. Thus, the contribution of semiconducting properties is in the π bond.

The semiconducting properties of organic molecules were first realised by Eley (1948) when he examined the conductivity of phthalocyanines and other aromatic compounds (Eley et al. 1953, Eley & Parfitt 1955). Similar observations were also made by Akamatu et al. (1954) on a perylene-bromide complex in 1954. Notably, Bernanose (1955) obtained electroluminescence for several organic molecules by applying a high voltage alternating current as early as 1955. However, the work of organic semiconducting materials only began in the 1960s with the classic studies of ground- and excited-state electronic structure of model molecules, such as anthracene, performed by Pope et al. (1999). Also, a derivative of tetraiodopyrrole was shown to have conductivity in 1963 (McNeill et al. 1963). Since then, various semiconducting organic molecules and polymers have been steadily developed. The use of organic semiconductors in xerography gave the field a particular boost during the 1980s. As photoreceptor materials on photocopier and laser printer drums, organic materials could generate and transport charge, usually as solid mixtures of molecular semiconductors in inert polymer hosts. The vast majority of copiers and laser printers now use those materials systems, and the underlying science has matured, especially in industrial applications.

From the 1980s, several vital experiments demonstrated the fabrication and practical use of cost-effective OFET (Ebisawa et al. 1983, Koezuka et al. 1987), OLED (Tang & VanSlyke 1987, Baldo et al. 1998), thin-film transistors (Burroughes et al. 1988, Horowitz et al. 1989) and OPV devices (Granström et al. 1998, Hoppe & Sariciftci 2004). The situation changed rapidly in the early 2000s due to critical advances in fabricating organic electronic devices that enabled the reproducible measurements of intrinsic charge mobilities in single-crystal devices for a range of molecules in thin-film transistor configurations (Podzorov et al. 2003). These experiments and the increasing demand for low-cost semiconducting materials had unanticipated effects on establishing theories and developing technologies, becoming the pillars of modern organic electronics.

1.4 DPP, T and TT Containing Organic Semiconductors

Among electron acceptor building blocks, 1,4-diketopyrrolo[3-4-*c*]pyrroles (DPP)-based materials have been extensively studied in the past few years for a large amount of high-performance organic electronics such as high-performance pigments (Kaur & Choi 2015) and light-harvesting (LH) chromophores in organic semiconductors (OSCs) (Li et al. 2013). In 1974, Farnum et al. (1974) first isolated DPP-based dye. It has a brilliant red colour, thermal stability, higher melting point and excellent photochemical properties. The DPP units have strong intermolecular donor-acceptor interactions, promoting self-assembly of the polymer and enhancing the charge transport (Chandran & Lee 2013). However, it remained unnoticed for more than a decade due to its poor solubility in halogenated and other common organic solvents, which makes its structure hard to be modified and fabricated. The insolubility is caused by the strong intermolecular hydrogen bonding between nitrogen, hydrogen and oxygen, as well as the π-π interactions among the lactam rings (Naik & Patil 2013). In 1989, Mizuguchi & Homma (1989) developed this dye into 1,4-dithioketo-3,6-diphenyl-pyrrolo-[3,4-*c*]-pyrrole (DTPP), which significantly enhanced the absorption and photoconduction of DPP type materials in the near infrared (IR). This morphological transformation has attracted chemists to explore more possibilities in DPP-containing compounds as important building blocks for PV devices (Chan et al. 1993, Yu et al. 1996).

On the other hand, thiophene (T) is one of the essential classes of heterocyclic compounds in the field of material chemistry. T-based functional materials have played an indispensable role in developing organic optoelectronics. These materials are beneficial due to their semiconducting natures, nonlinear optical responses and effective electron transport properties (Turkoglu et al. 2019). Oligomers and polymers based on T have attracted considerable interest from experiments and theory. Their well-defined physicochemical relationships provide outstanding synthetic control of their molecular electronic structures through control of the T chain length, and substituent variety can be used to tune the molecular orbital energies, charge carrier mobilities and spectral properties of the individual molecular species (Wegner et al. 2008).

Thieno[3,2-*b*]thiophene (TT), also known as thienothiophene, is a heterocyclic compound. It belongs to the family of fused thiophenes and is widely used as an intermediate for synthesising small molecules and polymers in the application of OFETs and OPV. Fused thiophenes are more electron-rich and more structurally rigid, with extended π-conjugation. Therefore, they are ideal candidates for adjusting the bandgap of organic semiconducting materials. TT has been proven a good building block for high mobility p-type semiconductor polymers that show excellent hole mobility (Li et al. 2010). An illustration of these building blocks is shown in Figure 1.1.

Among the different types of DPP derivatives, incorporation of DPP with other aromatic moieties such as T and/or TT into the backbone creates the planarity of the molecule. They are employed as electron donating blocks,

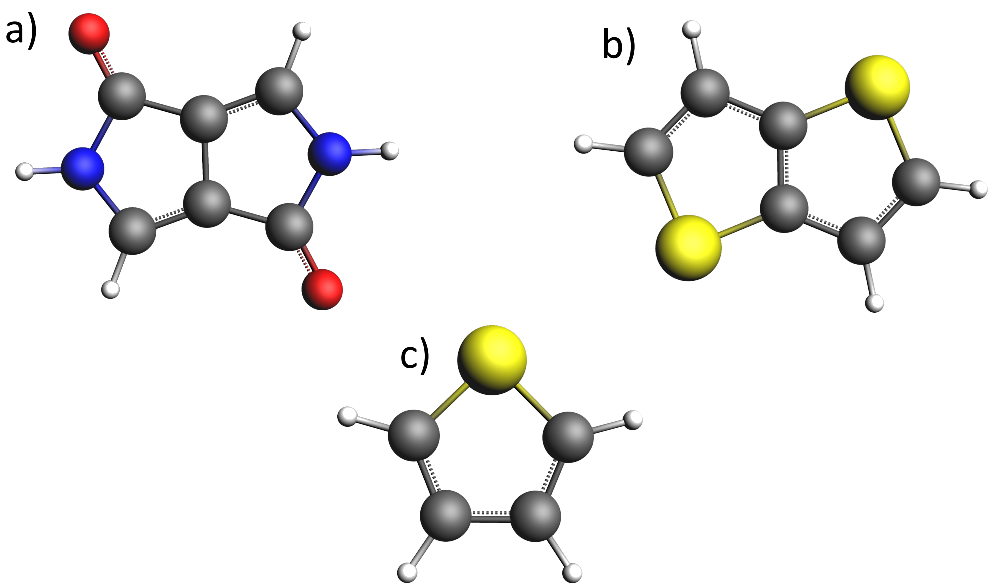

Figure 1.1: Building blocks for molecular crystals and conjugated polymers studied in this thesis: a) DPP, b) TT and c) T.

which can raise the HOMO level, make the materials more efficient at hole transport and result in low-band-gap conjugated systems. In 1,4-diketo-3,6-dithienylpyrrolo[3-4-*c*]pyrrole (TDPP) derivatives, the DPP core is attached by one T unit on each side. They can be the repeating units for the simplest doner-acceptor (D-A) homopolymers (Zoombelt et al. 2010, Li et al. 2012) or can be molecular crystals (Dhar et al. 2015, Naik et al. 2012, Pop et al. 2016). The TDPP-based materials can also form copolymers with multiple T, TT and other groups to enhance the power conversion efficiency (PCE) (Naik et al. 2012). Another typical type called thienothiophene-flanked diketopyrrolopyrrole (DPPTT)-based derivatives contains a DPP unit in the middle and one TT unit on each side (Bronstein et al. 2011, 2013, Meager et al. 2013). Similar to TDPPs, they can connect to additional T, TT or other moieties to construct copolymers (Shin et al. 2015). The TT units extend the polymer coplanarity and promote a more delocalised HOMO distribution along the backbone, which enhances intermolecular charge-carrier hopping. Furthermore, substituting the nitrogen atoms in the DPP core with various linear and branched alkyl groups can achieve higher solubility (Zhu, Dorh, Zhang, Vegesna, Li, Luo, Tiwari & Liu 2012, David et al. 2011, Lee et al. 2012, Li et al. 2013).

Therefore, DPP-based copolymers, in particular TT-flanked DPP and T-containing π-extended conjugated polymers, have emerged as desirable materials for both thin-film transistors and solar cell devices in recent years. The DPP core's electron-deficient nature has been exploited to synthesise extremely narrow bandgap donor-acceptor-type materials that are well-suited for use in OPVs with high PCEs reported from small molecules and polymers. Furthermore, the planarity of the DPP skeleton and its ability to accept hydrogen bonds (and other types of electrostatic interactions) result in copolymers that encourage $\pi - \pi$ stacking. Over the past few years, DPP-based semiconductors have demonstrated remarkable improvements in the performance of both OFET and OPV devices. DPP-based materials are now being exploited in various electronic devices, including complementary circuits, memory devices, chemical sensors, photodetectors, perovskite solar cells, and organic light-emitting diodes. Thus, fused rings flanked DPP is expected to be an effective strategy to extend conjugation length, allowing many possible optoelectronic properties due to the strong electron coupling effect that provides the potential to achieve high performance in electronic devices for a single molecule through smart molecular design (Liu, Bottle & Sonar 2020).

1.5 Excitation Energy Transfer in Molecular Aggregates

1.5.1 Excited States in Isolated Organic Molecule

The ground state of most organic molecules is electrically neutral and has a net spin of zero. An electronically excited state is created, for example, when a photoactive material absorbs an incoming photon. This process can be roughly described as one electron being promoted from an occupied to an unoccupied molecular orbital. Usually, electronic states with net spin zero (i.e. spin quantum number s = 0) or one (spin quantum number s = 1) are referred to as singlets or triplets, respectively. The singlet state is attributed to the appearance of a single spectral line, while the triplet indicates the triple splitting of spectral lines. By absorbing radiation, an electron in a molecule (singlet ground state) is excited to a higher energy level (excited state). This new excited state can be singlet or triplet.

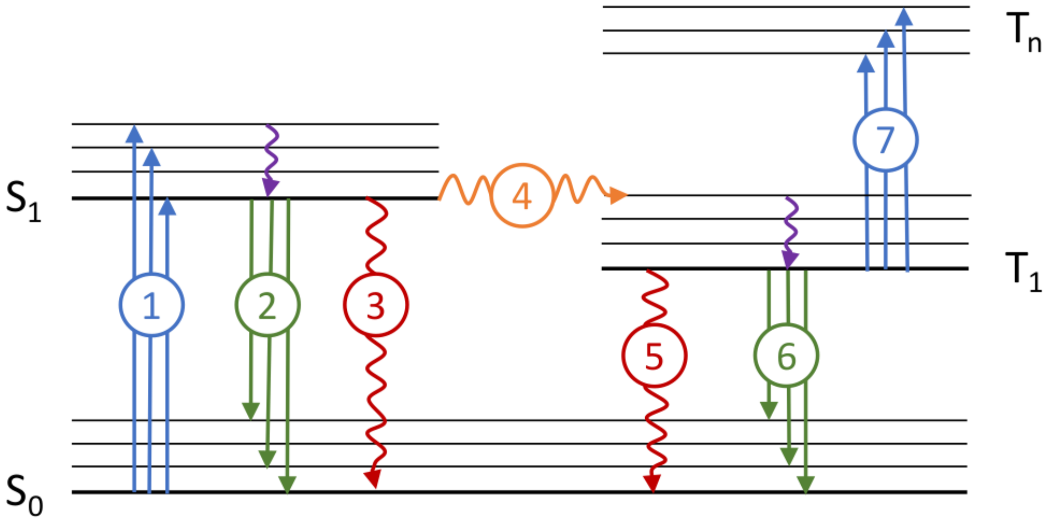

Figure 1.2: The Jablonski diagram of possible transitions between electronic states in organic semiconductors. These transitions are discussed in details in the text.

The Jablonski diagram (Figure 1.2) illustrates transitions between electronic states of an isolated molecule. The straight arrows show all the radiative processes (absorption or emission of a photon), whereas the wavy arrows demonstrate nonradiative processes (e.g. internal conversion). Arrow 1 represents the absorption of a photon that brings a molecule from the ground singlet state S_0 to the first singlet excited state S_1; transitions to other singlet excited states are also possible. After being promoted to an excited state, the electron might simply drop down immediately; a photon would be emitted of exactly the same wavelength as the one that was previously absorbed. However, if the molecule relaxes into a lower vibrational state, some of the initial energy will have been lost as heat. When the electron relaxes, the “distance” back to the ground state is a little shorter. The emitted photon will have lower energy and a longer wavelength than the initial one. This process is called fluorescence and is indicated by arrow 2. The triplet excited state T_1 can be created via the intersystem crossing 4. The radiative transition 6 is called phosphorescence. Fluorescence and phosphorescence can also be referred to as photoluminescence when these transitions are initiated by the absorption of a photon. Nonradiative de-excitation processes are also possible through internal conversion for singlet (arrow 3) and triplet states (arrow 5). Often, the nonradiative transitions 3 and 5 compete with fluorescence and phosphorescence. Finally, transition 7 is the absorption of a photon that brings state T_1 to higher triplet excited states T_n. The time for radiative transitions in singlet states has an order of several nanoseconds, whereas the time in triplet states is tens of milliseconds. The vibrational relaxation of the vibrational energy into the surrounding environment is fast, usually occurring in femto- to picoseconds. In some cases, the singlet exciton can result in two triplet excitons under a fission process.

1.5.2 Excited States and Excitons in Molecular Aggregates

In a molecular aggregate, the excitation energy can be shared between molecules or fragments, leading to the delocalisation of the excited state. The interactions of an excited molecule with its neighbours impose reorganisation of intermolecular distances and partial polarisation of the electronic configuration of the surrounding. The attraction between electron and hole is stabilised by the electrostatic Coulombic force, and the resultant electron-hole pair is termed the exciton.

Exciton plays a vital role in the fundamental study of optical and electronic properties of molecular aggregates. It is a collective response from the interaction of an excited molecule or group of molecules with its neighbours. A characteristic feature of excitons is that their formation does not lead to the separation of charge carriers. Therefore, the excitons are electrically neutral excitations. The concept of exciton was initially proposed by Frenkel (1931) to explain the light absorption in crystals which does not lead to photoconductivity. He proposed that this excited state would be able to travel in a particle-like fashion without the net transfer of charge. Excitons with a total spin of zero or one are called singlet or triplet, respectively. Although the Jablonski diagram describes isolated molecules, transitions in organic solids are usually similar. Therefore, singlet and triplet excitons are often denoted as S_1 and T_1. Excitons are often treated in the two limiting cases of small dielectric constant versus large dielectric constant, corresponding to Frenkel exciton and Wannier–Mott exciton.

In materials with a relatively small dielectric constant, the Coulomb interaction between an electron and a hole may be strong, and therefore, the excitons tend to be small. Molecular excitons may even be entirely located on the same molecule, like in fullerenes. Frenkel excitons are typically found in organic molecular aggregates composed of aromatic molecules, including molecular crystals, conjugated polymers and light-harvesting complexes. For example, the Frenkel model is a good approximation for molecular crystals with van der Waals (vdW) bonding, where the exciton is well localised within one molecule. Due to the translation symmetry of the crystal, the exciton can move along the lattice sites transferring the energy to the luminescence centres (Nematiaram et al. 2021). Similarly, the Frenkel model is frequently employed to unravel the nature of energy transport in multi-chromophoric photosynthetic complexes (Kriete et al. 2019) and conjugated polymeric systems (Barford 2013). Thus, excitons play a crucial role in light emission processes.

For semiconducting materials with high dielectric constants, the Coulomb interactions are screened (damped) by the valence electrons. In this case, the electrons and holes are weakly bound, which allows the exciton to spread over several molecular units in the aggregates. Therefore, the exciton is described better with the Wannier-Mott model. This type of exciton is often found in inorganic semiconductors. An intermediate case between Frenkel and Wannier excitons is the charge-transfer exciton, formed when the electron and the hole occupy adjacent molecules. This type of exciton is also found frequently in organic and molecular aggregates. In this case, unlike Frenkel and Wannier excitons, charge transfer excitons display a static electric dipole moment.

1.5.3 Exciton Dynamics

In organic aggregates, an exciton can be transferred from an excited donor to an acceptor via non-radiative energy transfer. At the end of this process, the donor molecule is in the ground state, and the acceptor molecule is in the excited state. The collective relocation of the exciton between molecules (chromophores) in the aggregate is often called exciton dynamics or exciton diffusion. The transport of the exciton can occur via Förster (through-space) (Förster 1948) or Dexter (through-bond) (Dexter 1953) mechanisms (Figure 1.3a and 1.3b). In the Förster mechanism, the rate of energy transfer between two chromophores (energy donor and energy acceptor) depends on the spectral overlap between the donor emission and acceptor absorption spectra (i.e. resonance between their excitation energies), and on the Coulombic interaction (coupling) between their transition densities. Therefore, this type of energy transfer is called Förster resonant energy transfer (FRET). Usually, only singlet excitons can be transferred via the Förster mechanism; however, a triplet exciton that is located at a phosphorescent donor also can undergo FRET. The actual exchange of electrons between donor and acceptor takes place during the Dexter energy transfer (1.3b) when there is a significant overlap of the donor's and acceptor's molecular orbitals. This may happen when the donor and acceptor are only about 1 nm apart. Both singlet and triplet excitons may be transferred by the Dexter mechanism. The exciton can be separated into electron and hole when their binding energy is overcome. If the energy of the LUMO of the acceptor is significantly lower than that of the LUMO of the excited donor molecule, then electron transfer from donor to acceptor may take place (1.3c). This process is called charge transfer (CT); it is a short-range interaction that takes place when there is a significant spatial overlap between wavefunctions of the donor and acceptor molecules.

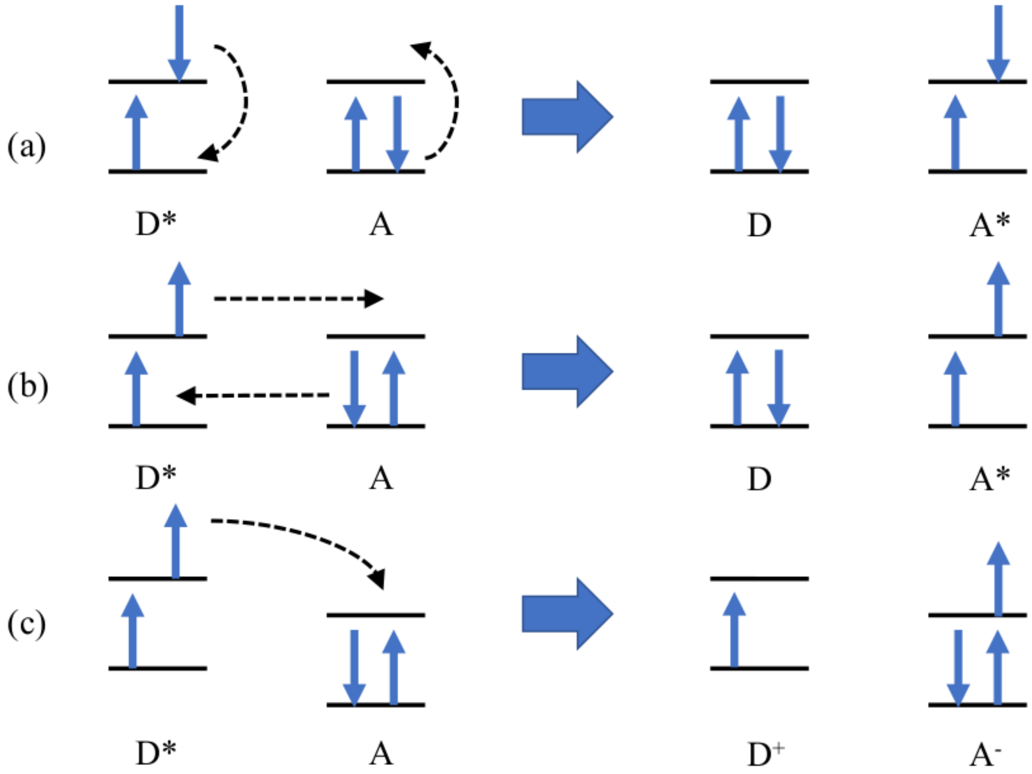

Figure 1.3: Different excitation energy transfer mechanisms in organic semiconductors. (a) Förster energy transfer. (b) Dexter energy transfer. (c) Electron transfer.

The Coulombic interaction (excitonic coupling) term in the Förster mechanism is often approximated by the interaction between the transition dipole moments (point dipoles placed on the chromophores' centres of mass). However, this only works well when the inter-chromophore distance is very large compared to the chromophore size. When the distance between molecules is comparable to the molecular sizes, one can discretise the transition density, expressing it as charges centred on the atoms (atomic transition charges (ATC)) (Chang 1977, Yamagata et al. 2011), and uses these to compute the couplings. For closely packed molecular aggregates, whose intermolecular interactions are dominated mainly by vdW forces (e.g. molecular crystals), these approximations often inadequately describe the excitonic coupling between chromophores, as other effects may contribute to the excitonic coupling. Scholes & Ghiggino (1994) and Harcourt et al. (1994) characterised the nature of these short-range contributions by studying the interactions between Frenkel and CT excited configurations. They identified that the dominant non-Coulombic short-range contributions in molecular aggregates are (i) a penetration interaction, generally reinforcing the Coulombic term and (ii) a Dexter-type exchange term which opposes it but is of smaller magnitude. Short-range contributions to the excitonic couplings were found to play an essential role in the exciton dynamics of molecular aggregates, especially molecular crystals (Aragó & Troisi 2015*a*, Aragó & Troisi 2015*b*). The short-range contributions can cause significant fluctuations in the couplings due to their strong dependence on the intermolecular overlap. Thus, the accuracy with which they are computed affects the sensitivity of the system's properties to both static and dynamic disorder.

1.6 Challenges for Organic Semiconductors

Although organic semiconductors have an excellent potential for optoelectronic devices, their charge transport efficiency is the limiting factor that prohibits their development. For electron mobility, the theoretical limit of organic semiconductors is less than the typical values of pure silicon crystal semiconductors (~ 1000 cm^2 V^{-1} s^{-1}). In the 1980s, the mobility of organic semiconductors was only 10^{-5} cm^2 V^{-1} s^{-1} when the fabrication of OFETs was reported (Tsumura et al. 1986). After a decade, in the 1990s, Bao et al. (1996) showed an impressive improvement in the mobility to nearly a thousand times (0.1 cm^2 V^{-1} s^{-1}). The inherent challenges have been significantly mitigated over the next two decades by synthesising a wide range of chemical structures to search for materials with high charge transport properties (Himmelberger & Salleo 2015, Schott et al. 2015, Takeda et al. 2016). The mobility was increased to more than 10 cm^2 V^{-1}, s^{-1} (Sundar et al. 2004, Huang et al. 2015, Hamai et al. 2018, Chu et al. 2018) and some theoretical calculations predict the mobility of organic semiconductors can be even above 100 cm^2 V^{-1} s^{-1} (Zhu, Yi, Li, Kim, Coropceanu & Brédas 2012, Zhang et al. 2016).

Despite significant efforts in the past few decades, charge transport efficiency in organic semiconducting materials remains much lower than their inorganic counterparts. There are various ways to improve the performance of organic electronics, such as updating device architecture, considering different electrodes and encapsulation materials, and the ease of processing. Nevertheless, the most challenging and vital part is to obtain a clear picture of the CT and/or exciton transport properties of the active materials - a quest that has been actively under investigation by both experiment and theory for decades.

Theory and computational chemistry tools play a significant role in searching for new organic materials with improved mobility by rationalising the available results and guiding the synthesis of new materials. Despite remarkable improvement in the accuracy of the electronic structure calculations and the accessible simulation time scale of a broad range of organic semiconducting materials, it is still not possible to predict the relative mobility of many compounds. Many attempts have been made to characterise organic semiconductors using theories and methods analogous to those used for inorganic semiconductors. It became apparent only recently that this analogy can be somewhat misleading. For example, the transport in crystalline anthracene cannot be described as simple hopping between localised sites or by a band transport model without contradicting part of the experimental evidence (Aragó & Troisi 2015*a*). Subsequently, exciton or charge transport in organic crystalline materials remains highly controversial despite impressive progress during the past few decades.

Two limiting transport regimes (hopping and band transport) are often invoked to describe the exciton diffusion in molecular aggregates. However, none of these limits is appropriate for exciton transport in most studied materials. Even though many theories also deal with the transition regime between hopping and band transport, an additional complication has become evident for molecular semiconductors. The thermal motion of molecules at room temperature is sufficient to cause a fluctuation of the transfer integrals between neighbouring molecules of amplitude comparable to that of the average transfer integral (Troisi & Orlandi 2006*a*). This dynamic disorder appeared to be one of the limiting factors to charge mobility, a specific feature of molecular semiconductors. It mainly originates from the softness of the intermolecular interactions. It is also due to the sensitivity of the transfer integral to the small relative displacements of the molecules (Brédas et al. 2002). This observation dramatically affects the description of exciton transport in, for example, organic crystals that originate from an exciton in a molecular crystal or thin film.

The qualitative features of charge and exciton transport in polymeric semiconductors have been investigated (primarily based on phenomenological theories) for over a decade (Tessler et al. 2009, Rivnay et al. 2012). However, it is still challenging to establish a correlation between chemical structures and the exciton transport properties of these materials. This is one of the main reasons that accounts for the failure to fully exploit polymer electronic devices. It was believed for many years that increased local order was the key ingredient for high exciton mobility (McMahon et al. 2011). However, the introduction of new high-mobility amorphous polymers (Nielsen et al. 2013) indicates that we have not identified all the elements that make an excellent polymeric semiconductor. Conjugated polymers exhibit strong electron-electron interactions and electron-nuclear coupling and are subject to spatial and temporal disorder. The exciton transport in polymeric materials is characterised by multiple (and often overlapping) time scales; it is determined by both intrinsic processes (e.g., coupling to nuclear degrees of freedom and electrostatic interactions) and extrinsic processes (e.g., polymer-solvent interactions); and it is both an intrachain and interchain process. Consequently, simplified but realistic models are needed to make progress in both characterising exciton states and correctly describing their dynamics (Barford 2013).

In general, exciton transport models are constructed by assuming the shape of the density of state (DOS) and the hopping rate between states. The latter is influenced by the localisation length of the charges and determines the type of variable range hopping methods used. Phenomenological models of transport can describe the electrical characteristics of the device. However, they are too coarse to provide insights into the structural and chemical properties of the active layers (polymers) and their relationships with exciton transport. Furthermore, electronic structure calculations based on realistic polymer conformation show that the shape of the DOS cannot be assumed to be a simple function (typically a Gaussian). Also, the hopping rate depends on the carrier's energy, with higher energy carriers being able to hop at longer distances. Thus, to progress in this, it is necessary to go beyond the phenomenological models, taking advantage of recent advances in electronic structure calculations and molecular simulations.

Moving away from phenomenological models requires constructing an atomistic model of the organic semiconducting materials (e.g. small molecules, molecular crystals, polymers etc.) and evaluating its electronic structure. Both tasks are particularly challenging from the computational point of view (especially for polymers), and the majority of efforts have focused only on one of them at a time. Classical molecular dynamics (MD) simulations have recently found application in the study of optical and electronic properties of materials and biomolecules. For this class of applications, MD simulations are used to generate the structures explored by the system under the experimental conditions and to interpret experimental results in conjunction with quantum chemical methods. In other words, the nuclear degrees of freedom are treated classically, whereas the excitation energies are calculated quantum mechanically along the classical trajectory. Thus, the quality of the results will be almost entirely determined by the quality of the force fields used.

For all applications where MD is a preliminary step toward the study of electronic structure properties, it is challenging to find sufficiently accurate force fields. All single molecules and semiconducting polymers of interest display a complex chemical structure with extended π-conjugation that prevents the use of standard force fields. For example, the bonds between sp^2 carbon atoms usually have different bond orders (hence different distances and force constants). Standard classical force fields usually cannot properly describe systems containing many heteroatoms within the conjugated frame (Do & Troisi 2015, Claridge & Troisi 2019). Errors of the order of 0.05 Å on the bond distances can be tolerable for thermodynamic properties but lead to unacceptable electronic structure properties. Force fields suitable for large conjugated molecules need to use many atom types and parameters. They also tend to be highly system-specific and not transferable. Moreover, an obstacle one often has to confront here is the mismatch in the force fields describing the interactions at the classical level and the electronic structure methods employed for subsequent quantum chemistry calculations (Andreussi et al. 2017).

1.7 Aims and Objectives

In this thesis, we utilise multiscale computational chemistry methods to characterise the electronic structure properties of organic semiconducting materials containing DPP, TT and T. We investigate the effects of the dynamic disorder on the transport of the exciton in molecular crystals of several recent synthesised mono- and di-alkylated TDPP derivatives. These systems exhibit great potential for PV applications due to their broad optical absorption and efficient charge transport. However, little is known about the relationship between dynamic disorder and exciton transport. The ability to control this inherent property will provide valuable tools for designing and developing efficient organic semiconductors using molecular crystals.

DPP-based conjugated polymers have emerged as desirable materials for thin-film transistors and solar cell devices. The electron-deficient nature of the DPP core has been exploited to synthesise extremely narrow bandgap donor-acceptor-type materials well suited for use in organic photovoltaics with high power conversion efficiencies reported in both small molecules and polymers. However, the detail of the relationship between the morphology and electronic structure properties of this class of conjugated polymers is still unclear, and a fundamental understanding is necessary for their design and development. Thus, one of the goals of this thesis is to provide insights into the electronic excited states of the polymer chains and their connections to the dynamical disorder of the nuclei.

To confront the mismatch in the description of the interactions at the classical level and the electronic structure methods employed for subsequent quantum chemistry calculations, we parameterise the force fields for the studied molecular crystals and conjugated polymers. The goal is to find a set of parameters that minimises the differences between the classical and the *ab initio* forces. Thus, by design, the force fields used to propagate the nuclear dynamics are comparable to those targeted *ab initio* methods used in the subsequent electronic structure calculations.

1.8 Thesis Outline

This thesis is organised into the following six chapters:

Chapter 1 gives a brief introduction to the field of organic electronics and organic semiconducting materials. It identifies DPP-based organic semiconductors, particularly TT-flanked DPP and T-containing π-extended conjugated polymers, which are emerging materials for thin-film transistors and solar cell devices in recent years. It motivates the need to characterise the role of dynamic disorder to exciton dynamics in ordered systems (molecular crystals) and the structure-property relationships in disordered systems (amorphous polymers). Furthermore, it emphasises the need for an accurate and robust approach for rapidly parameterising the force field for medium-to-large conjugated molecules so that the empirical forces are as close as possible to those computed with any predetermined electronic structure calculation method.

Chapter 2 describes the theoretical background underpinning the work of the thesis. It starts with a description of the strategy for optimising the force fields for macromolecular assemblies containing DPP, TT and T. It then overviews the theoretical methods commonly used to describe excited states in molecular aggregates and charge and exciton transport in organic semiconductors.

Chapter 3 starts the investigation into exciton dynamics and structure-property relationships in organic semiconductors containing DPP, TT and T by extending the adaptive force-matching technique to rapidly parameterise the force fields for complex conjugated systems. The strategy is to fragment the larger molecule into smaller segments, obtain their parameters, and then assemble them to derive the parameters for the larger molecule. The aim is to obtain force fields consistent with any predefined electronic structure calculation method. Subsequently, the nuclear dynamics (potential energy surfaces) obtained using classical MD simulations are comparable and consistent with the targeted quantum chemical methods used to compute the electronic structure properties.

Chapter 4 investigates the effects of the dynamic disorder on the transport of the exciton in molecular crystals of several recent synthesised mono- and di-alkylated 1,4-diketo-3,6 dithiophenylpyrrolo[3-4-c]pyrrole derivatives. These systems exhibit great potential for photovoltaic applications due to their broad optical absorption and efficient charge transport. The exciton dynamics are studied using a model Hamiltonian, in which the thermal fluctuations of the excitonic coupling and the non-local exciton-phonon couplings have been appropriately taken into account. The chapter concludes that dynamic disorder is the crucial property that drives the excitation energy transfer in molecular crystals and is a valuable tool for designing and developing efficient organic semiconductors.

Chapter 5 characterises the structure-property relationship in amorphous polymers containing DPP, TT and T. It demonstrates clear evidence of the correlations between the structure and electronic properties in this class of amorphous conjugated polymers. It suggests that these relationships should provide valuable tools for designing and developing efficient organic semiconductors from this class of conjugated polymer.

Finally, Chapter 6 summarises research efforts into exciton dynamics and structure-property relationships in organic semiconductors and contributions made by theoretical and computational studies to the field of optoelectronics. The chapter ends by highlighting potential extensions and future research interests.

Chapter 2

Methodology

2.1 Synopsis

This chapter begins by describing the challenge of modelling organic semiconductors, which involves using various computational tools and techniques. It then gives an overview of the core methodologies that allow us to model electronic states and transport properties in organic semiconductors, spanning different time and length scales. These include the use of MD simulation to sample the nuclear coordinates, approaches to parameterise accurate force field for conjugated molecular systems, density functional theory to obtain electronic and excited states properties, and finally, tight-binding (TB) model Hamiltonian for determining electronic and transport properties for a large-scale molecular system. Other specific methods and techniques are discussed, where it is appropriate, in the method appendix section of each results chapter (Chapters 3, 4 and 5).

2.2 Modelling Organic Semiconductors

Charge and exciton transport in organic semiconductors often involves many processes occurring on different length- and time scales. Modelling these processes involves using theory and simulation techniques that span these. The different length- and time scales used for studying organic semiconductors are illustrated in the schematic in Figure 2.1

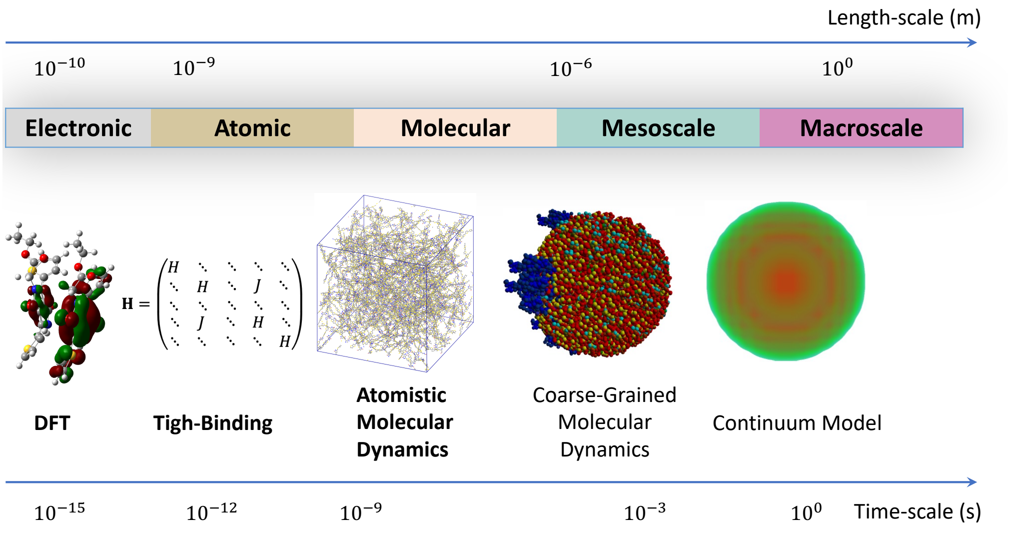

Figure 2.1: Schematic showing different length- and time scales relevant to the modelling of organic semiconductors. Computational methods employed in the thesis are highlighted in bold.

Macroscopic properties of devices based on OSCs can be characterised using quantum mechanics and molecular modelling. To study the excited state dynamics, we need relatively large systems of many thousands of molecules since thin films used in devices are of order 100 nm thick. Disorder in the films also means that we must sample many realisations of the system to obtain useful statistics. This motivates the need for using multiscale modelling approaches and computationally efficient methods to access large assemblies of molecules based on molecular modelling and electronic structure calculations. Figure 2.1 shows that the computational methods used in this thesis span length scales from a few to several thousands of angstroms, and time scales from femto- to microseconds. The different length- and time-scale calculations inform each other. For example, density functional theory (DFT) and MD simulations are used to compute parameters for TB, and molecular structures generated by MD simulations are utilised in electronic structure calculations.

We are interested in individual molecules' chemical and electronic structure properties, which we investigate with DFT. In addition, DFT is used to obtain parameters that feed into other aspects of our works, e.g. parameters for the TB model Hamiltonian and force field parameterisation for classical MD simulations. DFT is also employed to compute the excited state properties of an individual polymer chain. Furthermore, the excitonic couplings between pairs of molecules are also characterised within the DFT framework.

To characterise the electronic structure properties and excited state dynamics in organic semiconductors, we first need to obtain the structures and ensembles of the systems of interest. We use crystal structure databases for molecular crystals and build up supercells of the complete structure. For amorphous systems, polymer chains are built by growing segment by segment. The result of this procedure is that low-energy sites are preferred over high-energy sites. Thus, disordered bulk systems containing chains in realistic equilibrium conformations are created. MD simulations are employed to propagate nuclear dynamics and generate ensembles of equilibrium structures.

In MD simulations, it is vital that the force fields used to describe the nuclear dynamics are accurate enough to capture the actual molecular motion of the system. A challenge that one often has to confront here is the mismatch in the description of the interactions at the classical level and the electronic structure methods employed for subsequent quantum chemistry calculations. To overcome this, we systematically parameterise the force fields for all studied semiconducting materials in this thesis. By design, the force fields used to propagate the nuclear dynamics are comparable to those targeted *ab initio* methods used in the subsequent electronic structure calculations.

Depending on the properties of the organic semiconducting materials we are interested in, we use a subset of these methods to investigate the nuclear dynamics, the electronic structure properties, excitation energy transfer and exciton transport in them.

2.3 Molecular Dynamics Simulations

MD allows detailed microscopic modelling on the molecular scale. This approach gives us an insight into how microstructure and interactions between molecules influence bulk properties. In a nutshell, MD simulation consists of the numerical, step-by-step solution of the classical equations of motion, which for a simple atomic system may be written as

$$m_i \ddot{\boldsymbol{r}}_i = \boldsymbol{F}_i \tag{2.1}$$

$$\boldsymbol{F}_i = -\frac{\partial \mathcal{U}}{\partial \boldsymbol{r}_i} \tag{2.2}$$

where $\boldsymbol{F}_i$ is the force acting on atom i, m_i is the mass of the atom and $\boldsymbol{r}_i$ is the position of atom i. $\mathcal{U}$ or to be exact $\mathcal{U}(\boldsymbol{r}^N)$ is the potential energy of the system that consists of N atoms. Here, $\boldsymbol{r}^N = (\boldsymbol{r}_1, \boldsymbol{r}_2, ...\boldsymbol{r}_N)$ represents the complete set of $3N$ atomic coordinates. To propagate the dynamics, we need to be able to calculate the forces $\boldsymbol{F}_i$, and these are usually derived from a potential energy $\mathcal{U}(\boldsymbol{r}^N)$. Ideally, the potential energy $\mathcal{U}(\boldsymbol{r}^N)$ should be computed from the first principles. However, this is prohibitively expensive; therefore, empirical force fields are often employed to approximate the potential energy surface.

Force-fields are complex equations, but they are easy to calculate. The simplicity of the force-field representation of molecular features: springs for bond length and angles, periodic functions for bond rotations, Lennard–Jones potentials for vdW, and the Coulomb's law for electrostatic interactions, respectively, assure that energy and force calculations are fast even for large systems. Force fields currently used in atomistic molecular simulations differ in how they are parameterised. Parameters are not necessarily interchangeable, and not all force-fields allow to represent all molecule types, but simulations conducted using modern force-fields are generally equivalent. Once the forces acting on individual atoms are obtained, classical Newton's law of motion is used to calculate accelerations and velocities. The trajectories of individual atoms are propagated in time with a symplectic integrator, for example, the Verlet algorithm (Verlet 1967), which conserves the total energy of the system. As the integration of movement is done numerically, a time step shorter than the fastest movements in the molecule should be used to avoid instability. This usually is between 1 and 2 fs for atomistic simulations and is the major bottleneck of the simulation procedure.

A thermostat and barostat are applied to the system to reproduce thermodynamic observables. In our work, the Langevin thermostat (Hoover et al. 1982) is employed to maintain the temperature of the system. This is achieved through a modification of Newtons's equations of motion as

$$m_i \ddot{\boldsymbol{r}}_i = -\frac{\partial \mathcal{U}}{\partial \boldsymbol{r}_i} - \gamma m_i \dot{\boldsymbol{r}}_i + \boldsymbol{f}_i \tag{2.3}$$

where γ_i is a friction coefficient, and $\boldsymbol{r}_i$ is a random force simulating the random kicks by the damping of particles between each other due to friction. The random numbers are chosen from a Gaussian distribution with the following variance

$$\sigma_i^2 = 2\gamma m_i k_B T / \Delta t \tag{2.4}$$

where k_B is the Boltzmann constant, T is the temperature and Δt is the time-step used in the MD to integrate the equations of motion. From equations 2.3 and 2.4, it is obvious that the Langevin dynamics is identical to the classical Hamiltonian (or Newtonian) in the limit of vanishing γ.

To control the pressure, we use a modified Nosé-Hoover method in which

Langevin dynamics is used to control fluctuations in the barostat. In general, the pressure is controlled by dynamically adjusting the size of the unit cell and rescaling all atomic coordinates (other than those of fixed atoms) during the simulation. The Langevin piston Nose-Hoover method is a combination of the Nose-Hoover constant pressure method (Martyna et al. 1994), with piston fluctuation control implemented using Langevin dynamics as described in Feller et al. (1995). The equations of motion resemble Martyna et al. (1994) equations, but an additional damping (friction) force and stochastic force are introduced. A suitable choice of collision frequency then eliminates the unphysical oscillation of the volume associated with the piston mass. In this way, it is similar to the weak coupling Berendsen algorithm, but in contrast, it yields the correct ensemble.

2.4 Optimise Force Fields for Conjugated Molecular Systems

In this thesis, we extend the adaptive force-matching technique (Do & Troisi 2015) to rapidly parameterise force fields for complex conjugated molecular systems. The idea behind this procedure is to find a set of parameters that minimises the differences between the classical forces and the *ab initio* forces. Here, the latter can be computed using any reference electronic structure method. Generally, this is chosen to be consistent with the method employed in subsequent quantum chemistry calculations. In addition, an appropriate force field that best represents the system of interest has to be determined in advance. The errors between the two types of forces are computed from a set of uncorrelated configurations generated from MD simulations during the production runs. In our approach, a set of parameters $\{p_j\}$ is optimised by minimising an objective function $O(\{p_j\})$, which is defined as the root mean square deviation of two types of forces:

$$O(\{p_j\}) = \sqrt{\frac{1}{3MN}\sum_{k=1}^{M}\sum_{i=1}^{N}\left\|\mathbf{f}_{i,k}^{AB} - \mathbf{f}_{i,k}^{FF}\right\|^2} \tag{2.5}$$

where N is the number of atoms in the molecule and M is the number of configurations used. $\mathbf{f}_{i,k}^{AB}$ denotes the *ab initio* forces exerted on atom i of configuration k and $\mathbf{f}_{i,k}^{FF}$ are the equivalent forces calculated using the force fields. $\|...\|$ denote the norm. The optimisation is carried out using a Monte Carlo (MC) method. More details on this can be found in the computational details section of Chapter 3.

The optimisation process starts from an initially guessed force field with appropriate atom types assigned. The key idea in selecting different atom types is to maintain the alternation of single and double bonds along the backbone. This is crucial for conjugated molecules, especially for semiconducting polymers, which often display complex chemical structures with extended π-conjugation that prevents the use of standard force fields. Hence, we tend to have more atom types than standard force fields. In addition, we also employ symmetry and chemical intuition to reduce the number of types of atoms where it is possible. The force constants and torsional energy barriers for this initial guess can be taken from the literature, e.g., CHARMM, AMBER, OPLS, etc., force fields, depending on the force field style employed. The equilibrium bonds and angles are taken from the quantum mechanical equilibrium structures. An initial set of M geometries close to the equilibrium structure are then generated from an MD simulation, followed by M computations of the *ab initio* forces of these geometries.

The force field parameter set $\{p_j\}$ is then modified until the objective function $O(\{p_j\})$ is minimised. After the force field is parameterised, the newly constructed force field is used as the new guess force field, and the procedure is repeated until convergence is met. In general, 2–3 iterations are sufficient, we found. The method produces a force field that best matches the *ab initio* forces for the structure visited at a given temperature. Therefore, it is suitable for all the "rigid" degrees of freedom, i.e. all intermolecular degrees of freedom except the torsions, whose barrier is easily overcome at room temperature.

For molecules with more than one chromophore, we fragment them into smaller segments, obtain their parameters and assemble them to derive the force field for the whole molecule. We perform a torsional scan for each missing flexible dihedral angle to obtain the torsion potentials. This is done by first carrying out an *ab initio* scan (constrained optimisation) at the appropriate level of theory, followed by a "classical" scan using the force field derived from the first stage. The difference between the two scans is the torsion potential for the dihedral angle of interest. Finally, the torsion potential is fitted to a truncated cosine series.

For any specific problem, one must decide on the parameters to be optimised and the number of reference structures needed (to be discussed in Chapter 3). Since we are only interested in the intramolecular interactions, the intermolecular part (electrostatic and vdW interactions) is not optimised. Instead, the non-bonded parameters are directly taken from the existing force fields, and the charges are computed following the same approach as those of the selected force field family.

2.5 Electronic Structure Calculations

Electronic structure theory is the study of electrons in matter. The correlated motion of the electrons in such systems gives rise to the wide variety of phenomena observed in nature. The Schrödinger equation of quantum mechanics governs the behaviour of these electrons, and much work is devoted to solving these equations using a variety of methods, from highly accurate quantum MC and quantum chemistry, through DFT, including linear-scaling methods for thousands of atoms, to *ab initio* and semi-empirical TB. These simulations are being used to study a wide variety of systems, including nanostructures, liquids and interfaces, as well as to discover new structures of matter under extreme conditions and design materials with properties to order. Here, we are interested in charge and exciton transport in organic molecular aggregates. In particular, we seek to understand the nature of the charge carrier (electron or hole) in the material, along with its relationship with the chemical structure, defects and disorder, and how it changes in time. We calculate electronic structure with DFT and TB methods. These are approximate solutions to the time-independent Schrödinger equation. In addition, we calculate the optical properties of molecules with linear response time-dependent density-functional theory (TD-DFT) to characterise the excited states of molecules and aggregates.

2.5.1 The Schrödinger Equation

The time-independent, nonrelativistic Schrödinger equation is given as $\hat{H}\psi = E\psi$, where $\hat{H}$ is the Hamiltonian operator and ψ is a set of solutions, or eigenstates, of the Hamiltonian (the wavefunction). Each of these solutions, ψ_n, has an associated eigenvalue, E_n, a real number that satisfies the eigenvalue equation. The detailed definition of the Hamiltonian depends on the physical system being described by the Schrödinger equation. There are several well-known examples, such as the particle in a box or a harmonic oscillator, where the Hamiltonian has a simple form, and the Schrödinger equation can be solved exactly. Generally, we are interested in more complicated molecular systems in which multiple electrons interact with multiple nuclei in most cases. In these instances, a complete description of the electronic Schrödinger is given as

$$\left[-\frac{\hbar^2}{2m_e}\sum_{i=1}^{N}\nabla_i^2-\sum_{i=1}^{N}V(\mathbf{r}_i)+\sum_{i=1}^{N}\sum_{j<i}U(\mathbf{r}_i,\mathbf{r}_j)\right]\psi=E\psi \tag{2.6}$$

Here, m_e is the electron mass. The three terms in brackets define, in order, the kinetic energy of each electron, the interaction energy between each electron and the collection of atomic nuclei, and the interaction energy between different electrons. For the Hamiltonian we have chosen, ψ is the electronic wave function, which is a function of each of the spatial coordinates of each of the N electrons, i.e. $\psi = \psi(\mathbf{r}_1, ..., \mathbf{r}_N)$, and E is the ground-state energy of the electrons. The ground-state energy is independent of time, so this is the time-independent Schrödinger equation.

Equation 2.6 indicates that the Schrödinger equation is a many-body problem. The individual electron wave function, $\psi_i(\mathbf{r})$, cannot be found without simultaneously considering the individual electron wave functions associated with all the other electrons. The full wave function solution to the Schrödinger equation is a function of $3N$ coordinates. Furthermore, the number of electrons is considerably larger than the number of nuclei in a molecule. Thus, solving the Schrödinger equation for practical materials poses significant challenges. For example, if we were interested in a single molecule, e.g. CO_2, the total wave function is a 66-dimensional function, which is manageable. However, if we dealt with a nanocluster of several thousand atoms or a long-chain polymeric system, the full wave function requires several tens of thousands of dimensions, making it impossible to solve with current computing technology.

Although solving the Schrödinger equation can be viewed as the fundamental problem of quantum mechanics, the wave function for any particular set of coordinates cannot be directly observed. The quantity that can (in principle) be measured is the probability that the N electrons are at a particular set of coordinates, $\mathbf{r}_1, ..., \mathbf{r}_N$. This probability is equal to $\psi^*(\mathbf{r}_1, ..., \mathbf{r}_N), \psi(\mathbf{r}_1, ..., \mathbf{r}_N)$, where the asterisk indicates a complex conjugate. A closely related quantity to this is the density of electrons at a particular position in space, $n(\mathbf{r})$. This can be written in terms of the individual electron wave functions as $n(\mathbf{r}) = 2\sum_i \psi^*(\mathbf{r})\psi(\mathbf{r})$. Here, the summation goes over all the individual electron wave functions occupied by electrons. Hence, the term inside the summation is the probability that an electron in an individual wave function $\psi_i(\mathbf{r})$ is located at position $\mathbf{r}$. The factor of 2 indicates that electrons have spin, and the Pauli exclusion principle states that each electron wave function can be occupied by two separate electrons, provided they have different spins. This is a purely quantum mechanical effect with no counterpart in classical physics. The point here is that the electron density, $n(\mathbf{r})$, a function of only three coordinates, contains a significant amount of the information that is physically observable from the full wave function solution to the Schrödinger equation, which is a function of $3N$ coordinates.

2.5.2 Density Functional Theory

The entire field of DFT rests on two fundamental mathematical theorems proved by Hohenberg & Kohn (1964) and the derivation of a set of equations by Kohn & Sham (1965) in the mid-1960s. The first Hohenberg and Kohn's theorem states that the ground-state energy from Schrödinger's equation is a unique functional of the electron density. In other words, there exists a one-to-one mapping between the ground-state wave function and the ground-state electron density. The ground-state electron density uniquely determines all properties, including the energy and wave function, of the ground state. This means it is possible to solve the Schrödinger equation by finding a function of three spatial variables, the electron density, rather than a function of 3N variables, the wave function. The second Hohenberg–Kohn theorem defines a critical property of the functional: The electron density that minimises the energy of the overall functional is the true electron density corresponding to the full solution of the Schrödinger equation. Thus, the second theorem provides a variational approach to obtaining the electron density using approximate forms of the functional.

$$E[\{\psi_i(\mathbf{r})\}] = E_{\text{known}}[\{\psi_i(\mathbf{r})\}] + E_{XC}[\{\psi_i(\mathbf{r})\}] \tag{2.7}$$

where the energy functional $E[\{\psi_i\}]$ is split into a "known" term, $E_{\text{known}}[\{\psi_i\}]$, that can be expressed in simple analytical form, and everything else, $E_{XC}[\{\psi_i\}]$. Here, the single-electron wave functions, $\psi_i(\mathbf{r})$, collectively define the electron density, $n(\mathbf{r})$. The term $E_{XC}[\{\psi_i\}]$ is the exchange–correlation functional, and it is defined to include all the quantum mechanical effects that are not included in the "known" terms. The "known" functional includes four contributions:

$$\begin{aligned} E_{\text{known}}[\{\psi_i\}] = -\frac{\hbar^2}{m_e}\sum_i \int \psi_i^*(\mathbf{r})\nabla^2\psi_i(\mathbf{r})\mathrm{d}\mathbf{r} + \int V(\mathbf{r})n(\mathbf{r})\mathrm{d}\mathbf{r} \\ + \frac{e^2}{2}\int\int \frac{n(\mathbf{r})n(\mathbf{r}')}{|\mathbf{r}-\mathbf{r}'|}\mathrm{d}\mathbf{r}\mathrm{d}\mathbf{r}' + E_{\text{ion}}. \end{aligned} \tag{2.8}$$

The terms on the right are, in order, the electron kinetic energies, the Coulomb interactions between the electrons and the nuclei, the Coulomb interactions between pairs of electrons, and the Coulomb interactions between pairs of nuclei. Assuming that we can express the as-yet-undefined exchange-correlation energy functional in some useful way. It is still challenging to obtain the ground state energy and the electron densities from Kohn and Hohenberg's theorem due to the inherent many-body problem of interacting electrons in a static external potential (the third term on the right-hand side of Eq. 2.8).

The Kohn and Hohenberg's theorem was further developed by Kohn and Sham to produce Kohn-Sham DFT. Within this framework, the intractable many-body problem of interacting electrons in a static external potential is reduced to a tractable problem of noninteracting electrons moving in an effective potential.

The task of finding the correct electron density could be expressed in a way that involves solving a set of equations in which each equation only involves a single electron. Therefore, the solution of the Kohn–Sham equations are single-electron wave functions that depend on only three spatial variables, $\psi_i(\mathbf{r})$. The Kohn–Sham equations have the general form

$$\left[-\frac{\hbar^2}{2m_e}\nabla^2 + V(\mathbf{r}) + V_H(\mathbf{r}) + V_{XC}(\mathbf{r})\right]\psi_i(\mathbf{r}) = \epsilon_i\psi_i(\mathbf{r}). \tag{2.9}$$

There are three potentials on the left-hand side of the Kohn–Sham equations, V, V_H, and V_{XC}. The first of these also appeared in the full Schrödinger equation (Eq. 2.6) and in the "known" part of the total energy functional given above (Eq. 2.8). This potential defines the interaction between an electron and the collection of atomic nuclei. The second term (V_H) is called the Hartree potential and is defined as

$$V_H(\mathbf{r}) = e^2\int\frac{n(\mathbf{r}')}{|\mathbf{r}-\mathbf{r}'|\mathrm{d}\mathbf{r}'}. \tag{2.10}$$

The Hartree potential accounts for the Coulomb repulsion between an electron and the total electron density defined by all electrons. Thus, this potential includes a so-called self-interaction contribution because the electron described in the Kohn–Sham equation is also part of the total electron density. The self-interaction is unphysical, and the correction for it is one of several effects lumped together into the final potential in the Kohn–Sham equations, V_{XC}, which defines exchange and correlation contributions to the single-electron equations. Finally, $V_{XC} = \delta E_{XC}(\mathbf{r})/\delta n(\mathbf{r})$, is defined as a functional derivative of the exchange-correlation energy. To solve the Kohn– Sham equations, we need to define the Hartree potential, and to define the Hartree potential, we need to know the electron density. However, we must know the single-electron wave functions to find the electron density. Furthermore, to know these wave functions, we must solve the Kohn–Sham equations. Thus, the Kohn–Sham equations must be solved iteratively, as outlined in the following algorithm: (i) Define an initial, trial electron density, $n(\mathbf{r})$, (ii) Solve the Kohn-Sham equations using the trial electron density to find the single-particle wave functions, $\psi_i(\mathbf{r})$, (iii) calculate the Kohn-Sham electron density, $n_{KS}(\mathbf{r}) = 2\sum_i \psi_i^*(\mathbf{r})\psi_i(\mathbf{r})$, and (iv) compare the computed electron density $n_{KS}(\mathbf{r}$ with the guessed electron density $n(\mathbf{r})$. If the two densities are the same, then this is the ground-state electron density. If the two densities are different, then the trial electron density must be updated.

Exchange-Correlation Functional

Thus far, we would like to find the ground-state energy of the Schrödinger equation, but this is extremely difficult because this is a many-body problem. The works of Kohn, Hohenberg, and Sham allow us to obtain the ground state by minimising the energy of an energy functional, and this can be achieved by finding a self-consistent solution to a set of single-particle equations. There is just one critical complication in this approach: to solve the Kohn–Sham equations, we must specify the exchange-correlation function, $E_{XC}[\mathbf{r}]$. Therefore, the accuracy of the ground state energy and density is limited by the approximate form of this exchange-correlation functional.

The true form of the exchange-correlation functional, whose existence is guaranteed by the Hohenberg–Kohn theorem, is generally unknown, except for the uniform electron gas whose density is constant at all points in space. This provides a practical way to approximate the exchange-correlation functional and use the Kohn–Sham equations. To do this, we set the exchange-correlation potential at each position to be the known exchange-correlation potential from the uniform electron gas at the electron density observed at that position, i.e. $V_{XC}(\mathbf{r}) = V_{XC}^{\mathrm{elec}_{\mathrm{gas}}}[n(\mathbf{r})]$. This approach uses only the local density to approximate the exchange-correlation functional. Thus, it is called the local density approximation (LDA).

Another class of functional after the LDA uses information about the local electron density and the local gradient in the electron density to approximate $E_{XC}[\mathbf{r}]$. This approach defines a generalised gradient approximation (GGA). There are many ways in which information from the gradient of the electron density can be included in a GGA functional. Hence, many distinct GGA functionals are often found in the literature. Some widely used functionals of this class are the Perdew–Wang functional (PW91) (Perdew, Burke & Wang 1996) and the Perdew–Burke–Ernzerhof functional (PBE) (Perdew, Burke & Ernzerhof 1996). If the information of the first and second derivatives of the electron density is included, then we will have another class of functional called meta-GGA. The Tao–Perdew–Staroverov–Scuseria (TPSS) functional (Tao et al. 2003) is an example of a nonempirical meta-GGA functional.

On the other hand, hybrid functionals add the correlation energy from the LDA or GGA to the exchange energy made up of the Hartree-Fock exchange energy and LDA or GGA approximated exchange energy. The Hartree-Fock exchange energy arises due to enforced antisymmetry of the wavefunction. By far, the most widely used of these functionals is the B3LYP functional (Lee et al. 1988). The B3LYP functional, and some other similar functionals, have been very successful in predictions of properties of small molecules. However, the B3LYP functional does not capture long range dispersion effects and often fails to predict the properties of CT processes. Therefore, other functionals such as CAM-B3LYP (Yanai et al. 2004*a*) and ωB97XD (Chai & Head-Gordon 2008) have been developed to overcome these problems. These functionals are known as range-separated functionals. In this thesis, we primarily use hybrid and range-separated functionals for our DFT calculations, particularly the B3LYP, CAM-B3LYP and ωB97XD functionals.

Basis Sets

Generically, a basis set is a collection of vectors spanning (defines) a space in which a problem is solved. For example, a set of orthogonal unit vectors $\{\hat{i}, \hat{j}, \hat{k}\}$ defines a Cartesian, 3-dimensional linear vector space. In quantum chemistry, the basis set usually refers to a set of (non-orthogonal) one-particle functions used to build molecular orbitals. The wavefunction is typically represented as a linear combination of basis functions. These can be atomic orbitals (linear combination of atomic orbitals (LCAO)) or plane waves. For the LCAO approach, Slater-, Gaussian-, or contracted Gaussian-type orbitals are normally employed.

Slater-type orbitals (STOs) are solutions to the Schrödinger equation for hydrogen-like atoms and are defined as

$$\phi_{abc}^{STO}(x, y, z) = N x^a y^b z^c e^{-\zeta r} \tag{2.11}$$

where N is a normalised constant factor, a, b, and c control the angular momentum (L = a + b + c), and ζ controls the width of the orbital (large ζ gives tight function, small ζ gives diffuse function). These Hydrogen-atom-like orbitals decay exponentially with distance from the nucleus, which is a physically intuitive representation of atomic orbitals. They correctly describe the short- and long-range behaviour of the atomic orbitals. However, they lack radial nodes and are not pure spherical harmonics. Moreover, integrating over orbitals in a Slater-type orbital basis can be very computational demanding.

On the other hand, Gaussian-type orbitals (GTOs), defined as

$$\phi_{abc}^{GTO}(x, y, z) = N x^a y^b z^c e^{-\zeta r^2}, \tag{2.12}$$

is much easier to compute but no longer is Hydrogen-atom-like, even for the

1s atomic orbital. Nevertheless, Slater-type orbitals can be approximated as a linear combination of Gaussian-type orbitals. These are often known as contracted Gaussian-type orbitals (CGTOs) and are expressed as

$$\phi_{abc}^{GTO}(x, y, z) = N \sum_i c_i x^a y^b z^c e^{-\zeta r^2}, \tag{2.13}$$

As the Gaussian-Gaussian overlaps are analytic (because a product of two Gaussians can be written as a Gaussian), the expansion in the size of the basis set is more than compensated for by the computational savings.

A minimal basis set is the one in which one basis function (STO, GTO, or CGTO) is employed for each atomic orbital in the atom. We have a double-zeta basis set when two basis functions are used for each atomic orbital. Similarly, a triple-zeta basis set is formed when three basis functions are used for each atomic orbital and so on. Since valence electrons are the primary electrons involved in bonding, a split-valence basis set, which uses only one basis function for each core atomic orbital, and a larger basis for the valence, may be employed to save the computational time. It is important to note that when counting basis functions with a basis set that includes CGTOs, each CGTO counts as a single basis function. We do not count the "primitive" GTO functions inside a CGTO as "basis functions". For example, we use the 6-31G* basis set for most of our calculations. In this basis, 6 refers to the number of Gaussians representing the core atomic orbitals (one basis function); 3 and 1 indicate that the valence orbitals are composed of two basis functions each, one with a linear combination of 3 Gaussians and one with 1 Gaussian; the * means that additional polarisation functions are included on heavy atoms only.

Gaussian-type basis set represents a compromise between accuracy and computational time, and its combination with the B3LYP functional is widely used in the literature for studying the properties of organic molecules. Although there are limitations, both with accuracy (compared to larger basis sets or better functionals) and the lack of diffuse basis functions, we can benchmark our calculations against other published work using the same functional and basis set.

2.5.3 Time-Dependent Density Functional Theory

TD-DFT extends the basic ideas of ground-state DFT to the treatment of excitations or more general time-dependent phenomena. TD-DFT can be viewed as an alternative formulation of time-dependent quantum mechanics but, in contrast to the standard approach that relies on wavefunctions and the many-body Schrödinger equation, its basic variable is the one-body electron density, $n(\mathbf{r},t)$, i.e. it is based on Kohn-Sham DFT. Thus, it is described by a time-dependent Schrödinger-like equation as

$$i\hbar\frac{\psi_i(\mathbf{r},t)}{dt} = \hat{H}\psi_i(\mathbf{r},t) \tag{2.14}$$

where $\psi_i(\mathbf{r},t)$ is the electronic wavefunction at a particular time t, and $\hat{H}$ is the electronic Hamiltonian. The effective time-dependent Hamiltonian can be expressed in the form

$$\hat{H}_{eff} = -\frac{\hbar^2}{2m_e}\nabla^2 + V(\mathbf{r},t) + V_H(\mathbf{r},t) + V_{XC}(\mathbf{r},t) \tag{2.15}$$

where all the potentials are functions of $\mathbf{r}$ and t. Most TD-DFT methods use an adiabatic approximation so that the exchange-correlation potential is a time-independent functional of the density. In this work, we use TD-DFT to calculate the excitation energies of molecules. These calculations are based on the fact that the frequency-dependent linear response function, i.e. how the electron density changes when the external potential change, has poles at the exact excitation energies of the system.

2.5.4 Tight-Binding

For systems containing up to a few hundred atoms, we can afford to use DFT to find the true ground-state density and ground state energy of the interacting system without explicitly calculating the many-electron wavefunction. However, for larger systems (thousands of atoms), we can no longer use self-consistent DFT calculations to take into account the full interaction. To calculate the band structure and a set of approximate single-particle states, we instead try to include the effects of the interaction in a semi-empirical way, using parameters that we can adjust to match the experiment. TB is a further approximation to describe the electronic structure based on localised electronic states, i.e. electronic states that are "tightly bound" to sites. It was developed by Bloch in 1928 based on only s-orbitals and later expanded to other atomic orbitals by Jones, Mott and Skinner in 1934 (Probert 2011).

The semi-empirical TB method can be directly deduced as a rigorous approximation to DFT and is the limit of DFT with no electron correlation (Sutton et al. 1988, Finnis 2003). The method is linear and can be solved directly without iterative (self-consistent) methods. This approach was initially based on atomic orbitals. However, since there are different interactions between atoms in the same and different molecules in molecular assemblies, a natural extension of the atomic orbital-based TB method is to "coarse-grain" groups of atoms or segments into a single unit (chromophore). This requires that only the energies of these units and the direction and orientation-dependent interactions (or electronic coupling) between them must be known.

Organic materials are generally characterised by a low dielectric constant. Hence, the more strongly bound electron-hole pair is better described starting from a singlet excitation spatially confined on a subunit of the aggregate. Such a localised singlet excited state is referred to as a Frenkel exciton. The interactions between different subunits (which can be molecules, fragments, monomers, or chromophores) lead to the delocalisation of the excitons, and the spectroscopy of the aggregate will differ from that of the isolated chromophore. In this framework, a molecular aggregate can be described by the (static) excitonic Hamiltonian

$$\hat{H}_{TB} = \sum_i E_i |i\rangle\langle i| + \sum_i \sum_{j \neq i} J_{ij} |j\rangle\langle i| \tag{2.16}$$

written in the basis of the diabatic states $|i\rangle$ (Frenkel exciton localised on chromophore i), whose excitation energy is E_i. The interaction between any pair of chromophores i and j is given by the excitonic coupling J_{ij}. The eigenstates of this Hamiltonian are the adiabatic excitonic states which can be delocalised over several chromophores if the couplings between them are strong enough. Therefore, the properties of the system will strongly depend on the strength of the excitonic couplings. Thus, it is crucial to accurately describe the excitonic couplings for the system of interests, especially for molecular aggregates whose short-range contributions are unavoidable. In our work, we employ the diabatisation scheme proposed by Aragó & Troisi (2015*b*), which is capable of dealing with multiple excited states and also taking into account both short- and long-range effects of the couplings. The model Hamiltonian can also be modified or improved to provide the best prediction of the problems at hand, e.g. to include environment effects (Shi & Willard 2018), or electron-phonon couplings (Strong & Hestand 2020).

TB models have been applied to organic semiconductors, such as for hole transport in DNA (Senthilkumar et al. 2005), charge transport along Poly(p-phenylene vinylene) wires (Prins et al. 2006) and in organic crystals (Li et al. 2014), and the electronic structure of fullerenes (d'Avino et al. 2016). They have also successfully been employed to compute circular dichroism spectra (Woody 2012, Rogers et al. 2019) and model exciton transport in light-harvesting complexes (Kreisbeck & Kramer 2012).

In the molecular TB model, the sites are conjugated segments, e.g. monomers or chromophores, from a polymer or small organic molecules. Thus, they are described by the frontier molecular orbitals rather than atomic orbitals. The model generally has one molecular orbital per site. For example, for a polaron, if the excess charge carrier is an electron, this is taken as the LUMO of the molecule (site) and if the excess charge carrier is a hole, it is the HOMO of the molecule. In chapter four, we use this molecular TB framework (a Frenkel–Holstein like Hamiltonian) to develop a model of exciton transport in disordered molecular assemblies. In our model Hamiltonian, an appropriate theoretical approximation where the thermal excitonic coupling fluctuations (non-local exciton-phonon couplings) are appropriately taken into account. The method section of chapter four details the calculations required to obtain parameters for the TB Hamiltonian.

2.6 Concluding Remarks

In this chapter, we first described the modelling of organic semiconductors and then listed the primary methodologies behind our works, such as MD simulations, approaches to parameterise accurate force fields, DFT and TB model Hamiltonian. In the following chapters, we will apply these methods to characterise the electronic and transport properties of organic semiconducting materials, including the influence of dynamic disorder on the exciton dynamics in molecular crystals and the structure-property relationships in amorphous conjugated polymers. However, before we proceed further, we shall explain our procedures for optimising force fields for conjugated molecules in chapter 3.

Chapter 3

Force Fields for Macromolecular Assemblies Containing Diketopyrrolopyrrole, Thiophene and Thienothiophene

*

3.1 Synopsis

This chapter utilises a force matching procedure to parameterise new force fields systematically for large conjugated systems. We model both conjugated polymers and molecular crystals that contain DPP, T, and TT units. These systems have recently been found to have low band gaps, which exhibit high efficiency for photovoltaic devices. The equilibrium structures, forces and energies of the building block chromophores: DPP, T, and TT computed using our parameters are comparable to those computed using the reference electronic

---

[*] The work in this chapter was published in:

Jiang, L., Rogers, D. M., Hirst, J. D. & Do, H. (2020), 'Force fields for macromolecular assemblies containing diketopyrrolopyrrole and thiophene', *Journal of Chemical Theory and Computation* **16**(8), 5150–5162.

structure method. We assess the suitability of this new force field for electronic property calculations by comparing the electronic excitation properties computed along classical and *ab initio* MD trajectories. For both trajectories, we find similar distributions of TD-DFT calculated excitation energies and oscillator strengths for the building block chromophore DPP-TT. The structural, dynamical, and electronic properties of the macromolecular assemblies built upon these chromophores are characterised. For both polymers and molecular crystals, pronounced peaks around 0^o or 180^o are observed for the torsions between chromophores under ambient conditions. The high planarity in these systems can promote local ordering and π-π stacking, thereby potentially facilitating charge transport across these materials. For the model conducting polymers, we found that the fluctuations in the density of states per chain per monomer are negligibly small and do not vary significantly with chains comprising 20 to 40 monomers. Analysis of the electron-hole distributions and the transition density matrices indicates that the delocalised length is approximately four to six monomers, which is in good agreement with other theoretical and experimental studies of different conducting polymers. For the molecular crystals, our investigation of the characteristic timescale of the fluctuation in the excitonic couplings shows that low frequency vibration below 10 cm^{-1} is observed for the nearest neighbours. These observations are in line with previous studies on other molecular crystals, in which low frequency vibrations are believed to be responsible for the large modulation of the excitonic coupling. Thus, our approach and the new force fields provide a direct route for studying the structure-property relations and the molecular level origins of the high-efficiency of these classes of materials.

3.2 Introduction

Semiconductors based on small organic molecules and conjugated polymers offer the opportunity for large-area deposition on substrates and they can be chemically tuned or fictionalised for many specific applications (Rivnay et al. 2012). In the last two decades, they have emerged as excellent materials for displays, solid-state lighting, sensors and solar cells (Brunner et al. 2004, Huang et al. 2011, Lei et al. 2011, Bronstein et al. 2011). Their main advantages are the significant reduction in production cost compared to their organic counterparts and their processes can be easily scaled-up, since organic materials can be solution-processed. Conjugated organic molecules exhibit a wealth of structures and properties due to the range of possible molecular constituents. They can be completely disordered polymers formed by interlaced chains, partially ordered polymers, polycrystalline small molecule-based structures, or small molecule-based single crystals (Rivnay et al. 2012, Noriega et al. 2013a). The detailed characterisation of the structure of conjugated organic assemblies remains a challenging task, often requiring simplified and qualitative morphological descriptions. In addition, the variety of these materials, their possible structures, and their complexity hinder the full elucidation of the relationship between the structures of conjugated organic assemblies and their electronic properties (Noriega et al. 2013a, Qin & Troisi 2013).

To investigate the fundamental processes that determine the efficiency of charge transport in organic semiconductors, many efforts have been devoted to understand their structure-property relationships (Kline & McGehee 2006, Guo et al. 2013, Alberga et al. 2014, Marsh et al. 2014), including the influence of molecular morphologies on optical and CT events. However, the interplay between microstructure and electronic properties in these materials remains unclear (Mollinger et al. 2015, Sweetnam et al. 2016). Amorphous materials or poly-crystalline materials especially are poorly understood (Noriega et al. 2013a). In particular, a molecular level comprehension of the exciton transport and charge generation mechanisms is crucial, for example, to the rational design and enhancement of conjugated organic semiconductors for highly efficient photovoltaic devices. Theoretical and computational approaches can play a major role in the study of this important aspect because they provide direct access to the microscopic and electronic properties of materials.

Molecular simulations offer a direct route to explore the relationship between molecular morphology and charge mobility. Amongst several morphology simulation techniques (Peumans et al. 2003), classical MD is the most popular approach, as it gives atomic detail comparable with experimental observations. In the last decade, MD simulations have penetrated into the study of optical and electronic properties of materials and biomolecules, where they are primarily used to sample the equilibrium structures explored by the system of interest (Robinson & Besley 2010, Abramavicius et al. 2010, Qin & Troisi 2013, Aghtar et al. 2017). These equilibrium trajectories are utilised in large-scale quantum chemistry calculations to correlate the local structure with the observable electronic structure properties (Ma et al. 2014). Consequently, the force fields used to describe the molecular motion of the system must be accurate enough to reproduce experiments. The main concern here is the mismatch in the force fields describing the interactions at the classical level and the electronic structure methods employed for subsequent quantum chemistry calculations.

Historically, force fields employed in classical MD simulations have been designed mainly for biochemical systems, e.g. protein simulations. Although these force fields contain parameters that are transferable to conjugated systems, many aspects require careful parameterisation due to the conjugation (Wildman et al. 2016). For large conjugated systems such as polymers, force fields need to employ many atom types and parameters. Generally, the force fields used to describe the motions of molecular systems are seldom parameterised to reproduce electronic processes, such as electronic excitations, which are sensitive to the underlying description of the molecular structure. It still remains a challenge to find satisfactorily accurate force fields for applications where MD is the preliminary step toward the study of electronic structure properties (Wildman et al. 2016, Andreussi et al. 2017, Claridge & Troisi 2019).

Most existing procedures (Vanommeslaeghe et al. 2010, Wang et al. 2004, Dodda et al. 2017, Huang & Roux 2013) are general tools for constructing force fields for small organic molecules, either in the gas phase or in a continuum solvent. When applied to specific problems in condensed phases, these force fields may not be directly transferable to the systems under investigation. For example, several recent studies of excitation energy transfer in LH complexes have shown that force fields used to describe the chromophores have a great influence on the resulting spectral density (Kreisbeck & Kramer 2012, Kim et al. 2015, Chandrasekaran et al. 2015). This problem is often referred to as the geometry mismatch, i.e. the mismatch between the classical and *ab initio* potential energy surfaces. As such, Prandi et al. (2016) proposed a new set of parameters for the different carotenoids found in the LH complexes of photosystem II, optimised to reproduce electronic excitation properties obtained by DFT. To investigate this further, Andreussi et al. (2017) systematically checked the feasibility of using classical force fields for quantum mechanics applications. They concluded that for photoinduced processes, as an example, poor results are obtained from standard transferable force fields. Thus, in order to mitigate the mismatch in the geometry, the classical potential energy surface and/or its gradients of the system of interest should be mapped onto the *ab initio* ones by optimising the force fields. This would also implicitly incorporate many-body effects, which is crucial in the study of condensed phase systems. To address this, Ercolessi & Adams (1994) proposed the force-matching (FM) approach, which was first employed to develop interatomic potentials that reproduce those computed from first principles. To overcome the computational cost incurred by using *ab initio* MD or quantum mechanics (QM)/molecular mechanics (MM), Wang and coworkers introduced the adaptive force matching technique (Akin-Ojo et al. 2008, Wei et al. 2011). Instead of using *ab initio* MD, the adaptive force matching approach uses MM force fields to generate ensembles of equilibrium structures followed by decoupled QM/MM calculations on each configuration with the environment represented by point charges. The procedure starts with a set of guessed parameters and is repeated until convergence is reached. Since then, the method has been applied to systems including transition metal complexes (Wu et al. 2011, Handley & Deeth 2012), anions (Wright et al. 2013), ionic liquids (Sala et al. 2011), and microporous materials (Gabrieli et al. 2014). Recently, the force-matching technique has also been employed to develop force fields for water (Koziol et al. 2017, Lindsey et al. 2019), water on graphene surface (Li & Wang 2017), and explicit three-body interactions for molten carbon (Lindsey et al. 2017).

In this work, we extend the adaptive force matching technique to rapidly parameterise force fields for complex conjugated systems. We develop a strategy for fragmenting the "larger" molecule into smaller segments, obtain their parameters, and then assemble them together to derive the force fields for the "larger" molecule. This was a challenge, which was presented, but not achieved, in the previous work by Do & Troisi (2015). Do & Troisi (2015) reported parameters for the monomer DPP and for the chromophore-triple DPP-TT-T, but for no other species, precluding the characterisation of the dynamics of the polymer and crystal systems that we study herein. Moreover, the suitability of the force field for electronic property calculations by comparing the electronic excitation properties computed along classical and *ab initio* MD trajectories was not assessed. This is important and should be tested, at least, for the monomer. In the current study, we build on and go beyond the earlier work (Do & Troisi 2015) to address three important aspects. (i) In the current work, we fragment the "larger" molecule into smaller segments, obtain their parameters, and then assemble them together to derive the force field for the"larger" molecule. This was a challenge, which was presented, but not achieved for the chromophore-quadruple (the monomer of the model polymer) in the previous work (Do & Troisi 2015).(ii) We validate the force field with the first MD simulation of the model polymer (for a single chain 1-mer) by comparing against counterpart *ab initio* MD simulations. (iii) We then predict the structural and the electronic excitation properties for the model polymer and also for a newly synthesised molecular crystal. The thrust of our approach is to obtain parameters consistent with any pre-defined electronic structure calculation method. As an example, we parameterise force fields for conducting polymers and molecular crystals containing DPP, T, and TT. The DPP units have strong intermolecular donor-acceptor interactions, which can promote self-assembly of the polymer and enhance the charge transport (Chandran & Lee 2013). In addition, the incorporation of DPP into an oligothiophene or polythiophene backbone results in low band gap conjugated systems exhibiting high efficiency for photovoltaic devices (Kanibolotsky et al. 2015). Thus, force fields that generate accurate equilibrium structures via MD simulations of these systems are crucial for analysing and understanding the structure-property relationships of conjugated semiconductors.

3.3 Computational Details

To start with, a set of M equilibrium configurations is generated using an initially "guessed" force field. The atom-type is carefully assigned to take into account the complex chemical structure of the system. As such, we tend to have more atom-types than standard force fields. A description of how the different atom types are chosen can be found in the Appendix A. Apart from the point charges and equilibrium bonds and angles, all other "guessed" parameters are taken from optimised potentials for liquid simulations (OPLS) (Jorgensen et al. 1996, Robertson et al. 2015, Dodda et al. 2017, Robertson et al. 2019). For missing parameters, we use analogy and quantum chemistry calculations to assign the parameters (e.g. equilibrium bonds and angles). Equilibrium structures are obtained from MD simulations under ambient conditions (i.e. 300 K and 1 bar). All MD simulations are carried out using the nanoscale molecular dynamics (NAMD) software (Phillips et al. 2005). After an energy minimisation of 10000 steps, a 200 ps equilibration run is carried out, followed by a 1 ns production run, using a 1 fs time step. Equilibrium structures are saved during the production run at 2 ps intervals to form a set of 500 snapshots. M uncorrelated equilibrium configurations are drawn randomly from this set. The number of structures, M, used in the optimisation process is critical and must be determined beforehand. One should not use too few structures, as that would lead to overfitting. On the other hand, with too many structures the computational cost would increase. To work out the "ideal" number of structures, we follow a suggestion from previous work (Do & Troisi 2015): $M > (50 \times N_p)/(3 \times N_a)$, where N_p is the number of parameters, N_a is the number of atoms in the molecule of interest. We found that a value of M between 100 to 150 seems reasonable.

Ab initio MD simulations are carried out using the Atom Centred Density Matrix Propagation (ADMP) MD model (Schlegel et al. 2001, Iyengar et al. 2001, Schlegel et al. 2002), as implemented in the Gaussian 16 package (Frisch et al. 2016). B3LYP/6-31G* level of theory and a time step of 1 fs are employed throughout, with an initial equilibration run of 10 ps, followed by a production run of 50 ps, from which 100 uncorrelated configurations (frames) are obtained by sampling every 0.5 ps. These 100 frames are utilised to compute the electronic excitation properties of the building block chromophores. Gaussian 16 (Frisch et al. 2016) was also employed to perform TD-DFT calculations, at the B3LYP/6-311G(d,p) level, to compute transition energies and oscillator strengths for 20 singlet excited states for each chromophore using frames from the classical and the *ab initio* MD.

The *ab initio* forces (reference forces) are computed with DFT using the B3LYP functional and the 6-31G* basis set, using the Gaussian 16 package

(Frisch et al. 2016). Depending on the applications and the methods used in the quantum chemistry calculation stage, other combinations of functionals and basis sets and/or higher levels of theory can be employed. In our work, we find B3LYP/6-31G* is sufficient for the systems under investigation. The optimisation procedure starts with computing the initial objective function, $O(\{p_j^{init}\})$, using equation 2.5. The algorithm proceeds by randomly selecting a parameter p_j from the set and modifies it by adding a random number δp_j uniformly distributed between $-\delta p_j^{max}$ and δp_j^{max}. In other words, δp_j^{max} is the maximum "displacement" of the parameter δp_j. This value is initialised to $0.3 \times p_j$ at the beginning of the optimisation , and is adjusted in the course of the process to keep the acceptance rate of the MC moves at about 30%. The optimisation is divided into MC "blocks". Each consists of $100 \times N_p$ attempts to randomly select and change a parameter p_j. The idea here is to allow each parameter to be selected roughly 100 times in each MC block. This number can be adjusted and we found 100 times is sufficient. The acceptance rate is calculated at the end of each block and the maximum "displacement" δp_j^{max} is adjusted accordingly. The optimisation is converged when $\delta O < 10^{-10}$ kcal mol^{-1}Å^{-1}, where δO is the change in the objective function between two consecutive MC steps. Having completed the optimisation process, the parameters are then used as the new guess for the next iteration. In general, two or three iterations are sufficient, as shown in the results section.

To investigate the nature of the electronic excitation of the polymer, we analyse the electron-hole (e-h) distributions and the transition densities for the lowest three singlet excitations of a single chain (in the absence of the interchain electronic coupling) using the Multiwfn codes (Lu & Chen 2012). In general, electronic excitations are represented as transitions involving multiple, weighted molecular orbitals (MO) pairs. When there is no single dominant MO pair transition to represent the electron and hole, the natural transition orbital (NTO) analysis is often utilised. However, for complex molecular systems, there is no guarantee that a dominating NTO pair exists. Thus, to overcome this, several key indices have been proposed to characterise the electronic excited states. Notable are the Λ-index (Peach et al. 2008), Δr-index (Guido et al. 2013), and other descriptors e.g. e-h overlapping index ($\mathrm{S_r}$-index) and CT length index (D-index) etc. proposed by Lu & Chen (2012).

The overlap function $\mathrm{S_r}(\mathbf{r})$ between a hole and an electron can be defined as $\mathrm{S_r}(\mathbf{r}) = \sqrt{\rho^{\text{hole}}(\mathbf{r})\rho^{\text{elec}}(\mathbf{r})}$, where ρ^{hole} and ρ^{elec} are the charge densities of the hole and electron, respectively. Thus, the $\mathrm{S_r}$-index is the integration of the $\mathrm{S_r}(\mathbf{r})$ function over all space, which provides the extent of the overlap between hole and electron. The CT length can be estimated by computing the distance between the centroid of hole and electron. To compute the X component of the centroid of the electron, for example, we integrate the x-coordinate of the position vector $\mathbf{r}$ weighted by the electron density i.e. $X_{\text{elec}} = \int x\rho^{\text{elec}}(\mathbf{r})\mathrm{d}\mathbf{r}$. The total magnitude of CT length is referred to as the D-index and can be computed as D-index $= \sqrt{D_x^2 + D_y^2 + D_z^2}$, where $D_x = X_{\text{elec}} - X_{\text{hole}}$, $D_y = Y_{\text{elec}} - Y_{\text{hole}}$, $D_z = Z_{\text{elec}} - Z_{\text{hole}}$. The extent of the spatial distribution of the hole and electron can be characterised by the root mean squared deviation. The x-component of the root mean square deviation (RMSD) of the hole can be expressed, for example, as $\sigma_{\text{hole},x} = \sqrt{\int (x - X_{\text{hole}})^2 \rho^{\text{hole}}(\mathbf{r})\mathrm{d}\mathbf{r}}$. Then, the differences between the RMSD of electron and hole, $\Delta\sigma_\lambda$, can be calculated via $\Delta\sigma_\lambda = \sigma_{\text{elec},\,\lambda} - \sigma_{\text{hole},\,\lambda}$, where $\lambda = \{x, y, z\}$. Subsequently, the total difference can be measured via the $\Delta\sigma$-index, which is $|\boldsymbol{\sigma}_{\text{elec}}| - |\boldsymbol{\sigma}_{\text{hole}}|$. On the other hand, the H-index, which is given by $(|\boldsymbol{\sigma}_{\text{elec}}| + |\boldsymbol{\sigma}_{\text{hole}}|)/2$ provides the average degree of spatial extent of the hole and electron distribution in space. For CT excitations, the t-index is often employed to describe the separation degree of hole and electron in the CT direction. This descriptor is defined as the difference between the D-index and a quantity called $\mathrm{H_{CT}}$, which is defined as $H_{CT} = |\mathbf{H} \cdot \mathbf{u}_{CT}|$. Here, $\mathbf{u}_{CT}$ is a unit vector in the CT direction and can be derived from the centroid of hole and electron, and the component H_λ of vector

H is the average spatial extension of the hole and electron in the λ-direction, i.e. $H_\lambda = (\sigma_{\text{elec, }\lambda} + \sigma_{\text{hole, }\lambda})/2$. In addition, the exciton binding (Coulomb attraction between hole and electron) is another meaningful descriptor that can be utilised to describe the separation of hole and electron.

3.4 Force Field Development

Recently, a series of interesting DPPTT-based copolymers with various branched alkyl side-chains have been synthesised (Bronstein et al. 2011, 2013, Meager et al. 2013, Shin et al. 2015). However, there have not been many reports in the literature regarding reliable force fields to study these polymers. The second system of interest is a molecular crystal also recently synthesised: diethyl 2,2'-(1,4-dioxo-3,6-bis(2-thienyl)pyrrolo[3,4-*c*]pyrrole-2,5(1H,4H)-diyl)diacetate (UBEQOK) (Cambridge Crystallographic Data Centre (CCDC) crystal code) (Pop et al. 2016).

For all force fields, the general functional expression is the sum of the potential energy of the bonded and nonbonded interactions. The bonded part involves terms of bonds, angles and dihedrals, while the nonbonded part comprises vdW interactions and electrostatics. The force field parameters needed for the bonded and nonbonded terms are defined for each type of atom. The exact form of these terms may vary depending on the specific force field and system. In this case, the OPLS force field (Jorgensen & Tirado-Rives 1988, Jorgensen et al. 1996) (shown in the Appendix A) is employed. Here, our focus is on the intramolecular components for which the available parameters perform poorly (Bhatta & Tsige 2014, Qin & Troisi 2013). We employ the corresponding vdW parameters from OPLS and compute charges using the restrained electrostatic potential (RESP) method (Cornell et al. 1993) at the B3LYP/6-31G* level of theory. The intermolecular parameters are kept constant during the optimisation.

In this section we shall describe the procedure to construct the force fields for the above mentioned conducting polymers and molecular crystals that contain DPP, T and TT chromophores. Instead of optimising the parameters for the whole system in one go as in the work of Do & Troisi (2015), our strategy is to fragment the "larger" molecule into smaller segments, obtain their parameters, and then assemble them together to derive the force fields for the "larger" molecule. The idea is to parameterise the force fields for each single chromophore (e.g. DPP, TT and T) and utilise them to construct the force fields for larger segments, e.g. segments that contain two or more chromophores. This can be achieved by running the optimisation procedure for the "larger" molecules and only allow the missing parameters to be optimised while keeping the rest fixed at those obtained from the single chromophores. In practice, we perform a further optimisation for the whole "larger" molecules (including side-chains if there is any) to obtain better sets of parameters. These calculations are fairly quick, as the original "guessed" parameters are near optimum. Thus, our fragmentation approach is particularly suitable for large systems with many parameters, for which the previous technique (Do & Troisi 2015) is less well suited.

Chromophore-quadruple

Force fields developed for the single chromophores and chromophore-pairs are presented in the Appendix A. For the chromophore-triple (DPP-TT-T), our parameters are comparable with those published in the previous work by Do & Troisi (2015), in terms of predicting the structural properties of this molecule. It is important to note that our parameters and those of Do & Troisi (2015) are obtained using two different procedures. In our work, the parameters are obtained using the fragmentation scheme, while those in Do & Troisi (2015) are obtained by optimising all parameters in the chromophore-triple in one go. The main problem in their approach is the cost in the computational time and thus we find it can be impractical for larger molecules, e.g. for the chromophore-quadruple in this instance. For molecular crystals, parameters for the chromophore-pairs DPP-T (which have not been published) are sufficient (for UBEQOK). However, for the polymer, parameters for the chromophore-quadruple (the monomer of the polymer) are required. The model shown in Figure 3.1a contains all information needed to construct the force fields for an oligomer of any arbitrary length, and parameters taken from the single chromophores and the chromophore-pairs are sufficient to obtain the parameters for the chromophore-quadruple. Parameters for the bonds, angles, and dihedrals that involved TC7 and TH0 atom types (Figure 3.1b) are not defined in the chromophore-quadruple. Thus, these parameters are taken from the single chromophore TT, which is a reasonable approximation. In addition, sidechains are also treated as fragments and can be readily added if required.

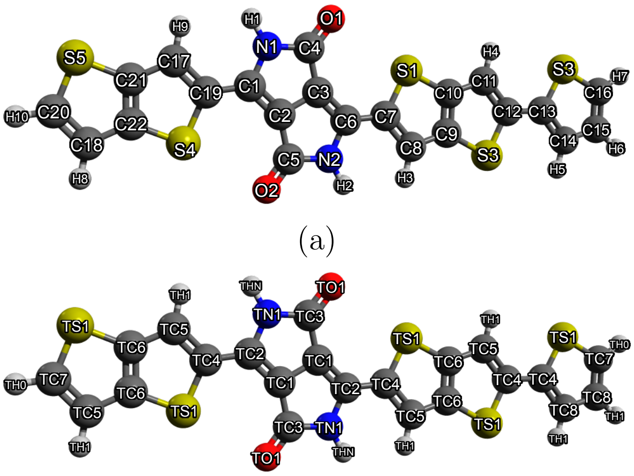

(a)

(b)

Figure 3.1: The structure of the TT-DPP-TT-T molecule: (a) are atom names and (b) are atom types.

The procedure for obtaining the parameters for the chromophore-quadruple is similar to that of the chromophore-pairs. In the first stage, all parameters apart from those of the "soft" dihedrals are obtained using the planar structures. In these geometries, the forces of the "soft" dihedrals are essentially zero. The initial "guessed" parameters are taken from the single chromophores. Missing parameters due to the combination of two chromophores (e.g. the bond parameters for C6-C7 or the angle parameters for C6-C7-S1) are taken from the chromophore-pairs. In the optimisation process, it is possible to allow only the missing parameters to be optimised while the rest remain fixed at those obtained from the parameterisation of the single chromophore. This approach is particular suitable for very large molecules with many parameters that require a long optimisation time. For the case of the chromophore-quadruple (and also the chromophore-pair), it is possible to carry out the optimisation processes for the whole molecule, and since the initial "guessed" parameters are reasonably good, it only required two iterations to converge. For chromophore-quadruple (and larger molecules e.g. oligomers), the "soft" dihedrals are not parameterised individually, and their parameters are taken directly from those in the chromophore-pairs. Figure 3.2 shows that the inclusion of the T ring slightly alters the torsion potential of the DPP-TT torsion. However, this effect is small enough to be safely neglected.

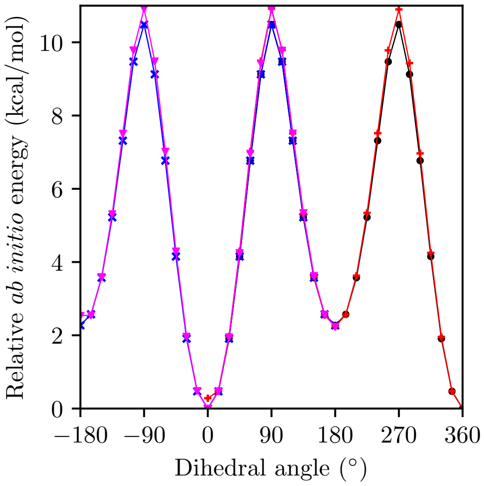

Figure 3.2: Comparison of the torsion potential of DPP-TT soft dihedral without the presence of chromophore T (black and blue lines) and with the presence of the chromophore T (red and purple lines). The scans are carried out using B3LYP/6-31G*.

3.5 Results and Discussion

3.5.1 Validation of the Parameters for the Chromophore-quadruple

A comparison of the force and energy RMSD is shown in Table 3.1. Similar to the cases for single chromophores and chromophore-dimers (See Tables A.1 and A.2 in the Appendix A), AM1 gives the largest deviation for forces followed by HF/6-31G*. B3LYP/3-21G* gives the smallest deviation from the reference method B3LYP/6-31G* for both forces and energies. The force RMSD is comparable to that of B3LYP/3-21G*, while the energy RMSD is comparable to HF/6-31G*.

Method	Force RMSD (kcal mol^{-1} Å^{-1})	Energy RMSD (kcal mol^{-1})
force field	8.87	6.38
AM1	22.45	5.22
HF/6-31G*	16.95	6.13
B3LYP/3-21G*	5.78	3.24

Table 3.1: Force and energy RMSD between calculations at B3LYP/6-31G* levels and the optimised force field or other levels of theory, for 100 arbitrary geometries of the chromophore-quadruple TT-DPP-TT-T not used in the force field optimisation process.

To demonstrate that our parameters are reliable for generating structures for quantum chemistry calculations, we compare the electronic excited state properties of the chromophore-triple computed using trajectories from both classical and *ab initio* MD simulations. The distributions for the excitation energies and oscillator strengths are shown in Figure 3.3. These data show significant overlaps in both the transition energies and the oscillator strengths for the lowest two excited states S_1 and S_2, along the classical and *ab initio* trajectories. Similar trends are also observed for other transitions in this chromophore and also in other building blocks. Data for other chromophores can be found in the Appendix A. Thus, these further suggest that the potential energy surfaces generated by using our force fields are comparable to those generated using

DFT.

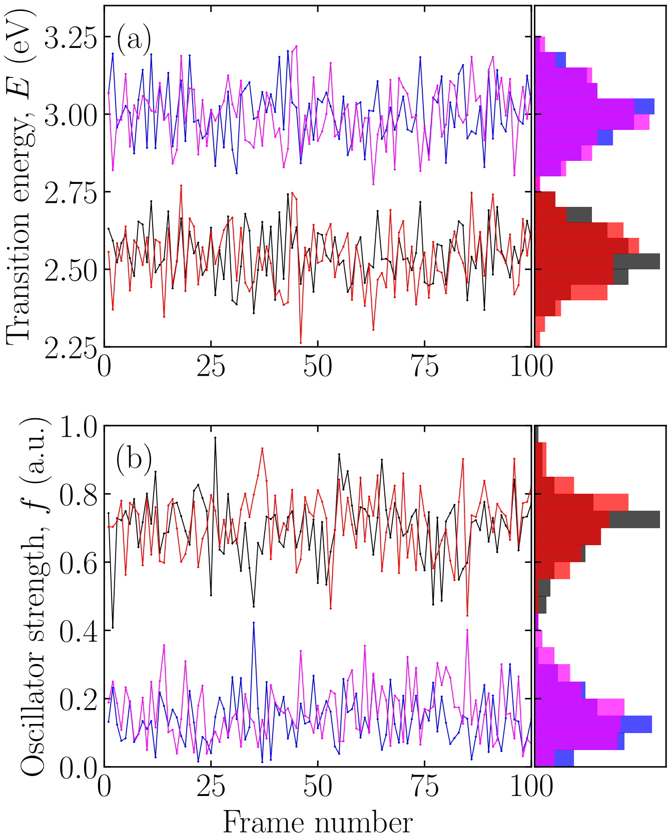

Figure 3.3: Comparison of the transition energies (a) and oscillator strengths (f) (b) of the lowest two excited states computed using 100 uncorrelated frames taken from the classical (black and blue) and the *ab initio* (red and magenta) trajectories for chromophore-triple (DPP-TT-T). All calculations are performed at the B3LYP/6-311G(d,p) level of theory.

Finally, Figure 3.4 compares the structural properties of the chromophore-quadruple computed for 100 snapshots along the classical and *ab initio* trajectories. As an example, we only show distributions for a bond, an angle and a soft dihedral of the chromophore in this figure. Other bonds, angles and dihedrals show the same trend. The good agreement observed for the structural properties in Figure 3.4 for the chromophore-quadruple underpin the agreement of the electronic excitation properties observed in Figure 3.3. Hence, this provides further confidence that our force fields can reproduce the *ab initio* potential energy surfaces, to which their parameters are fitted.

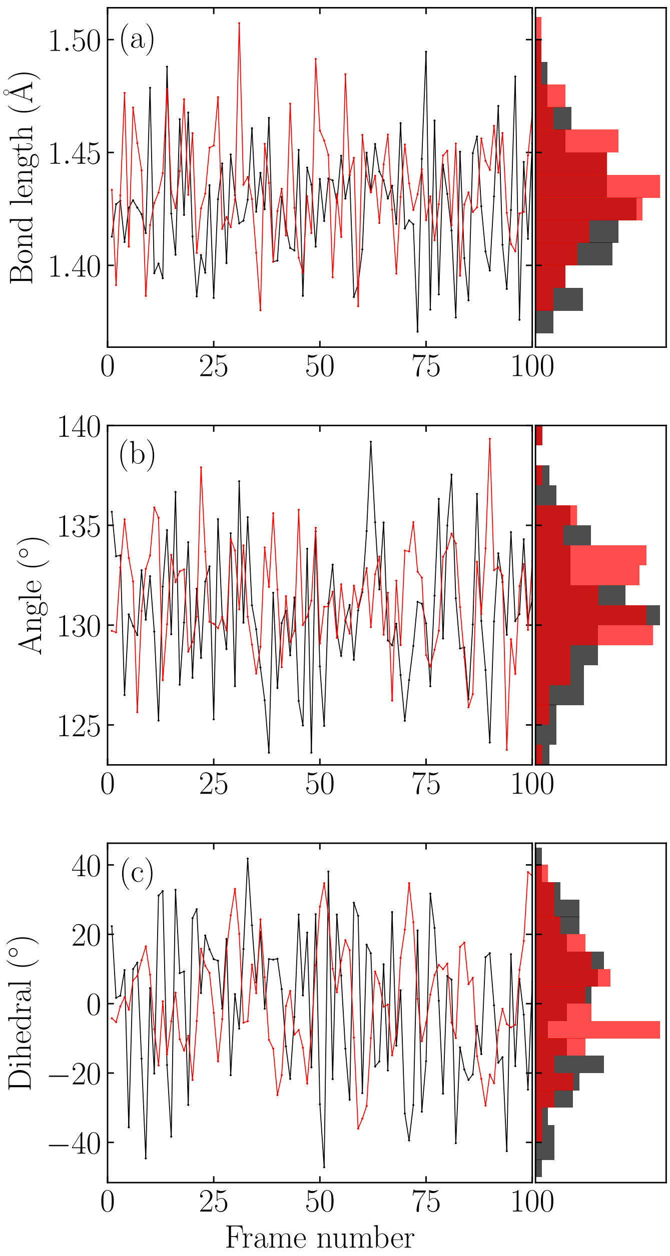

Figure 3.4: Comparison of the structural properties of chromophore-quadruple computed using 100 uncorrelated frames taken from the classical (black) and the *ab initio* (red) trajectories: (a) bond between C6 and C7, (b) angle between C3, C6 and C7, and (c) dihedral between C3, C6, C7 and S1.

3.5.2 Conjugated Polymers

MD Simulations

MD simulations are carried out with NAMD (Phillips et al. 2005) for 20 40-mers of the poly(thieno[3,2*b*]thiophene-diketopyrrolopyrrole-*co*-thiophene (PTPPTT-T) bulk conducting polymer. The monomer of PTPPTT-T is the chromophore-quadruple described in the previous section. Thus, the topology and parameters for PTPPTT-T oligomers are built upon the chromophore-quadruple. The polymer is initially placed into a cubic box of $109 \times 109 \times 109$ Å^3 at a density of 0.5 g/cm^3 without overlaps. To achieve this, polymer chains are added into the box by growing segment by segment using the configurational bias MC technique (Siepmann & Frenkel 1992). To avoid steric clashes, the growing process takes into account interaction with all atoms already positioned, whilst continuously monitoring the single chain conformations. The result of this procedure is that low energy sites are preferred over high energy sites. Thus, bulk disordered systems containing chain molecules in realistic equilibrium conformations are created.

Three-dimensional periodic boundary conditions are implemented. The system is minimised for 5000 steps and gradually heated to 300 K using 50 ps in the NVT ensemble. Then, the NPT ensemble at 1 atm and 300 K is employed for 200 ns to equilibrate the system. Finally, a further 100 ns is simulated in the NVT ensemble for calculating ensemble average properties. The Langevin thermostat (Hoover et al. 1982) with a damping coefficient equal to 1 ps^{-1} is employed to keep the temperature constant. The period and decay parameters of the Langevin piston are set to 100 and 50, respectively, to maintain the pressure. A time step of 1 fs for integration of the equations of motion is used throughout the simulation. A cutoff of 12 Å is used for nonbonded interactions. The particle mesh Ewald algorithm (Herce et al. 2007) is used to calculate long-range electrostatic interactions. Figure 3.5 gives a visualisation of the system and Figure 3.6 shows the density variation with respect to the simulation time. Starting from 0.5 g/cm^3, the system reaches about 1 g/cm^3 after 100 ns, and eventually converges to about 1.035 g/cm^3. A density of around 1 g/cm^3 is a typical value for conducting polymers. The same final density is also observed for different starting densities and different chain lengths.

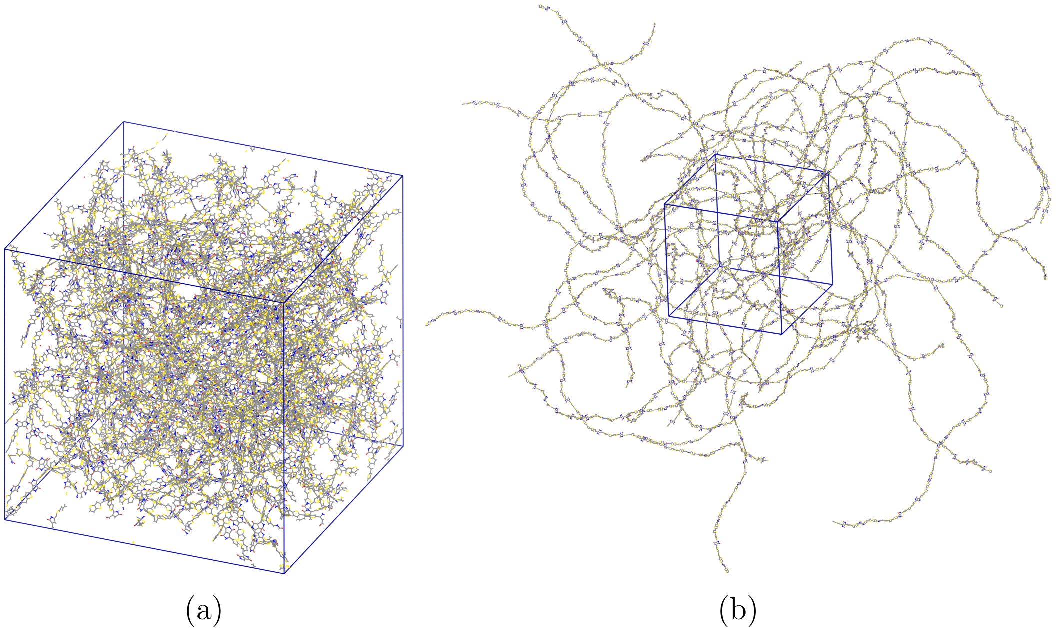
(a) (b)

Figure 3.5: PTPPTT-T amorphous cell: 40 monomers/chain, 20 chains, density 0.5 g/cm^3. (a) In-cell display style. (b) Out-cell display style.

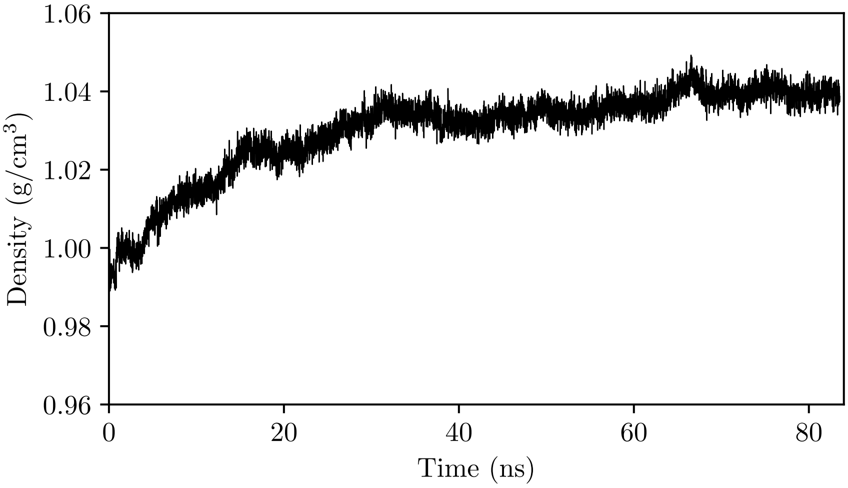

Figure 3.6: Time evolution of the density in the last 100 ns of the 200 ns NPT ensemble simulation.

First of all, we inspect the radius of gyration of the polymer under ambient conditions. The range of gyration radii (Figure A.28) is between 125 to 160 Å, which indicates these chains are rather elongated. The length of the extended polymer chain (40 monomers) is about 200 Å. This property of the polymers very quickly reaches equilibrium and remains essentially unchanged during the course of the simulations at 300 K. This behaviour has been observed previously for other conducting polymers (Qin & Troisi 2013).

In general, the flexible dihedral angles play an important role in the electronic properties of conducting polymers. A planar configuration leads to high hole mobility, due to the formation of the π orbitals along the backbone (Kawanabe et al. 2014). To examine the planarity of this polymer, we compute the distribution of the soft dihedrals along the chain backbone. Figure 3.7 shows the distribution between DPP and TT of the first monomer in chain one. A strong peak near 0° is observed. This distribution is also found for the torsion DPP-TT along chain number one and in other chains. Similarly, for the distribution of the torsions between TT and T and between DPP and T, we also observe peaks around 180° or 0°. This suggests that dihedral angles near 0° and 180° are favoured thermodynamically, which indicates planar configurations for PTPPTT-T at the temperature and density studied.

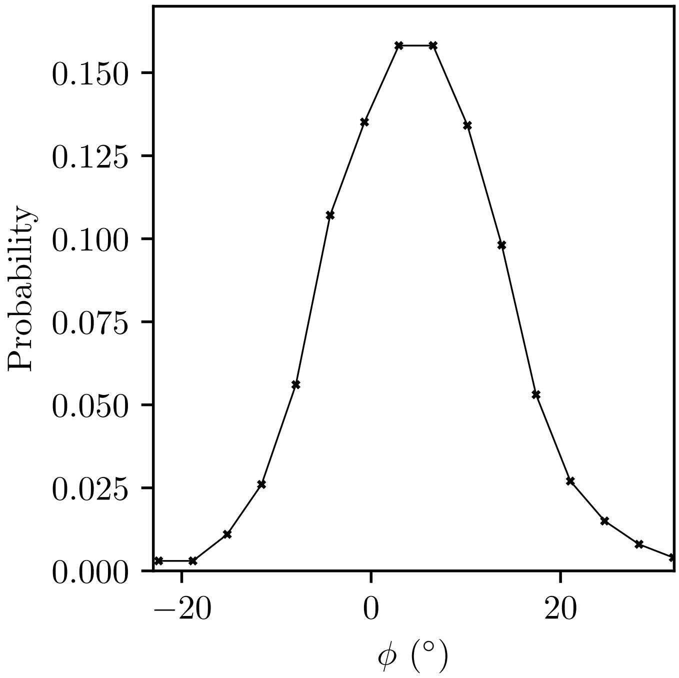

Figure 3.7: Distribution of dihedrals of polymer during 100 ns NVT simulation.

Figure 3.8 shows the radial distribution functions (RDFs) of all N1, S1 and O1 atoms in the system, respectively.

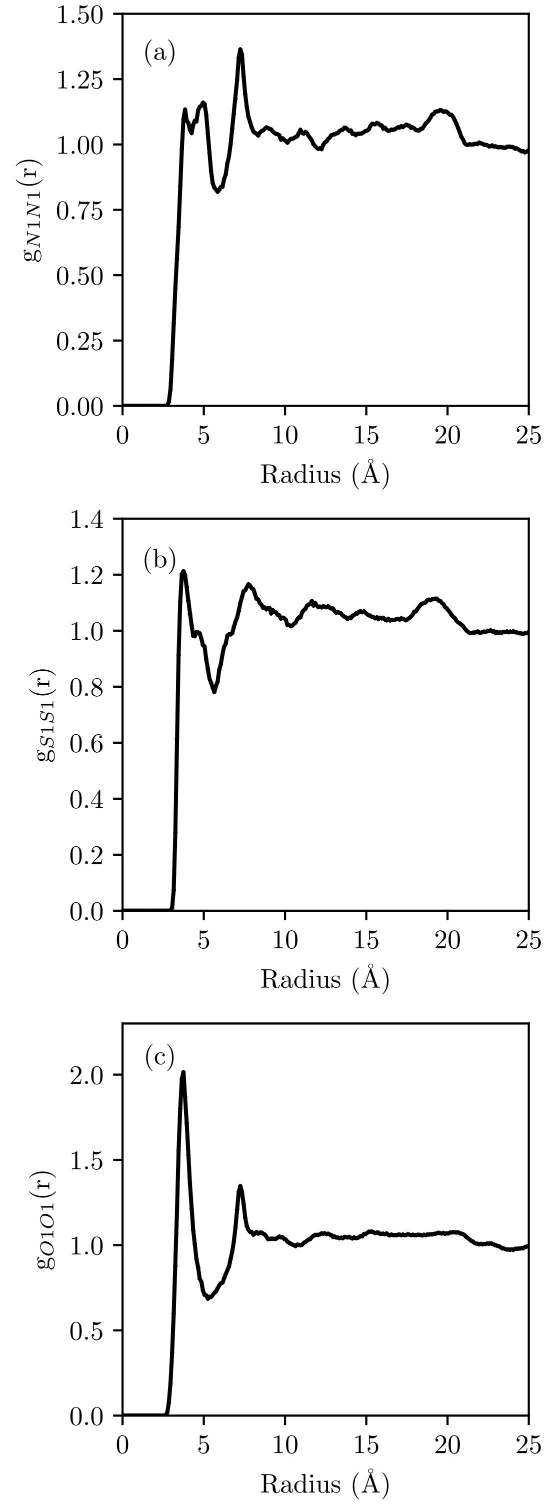

Figure 3.8: RDF for given atoms in the polymer. (a) N1, (b) S1 and (c) O1.

These RDFs give quantitative information about the separation (or packing) of surrounding atoms from any given atom. There are three distinctive peaks observed for all three atom types at roughly 4, 8 and 20 Å. These are the radii for which other atoms most likely to be found. The first two peaks in the RDF for sulfur atoms (Figure 3.8b) are similar to that observed for the one chain simulations of the poly[*N*-9"-hepta-decanyl-2,7-carbazole-*alt*-5,5-(4',7'-di-2-thienyl-2',1',3'-benzothiadiazole)]:[6,6]-phenyl (PCDTBT) conducting polymer, where sulfur peaks at about 5 and 9 Å were observed (Kawanabe et al. 2014). Thus, the first two peaks at short distances in our RDFs can be associated with the distributions of atoms along the chain (i.e. intra-chain packing) and the last peak (at about 20 Å) gives the inter-chain distributions.

Electronic Structure Properties

To gain insights into the electronic structure of the polymer, we first study the bulk DOS. Figure 3.9 shows the bulk DOS for the system of 20 chains of 40-mers averaged over ten snapshots from 10 to 100 ns each separated by 10 ns.

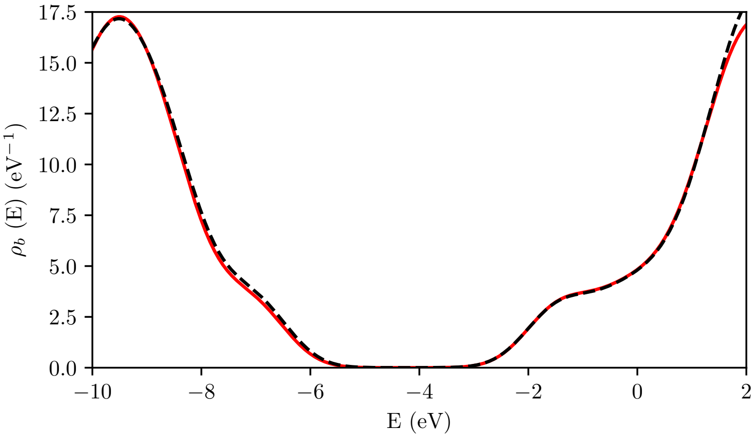

Figure 3.9: Bulk density of states computed for the 40-mer chains using the long-range corrected functional ωB97XD. Solid red line is the result using 3-21G* basis set averaged over 10 snapshots from 10 to 100 ns separated by 10 ns. Dashed black line is the result using 6-31G* basis set for a single chain at 100 ns.

Here, the background charges are not included to save the computational time, due to the effect of electrostatic disorder, which is relatively weak for semiconducting polymer (Qin & Troisi 2013). The long-range corrected functional ωB97XD is employed along with the 3-21G* basis set for this task. We found that the fluctuations in the DOS per chain per monomer for this system are almost negligible. Similarly, the DOS does not vary significantly with the chain lengths between 20 to 40 monomers, which agrees with a similar study on amorphous Poly[2-methoxy-5-(2'-ethylhexyloxy)-1,4-phenylene vinylene] (MEH-PPV) polymers (Qin & Troisi 2013). Calculations (only for one snapshot) using a larger basis set, i.e. 6-31G*, indicate that the discrepancy in the computed DOS between the two basis sets is negligible, especially around the HOMO-LUMO gap. Thus, it is sufficient to employ the smaller basis set (3-21G*) for characterising the electronic excitation in this type of conducting polymer using TD-DFT.

To investigate the nature of the electronic excitation of the polymer, we analyse the e-h distributions and the transition densities for the lowest three singlet excitations of a single chain. Among several other descriptors, the Λ-index proposed by Peach et al. (2008) has gained much attention, and has been widely employed as a diagnostic tool for monitoring TD-DFT results (Le Bahers et al. 2011). This method is based on the overlap of molecular orbital moduli. However, in some difficult cases, this index may not be able to locate problematic excitations (Peach et al. 2009). To provide a robust tool for exploring the excited state metric, another index called the Δr-index has been introduced (Guido et al. 2013). This index is based on the charge centroids of the orbitals involved in the transition. It is easy to interpret, because it measures the average e-h distance upon excitation. The Δr-index works particularly well for the CT excitations for which reliable CT length can be obtained.

To characterise the electronic excitation of the conducting polymer, we computed all the descriptors discussed previously and we present the results for the three lowest singlet excitations for the 40-mer chain in Table 3.2. All TD-DFT

Transition	D (Å)	S_r (a.u.)	H (Å)	t (Å)	$\delta\sigma$ (Å)	E_{coul} (eV)	Λ-index	Δr-index
$S_0 \rightarrow S_1$	0.55	0.91	7.70	-4.37	-0.48	2.03	0.81	2.40
$S_0 \rightarrow S_2$	7.45	0.72	20.26	-8.31	-3.13	0.45	0.62	16.75
$S_0 \rightarrow S_3$	9.93	0.48	19.73	-5.84	0.22	0.27	0.59	25.34

Table 3.2: Electronic excitation indices for the three lowest singlet excited states.

calculations are performed at the ωB97XD/3-21G* level of theory. Table 3.2 shows that the $S_0 \rightarrow S_1$ is clearly a local excitation with a relatively small D-index and Δr-index, which indicate that the hole and electron are quite close. This is also confirmed by, for example, the high value in the exciton binding energy and the overlap S_r-index. Further investigation of this transition using the contributions of the molecular orbitals of atoms and chromophores in the polymer chain to the e-h (Figure 3.10) shows that both the hole and electron originate from monomer number 30 and the e-h also resides on this monomer (mainly on the DPP chromophore).

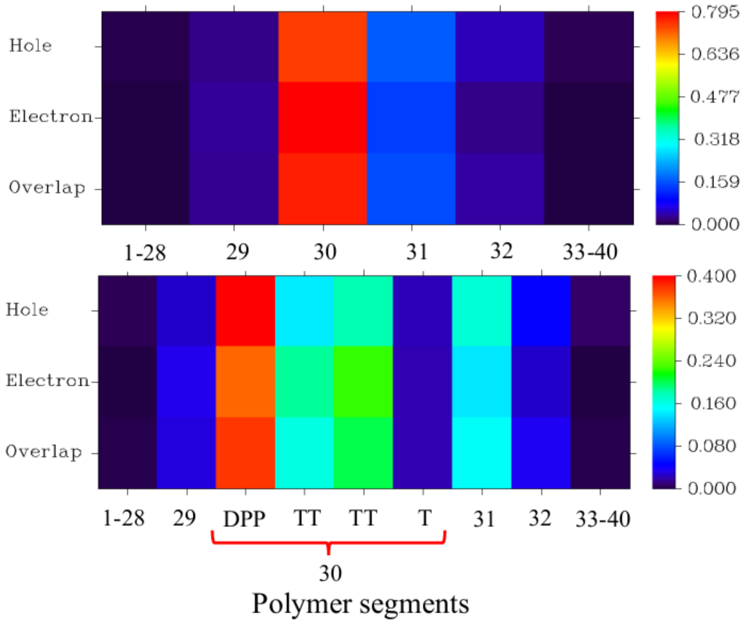

Figure 3.10: Heat map of fragment contributions (percentage contribute) to hole and electron for the $S_0 \rightarrow S_1$ transition. The numeric ticks in the x-axis denote the monomer sequence while the letters indicate the chromophore within the monomers.

This is confirmed by a plot of the fragment transition density matrix (Figure 3.11), which shows the distribution of charges along the polymer chain. According to the heat map shown in Figure 3.11, we can also observe that the electron and hole are mainly distributed on monomer 30. Since there is no clear off-diagonal element, this transition does not cause significant electron transfer between monomers. Although there are some small fractions of charge on the nearest neighbours, as can be observed from Figures 3.10 and 3.11, the main character of this excitation is its localisation on monomer 30.

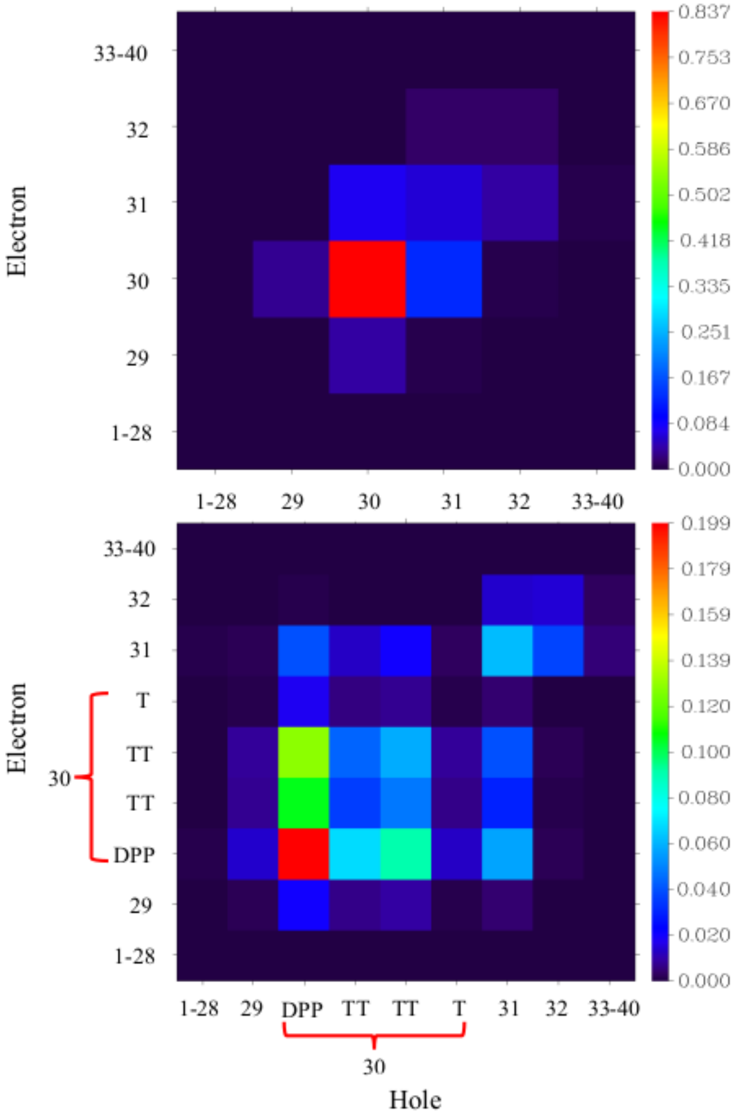

Figure 3.11: Heat map of fragment transition density matrix for the $S_0 \rightarrow S_1$ transition. The numeric ticks in the x-axis denote the monomer sequence while the letters indicate the chromophore within the monomers.

From Table 3.2, we can see that the CT character for the $S_0 \rightarrow S_2$ and $S_0 \rightarrow S_3$ transitions is quite strong with much larger D- and Δr-indices and substantial smaller exciton binding energies than the $S_0 \rightarrow S_1$ transition. In addition, the average degree of spatial extension of the hole and electron distribution (H-index) is also greater for the latter two excitations. Thus, the $S_0 \rightarrow S_2$ and $S_0 \rightarrow S_3$ transitions are delocalised CT states. The degree of delocalisation can be observed from the e-h distribution and the transition density matrix plots, which are shown in Figures 3.12 and A.31 for the $S_0 \rightarrow S_2$ transition and Figures A.32 and A.33 in the Appendix A for $S_0 \rightarrow S_3$.

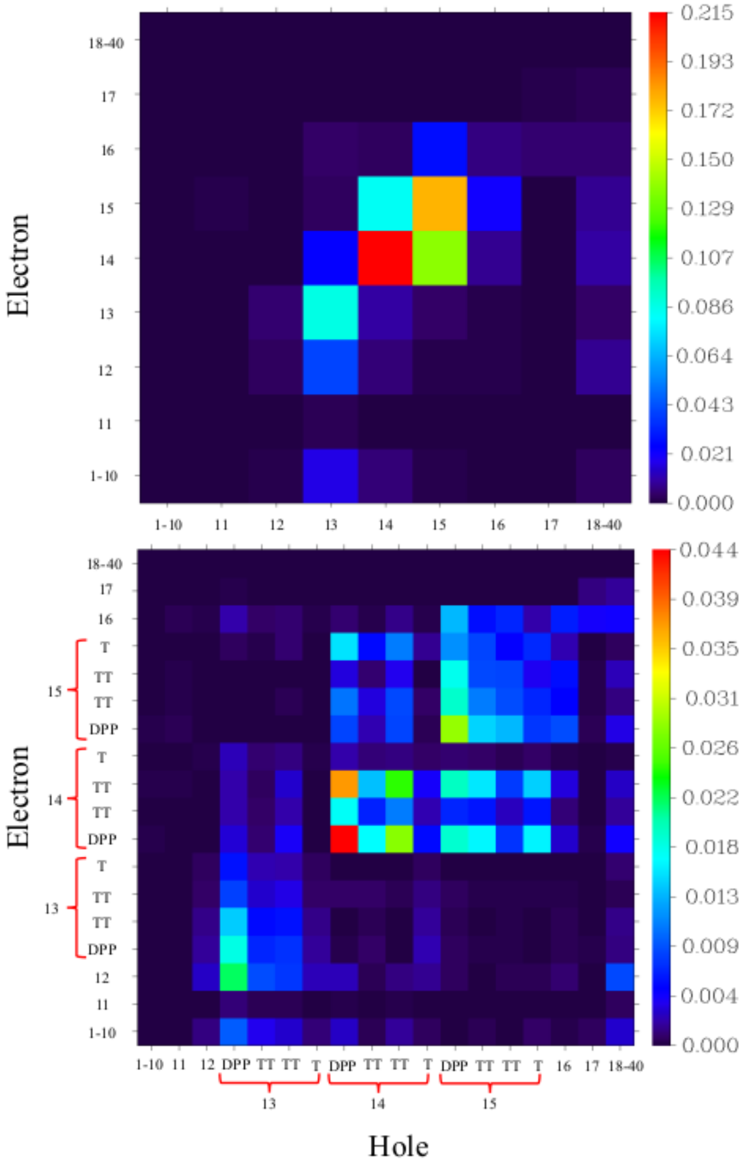

Figure 3.12: Heat map of fragment transition density matrix for the $S_0 \rightarrow S_2$ transition. The numeric ticks in the x-axis denote the monomer sequence while the letters indicate the chromophore within the monomers.

For example, in the $S_0 \rightarrow S_2$ transition, the electron and hole are mainly contributed to by monomers 13, 14 and 15 and the overlap is centred around monomer 14. However, contributions to both electron and hole from other monomers away from the three central monomers are also observed. The conjugation length (delocalisation length) is approximately four to six monomers based on the analysis of the e-h distributions and the transition density matrices for both CT states. This is in good agreement with other theoretical and experimental studies for amorphous conducting polymers (Qin & Troisi 2013, Ma et al. 2014, Köhler et al. 2012). Calculations for another 40-mer chain also show a similar trend for the first three lowest singlet excitations, which indicate that the two chains may share some similarities in their geometries. As the main focus of this work is on force field development, a thorough investigation of the relationship between the structures and electronic excitation properties of this class of conducting polymers will be carried out in future work.

3.5.3 Molecular Crystals

Molecular Dynamics Simulations

As another example, we study the dynamics of the molecular crystal UBEQOK, which has been synthesised recently (Figure A.34) (Pop et al. 2016). The equilibrium structures generated from MD simulations will be valuable for understanding the exciton dynamics in this new material. First of all, a 3 × 8 × 2 supercell, which comprises 192 molecules is created. Then, the system is minimised using 5000 steepest descent steps followed by 0.5 ns heating in the NPT ensemble (at 300 K and 1 atm). It is equilibriated for another 100 ns and continued for another 10 ns for production. All other simulation parameters are kept the same as those in the simulations of the polymeric system.

Since the simulations are performed under ambient conditions, it is expected that the molecules do not move very far from the original crystal structure and this can be observed from the root mean squared displacement of all molecules in the system (see Figure A.27 in the Appendix A). In other words, there is no melting and the molecules vibrate about their lattice points. Further insight into the microscopic structure of molecular crystal UBEQOK can be obtained from the distribution of torsional angles (Figure A.30). The peak around 0^o confirms that the molecular crystal UBEQOK's backbone is planar.

To gain insights into the nature of the fluctuation of the excitonic coupling between neighbouring molecules in UBEQOK molecular crystal due to thermal motions, the magnitude and time scale of the fluctuation of the excitonic coupling are investigated using a combined QM and MD approach. To compute the excitonic couplings for a pair of molecules, we employ the general diabatisation scheme proposed by Aragó & Troisi (2015*a*), which is capable of taking into account both short- and long-range effects. The short-range excitonic coupling contribution is inherent in molecular crystals and aggregates and is responsible for the fluctuation of the excitonic coupling in the presence of the nuclear thermal motions (Aragó & Troisi 2015*a*). Here, only the couplings of nearest neighbours are considered, as they have been shown to be adequate to describe quantitatively the excited state properties of molecular crystals (Yamagata et al. 2011). In addition, the coupling between molecular pairs at longer distances is dominated by the electrostatic term, which is not sensitive to small thermal fluctuations (Aragó & Troisi 2015*a*).

Two types of dimers with closest intermolecular contact for the exciton transport in UBEQOK molecular crystal are identified. Figure 3.13 shows the arrangement of these two structures with structure labelled (A) the parallel π-stacked columns where the intermolecular distance is around 5.7 Å and (B) a tilted structure. To construct the time evolution of the excitonic coupling in UBEQOK, nearest neighbours are extracted from 1000 equilibrium MD snapshots each separated by 50 fs. Then, the excitonic couplings for dimers (A) and (B) are computed using TD-DFT at the ωB97XD/6-31G* level of theory.

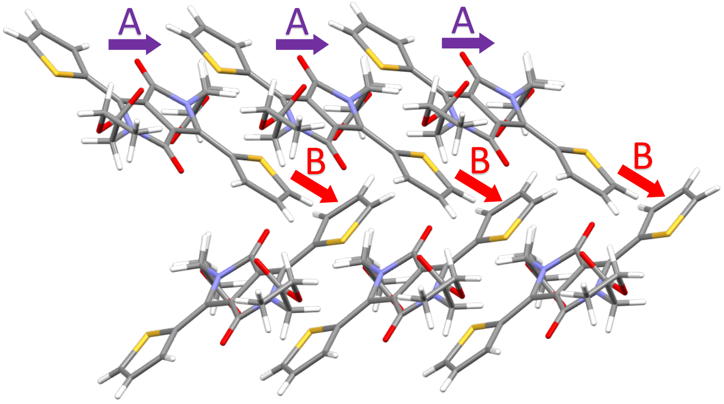

Figure 3.13: Example of crystal packing of the UBEQOK showing the most relevant dimers for the exciton transport: Parallel (A) and tilted (B) structures.

Figure 3.14 shows the time evolution and the distribution of the excitonic couplings computed for the two UBEQOK dimers (A) and (B). The excitonic couplings are bimodal distributions with each one being normally distributed (positive- and negative-coupling distribution). Both distributions of coupling values have approximately the same absolute mean and the probability of having a positive or a negative coupling is equally likely. The formation of a bimodal distribution is due to the flexibility between DPP and T chromophores, which causes the change in the signs of the transition dipole moments. Figure 3.14 shows that the magnitude of the couplings for UBEQOK falls into the same range as those computed for other molecular crystals e.g. DCVSN5 (Aragó & Troisi 2016) and $H_2 - OBP_c$ (Fornari et al. 2016). In addition, the largest excitonic coupling is also observed for the parallel structure for this system.

To investigate the characteristic timescale of the fluctuation in the excitonic couplings, Fourier transforms of the autocorrelation functions $\langle \delta J(0) \delta J(t) \rangle$, where $J(t)$ is the coupling as function of time, are computed for both positive- (Figure 3.15) and negative-coupling distributions (Figure A.35 in the Appendix A).

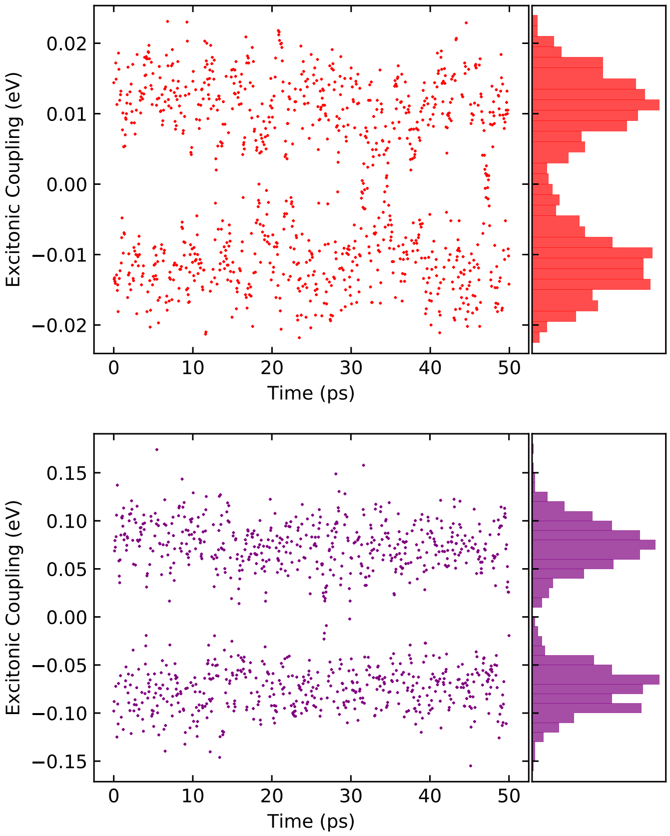

Figure 3.14: Time evolution and distribution of the excitonic couplings computed at 300 K for dimer A (bottom panel) and B (top panel).

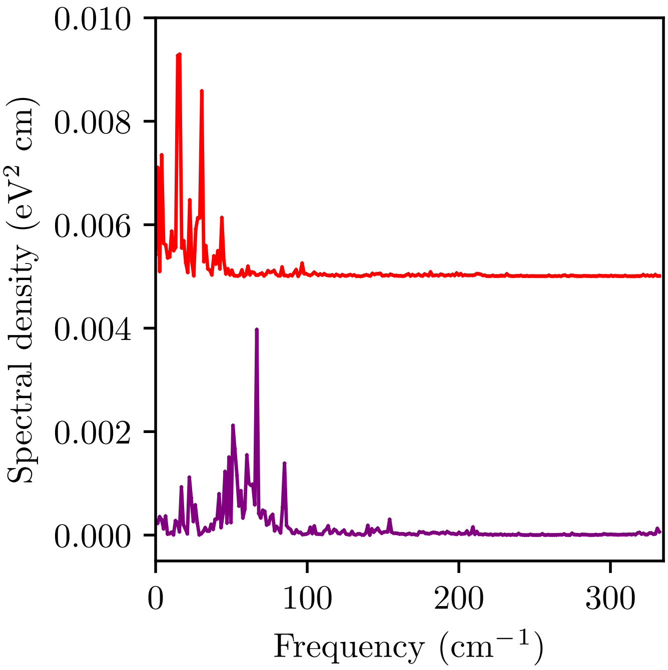

Figure 3.15: Fourier transformation of the autocorrelation function of the excitonic couplings computed at 300 K for the dimers A (purple) and B (red). The spectral density for dimer B is shifted upward by 0.003 eV^{2}cm.

Here, the deviation from the average excitonic coupling is defined as $\delta J(t) = J(t) - \langle J(t) \rangle$. Figures 3.15 and A.35 show that low frequency vibrations below 100 cm^{-1} are observed for both dimers (A) and (B), which is in good agreement with previous studies on other molecular crystals. (Aragó & Troisi 2015*a*, Aragó & Troisi 2016, Fornari et al. 2016) These low frequency vibrations are believed to be responsible for the large modulation of the excitonic coupling.

3.6 Conclusion and Outlook

A robust approach for generating accurate force fields for conjugated systems has been applied and extended for applications where subsequent quantum chemical calculations are employed. Built upon the force-matching technique, the method provides a consistency between the potential energy surface generated by empirical force fields and that generated by any *ab initio* method of choice. The approach is particularly suitable for applications that involve excited state calculations where accurate force fields to describe the excited state potential energy surface are needed. As an example, we parameterise the force fields and study the dynamics as well as the electronic excited properties of conjugated conducting polymers and molecular crystals containing DPP, T, and TT. The good agreement observed for both the structural and electronic excitation properties for all building block chromophores provides confidence that our force fields can reproduce the *ab initio* potential energy surfaces, for which their parameters are fitted to.

In this work, we employ OPLS force fields and the DFT at the B3LYP/6-31G* level of theory to illustrate how the desired optimised parameters can be obtained. However, the procedure is general and can be applied to any other combination of force field functional form and electronic structure method. The force RMSD between *ab initio* and empirical force fields can be improved by including more fitting parameters, such as introducing more atom types, including coupling between degrees of freedom and anharmonicity, or modifying the force field functional form. Our optimised force fields, by construction, are not transferable by atom types. However, the conjugated core such as DPP, TT, T, DPP-TT, DPP-T and TT-T could be treated as transferable. force fields for larger molecules can be constructed from these basic units, and thus allow access to the dynamics of conjugated macro-assemblies.

Chapter 4

Dynamic Disorder Drives Exciton Dynamics in Molecular Crystals

†

4.1 Synopsis

There is a growing interest in controllable molecular materials for potential nanophotonic and quantum information applications where excitons move beyond the incoherent transport regime. Thus, the ability to identify the key parameters that correlate with the efficiency of the transport of the excitation energy is highly desirable. Chapter 4 investigates the effects of the dynamic disorder on the transport of the exciton in molecular crystals of several recent synthesised mono- and di-alkylated TDPP derivatives. These systems exhibit great potential for photovoltaic applications due to their broad optical absorption and efficient charge transport. The exciton dynamics are studied

---

† Some of the work in this chapter has been submitted for publication in:

Jiang, L., Hirst, J. D. & Do, H. (2022), 'Dynamic disorder drives exciton dynamics in molecular crystals', *Journal of Physical Chemistry C* **Under Review**

using a model Hamiltonian, in which the thermal fluctuations of the excitonic coupling as well as the non-local exciton-phonon couplings have been properly taken into account. The computed reorganisation energies for the most feasible transport pathway (π-π stacking) for the excitons in UBEQUQ and UBEQOK molecular crystals are 0.366 eV and 0.357 eV, respectively. These values are comparable with the magnitude of the average excitonic coupling $\langle J \rangle$ (≈ 0.1 eV) for these two molecular crystals. In this instance, the local exciton-phonon coupling is not large enough to form a small exciton-polaron. In addition, substantial coherences are observed on a time scale of less than 100 fs, which indicates that the dynamic disorder is sufficient to overcome quantum dephasing and help drive exciton transport in this class of organic semiconductors. On the other hand, the diffusion of the excitons reduces significantly when the thermal fluctuations of the excitonic coupling and the nuclear dynamics are omitted. Thus, dynamic disorder plays a vital role in the transport of the exciton, and the ability to control this inherent property in molecular aggregates will provide valuable tools for the design and development of efficient organic semiconductors.

4.2 Introduction

Organic semiconducting materials have the potential to overcome some of the shortcomings associated with inorganic materials and offer new and exciting opportunities for the next generation of electronic devices. (Forrest 2004) These organic molecules contain a wide variety of structures and properties due to the many possible molecular constituents. They could be completely amorphous polymers with interlaced chains, partially ordered polymers, polycrystalline molecules, or molecular crystals (Rivnay et al. 2012, Noriega et al. 2013b). Moreover, organic materials can be processed from solution and their electronic properties can be controlled through conventional wet chemistry. Furthermore, they are economical, easily fabricated, biodegradable, and lightweight. Hence, these unique properties make them highly attractive complements to traditional inorganic semiconductors for the development of flexible electronic devices (Moorthy 2015, Dantanarayana et al. 2020, Liu et al. 2013, Meredith & Armin 2018, Patel & Diao 2017).

In recent years, molecular OSCs have been extensively investigated as active components in optoelectronic devices, including OPVs for light-harvesting and power conversion, OLEDs used as light sources and organic field-effect transistors (Schweicher et al. 2020, Dou et al. 2013, Sirringhaus 2014, Lin & Yan 2012, Jou et al. 2015, Krämer et al. 2020). Despite impressive progress during the past few decades, exciton transport in organic materials remains highly controversial. Two limiting transport regimes (coherent and incoherent) are often invoked to describe the exciton diffusion in molecular materials or aggregates. However, none of these limits is appropriate for exciton transport in the most studied materials because the excitonic coupling in molecular crystals undergoes a considerable fluctuation at room temperature due to the combined thermal motions of the nuclei (Aragó & Troisi 2015*a*). This observation dramatically affects the description of exciton transport in organic crystals that originates from an exciton in a molecular crystal or thin film.

Efficient exciton diffusion in molecular crystals (or aggregates) over long distances is crucial for the performance of optoelectronic devices. The driving force of the exciton diffusion is the excitonic coupling (J) between excited states localised on the molecular units. The excitonic coupling can be separated into long-range (Coulombic) and short-range (exchange and overlap) contributions (Harcourt et al. 1994, Yamagata et al. 2014, Hestand et al. 2015, Krausko et al. 2015). In general, the long-range coupling between the neighbouring molecules is the only term considered for excitation energy transfer in molecular aggregates separated by long intermolecular distances. On the other hand, the short-range coupling arises mainly from the orbital overlap effect, and is crucial for organic molecular crystals whose intermolecular distances are between 3.5 and 5.0 Å (Hsu, You & Chen 2008, Aragó & Troisi 2015*a*). In addition, molecular crystals have low-frequency intermolecular vibrations that often cause dynamic disorder (large lattice displacement) (Eggeman et al. 2013). The short-range excitonic coupling is sensitive to the relative arrangement of the neighbouring molecules. And, it can fluctuate significantly due to thermal molecular motions of the system (Aragó & Troisi 2015*a*). This phenomenon is referred to as the non-local exciton-phonon coupling and plays a vital role in the modulation of the exciton transport (Aragó & Troisi 2016). Thus, thermal fluctuation of the excitonic couplings must be taken into account for an accurate description of the exciton diffusion in molecular crystals and aggregates with short-range interactions (Renaud & Grozema 2015).

Indeed, exciton transport in crystalline organic semiconductors is intrinsically limited by the presence of large thermal molecular motions. These induce a localisation of the electronic wavefunction, which survives up to the typical time scales of the intermolecular vibration (Fratini et al. 2016, Troisi & Orlandi 2006*a*). Generally, these problems are difficult to solve using analytical theory due to the thermal fluctuations and spatial symmetry breaking in the crystal (Rispens et al. 2003, Cheung & Troisi 2010, Reyes-Reyes et al. 2005). Experimental data are invaluable for characterising the utility of materials for devices, but they often do not give detailed insight into the nature of the exciton transport. Thus, theoretical and computational approaches can be a crucial complement to experiments by providing direct access to microscopic and electronic properties of OSCs and help to guide their development.

Although coherent transport would be highly desirable in terms of efficiency, exciton diffusion in most molecular materials used for optoelectronic applications takes place via a series of hopping events between neighbouring molecules, with exciton diffusion lengths that rarely exceed 100 Å(Menke & Holmes 2014).

The coherent regime is less frequent but potentially of great technological importance in the design of efficient exciton transport molecular materials. It is clear now that dynamic disorder is related directly to exciton mobility (coherent regime) in OSCs. There is growing interest in obtaining controllable molecular materials for potential nanophotonic and quantum information applications where excitons move beyond the incoherent transport regime (Dostál et al. 2018, Roy et al. 2021). In addition, by controlling the amount of dynamic disorder, with a suitable mechanical deformation, the performance of molecular films can be greatly improved (Kubo et al. 2016). These examples demonstrate the importance of dynamic disorder in relation to the design principles for OSC materials. A fundamental understanding of the dynamics of the excitonic coupling and the regime of exciton transport in molecular crystals is a crucial first step in this regard.

Derivatives of small organic molecules such as DPPs have attracted much attention for photovoltaic applications due to their broad optical absorption and efficient charge transport (Chandran & Lee 2013). Moreover, these materials are chemically and thermally stable, facile to synthesise, and have good solution processability (Naik & Patil 2013). Thus, DPPs are intensively studied organic building blocks for high-performance pigments (Kaur & Choi 2015) and light harvesting chromophores in OSCs (Li et al. 2013). Of the wide variety of chromophores derived from DPP, the series of TDPP derivatives is one of the most investigated. These molecules are synthetically accessible and highly planar, resulting in high π-delocalisation and favourable π-π intermolecular interactions (Pop et al. 2016). Among all the side chains, the alkyl side chain is almost coplanar with the DPP and shows close packing of the molecules (Naik et al. 2012), which may enhance the occurrence of singlet exciton fission, allowing high efficiency of OSC devices (Hartnett et al. 2016). Recently, Pop et al. (2016) synthesised and analysed the structural and spectroscopic properties of a series of mono- and di-alkylated substituted TDPP molecular crystals. They suggested that the ethyl acetate substituents have good potential for modulating and optimising the charge transport in materials for organic electronic applications, as they promote molecular planarity and close crystal packing (due to the enhancement of the intermolecular hydrogen bonding network). Thus, it is important to characterise the dynamics of the excitonic coupling in this new class of OSC materials to reveal their exciton transport regimes in the presence of thermal disorder.

In this chapter, we investigate the exciton transport of these recently synthesised mono- and di-alkylated substituted TDPP molecular crystals utilising computational chemistry tools. First of all, we employ a force-matching procedure to parameterise new force fields systematically for mono- and di-alkylated substituted TDPP. In order to mitigate the mismatch in the geometry, the classical potential energy surface and its gradients of the system of interest are mapped onto *ab initio* ones by optimising the force field parameters. These new force fields are used to propagate the dynamics of the systems and the equilibrium trajectories (nuclear dynamics) are sampled for electronic structure calculations. After this, the excitonic couplings between all the relevant excited states in the molecular crystal pairs are computed and their fluctuations due to thermal disorder are analysed. Finally, the exciton dynamics are studied using a Frenkel–Holstein like Hamiltonian with an appropriate theoretical approximation where the thermal excitonic coupling fluctuations (non-local exciton-phonon couplings) have been properly taken into account.

4.3 Computational Details

4.3.1 Time-Dependent Model Hamiltonian

The exciton transport of the TDPP molecular crystals we study here can be assumed to take place mainly along the one-dimensional π-stacking columns due to the dominance of their excitonic couplings compared to other intercolumnar excitonic couplings. For example, in the case of UBEQOK (see Figure B.1 for the chemical names and structures of the studied molecular crystals), the average coupling value of the π-stacking columns is at least ten times greater than those of other intercolumnar stackings (Jiang et al. 2020). Similar trends are also observed for other crystals. In addition, as the excitonic coupling between molecular pairs in the π-stacking columns is comparable to the reorganisation energy, the coherent transport regime can be invoked (see the Results and Discussion section for more details) (Aragó & Troisi 2016). Thus, a one-dimensional time-dependent model Hamiltonian that includes all the important physical ingredients can be utilised. This kind of model Hamiltonians are routinely employed to characterise exciton and charge transport in organic semiconducting materials (Kunsel et al. 2021, Ghosh & Spano 2020, Aragó & Troisi 2016). Furthermore, in molecular crystals, since the nuclei vibrate at a much lower frequencies than the intramolecular and electronic degrees of freedom, we can employ the semiclassical approach to separate the Hamiltonian into a classical part $\hat{H}^{\mathrm{cl}}$ that accounts for the low-frequency nuclear dynamics and a quantum mechanical part $\hat{H}^{\mathrm{qm}}$ that represents the high-frequency degrees of freedom (Troisi & Orlandi 2006*a*, Aragó & Troisi 2016, Fornari et al. 2016, Strong & Hestand 2020). Thus, the total Hamiltonian of the system is $\hat{H}(t) = \hat{H}^{\mathrm{qm}}(t) + \hat{H}^{\mathrm{cl}}(t)$.

For the quantum mechanical part, we employ a Frenkel-Holstein like Hamiltonian (Troisi & Orlandi 2006*b*,*a*, Troisi 2007), which is written as:

$$\begin{aligned}\hat{H}^{\mathrm{qm}}(t) = &\sum_i^N \left(E_i + \sum_k g^{(k)} r_i^{(k)} \right) |i\rangle\langle i| \\ &+ \sum_i^N \left(J + \sum_k \alpha^{(k)} \left(r_{i+1}^{(k)} - r_i^{(k)} \right) \right) \left(|i\rangle\langle i+1| + |i+1\rangle\langle i| \right)\end{aligned} \tag{4.1}$$

where i is the index of the molecular site in the one-dimensional aggregate and N is the total number of molecules (sites) in the system. The first sum accounts for the energy of the localised Frenkel excitons and the second sum describes the excitonic coupling between the nearest neighbours. Localised on each molecule are a single electronic state $|i\rangle$ (in principle, one can consider multiple electronic states) and some harmonic nuclear vibrations (indexed k) with the centre of mass displacement $r_i^{(k)}$. E_i is the energy of the lowest singlet excited state and J is the excitonic couplings between these excited states at adjacent sites. $g^{(k)}$ and $\alpha^{(k)}$ are the local exciton-phonon and the Peierls electron-phonon coupling constants, respectively. When the nuclear modes are in their equilibrium position (i.e. $r_i^{(k)} = 0$), the energy of state $|i\rangle$ is E_i and the excitonic coupling between adjacent states is J.

The electron-phonon couplings (the time-dependent part of the Hamiltonian) enter the Hamiltonian classically through the time-dependent fluctuations in the atomic coordinates $\mathbf{q}_i^N(t)$. The classical Hamiltonian can be expressed as:

$$\hat{H}^{\mathrm{cl}}(t) = \sum_i \frac{\mathbf{p}_i^2}{2m_i} + U\left(\{\mathbf{q}\}\right) \tag{4.2}$$

where $\mathbf{p}_i$ is the momentum conjugate to atomic coordinates $\mathbf{q}_i$, m_i is the mass of particle (atom) i, and $U\left(\{\mathbf{q}\}\right)$ is the total potential energy of the system. Here, we model these fluctuations using MD simulations of the crystals. Finally, the time-dependent Hamiltonian for a one-dimensional array of molecules is constructed by employing various *ab initio* techniques.

In this model, the nuclear modes couple to the charge carrier (exciton-phonon coupling) in two different ways. First, the nuclear displacement $r_i^{(k)}$ alters the site energy E_i of the charge carrier on site i according to the Holstein electron-phonon coupling term $g^{(k)} r_i^{(k)} |i\rangle\langle i|$, where $g^{(k)}$ is the local exciton-phonon coupling constant and is related to the reorganisation energy. Secondly, the nuclear displacements r_i^k and r_{i+1}^k modulate the transfer integral between sites i and $i+1$ with the term $\alpha^{(k)}\left(r_{i+1}^{(k)} - r_i^{(k)}\right)$. This is the Peierls electron-phonon coupling, often known as the non-local exciton-phonon coupling, and is identified as the main source of the dynamic disorder in molecular aggregates (Troisi & Orlandi 2006*b*).

4.3.2 Force Field Development

In recent years, MD simulations have found wide applications in the study of the optical and electronic properties of materials and biomolecules, where they are primarily employed to sample the equilibrium structures explored by the system of interest (the nuclear dynamics). These equilibrium trajectories can be utilised in large-scale quantum chemistry calculations to correlate the local structure with the observable electronic structure properties. Consequently, it is vital that the force fields used to describe the nuclear dynamics are accurate enough to capture the true molecular motion of the system. A challenge one often has to confront here is the mismatch in the force fields describing the interactions at the classical level and the electronic structure methods employed for subsequent quantum chemistry calculations. In other words, the potential energy surface of $\hat{H}^{\mathrm{qm}}$ does not coincide with that of $\hat{H}^{\mathrm{cl}}$.

To overcome this challenge, we employ our extension (Jiang et al. 2020) of the adaptive force-matching technique (Do & Troisi 2015) to parameterise the force fields for the studied molecular crystals in this work. The idea behind our procedure is to find a set of parameters that minimises the differences between the classical forces and the *ab initio* forces. Thus, by design the force fields used to propagate the nuclear dynamics should be comparable to those targeted *ab initio* methods. In addition, instead of optimising the parameters for the whole system in one go, which is computationally expensive, we fragment the "larger" molecule into smaller segments, obtain their parameters, and then assemble them together to derive the force fields for the larger molecule. Here, all the studied molecular crystals comprise a DPP core, a T ring and the side chains. Therefore, the building blocks are DPP, T and the side chains in these cases. The *ab initio* forces (reference forces) are computed using DFT at the same level of theory as the excitonic coupling and other quantum chemical properties (to mitigate the mismatch in the potential energy surfaces). The long-range-corrected functional ωB97XD is chosen for all quantum chemical calculations because it captures both short- and long-range interactions and describes CT states accurately (Chai & Head-Gordon 2008). All quantum chemistry calculations are performed using the Gaussian 16 package (Frisch et al. 2016).

For the chromophores, the initial "guessed" parameters are taken from the optimised parameters of DPP, T, and DPP-T in our previous work (Jiang et al. 2020). For the side chains, we use parameters from the OPLSs force field (Dodda et al. 2017) and keep these fixed during the optimisation scheme i.e. we only optimise the parameters for the chromophores and utilise the OPLSs parameters for the side chains. We follow the same procedures as in our previous work (Jiang et al. 2020) to obtain a new set of optimised parameters for DPP, T and DPP-T at the ωB97XD/6-31G* level of theory. Finally, we perform a further optimisation for the whole molecule including the side chains to obtain better sets of parameters. By construction our force fields are capable of reproducing the potential energy surfaces of those targeted quantum chemical methods. (Jiang et al. 2020) In other words, the sampled nuclear trajectories should be equivalent or very close to those that would have been sampled on the ωB97XD/6-31G* potential energy surface.

4.3.3 Classical Molecular Dynamics Simulations of the Crystals

To obtain the nuclear dynamics and evaluate the time fluctuation of the excitonic coupling subject to the thermal motions of the molecular crystals, simulations are performed using our new force fields within the NAMD package (Phillips et al. 2005). As we are interested in the transport of the excitons along the π-π-stacking direction, the supercell of each crystal is created by replicating the unit cell in a way to ensure that there are several hundreds of molecules in the π-stacking columns (to allow for the observation of the exciton diffusion). An example of a supercell of the ethyl (1,4-dioxo-3,6-bis(2-thienyl)-4,5-dihydropyrrolo[3,4-*c*]pyrrol-2(1H)-yl)acetate (UBEQUQ) (CCDC crystal code) is shown in Figure B.2.

For all molecular crystals, the systems are minimised using 10000 steepest descent steps followed by 10 ns heating in the NPT ensemble (at 300 K and 1 atm). They are then equilibrated for another 100 ns in the NVT ensemble and continued for another 10 ns in the NVE ensemble for production. The use of three different ensembles helps smoothly bring the systems to the desired conditions (in the NVE ensemble ultimately) without letting the atoms experience unnatural friction from the barostat and the thermostat. Three-dimensional periodic boundary conditions are applied. The Langevin thermostat (Hoover et al. 1982) with a damping coefficient equal to 1 ps^{-1} is employed to keep the temperature constant. The period and decay parameters of the Langevin piston are set to 100 and 50 fs, respectively, to maintain the pressure. A time step of 1 fs for integration of the equations of motion is used throughout the simulations. A cutoff of 12 Å is used for nonbonded interactions. The particle mesh Ewald algorithm (Herce et al. 2007) is used to calculate long-range electrostatic interactions. To construct the time evolution of the excitonic coupling, nearest neighbours are extracted from 1000 equilibrium MD snapshots each separated by 50 fs.

4.3.4 Quantum Chemical Calculations

All electronic structure properties including the excitation energies, transition dipole moments, and ATC for both the monomers and dimers are computed using TD-DFT at the ωB97XD/6-31G* level of theory. Reorganisation energies and Huang-Rhys factors are also computed using ωB97XD functional but with a larger 6-31G** basis set (see Appendix B for more details).

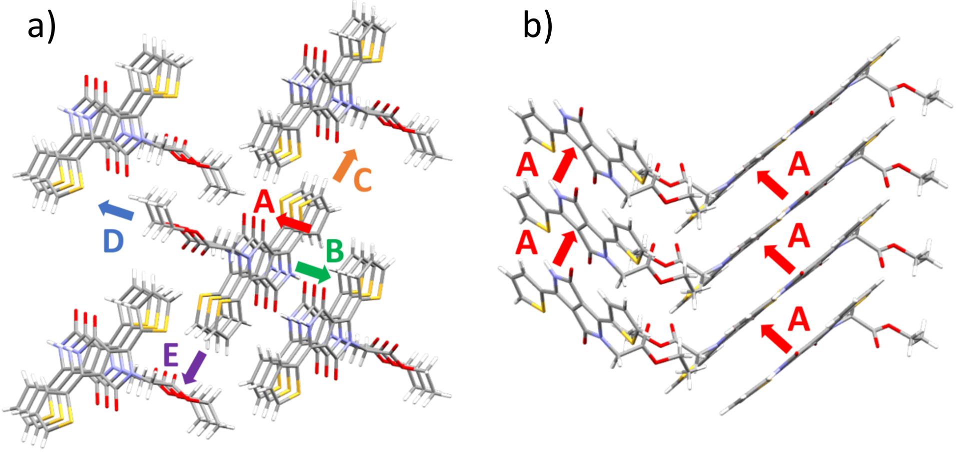

Figure 4.1: (a) Relevant dimers (coupling pathways A, B, C, D, E) for the exciton transport in UBEQUQ. (b) Coupling pathway A - the parallel π-stacked column.

For each molecular crystal, the most relevant dimers for the exciton transport are first identified by inspecting the crystal packing. For example, in the case of UBEQUQ (Figure 4.1), five different relevant dimers (called A, B, C, D and E) are identified. The excitonic couplings are computed using a diabatisation scheme, which is capable of dealing with multiple excited states and also taking into account both short- and long-range effects of the couplings (Aragó & Troisi 2015*a*, Aragó & Troisi 2015*b*). The technique makes use of molecular properties such as transition dipole moments or ATC to find the best adiabatic-to-diabatic orthogonal transformation matrix $\mathbf{C}$, which unitarily transforms the adiabatic Hamiltonian matrix $\mathbf{H}^{\mathrm{A}}$ to the corresponding diabatic Hamiltonian matrix $\mathbf{H}^{\mathrm{D}}$. The diagonal and off-diagonal elements of the diabatic Hamiltonian $\mathbf{H}^{\mathrm{D}}$ are the diabatic energies and excitonic couplings, respectively. The nature of the lowest-energy excitations of DPP derivatives is Frenkel type, with the exciton (charges plus holes) localised only on the DPP segment (Figure B.3).

The transition dipole moments and the ATC can be utilised directly to compute the long-range (Coulombic contributions) excitonic couplings, if the intermolecular interactions of the chromophores are dominated by the electrostatic terms. However, this is not the case for the molecular crystals studied in this work, whose intermolecular distances are relatively short (4 to 5 Å). A comparison of the excitonic couplings computed by using different approaches is shown in Figure B.4. The excitonic couplings are computed in vacuum i.e. the environment polarisation effects are not included, as only the Frenkel exciton states are considered. In general, the Frenkel exciton excited states are not sensitive to the relative changes in the dielectric constant in molecular crystals (Aragó & Troisi 2016). The polarisation effect is only significant for the excitonic coupling between molecules at greater separations and when there is a CT state.

4.3.5 Exciton Propagation

The time evolution of the exciton wave function can be computed by integrating the time-dependent Schrödinger equation (TDSE)

$$i\hbar \frac{\partial}{\partial t} |\psi(t)\rangle = \hat{H}^{\mathrm{qm}}(t) |\psi(t)\rangle \tag{4.3}$$

where the nuclear dynamics are treated classically. Expanding the exciton wave function $|\psi(t)\rangle$ in terms of the site basis $|n\rangle$ (i.e. $|\psi(t)\rangle = \sum_n c_n(t)|n\rangle$) and multiplying from the left by the complex conjugate basis vector $\langle m|$, equation 4.3 can be rewritten in terms of matrix elements as:

$$i\hbar\frac{\partial c_m(t)}{\partial t} = \sum_n H^{\mathrm{qm}}_{nm}(t)c_n(t) \tag{4.4}$$

Here, the site basis correspond to an exciton that is localised on a single molecule while the rest are in their ground states.

Equation 4.4 is solved numerically by updating the time-dependent Hamiltonian $\hat{H}^{\mathrm{qm}}(t)$ discretely every short time interval Δt corresponding to the nuclear dynamics (Bondarenko et al. 2020, Li, Buda, De Groot & Sevink 2020). The Hamiltonian is assumed to be constant (time-independent) within each block of time Δt. Thus, for the jth interval, the constant Hamiltonian is $H(t = j\Delta t)$ and labelled as H^j. Therefore, the individual TDSE that needs to be solved is

$$i\hbar\frac{\partial c_m(t)}{\partial t} = \sum_n H^{j}_{nm}(t)c_n(t) \tag{4.5}$$

where $t \in [j\Delta t, j\Delta t + \Delta t]$.

The choice of the time step δt is crucial to have a stepwise constant Hamiltonian. In other words, each update should introduce a relatively small perturbation to the Hamiltonian from the previous interval. As the relative motions between molecules are much slower than the intramolecular vibrational modes, we choose to update the time-dependent Hamiltonian every 1 fs (i.e. $\delta t = 1$ fs). In addition, the root mean square displacement of the nuclear coordinates of each molecule in the crystal does not vary significantly within 1 fs. For example, Figures B.5 and B.6 in the Appendix B show that the root mean square displacements for UBEQUQ and UBEQOK are only about 0.001 Å. In general, equation 4.5 can be solved directly by diagonalising the Hamiltonian matrix $\mathbf{H}^j$ to get the corresponding state basis $|\phi^j_k\rangle$ and hence the time-dependent exciton wave function $|\psi(t)\rangle$. However, to avoid repeatedly diagonalising the Hamiltonian as well as having to keep changing the basis in each time interval, we instead propagate always in the site basis. We solve each individual TDSE in equation 4.5 using the master equation solver (ZVODE) as implemented in the quantum toolbox in Python (QuTiP) package (Johansson et al. 2012, 2013). The initial state (wave function) $|\psi(0)\rangle$ is taken to be one of the electronic Hamiltonian eigenstates at $t = 0$. At the start of the simulation, the initial wave function is projected onto the site basis before the dynamics are propagated. The simulation is performed for one picosecond. A schematic of the algorithm is shown in Figure 4.2.

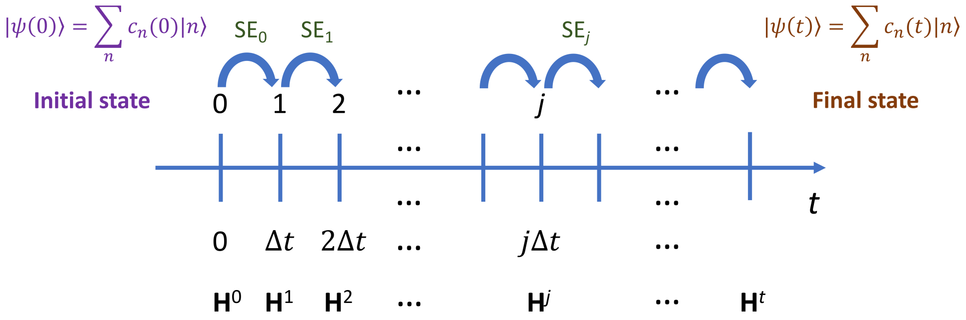

Figure 4.2: Schematic diagram of the exciton dynamics procedure.

The exciton dynamics trajectory is a collection of $|\psi(t)\rangle = \sum_n c_n(t)|n\rangle$ in the site basis and the exciton population at site n is $|c_n(t)|^2$. Since the environmental effects are taken into account (i.e. thermodynamic ensembles) for the studied systems, it is convenient to work with the density matrices, which also include coherence information. The density matrix $\rho(t)$ for any given wave function $|\psi(t)\rangle$ in the site basis is expressed as

$$\rho(t) = |\psi(t)\rangle\langle\psi(t)| = \sum_{i=1}^{N}\sum_{j=1}^{N} \rho_{ij}(t)|i\rangle\langle j| \tag{4.6}$$

where the diagonal terms $\rho_{ii}(t)$ give the populations of the exciton on each site i and the off diagonal terms $\rho_{ij}(t)$ describes the coherences between states i and j.

To calculate the average exciton energy, we use the density matrix in the state basis (the eigenstates ϕ_k^t of the Hamiltonian). The density matrix ρ^ϕ in the $|\phi_k^t\rangle$ representation is obtained from the density matrix in the site basis $\rho(t)$ as

$$\rho^\phi(t) = P^{-1}(t)\rho(t)P(t) = \sum_{k=1}^{N}\sum_{l=1}^{N} \rho_{kl}^\phi(t)|\phi_k^t\rangle\langle\phi_l^t| \tag{4.7}$$

where $P(t)$ is the projection matrix used to project $\rho(t)$ onto the eigenstate basis. For the j^{th} time interval (i.e. $t \in [j\Delta t, j\Delta t + \Delta t]$) the density matrix $\rho^\phi(t)$ is obtained as:

$$\rho^\phi(t) = P_j^{-1}\rho(t)P_j = \sum_{k=1}^{N}\sum_{l=1}^{N} \rho_{kl}^\phi(t)|\phi_k^j\rangle\langle\phi_l^j| \tag{4.8}$$

where P_j is the projection matrix composed of column vectors for the eigenstates $|\phi_k^j\rangle$. Thus, the average exciton energy $\bar{E}(t)$ for the j^{th} time interval is computed as $\bar{E}(t) = \sum_{k=1}^{N} \rho_{kk}^\phi \epsilon_k^j$, where ϵ_k^j is the eigenenergy of the state $|\phi_k^j\rangle$ (i.e. $H^j|\phi_k^j\rangle = \epsilon_k^j|\phi_k^j\rangle$).

4.4 Results and Discussion

4.4.1 Fluctuation of the Excitonic Couplings

To construct the time evolution of the excitonic coupling, nearest neighbours are extracted from 1000 equilibrium MD snapshots each separated by 50 fs. The excitonic couplings for all dimers are computed using TD-DFT at the ωB97XD/6-31G* level of theory. Figure 4.3 shows the time evolution and the distribution of the excitonic couplings computed for the five dimers A, B, C, D and E for UBEQUQ (see Figure 4.1). The excitonic couplings are normally distributed. This distribution is also observed for the case of UBEQOK (Jiang et al. 2020) and other studied molecular crystals (Figures B.7 to B.12). For each system, the largest excitonic coupling is found for the parallel π-stacked dimers, and among all the studied molecular crystals, those π-stacked dimers from UBEQUQ and UBEQOK have the strongest couplings. These results are in accord with the experimental observation (Pop et al. 2016) that UBEQUQ and UBEQOK have the strongest close packing and π-π stacking due to their intermolecular hydrogen bonding networks. In general, close packing parallel π-π stacking enhances excitonic couplings, which is one of the main factors promoting exciton transport in molecular aggregates. Therefore, UBEQUQ and UBEQOK (mono- and di-alkyl TDPP based on acetate alkyl units) are postulated to have superior charge carrier mobility due to the improved close packing (Dhar et al. 2015). Thus, our aim in this work is to shed light on the experimental observation by characterising the dynamics of the exciton in these two interesting molecular crystals.

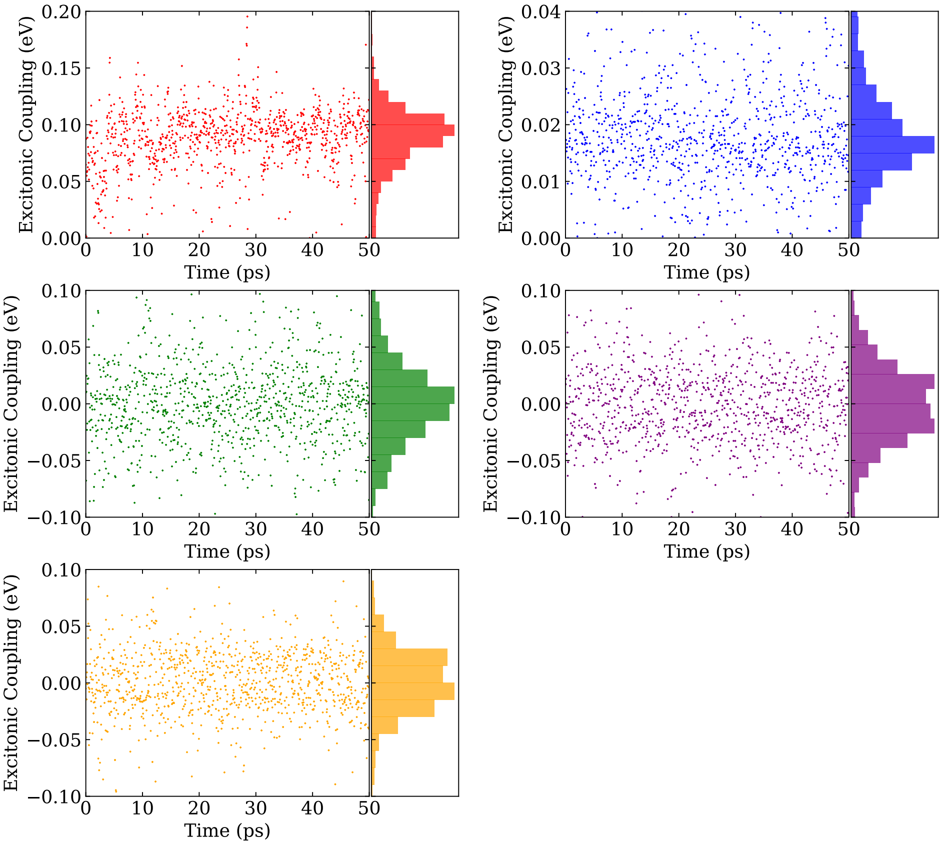

Figure 4.3: Time evolution and distribution of the excitonic couplings for UBEQUQ computed at 300 K for dimers A, B, C, D, and E, following the definition and colour-code in Figure 4.1.

To investigate the characteristic time scale of the fluctuation in the excitonic couplings, Fourier transforms of the autocorrelation functions $\langle \delta J(0)\delta J(t)\rangle$, where $J(t)$ is the coupling as function of time, are computed for dimers in UBEQUQ (Figure 4.4). Here, the deviation from the average excitonic coupling is defined as $\delta J(t) = J(t) - \langle J(t)\rangle$. Figure 4.4 shows that low frequency vibrations below roughly 50 cm^{-1} are observed for the π-stacked dimer A. The same trend is also observed for the parallel π-π stacking in UBEQOK. These low frequency vibrations are believed to be responsible for the large modulation of the excitonic coupling.

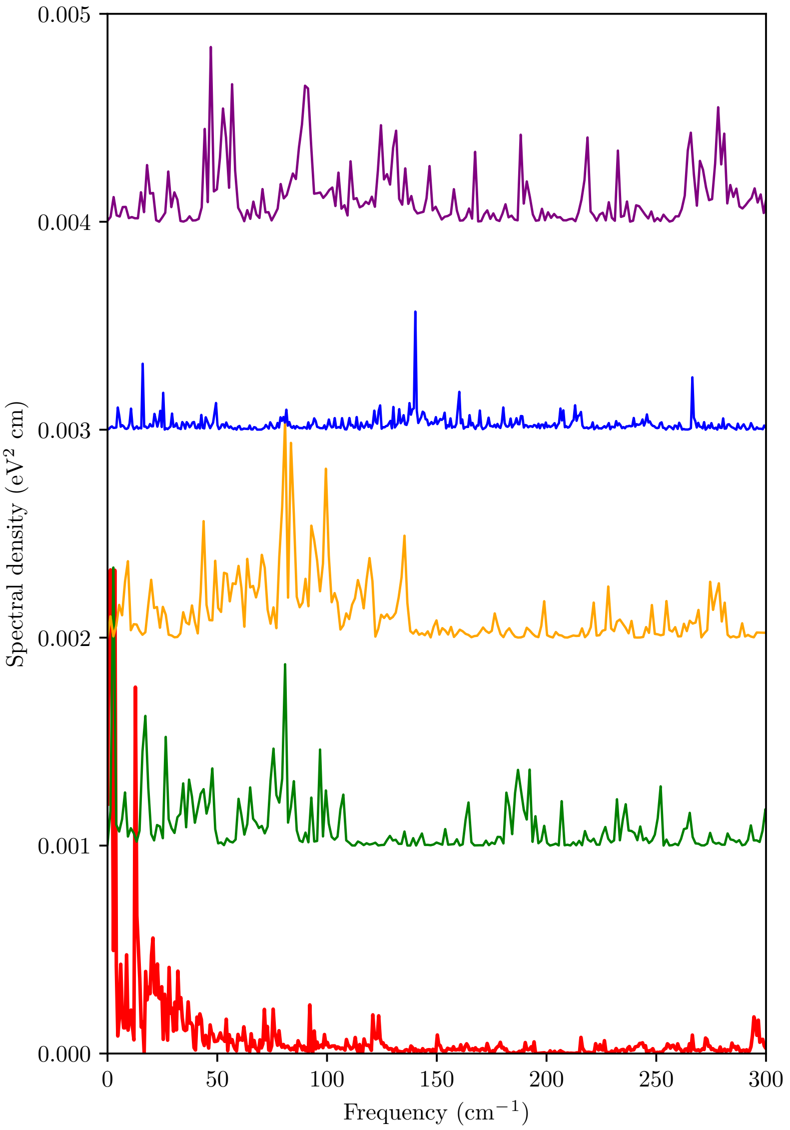

Figure 4.4: Fourier transformation of the autocorrelation function of the excitonic couplings computed at 300 K for dimers A, B, C, D, and E of UBEQUQ, following the definition and colour-code in Figure 4.1.

4.4.2 Exciton–Phonon Coupling

The reorganisation energy (λ) in an exciton transfer process relates directly to the coupling between the electronic and vibrational states in each molecule in the system. This coupling is known as the local exciton-phonon coupling and plays a vital role in the modulation of the exciton transport in molecular crystals (Aragó & Troisi 2016, Fornari et al. 2016). When the excitonic coupling is significantly smaller than the reorganisation energy, the exciton will not have enough "energy" to overcome the local exciton-phonon coupling, and therefore will tend to localise on a single site (molecule). In this scenario, the exciton transport will take place in a series of hopping from one site to the others (incoherent or "classical" regime). On the contrary, if the excitonic coupling is comparable or greater than λ, then the exciton is not affected much by the local exciton-phonon coupling, and thus the exciton can be delocalised over many sites. The transport of the exciton in this case will depend largely on the magnitude of the excitonic coupling fluctuation. The total reorganisation energies computed for UBEQUQ and UBEQOK (π-π stacking dimers) are 0.366 eV and 0.357 eV, respectively. These values are comparable with the magnitude of the average excitonic coupling $\langle J \rangle$ (≈ 0.1 eV) for these two molecular crystals. In addition, when $J > \lambda/4$, which is the case for the two studied molecular crystals, the local exciton-phonon coupling is not large enough to form a small exciton-polaron (Fassioli et al. 2014, Aragó & Troisi 2016). Thus, we cannot assume, in this case that, the transport of the excitons along the arrays of π-π stacking molecules in UBEQUQ and UBEQOK is incoherent hopping.

4.4.3 Parameters for the Model Hamiltonian

Referring to the model Hamiltonian shown in equation 4.1, the set of required parameters is the site excitation energy E_i, the excitonic coupling J between a dimer, the local Holstein exciton-phonon coupling constant g, the non-local exciton-phonon coupling constant α, and the nuclear displacement r_i. Here, E_i is set to zero, as each site has the same energy. The constant g is related to the Huang-Rhys factor, which is a unitless number representing the relative shift between two potential energy surfaces (e.g. between the ground state S_0 and the first excited state S_1 potentials). The analysis of the Huang-Rhys factors for UBEQUQ and UBEQOK is described in the Appendix B. For both systems (Figures B.16 and B.19), only the normal mode at around 1632 cm^{-1} couples strongly with the first electronic transition. These modes are attributed mostly by the stretching of the C-C/C=C bonds, and are responsible for the vibronic progressions often seen in conjugated materials (Aragó et al. 2011, Hestand et al. 2016, Ghosh & Spano 2020). Therefore, a single effective vibration can be associated to the total reorganisation energy of UBEQUQ and UBEQOK crystals. Following several other studies (Troisi & Orlandi 2006*a*, Aragó & Troisi 2016, Hestand et al. 2016, Ghosh & Spano 2020), we set this effective mode to 1400 cm^{-1} (i.e. $\omega^{(1)} = 1400$ cm^{-1}) and the mass $m^{(1)} = 6$ amu (the reduced mass of the C-C/C=C bonds). The local Holstein exciton-phonon constant, for example, for UBEQUQ is calculated as $g^{(1)} = \omega^{(1)}\sqrt{m^{(1)}\lambda} = 23015$ cm^{-1} Å^{-1} and the Huang-Rhys factor associated with this effective mode is 0.93.

The instantaneous excitonic coupling J between each pair of dimers (the off-diagonal element) in the time-independent Hamiltonian is randomly drawn from the distribution of the excitonic couplings. Since the Fourier transformation of the autocorrelation function of $J(t)$ (Figure 4.4) indicates that the low-frequency vibrations (below 50 cm^{-1}) modulate the excitonic coupling in both UBEQUQ and UBEQOK, we set $\omega^{(2)} = 25$ cm^{-1} as the vibrational frequency of the effective mode that couples strongly to the excitonic coupling. For the effective mass $m^{(2)}$, we use the molecular mass of the crystals. The standard deviation of the excitonic coupling is related to the non-local exciton-phonon coupling $\alpha^{(2)}$ as $\sigma_J = \alpha^{(2)}\sqrt{2k_BT/m^{(2)}(\omega^{(2)})^2}$ (Aragó & Troisi 2016).

Table 4.1 gives the parameters used in our model Hamiltonians.

Parameters	UBEQUQ	UBEQOK	Definition
N	100	100	Number of molecules
$\langle J \rangle$	726 cm^{-1}	645 cm^{-1}	Average excitonic coupling
$g^{(1)}$	23015 cm^{-1}Å^{-1}	22702 cm^{-1}Å^{-1}	Local exciton-phonon coupling constant
$\omega^{(1)}$	1400 cm^{-1}	1400 cm^{-1}	Frequency of mode (1)
$m^{(1)}$	6 amu	6 amu	Effective mass of mode (1)
$\alpha^{(2)}$	1068 cm^{-1}Å^{-1}	1091 cm^{-1}Å^{-1}	Non-local exciton-phonon coupling constant
$\omega^{(2)}$	25 cm^{-1}	25 cm^{-1}	Frequency of mode (2)
$m^{(2)}$	386.44 amu	472.53 amu	Effective mass of mode (2)

Table 4.1: Parameters for the model Hamiltonian

4.4.4 Exciton Dynamics

Figure 4.5 shows the time evolution of the exciton wave functions in UBEQUQ and UBEQOK molecular crystals under ambient condition. In both cases, the exciton is initially localised on a single chromophore at 300 K, and its wave function spreads quickly over the oscillating lattice due to the fluctuation of the excitonic couplings between adjacent molecules (dynamic disorder). Here, the regime of the exciton transport for the studied molecular crystals cannot simply be described by either band or hopping transport. In the band regime the charge carrier (wave function) is delocalised over the entire system (lattice), whereas in a hopping model the carrier is highly localised and moves by hopping from site to site. Band transport is observed in a perfect crystal, in which a free carrier is delocalised and moves as a plane wave without scattering. However, in real crystals there are always lattice vibrations or phonons that disrupt the crystal symmetry causing the scattering of the electron and reduce its mobility. Band transport can be recovered from the model Hamiltonian (equation 4.1) by reducing the amount of disorder (e.g reducing the strength of the non-local exciton-phonon couplings). On the other hand, the incoherent hopping regime (small polaron limit) can be obtained by increasing the magnitude of the Holstein local exciton-phonon coupling.

The nature of the non-stationary propagation (variation in the populations

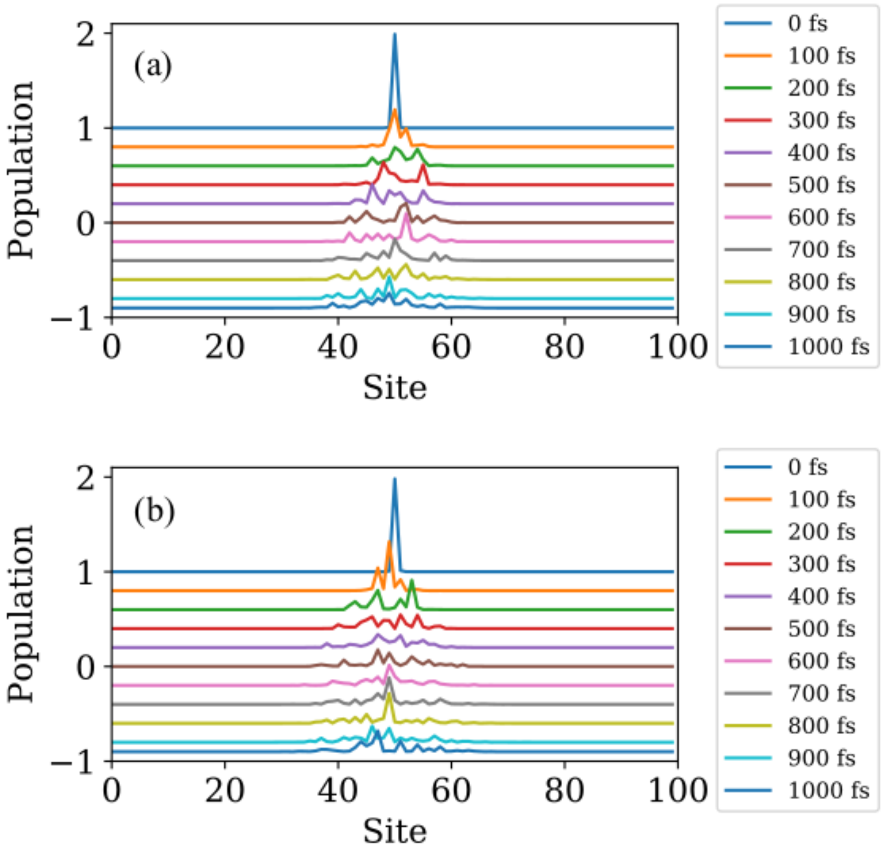

Figure 4.5: Time evolution of the exciton population for (a) UBEQUQ and (b) UBEQOK.

and coherences) of the exciton wave function is investigated by examining the evolution of the density matrix $\rho(t)$. As an example, we will discuss the case of the UBEQUQ molecular crystal. The same trend is observed for UBEQOK. Figure 4.6 shows that starting from the initial pure state at t = 0 fs where the exciton is fully localised on a single state, coherence gradually emerges as the exciton gets access to other nearby states. In other words, the exciton mixes from the initial state with other states in a close energy range. The picture becomes clear as time evolves, especially in the later stages when dynamic disorder introduces significant variation to the Hamiltonian. Furthermore, we observe substantial coherences on a time scale of less than 100 fs, which indicates that the dynamic disorder in $H(t)$ is sufficient to overcome quantum dephasing and help drive exciton transport.

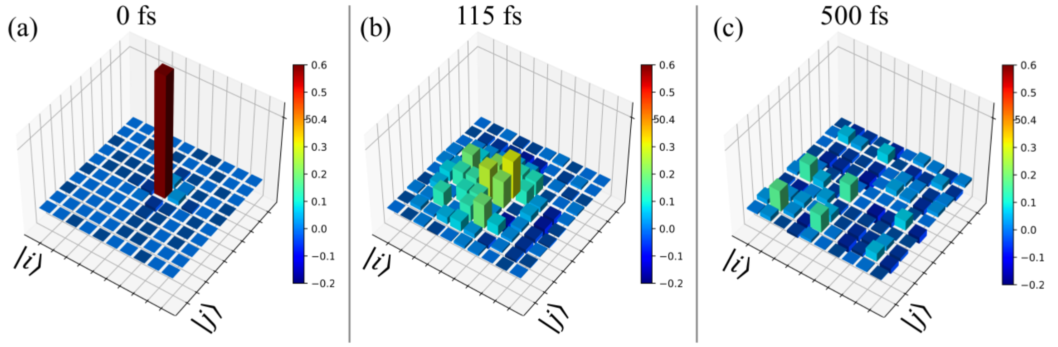

Figure 4.6: Snapshots of the evolution of the density matrix of UBEQUQ at (a) t = 0 fs, (b) t = 115 fs and (c) t = 900 fs. Only states with significant populations are included.

Figure 4.7 shows plots of the thermal fluctuation of the average exciton energies for UBEQUQ and UBEQOK at 300 K. The data indicate that the excitons in both systems are in thermal equilibrium throughout the one picosecond simulation time. The total average exciton energies are 1.0 and 1.1 eV for UBEQUQ and UBEQOK, respectively. These values are within the same range of those for other organic materials such as oligoacene (Van der Horst et al. 2001, Knupfer 2003, Hummer & Ambrosch-Draxl 2005).

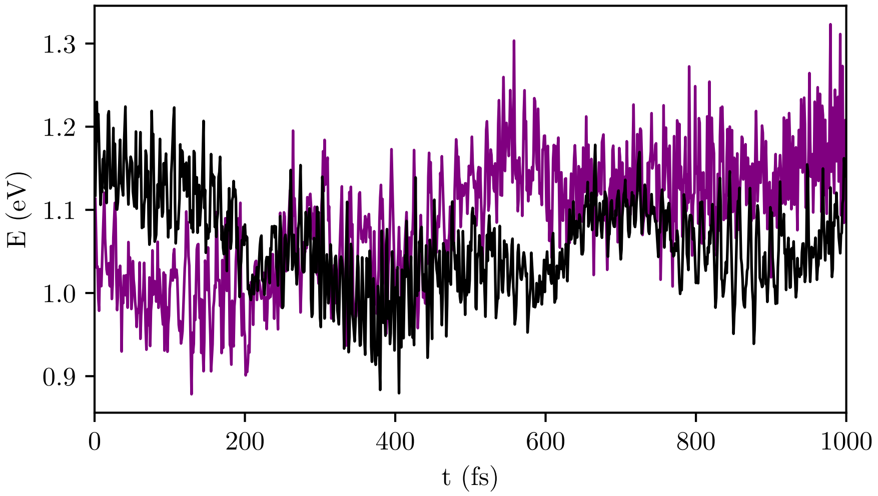

Figure 4.7: Average energy $\bar{E}(t)$ of the exciton computed for UBEQUQ (black) and UBEQOK (magenta).

To characterise the diffusion of the exciton, we compute the temporal evolution of the mean square displacement (MSD) of the centre of the exciton (x_i) in real space. Here, the MSD is defined as $(\bar{x}(t) - \bar{x}(0))^2$, where $\bar{x}(t) = \sum_i^N \rho_{ii} x_i(t)$. Figure 4.8 shows that the MSDs of the exciton in both UBEQUQ and UBEQOK vary approximately linearly with time (normal diffusion) and there is still free diffusion for the exciton beyond one picosecond. Since the average excitonic coupling of UBEQUQ is greater than that of UBEQOK, we can expect that the exciton diffuse faster (larger MSD values) in UBEQUQ, which is what observed in Figure 4.8. Taking the one-dimensional diffusion equation as a simple approximation (i.e. $\text{MSD}(t) = 2Dt$), we can extract the diffusion coefficient D from the gradients of the MSD plots (e.g. Figure 4.8). From these measurements, diffusivity values of $\approx 0.12(0.02)$ cm$^2 s^{-1}$ and $\approx 0.08(0.02)$ cm$^2 s^{-1}$ are found for UBEQUQ and UBEQOK, respectively. These values are within the same order of magnitude with those computed for other molecular crystals (Aragó & Troisi 2016) and a recently measured diffusion coefficient for metal-halide perovskites (Seitz et al. 2020).

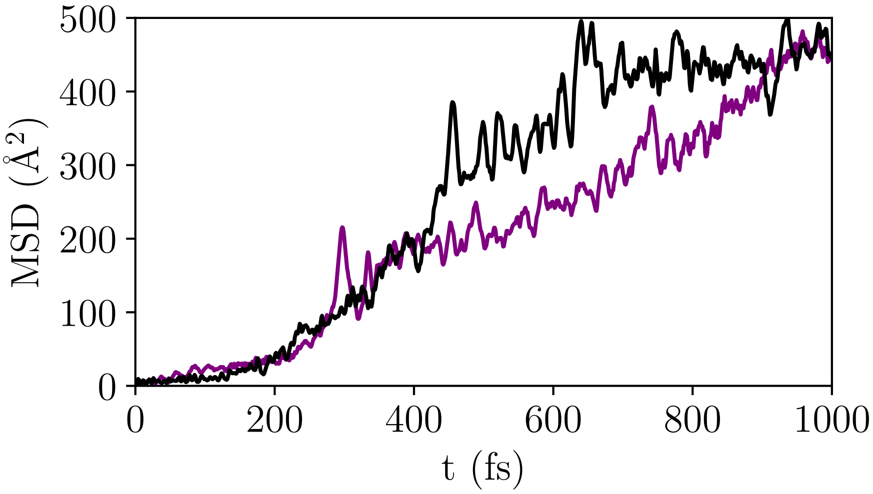

Figure 4.8: Time evolution of the MSD of the centre of the exciton for UBEQUQ (black solid line) and UBEQOK (magenta solid line).

To quantify the evolution of the exciton, we compute the survival probability $P_S(t)$ of the initial state defined as $|\langle\psi(0)|\psi(t)\rangle|^2$, which is essentially the square of the overlap integral between the initial wave function and the wave function at time t. In addition, to characterise the enhancement of the exciton transport by dynamic disorder, we also calculate the survival probability of the exciton for three different cases: (i) a fully "static" Hamiltonian, (ii) a partial "static" Hamiltonian with constant excitonic couplings, and (iii) a partial "static" Hamiltonian with constant nuclear displacement. Here, we choose to use H^1 as the initial starting Hamiltonian. Figure 4.9 shows that for the case of the fully "static" Hamiltonian H^1 of UBEQUQ, the exciton does not evolve significantly from the initial state after 1 ps, while for the dynamic case, $H(t)$, the overlap decreases quickly and reaches about 0 at 1 ps. The oscillatory behaviour of the survival probability observed for the case of the static Hamiltonian H^1 indicates that H^1 remains in the pure state (no environmental effects). In other words, H^1 is in a coherent superposition of the basis states. The sharp fall in $P_S(t)$ of the time-dependent Hamiltonian $H(t)$ between 0 to 400 fs demonstrates the role of the dynamic disorder in the transport of excitons. The original pure state H^0, which is stationary with no coherence between exciton states, is transformed into a mixed state due to the evolution of the Hamiltonian. Each update of the time-dependent Hamiltonian $H(t)$ disturbs the coherent evolution in the previous period and at the same time it introduces new coherences (Huijser et al. 2008, Li, Buda, De Groot & Sevink 2020). This indicates the complexity nature of the exciton transport in such a coherent regime. (Chenu & Scholes 2015)

In the second case, when the fluctuation in the nuclear displacement is introduced (while still keeping the fluctuation of the excitonic coupling constant), the evolution of the exciton from the initial state is observed (Figure 4.9). However, the rate of the evolution is much slower than that for the case of the time-dependent Hamiltonian $H(t)$. Subsequently, this introduces a drop in the mobility of the exciton as indicated in Figure 4.10. On the other hand, when the situation is switched in the third case (i.e. the fluctuation in the excitonic coupling is taken into account and the nuclear displacement is kept

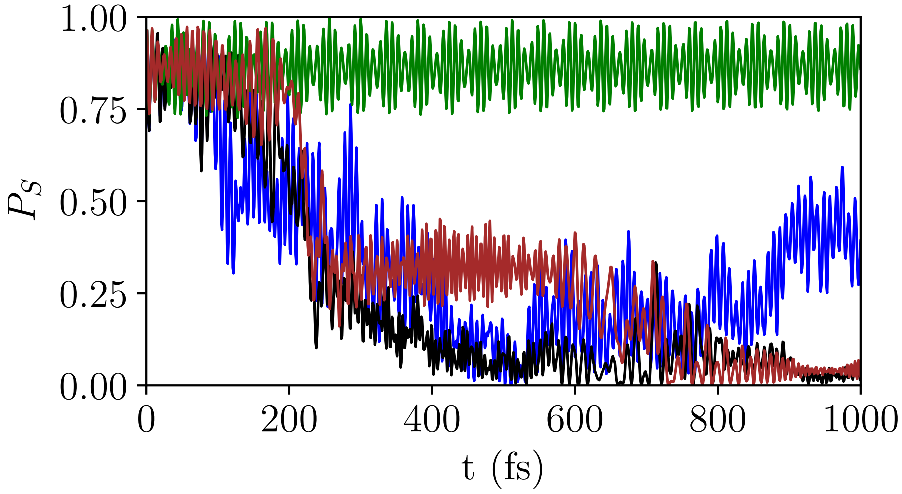

Figure 4.9: Survival probability P_S of the initial state of UBEQUQ in the case of the time-dependent Hamiltonian $H(t)$ (black solid line), static Hamiltonian H_1 (green solid line), constant coupling J (brown solid line) and constant nuclear displacement (blue solid line).

constant), the dynamics of the exciton are altered significantly compared to the case of the time-dependent Hamiltonian $H(t)$ (Figures 4.9 and 4.10). The wave function is still significantly overlapped with the initial states after 1 ps and the exciton mobility substantially reduces. The same trend is also obtained for UBEQOK (Figures B.20 to B.21). Thus, these results confirm the crucial role of the dynamic disorder of the excitonic couplings, and a simple average constant value often employed in the literature may not be adequate to fully describe the exciton transport in molecular aggregates.

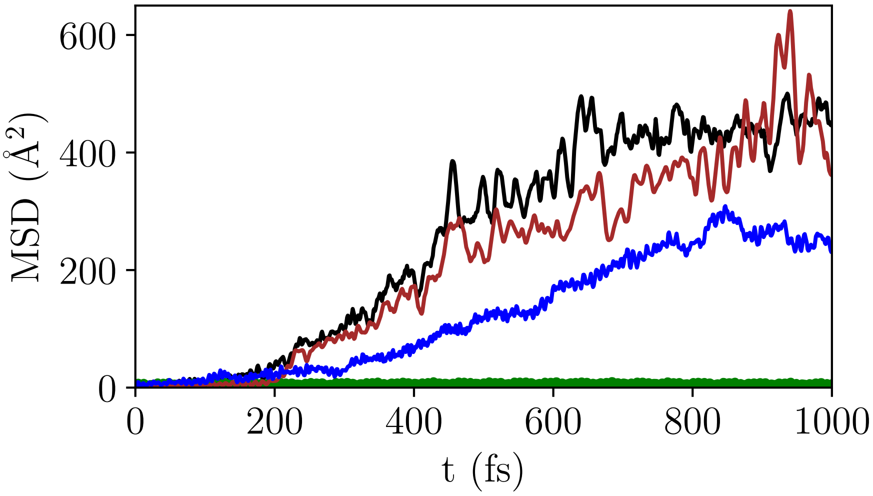

Figure 4.10: Time evolution of the MSD of the centre of the exciton of UBEQUQ in four different cases: time-dependent Hamiltonian $H(t)$ (black solid line), static Hamiltonian H_1 (green solid line), constant coupling J (brown solid line) and constant nuclear displacement (blue solid line).

4.5 Conclusion and Outlook

Dynamic disorder is the key property that drives the excitation energy transfer in molecular crystals and is a valuable tool for the design and development of efficient organic semiconductors. In this work, we present a systematic computational procedure to characterise the dynamics of the exciton in molecular crystals. We apply our approach to understand the excitation energy transfer in a recently synthesised class of molecular crystals containing diketopyrrolopyrrole and thiophene groups. Derivatives of these small organic molecules have attracted much attention for photovoltaic applications due to their broad optical absorption and efficient charge transport.

Out of all the studied molecular crystals, the π-stacked parallel columns of UBEQUQ and UBEQOK possess the strongest excitonic couplings and also exhibit a significant fluctuation in the excitonic couplings due to the the low-frequency intermolecular vibrations between 10 to 50 cm^{-1}. This is attributed directly to the closed packing nature and the geometry of the aromatic core (which is strongly influenced by the side substituent) of the two crystals. The excitonic couplings are normally distributed. Given the strength of the couplings in these systems, the exciton transport is assumed to occur in the coherent regime, in which the fluctuations of the excitonic couplings first induce the localisation of the exciton wave function. Subsequently, with the aid of the low-frequency modes that modulate the excitonic couplings, the exciton wave function spreads rapidly over neighbouring lattices.

The fluctuation of the excitonic couplings (dynamic disorder) is vital for the exciton transport in molecular crystals. In particular, the common approach of utilising a fixed average value for the excitonic coupling J for all pairs of chromophores in the model Hamiltonian seems not to be adequate. In theory, the coupling should be computed separately for each dimer in the system at each time step a long the exciton trajectories. However, in practice this is prohibitively expensive and is not accessible with current computing power. Nevertheless, to be more realistic, the excitonic couplings for each pair of dimers should be drawn from their statistical distribution that is dictated by the thermal energy. Alternatively, the excitonic couplings can also be taken from a coupling map or machine learned values and these approaches will be pursued in our future work to obtain a better description of the transport mechanism of the exciton in molecular aggregates.

Chapter 5

Structure-Property Relationships in Amorphous Conjugated Polymers

[‡]

5.1 Synopsis

Chapter 5 calculates the electronic structure properties of disordered conducting polymers containing DPP, TT and T. Atomistic force field parameters for the polymer were optimised to minimise the difference between the *ab initio* and empirical potential energy surfaces and their corresponding first derivatives. These new force fields are employed to propagate the nuclear dynamics, and the equilibrium trajectories are sampled for subsequent electronic structure calculations. We found that the fluctuations of the bulk density of states are negligibly small and do not vary significantly with the length of the backbone and the side-chains. The localisation length near the bandgap is between

---

[‡] Some of the work in this chapter has been submitted for publication in:

Jiang, L., Hirst, J. D. & Do, H. (2022), 'Structure-property relationships in amorphous thieno[3,2-*b*]thiophene-diketopyrrolopyrrole-thiophene-containing polymers', *Journal of Physical Chemistry C* **126**(26), 10842–10854

8 and 12 Å, which is about half of the length of the monomer and significantly less than the length of the extended polymer (∼ 200-400 Å). This indicates that the orbital localisation is not affected by the length of the polymer. The inter-chain excitonic couplings are usually smaller than 5 meV, suggesting that the transport mechanism across chains is described by incoherent hopping, and excitons mainly move along the chain. Furthermore, thermal fluctuations cause the evolution of the excitons along the chain. Characterisation of the relationships between the geometric disorder of the polymers and the distributions of the lowest excited states reveals that the low-energy excitons tend to localise in regions which are more planar and less folded. However, some excitons are also spread over defects. Thus, there is clear evidence of the correlations between the structure and electronic properties in this class of amorphous conjugated polymers. These relationships should provide valuable tools for designing and developing efficient organic semiconductors from this class of conjugated polymer.

5.2 Introduction

Interest in conjugated organic materials, particularly conjugated polymers, is constantly increasing due to the high demand for flexible, light-weight, large-area, easy-to-process and low-cost electronic applications, such as OPVs (Kippelen & Brédas 2009, Lin et al. 2016, Li, Guo, Peng, Qu, Yan, Ade, Zhang & Forrest 2020, Li et al. 2021), the active layer of field-effect transistors (FETs) (Schön et al. 2001, Muccini 2006), light-emitting diodes (LEDs) (Matsushima et al. 2019, Zou et al. 2020) and bioelectronics (Inal et al. 2018, Sekitani 2021). While crystalline molecular semiconductors possess exceptionally high charge mobilities (over 10 $\mathrm{cm^2 s^{-1} V^{-1}}$), limitations in processing techniques hinder their development due to an incomplete understanding of the crystallisation mechanism (Chen et al. 2021). On the other hand, polymeric semiconductors are more straightforward to process. The latter's ability to self-assemble, solution processability, flexible and light-weight, make them attractive materials for flexible electronic devices. However, polymer semiconductors suffer from charge mobilities that are approximately an order of magnitude lower than crystalline molecular semiconductors. Conjugated polymers with improved charge mobility would revolutionise the flexible electronics industry. Thus, this research field has seen substantial growth in the last couple of decades (Fratini et al. 2020) with the development of polymer semiconductors with charge mobility greater than 10 $cm^2s^{-1}V^{-1}$ (Kippelen & Brédas 2009, Lin et al. 2016, Zhu et al. 2022).

The $\pi-$conjugated backbone in organic semiconducting polymers allows their electronic states to be delocalised across the individual, covalently bonded molecular units. The spatial extent of these electronic states depends strongly on the molecular geometry, and their ability to delocalise across molecular units can be influenced by intermolecular packing. This implies a strong coupling between the electronic and structural dynamics that gives rise to unique and fascinating phenomena (Fratini et al. 2020). This coupling explains why, over the last two decades, experimental characterisations of the transport properties in organic semiconducting materials have led to a range of seemingly contradictory results (Brédas et al. 2002). Although qualitative features of charge transport in conjugated polymers have long been established, it is still challenging to quantify the structure-property relationships in these materials (Xu et al. 2017, Fratini et al. 2020). By analogy to their inorganic semiconductor counterparts, one might be persuaded that the key ingredient to increasing charge mobilities of organic semiconductors is to improve the local order (McCulloch et al. 2006, Wang et al. 2019). It turns out that this is only applicable to some but not all classes of conjugated polymers. Examples of high carrier mobility polymers are polythiophenes, e.g. poly(3-hexylthiophene-2,5-diyl (P3HT) and poly(2,5-bis(3-hexadecylthiophen-2-yl)thieno[3,2-*b*]thiophene (PBTTT), whose mobilities are in the range 0.1 to 1.0 $cm^2s^{-1}V^{-1}$ (Ong et al.

2004). These are highly ordered polymers with relatively large crystalline domains organized into lamellar structures with significant $\pi-$stacking (DeLongchamp et al. 2007). On the other hand, the recent discovery of new high charge mobility amorphous conjugated polymers (Nielsen et al. 2013, Venkateshvaran et al. 2014) suggests that not all parameters have been taken into account. These contrasting examples indicate the need for robust quantitative models of how (dis)order influences charge mobility in organic semiconducting materials. Therefore, it is crucial to go beyond phenomenological models to capture the interplay between electronic structure properties and the microscopic structure of organic semiconducting polymers.

Investigating the relationship between structure and electronic properties of materials requires constructing atomistic models of the systems of interest and calculating their electronic structure properties. *Ab initio* MD simulation is the natural choice for this task, as it provides a description at the atomistic scale directly from the first principles of quantum mechanics. However, this technique is limited to only small systems (a few hundred atoms) and is far from tractable for semiconducting polymers comprising tens of thousands of atoms. A remedy to this problem is to employ classical MD simulations to generate an ensemble of equilibrium structures, which are subsequently utilised in large-scale quantum chemistry calculations to obtain the structure-property relationships. However, atomistic modelling of polymers and computing their electronic structure properties are still challenging tasks in their own right from the computational point of view. In addition, one of the main concerns here is the mismatch in the force fields describing the interactions at the classical level and the electronic structure methods employed for subsequent quantum chemistry calculations. Thus, most computational studies in the optoelectronic polymer field have mainly focused on either the structural information using molecular simulations (DuBay et al. 2012, Gartner III & Jayaraman 2019, Wessels & Jayaraman 2019, Jiang et al. 2020) or the electronic structure of an isolated polymer chain by quantum chemical calculations (Nayyar et al. 2013, Panda et al. 2013, Roseli et al. 2017, Matta et al. 2020).

Some attempts have been made to combine MD and electronic structure calculations to characterise the structure-property relationships in conjugated polymers. For example, Simine and Rossky investigated the relationship between the ground-state optical gaps, the properties of the excited states, and the structural features of chromophores of a single molecule P3HT using QM/MM simulations (Simine & Rossky 2017). They reported a strong interdependence between the critical aspects of chromophoric disorder and conformational disorder in P3HT. For semi-crystalline polymers, it is possible to investigate the bulk electronic structure property by characterising one lamellar at a time, which drastically reduces the number of atoms in the system. Liu and Troisi used this approach to gain insights into the microscopic origin of the very high charge mobility in PBTTT (Liu & Troisi 2014). Cheung et al. (2009*a*,*b*) examined the connections between CT parameters and the structure of the most studied semiconducting polymer P3HT. The situation is less tractable computationally for amorphous conjugated polymers due to the slow relaxation time (μs time-scale) and the size of the systems. Quantum chemical calculations of large models of amorphous polymers are naturally very demanding due to the lack of translational symmetry that would otherwise reduce the size of the problem. Despite these challenges, research along this line has been pursued by several groups. Granadino-Roldán et al. (2011) built microscopic models for poly-2,5-bis(phenylethynyl)-1,3,4-thiadiazole (PhEtTh) using MD simulations and then studied the effect of disorder on the electronic couplings, the DOS and the wave function localisation. In the same spirit, Vukmirovic & Wang (2011) presented large-scale calculations of the electronic structure of strongly disordered P3HT conjugated polymer models using the DFT based charge patching method to construct single-particle Hamiltonian and the overlapping fragments method for the efficient diagonalisation of that Hamiltonian. On the other hand, Poelking et al. (2013) employed MD and quantum chemical calculations to establish a link between the microscopic ordering and the charge transport parameters for a highly crystalline polymeric organic semiconductor PBTTT. A similar strategy was also employed by Qin & Troisi (2013) and Ma et al. (2014) to understand the relationships between structure and electronic properties of the amorphous poly(phenylenevinylene) (PPV) derivative MEH-PPV. Despite significant successes, combined morphology-electronic structure study for the excited states of amorphous polymers is still limited by the computational challenges outlined above and by the lack of accurate force fields for conjugated systems.

DPP-based conjugated polymers have emerged as desirable materials for thin-film transistors and solar cell devices. The electron-deficient nature of the DPP core has been exploited to synthesise extremely narrow bandgap donor-acceptor-type materials well suited for use in organic photovoltaics with high power conversion efficiencies reported in both small molecules and polymers (Wienk et al. 2008, Bijleveld et al. 2009, Ashraf et al. 2011). Furthermore, the planarity of the DPP skeleton and its ability to accept hydrogen bonds result in copolymers that encourage $\pi-\pi$ stacking. Usually, the DPP units are flanked by co-monomers, and variation of the co-monomer yields polymers with attractive properties for both OPV and OFET devices (Shin et al. 2015). For instance, copolymerisation with T, TT derivatives or benzothiadiazole resulted in polymers with impressive ambipolar charge-carrier mobilities (Nelson et al. 2010). Particularly, the TT units extend the polymer coplanarity and promote a more delocalised HOMO distribution along the backbone, enhancing intermolecular charge-carrier hopping (Bronstein et al. 2011). Furthermore, DPP-based semiconducting polymers can achieve a surprisingly high mobility rate without having an overall crystalline structure (Nelson et al. 2010, Noriega et al. 2013a). However, detail of the relationship between the morphology and electronic structure properties of this class of conjugated polymers is still unclear, and a fundamental understanding is necessary for their design and development.

In this paper, we will focus on a recently synthesised TT-flanked DPP and T-containing π-extended conjugated polymers with branched alkyl side-chains poly[[2,5-bis(2-octyldodecyl)-2,3,5,6-tetrahydro-3,6-dioxopyrrolo[3,4-*c*]pyrrole-1,4-diyl]-*alt*–[[2,2'-(2,5-thiophene)bis-thieno[3,2-b]thiophen]-5,5'-diyl]] (PDPPTT-T-10) (Shin et al. 2015). The chemical structure of a monomer of this polymer is shown in Figure 5.1. This polymer has attracted much attention due to its excellent hole mobility and high PCE when integrated into heterojunction-type polymer solar cells (Shin et al. 2015). We first construct a reliable force field and then use MD simulations to generate several large-scale amorphous polymeric models of PDPPTT-T-10. Subsequently, quantum chemical calculations are employed to study the electronic structure properties of these models. Our goal is to provide insights into the electronic excited states of the polymer chains and their connections to the dynamical disorder of the nuclei.

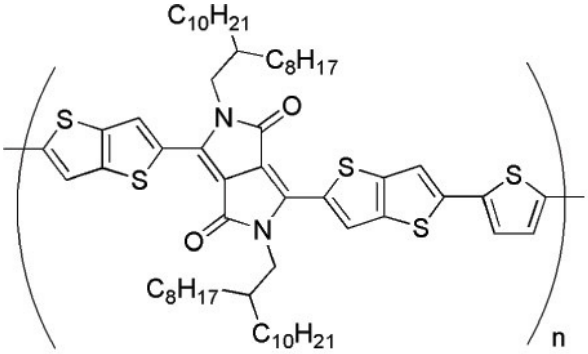

Figure 5.1: Chemical structure of a monomer of the PDPPTT-T-10 polymer

5.3 Computational Details

5.3.1 Force Field Development

In MD simulation, it is vital that the force fields used to describe the nuclear dynamics are accurate enough to capture the actual molecular motion of the system. A challenge one often has to confront here is the mismatch in the description of the interactions at the classical level and the electronic structure methods employed for subsequent quantum chemistry calculations. To overcome this, we employ our extension (Jiang et al. 2020) of the adaptive force-matching technique (Do & Troisi 2015) to parameterise the force fields for the studied conjugated polymers. The idea behind the procedure is to find a set of parameters that minimises the differences between the classical and the *ab initio* forces. Thus, by design, the force fields used to propagate the nuclear dynamics are comparable to those targeted *ab initio* methods used in the subsequent electronic structure calculations. The procedure for parameterising the force field is included in the Appendix C.

5.3.2 Classical Molecular Dynamics Simulations of the Conjugated Polymers

MD simulations are performed using our new force fields within the NAMD package (Phillips et al. 2005) to generate models of PDPPTT-T-10 bulk polymer. Systems of 20 chains of 20 monomers/chain (20ch_20mers) and 20 chains of 40 monomers/chain (20ch_40mers) are characterised. The initial structure is prepared with an arbitrary low-density arrangement for each system. Polymer chains are added into the simulation box by growing segment by segment using the configurational bias MC technique (Siepmann & Frenkel 1992). The result of this procedure is that low-energy sites are preferred over high-energy sites. Thus, disordered bulk systems containing chains in realistic equilibrium conformations are created. Details of the simulations are outlined in the Appendix C.

The variation of the density in the NPT ensemble simulations with respect to time is shown in Figure 5.2 for both the (20ch_20mers) and (20ch_40mers) models. After about 2 μs, both systems converge to the same density of about 1.0 g/cm^3. This value is closed to what was obtained for a similar conjugated

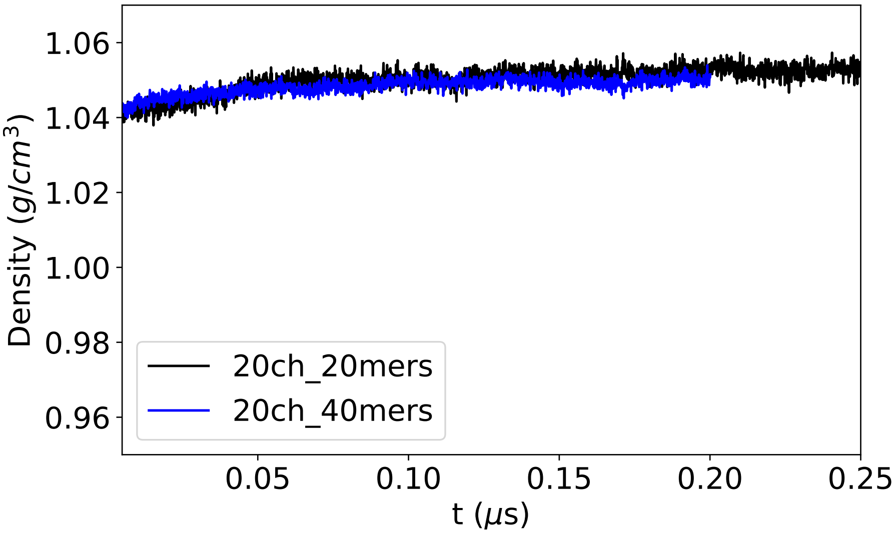

Figure 5.2: Time evolution of the densities of the 20ch_20mers (black line) and the 20ch_40mers (blue line) systems during the NPT ensemble equilibration.

polymer in our previous work (Jiang et al. 2020) and falls within the density range of amorphous conjugated polymers (Callaway et al. 2022, Reisjalali et al. 2021). The same final density is also found for other runs starting with different initial configurations. This suggests that reliable models for the amorphous phase of PDPPTT-T-10 can be generated from our procedure.

5.3.3 Quantum Chemical Calculations

To make the quantum chemical calculations tractable for the polymer models, the long-chain alkyl side group is replaced by an ethyl group, which speeds up the excited state calculations without altering the nature of the frontier orbitals. Point charges are added in the position of the surrounding atoms on other polymers to represent the electrostatic environment around the chain of interest. In addition, since the excitonic couplings between polymer chains are insignificant and could be neglected in amorphous conjugated polymers (Qin & Troisi 2013, Ma et al. 2014), the electronic structure properties are computed separately for each chain. This assumption is verified later in the Results and Discussion section.

We employ TD-DFT to characterise the electronic excitation of the amorphous polymer models. The long-range corrected ωB97XD (Chai & Head-Gordon 2008) functional in conjunction with the 3-21G* or 6-31G* basis set is utilised to compute the lowest five singlet states. The choice of the functional is based on its ability to capture both short- and long-range interactions and to describe CT states accurately. The effects of the size of the basis set and the number of electronic states included in the calculations are discussed in the Results and Discussion section. Results obtained using other popular functionals, including B3LYP (Hertwig & Koch 1997), CAM-B3LYP (Yanai et al. 2004*b*), M06-2X (Zhao & Truhlar 2010) are also reported and compared with the results obtained from ωB97XD. To investigate the excited state properties of the polymer, we analyse the DOS, the absorption spectra, the localisation length of the one-electron state (Qin & Troisi 2013), the natural transition orbitals and the e-h distributions. All quantum chemical calculations are performed with the Gaussian16 program package (Frisch et al. 2016), while the electronic structure-property analysis is done using the Multiwfn codes (Lu & Chen 2012).

The inter-chain excitonic coupling $J_{mn}^{\alpha\beta}$ between the exciton α in chain m and the exciton β in chain n is computed using the distributed monopole approximation expressed as a Coulomb interaction term

$$J_{mn}^{\alpha\beta} = \frac{1}{4\pi\epsilon_0\epsilon_r}\sum_{i\in m}\sum_{j\in n}\frac{q_i^t(\alpha)q_j^t(\beta)}{|\mathbf{r}_i - \mathbf{r}_j|} \tag{5.1}$$

where ϵ_0 is the vacuum permittivity, ϵ_r is the relative permittivity of the polymer, $\mathbf{r}_i$ is the position of atom i and $q_i^t(\alpha)$ is the atomic transition charge at atom i between the ground state and the α excited state of chain m.

The DOS per chain per monomer $\rho_{c,i}(E)$ is defined as $\rho_{c,i}(E) = \sum_m \delta(E -$

$E_i^m)/M$, where E_i^m is the energy of the molecular orbital m of chain i and M is the total number of monomer per chain (Qin & Troisi 2013). Since the inter-chain excitonic coupling is negligible (see the Results and Discussion section), the bulk DOS of the whole system is calculated by summing the contribution of individual chains as $\rho_b(E) = \sum_i \rho_{c,i}(E)/N_c$, where N_c is the total number of chains. Similarly, the absorption intensity of the ith chain is defined as $I_i(E) = \sum_n f_{0\rightarrow n}(i)\delta(E - E_i(n))$, where $f_{0\rightarrow n(i)}$ is the oscillator strength for the transition between the ground and the nth excited state of chain i and $E_i(n)$ is the corresponding transition energy. The bulk absorption intensity of the polymer is then calculated as $I_b(E) = \sum_i^N I_i(E)/N_c$.

We define the localisation length for molecular orbital m as (Qin & Troisi 2013)

$$L^m = 2\left(\sum_{k=1}^{M} |\mathbf{r}_k - \mathbf{R}^m|^2 P_k^m\right)^{1/2} \tag{5.2}$$

where $\mathbf{r}_k$ is the position of the centre of mass of monomer k and $\mathbf{R}^m = \sum_{k=1}^{M} \mathbf{r}_k P_k^m$ is the centroid of the molecular orbital m. P_k^m is the weight of the molecular orbital m on a given monomer k. More information on the definition and calculation of P_k^m can be found from the Appendix C. Then, an energy-dependent localisation length for chain i is defined as

$$L_{c,i}(E) = \frac{\sum_m L^m \delta(E - E_i^m)}{\sum_m \delta(E - E_i^m)} \tag{5.3}$$

and finally the bulk localisation length of the system is calculated as

$$L_b(E) = \sum_{i=1}^{N} L_{c,i}(E)/N_c \tag{5.4}$$

For numerical calculations, $\delta(E - E_i^m)$ and $\delta(E - E_i(n))$ are approximated with a normalised Gaussian of standard deviation $\sigma = 0.5$ eV.

A single-electron excitation is generally described as the process of an electron leaving the hole. The combination of the hole and the electron (if treated as quasi-particles) is often termed an exciton. For example, in the case of a HOMO → LUMO transition, the hole and the electron could be represented by the HOMO and the LUMO, respectively. In practice, the single molecular orbital pair representation (in the canonical form) of an excitation usually is not adequate. The excitation must be treated as a transition involving multiple molecular orbital pairs with corresponding weights. This poses a challenge in representing the hole and electron when there is no dominant molecular orbital pair in a transition. In this instance, canonical molecular orbitals are usually transformed to natural transition orbitals. A more robust approach is to define the hole and the electron in terms of their densities ρ^{hole} and ρ^{elec} (if the phase information is not required) as (Lu & Chen 2012, Liu, Lu & Chen 2020)

$$\begin{aligned}\rho^{\text{hole}}(\mathbf{r}) &= \rho^{\text{hole}}_{\text{loc}}(\mathbf{r}) + \rho^{\text{hole}}_{\text{cross}}(\mathbf{r}) \\ &= \sum_{i}^{\text{occ}}\sum_{a}^{\text{vir}}(w_i^a)^2\varphi_i(\mathbf{r})\varphi_i(\mathbf{r}) + \sum_{i}^{\text{occ}}\sum_{j\neq i}^{\text{occ}}\sum_{a}^{\text{vir}} w_i^a w_j^a \varphi_i(\mathbf{r})\varphi_j(\mathbf{r})\end{aligned} \tag{5.5}$$

$$\begin{aligned}\rho^{\text{elec}}(\mathbf{r}) &= \rho^{\text{elec}}_{\text{loc}}(\mathbf{r}) + \rho^{\text{elec}}_{\text{cross}}(\mathbf{r}) \\ &= \sum_{i}^{\text{occ}}\sum_{a}^{\text{vir}}(w_i^a)^2\varphi_a(\mathbf{r})\varphi_a(\mathbf{r}) + \sum_{i}^{\text{occ}}\sum_{a}^{\text{vir}}\sum_{b\neq a}^{\text{vir}} w_i^a w_i^b \varphi_a(\mathbf{r})\varphi_b(\mathbf{r})\end{aligned} \tag{5.6}$$

where i and a run over all occupied and virtual molecular orbitals, “loc” and “cross” stand for the contributions of the local and cross terms to the hole and electron distribution, w_i^a is the configuration coefficient (weight) of the corresponding $i \rightarrow a$ orbital pair transition and φ denotes the molecular orbital wavefunction. Since the molecular orbitals are orthonormal and the sum of the square of all configuration coefficients is one (i.e. $\sum_i^{\text{occ}}\sum_a^{\text{vir}}(w_i^a)^2 = 1$), it follows that the integration of the densities of the “hole” and the “electron” must also converge to one (i.e. $\int \rho^{\text{hole}}(\mathbf{r})\mathrm{d}\mathbf{r} = 1$ and $\int \rho^{\text{elec}}(\mathbf{r})\mathrm{d}\mathbf{r} = 1$), indicating an electron is excited. The contribution of an atom A to, for example, the hole, is evaluated using the Hirshfeld partition approach as $\int \rho^{\text{hole}}(\mathbf{r})w_A(\mathbf{r})\mathrm{d}\mathbf{r}$. Finally, the weight of the hole/electron on a given monomer is simply the sum of the contributions of the atoms that belong to the monomer.

To characterise the electronic excitation of the polymer, we analyse the e-h distributions and the transition density matrix (TDM) for the lowest five singlet states of single chains. The weight of the transition density from monomer k to an excited state S_n, $P_k^{S_0 \rightarrow S_n}$, is defined and explained in the Appendix C. The delocalisation extent of various electronic excitations is quantified by the participation index (PI), which is the count of the number of monomers that contribute more than 5% to those transitions. The exciton binding energy, which is the negative value of the Coulomb attractive energy between the hole and the electron, can be employed to investigate their degree of separation. This quantity is computed using the Coulomb formula as $E_{\text{coul}} = \int\int \rho^{\text{hole}}(\mathbf{r}_1)\rho^{\text{elec}}(\mathbf{r}_2)/|\mathbf{r}_1 - \mathbf{r}_2|\mathrm{d}\mathbf{r}_1\mathrm{d}\mathbf{r}_2$. The extent of the spatial distribution of the hole and the electron is characterised by the RMSD. The x component of the RMSD of the hole can be expressed, for example, as $\sigma_{\text{hole}}, x = \sqrt{\int (x - X_{\text{hole}})^2 \rho^{\text{hole}}(\mathbf{r})\mathrm{d}\mathbf{r}}$. Then, the differences between the RMSD of the electron and hole, $\Delta\sigma_\lambda$, can be obtained via $\Delta\sigma_\lambda = \sigma_{\text{elec},\lambda} - \sigma_{\text{hole},\lambda}$, where $\lambda = \{x, y, z\}$. Subsequently, the total difference is measured via the $\Delta\sigma$ index, which is $|\boldsymbol{\sigma}_{\text{elec}}| - |\boldsymbol{\sigma}_{\text{hole}}|$. The H-index, given by $\left(|\boldsymbol{\sigma}_{\text{elec}}| + |\boldsymbol{\sigma}_{\text{hole}}|\right)/2$ gives the average degree of the spatial extent of the hole and the electron distribution in space. In addition, we also use the Δr-index (Guido et al. 2013), which can be interpreted in terms of the hole-electron distance, to characterise the excited states of the polymer.

5.3.4 Folding and Nonplanarity Parameters

We use the folding and nonplanarity parameters (Qin & Troisi 2013) to characterise the relationships between the chain conformation and electronic structure properties in PDPPTT-T-10 polymer. The folding degree in a PDPPTT-T-10 chain is related to d_{12}, d_{34}, d_{56} and d_{78} (Figure 5.3a), which are distances between two carbon atoms in consecutive aromatic rings separated by another ring (within a monomer). The deviation of these distances from their equilibrium (perfect planar structure) values can represent the degree of chain folding at monomer k. Thus, we define the average folding degree of monomer k, $\bar{\Delta}_k^d$, as

$$\bar{\Delta}_k^d = \sum_{i=1}^{4}(d_i - d_i^e)/4 \tag{5.7}$$

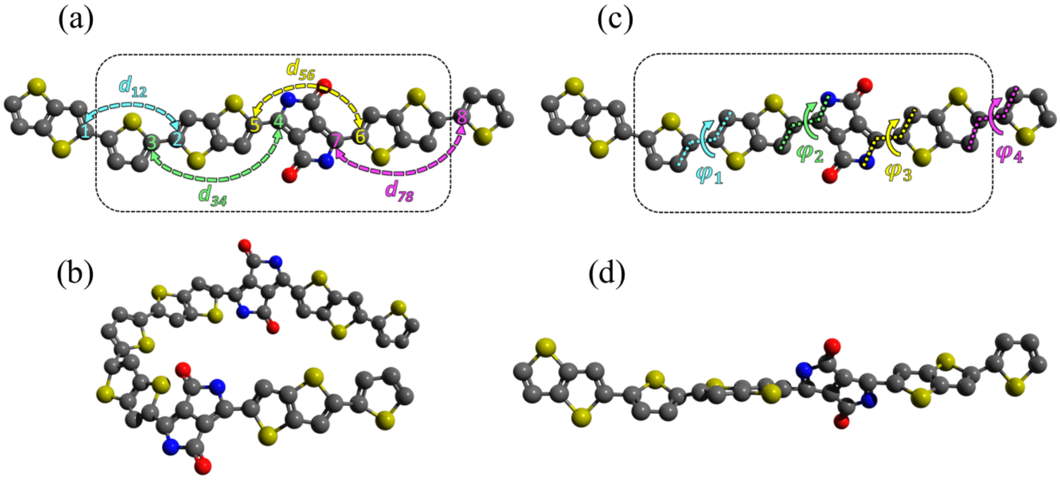

Figure 5.3: Definition and illustration of chain folding and chain nonplanarity within a PDPPTT-T-10 single chain. Only the backbone atoms are shown for clarity. Atoms within the dotted frames in (a) and (c) belong to a monomer unit. In panel (a), d_{12}, d_{34}, d_{56} and d_{78} are distances between two carbon atoms in consecutive aromatic rings separated by another ring. The average of these distances (within a monomer) gives the folding degree per monomer. In panel (c), Φ_1, Φ_2, Φ_3 and Φ_4 are dihedral angles that account for the nonplanarity within a monomer. Panels (b) and (d) depict the folding and nonplanarity in the polymer, respectively.

where d_i are d_{12}, d_{34}, d_{56} and d_{78}, and d_i^e are their corresponding equilibrium values in the perfect planar geometry. Similarly, we define a torsion angle displacement from planarity as $\Delta_k^{\Phi} = \min\{|\Phi|, 180 - |\Phi|\}$, where Φ denotes the four dihedral angles (Φ_1, Φ_2, Φ_3 and Φ_4) that mainly account for the nonplanarity within a monomer unit (Figure 5.3c). The nonplanarity degree of monomer k, $\bar{\Delta}_k^{\Phi}$, is then defined as

$$\bar{\Delta}_k^{\Phi} = \sum_{j=1}^{4} \Delta_k^{\Phi_j}/4 \tag{5.8}$$

5.4 Results and Discussion

5.4.1 Effects of Basis Set Sizes, Functionals, Side-chain and Chain Length

To assess the choice of DFT functionals on the computed electronic excitations of the amorphous PDPPTT-T-10 polymer, we use 20 polymer chains in the 20ch_20mers system at 200 ns (in the NVT ensemble) to make preliminary comparisons. Figure 5.4 shows the computed absorption spectra using TDDFT with the hybrid functional B3LYP, the hybrid meta functional M06-2X and the long-range corrected functionals CAM-B3LYP and ωB97XD. Out of all functionals, B3LYP noticeably under estimate the excitation energy. This is a limitation of the standard hybrid exchange-correlation functionals, which often fail to describe charge-transfer states and $\pi \rightarrow \pi^*$ transitions in extended conjugated systems. They do not exhibit the correct $1/r$ asymptotic behaviour (Adamo & Jacquemin 2013). A remedy to this is employing the long-range corrected exchange-correlation density functionals such as ωB97XD and CAM-B3LYP. The global hybrid M06-2X functional with double the amount of nonlocal exchange has also been shown to improve the description of valence excitations in π-conjugated systems (Zhao & Truhlar 2010). Figure 5.4 indicates that the differences in the computed absorption spectra using the three improved functionals (CAM-B3LYP, ωB97XD and M06-2X) are insignificant. Despite B3LYP reproduces experimental spectra quite well, we still employ the ωB97XD functional for all other excited state calculations because this functional has the correct $1/r$ asymptotic behaviour. The discrepancy between the computed and experimental spectra is partly due to the solvent effects, which the calculations could not capture precisely.

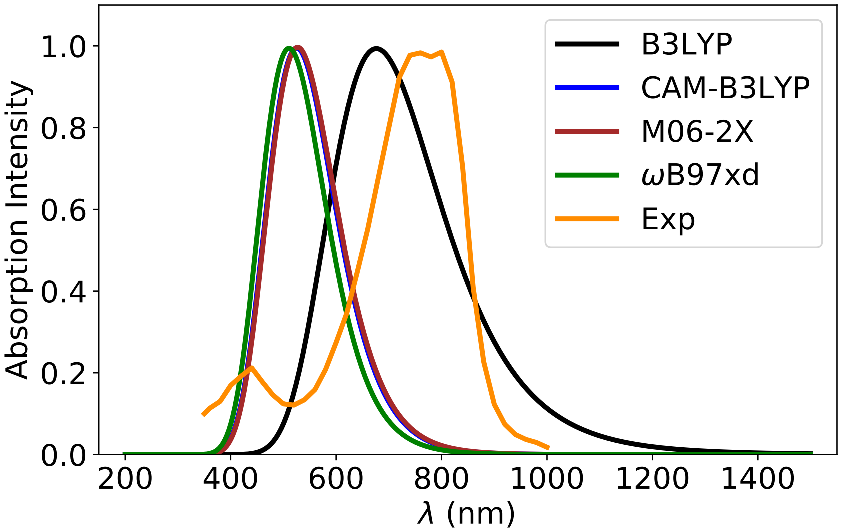

Figure 5.4: Absorption spectra for the last snapshot (t = 200 ns) in the NVT ensemble run of the 20ch_20mers system computed using the B3LYP (black line), CAM-B3LYP (blue line), M06-2X (red line) and ωB97XD (green line) functionals. All systems use the 3-21G* basis set. Five lowest singlet excitations are included in the absorption spectra calculation of each chain. Experimentally measured spectra for thin film polymer (Bronstein et al. 2011) is also included (orange line).

We analyse the snapshots of the amorphous polymers at 200 ns (in the NVT ensemble) to characterise the effects of the size of the basis sets, side-chain and the chain length on the computed excited state properties. Figure 5.5a shows that the difference in the computed DOS is almost negligible between the use of the 3-21G* and 6-31G* basis sets.

Likewise, Figure 5.5b illustrates that the alkyl side-chains do not significantly alter the bulk electronic structure properties of the polymer. The use of an ethyl group (in place of the long-chain alkyl side-chain) is adequate for calculating the excited state properties. Furthermore, the bulk DOS computed for the 20mers system is more or less the same as that computed for the 40mers (Figure 5.5c), suggesting that a chain of 20 monomers is sufficient to represent

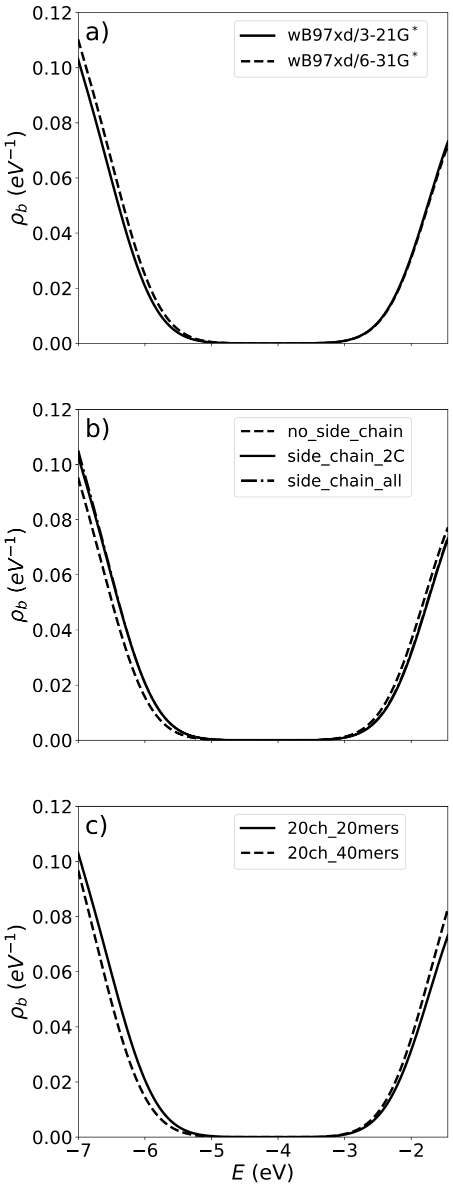

Figure 5.5: Comparison of the bulk density of states of PDPPTT-T-10 amorphous polymer using a) different basis sets, b) different side-chains and c) different chain lengths. The 20ch_20mers system is used to obtain results shown in a) and b). Data in b) and c) are computed at the ωB97XD/3-21G* level of theory.

the bulk amorphous PDPPTT-T-10 polymeric system. Similar trends are also observed for the computed bulk molecular orbital localisation lengths and absorption spectra of the amorphous polymers. Therefore, to save computational cost, we mainly focus on analysing the properties of the 20ch_20mers polymeric system using the smaller basis set (3-21G*) and the reduced side-chain (ethyl group).

Figure 5.6 shows the averaged (over ten snapshots) bulk DOS and bulk orbital localisation length (OLL_b) of the amorphous PDPPTT-T-10 polymer. The bottom panel (Figure 5.6b) indicates that the states near the gap tend to be localised. The localisation length in this region is about 8 Å, which is significantly smaller than the length of the extended polymer ($\sim$ 100 Å) and the average radius of gyration of the system ($\sim$ 40 Å). This is also an indication that the size of the studied polymer (20 to 40 monomers) is adequate and should not influence the orbital localisation. The convergence of the electronic properties observed here is based on the assumption that the change of the

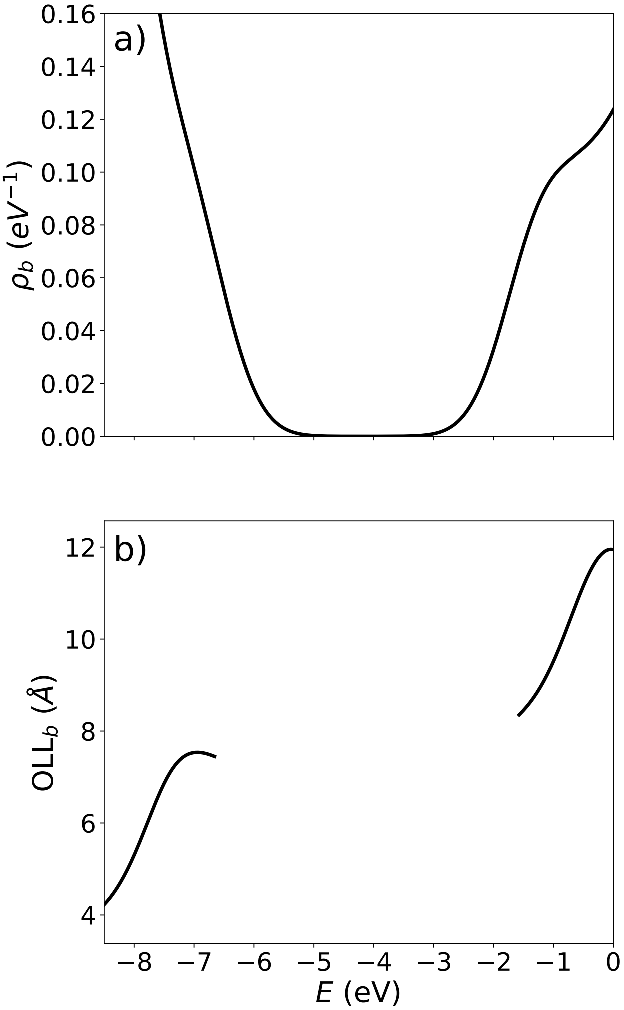

Figure 5.6: (a)Bulk density of states and (b) bulk orbital localisation length for the 20ch_20mers system averaged over ten snapshots using the trajectories taken from the 200 ns NVT equilibrium run. Each snapshot is separated by 20 ns. Results are obtained using TDDFT at the ωB97XD/3-21G* level of theory.

molecular weight does not significantly alter the polymer morphology. For higher molecular weight systems, chain entanglement and aggregation may become important, and in such instances, it is necessary also to correlate these morphological changes to the electronic structure properties.

5.4.2 Interchain Excitonic Coupling

To demonstrate that it is reasonable to consider only the electronic structure of individual chains (as mentioned in the Methods Section), we characterise the interchain excitonic couplings in the amorphous PDPPTT-T-10 polymers. For each chain pair, we evaluate a total of 9 excitonic couplings between the three lowest excited states of each chain. Figure 5.7 shows the histogram distribution of the absolute values of the interchain couplings $|J_{mn}^{\alpha\beta}|$ between the exciton α in chain m and the exciton β in chain n. Figure 5.7 shows that most couplings are less than 10 meV (more than 95%). There are a few cases where the couplings approach 25 meV, but their probabilities are negligibly small, and values beyond 25 meV are rarely observed. Furthermore, about 90% of the coupling values are less than 5 meV, which indicates that our excited state calculations based on the individual chain calculations are justifiable due to the low probability of exciton hopping between chains. Similar phenomenon is also observed for amorphous MEH-PPV polymers, (Ma et al. 2014) which implies that this could be a general feature, thus suggesting routes to construct a model for exciton transport in amorphous conjugated polymers.

5.4.3 Charge Transfer Character and Electron-Hole Distribution

To characterise the nature of the electronic transitions of the bulk PDPPTT-T-10 conjugated polymer, we analyse the e-h distributions and the transition densities for the lowest five singlet excitations of the 20ch_20mers from a snapshot taken at 200 ns from the production dynamics. We compute several key

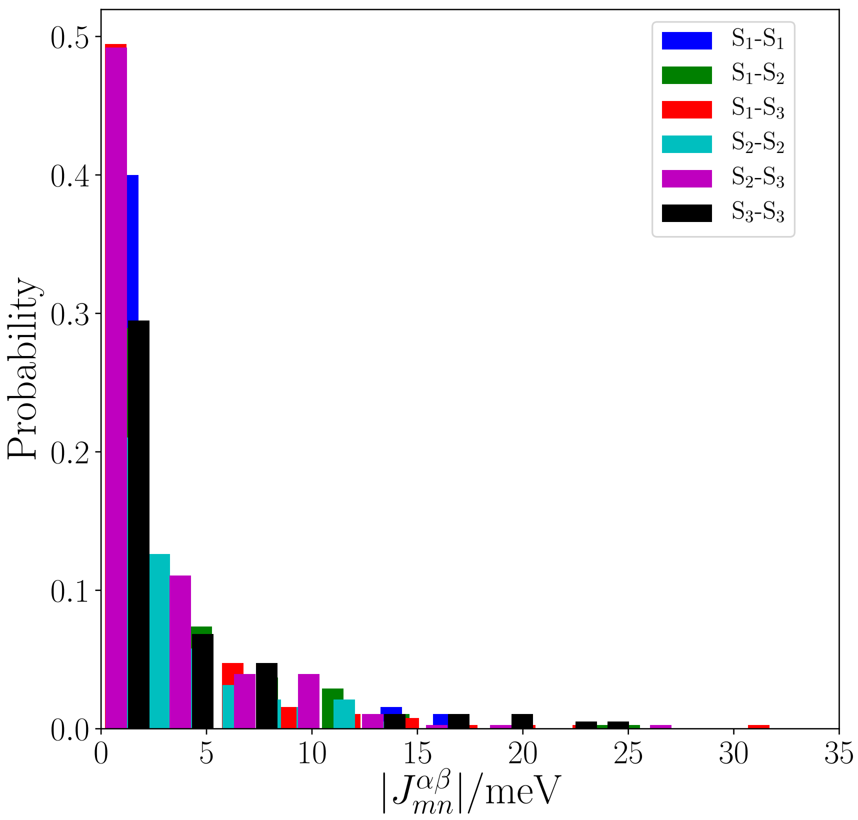

Figure 5.7: Distribution of the interchain excitonic couplings $(S_0 \rightarrow S_1) \Leftrightarrow (S_0 \rightarrow S_1)$ (blue), $(S_0 \rightarrow S_1) \Leftrightarrow (S_0 \rightarrow S_2)$ (green), $(S_0 \rightarrow S_1) \Leftrightarrow (S_0 \rightarrow S_3)$ (red), $(S_0 \rightarrow S_2) \Leftrightarrow (S_0 \rightarrow S_2)$ (cyan), $(S_0 \rightarrow S_3) \Leftrightarrow (S_0 \rightarrow S_3)$ (magenta) and $(S_0 \rightarrow S_3) \Leftrightarrow (S_0 \rightarrow S_3)$ (black) for 20ch_20mers chain pairs from an equilibrium snapshot (at 200 ns in the NVT ensemble simulation), respectively.

metrics (descriptors) of these excited states, including the participation index, the average degree of the spatial extent of the e-h distribution (H-index), the exciton binding energy (E_{coul}) and the average e-h distance upon excitation ($\Delta_{\mathbf{r}}$-index). The values of these descriptors are given in tables C.1-C.20, and histograms are shown in Figure C.2. The averages of the descriptors are summarised in Table 5.1. We can observe from this table that the lowest excited state S_1 has the smallest PI values (just over 2), indicating that, on average, this transition is mainly localised on two monomers. The second, third, and fourth excited states have similar PI values and are more delocalised with PI values around 3 repeating units. The fifth transition has the highest PI value.

This excited state, on average, is delocalised over about four monomers. The exciton energies also confirm this trend; the $S_0 \rightarrow S_1$ transition has the highest binding energy, while the $S_0 \rightarrow S_5$ has the lowest. Similarly, we can also observe the low values in the spatial extent of the excitons and the e-h distance of S_1 and S_2 compared to S_3, S_4 and S_5.

Transition	$\langle PI \rangle$	$\langle H \rangle$ (Å)	$\langle E_{\text{coul}} \rangle$ (eV)	$\langle \Delta\mathbf{r} \rangle$ (Å)
$S_0 \rightarrow S_1$	2.35	10.35	1.58	9.54
$S_0 \rightarrow S_2$	2.95	11.71	1.45	10.21
$S_0 \rightarrow S_3$	3.35	14.62	1.08	12.19
$S_0 \rightarrow S_4$	3.25	14.53	1.09	11.05
$S_0 \rightarrow S_5$	3.85	15.81	0.92	10.79

Table 5.1: Computed average electronic excitation indices for the five lowest singlet excited states of the 20ch_20mers system at 200 ns in the NVT ensemble.

Further investigation of these transitions using the contributions of the molecular orbitals in the polymer chain to the e-h shows that both the hole and the electron are distributed between one to two monomers in the case of S_1 and S_2. In contrast, for higher transitions (S_3, S_4 and S_5), the excitons spread out and delocalise over several monomers. As an example, Figure 5.8 shows the distribution of the hole and the electron for the lowest five singlet excited states of chain number one, which exhibits a typical e-h distribution for a chain in the bulk PDPPTT-T-10 conjugated polymer. The e-h distribution mainly comes from the DPP moiety with some contributions from the TT and T segments (Figure 5.9). Similar trends are also observed for other chains (e.g Figures C.2 and C.3). The difference in the extent of the delocalisation of the lowest five singlet excitations for PDPPTT-T-10 reveals that one-electron states at the band edge are usually more localised.

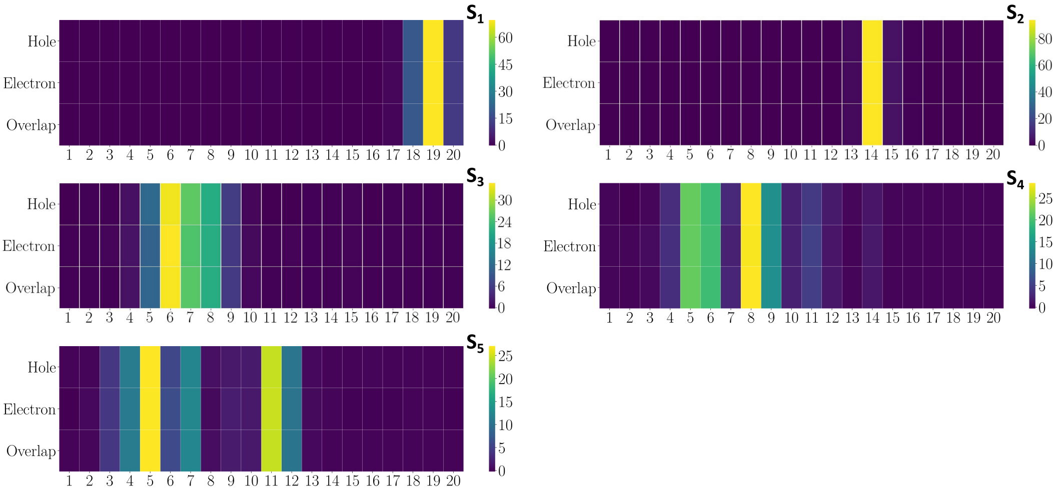

Figure 5.8: Heat map of the monomer contributions to the hole and electron for the lowest five excited states of chain number one.

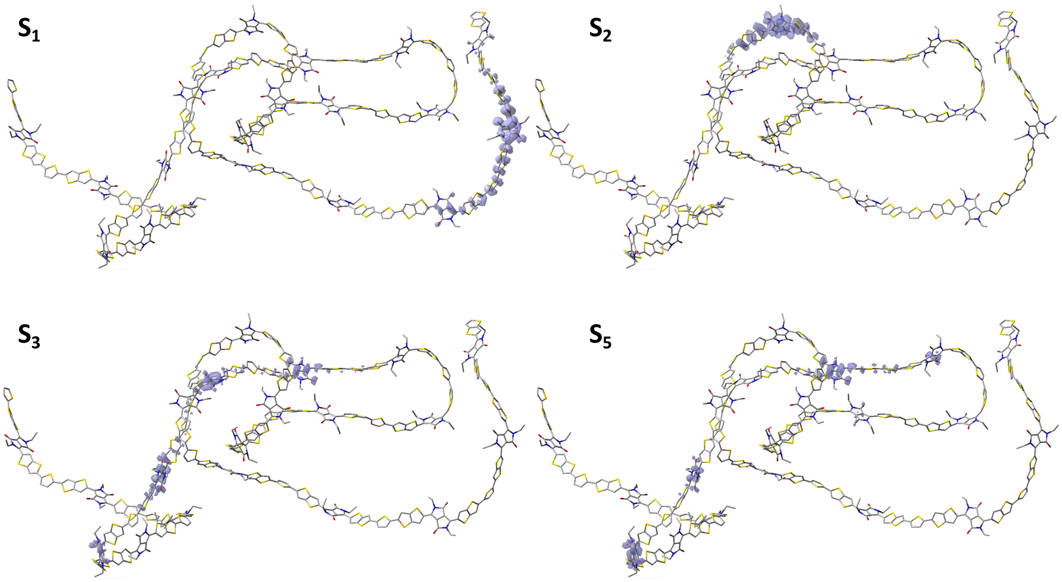

Figure 5.9: Hole distribution of S_1, S_2, S_3, S_4 and S_5 along chain number one.

5.4.4 Relationships Between Chain Conformation and Electronic Structure Properties

Figure 5.10 shows the folding parameter, nonplanarity parameter and the contribution of each monomer to the lowest five singlet excited states for chain number one in the 20ch_20mers system. Similar trends are also observed for other chains. Our main goal here is to establish the relationship between the geometric disorder of the polymer chain and its electronic structure properties.

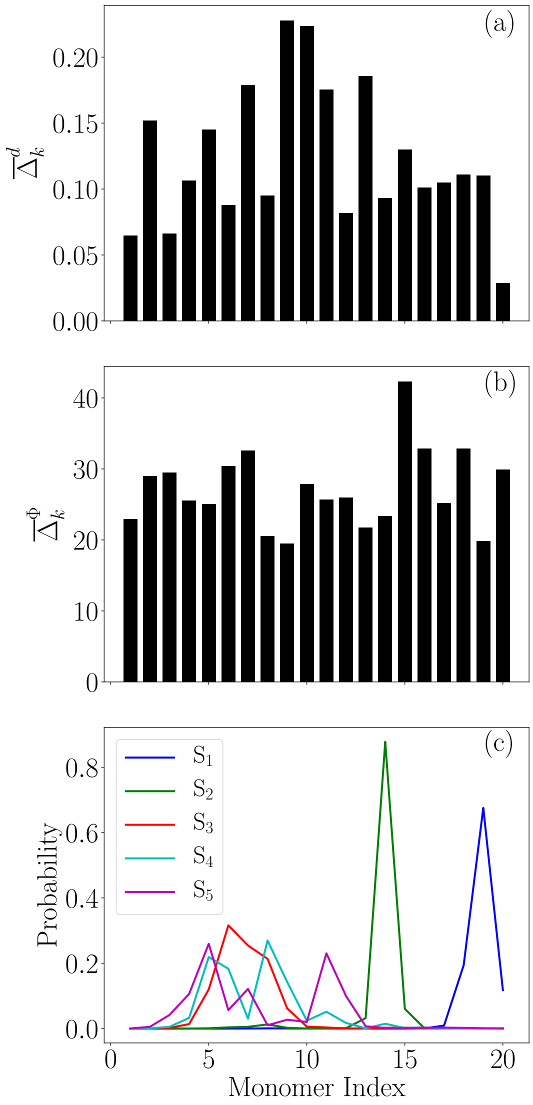

Figure 5.10: (a) Folding and (b) nonplanarity parameters together with (c) the weight of the transition density on each monomer for chain number one of the 20ch_20mers system.

It is not straightforward to find any direct correlations from the correspondence between Figures 5.10a, 5.10b and 5.10c. Nevertheless, we can extract some insights. For example, the lower-energy orbitals (i.e. S$_1$ and S$_2$) are localised in the region of the chain that is locally less folded and more planar (monomers 14 and 19). On the other hand, higher excitations such as S$_3$, S$_4$ and S$_5$ are more delocalised and have the tendency to spread over defects. For instance, there is a significant folding around monomer 9 in chain one (Figure 5.10a), but S$_3$, S$_4$ and S$_5$ cross this defect. This observation verified that it is challenging to define chromophores in amorphous polymers purely based on the concept of geometric conjugation breaks (Collini & Scholes 2009). An illustration of the distribution of the transition densities of the lowest five excited states along chain one is shown in Figure 5.11. In general, we find that the lowest excitations (S_1 and S_2) are typically localised without much overlaps with each other (e.g. see Figures 5.9 and 5.11). These excitons are often termed local exciton ground states (LEGSs) derived from empirical model calculations (Makhov & Barford 2010, Barford & Mannouch 2018). They are considered chromophores for absorption in low-energy windows, and their existence was confirmed for MEH-PPV (Ma et al. 2014) from first principle calculations. Here, our results for PDPPTT-T-10 further support the presence of LEGSs in amorphous conjugated polymers. Thus, the ability to describe them rigorously from quantum chemical calculations will help construct a reliable exciton transport model for organic semiconducting polymers.

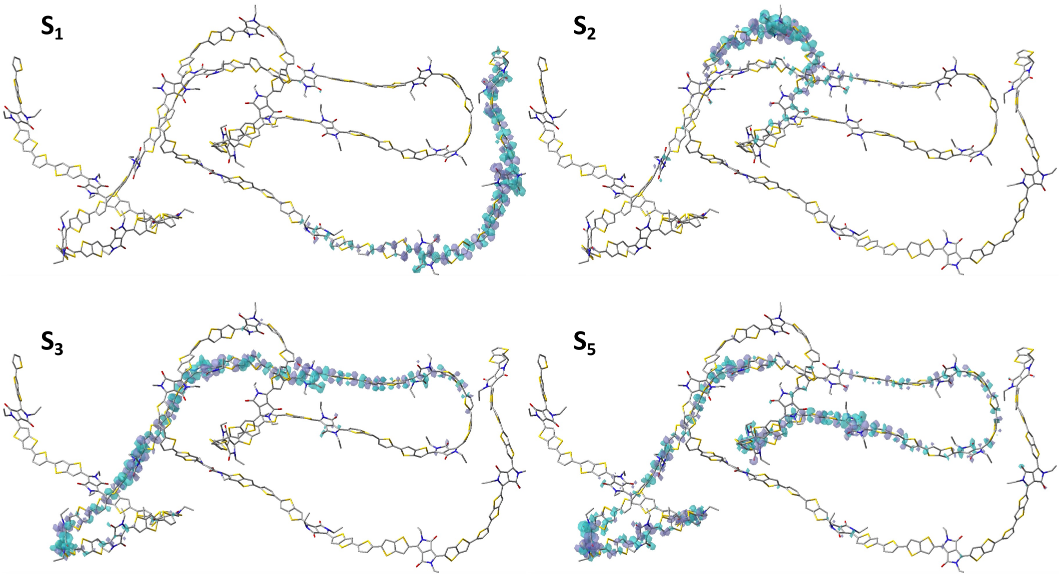

Figure 5.11: Distribution of transition densities of S_1, S_2, S_3, S_4 and S_5 along chain number one.

We have revealed the challenge in building a direct relationship between the geometric distortion and the electronic properties of amorphous conjugated polymers. However, we have discovered two interesting things: (i) low-energy excitons tend to avoid disorder and (ii) high-energy excitons may spread over defects. To confirm the preliminary observation more quantitatively, we define several further parameters. Firstly, we introduce $\lambda_f^{\text{chain}} = \sum_{k=1}^{M} \bar{\Delta}_k^d / M$ and $\lambda_p^{\text{chain}} = \sum_{k=1}^{M} \bar{\Delta}_k^\Phi / M$, which are essentially the folding and nonplanarity parameters averaged over the whole chain. Next, to obtain the correlation between these order parameters and excited state properties, we compute $\lambda_f^{\mathrm{S_0 \to S_n}} = \sum_{k=1}^{M} \bar{\Delta}_k^d P_k^{\mathrm{S_0 \to S_n}}$ and $\lambda_p^{\mathrm{S_0 \to S_n}} = \sum_{k=1}^{M} \bar{\Delta}_k^\Phi P_k^{\mathrm{S_0 \to S_n}}$, which are the average folding and nonplanarity parameters weighted by the $\mathrm{S_0} \to \mathrm{S}_n$ transition density $P_k^{\mathrm{S_0 \to S_n}}$ on each monomer k. These two parameters describe how folded and/or nonplanar a polymer chain is in the region where the transition $\mathrm{S_0} \to \mathrm{S}_n$ is located. In addition, we also compute the folding and nonplanarity degree of a chain in the region where the orbital (e.g. HOMO) is localised as $\lambda_f^{\text{HOMO}} = \sum_{k=1}^{M} \bar{\Delta}_k^d P_k^{\text{HOMO}}$ and $\lambda_p^{\text{HOMO}} = \sum_{k=1}^{M} \bar{\Delta}_k^\Phi P_k^{\text{HOMO}}$. Here, P_k^{HOMO} is the HOMO orbital density on monomer k.

By comparing the distribution of these parameters, we can establish the correlation between the order parameters and the position of the excitons. Figure 5.12 shows the histogram distribution of the folding (λ_f) and the nonplanarity (λ_p) for the chain (blue), HOMO (orange), $\mathrm{S_0} \to \mathrm{S_1}$ transition (green), and $\mathrm{S_0} \to \mathrm{S_5}$ transition (red) for the 20ch_20mers system. For clarity, we exclude data for other orbitals and transitions. Figure 5.12 shows that the order parameters (λ_f and λ_p) in the region of the HOMO have a similar distribution to those where the $\mathrm{S_0} \to \mathrm{S_1}$ and $\mathrm{S_0} \to \mathrm{S_5}$ transitions are distributed. This implied that the HOMO has a significant contribution to these transitions. Generally, if orbitals and/or the exciton try to avoid defects in the polymer chains, we will not observe any overlap between the distribution of the chain defects and others (e.g. between λ_p^{chain} and λ_p^{HOMO}). However, we can see that it is not the case here. For example, Figure 5.12b shows that λ_p^{chain} is distributed in the range [25°, 30°] with a peak at about 28°, while $\lambda_p^{\mathrm{S_0 \to S_1}}$ varies in a broad range between 13° and 37°. This means that although the $\mathrm{S_0} \to \mathrm{S_1}$ transition (also the HOMO) tend to stay away from the nonplanar region of the chain,

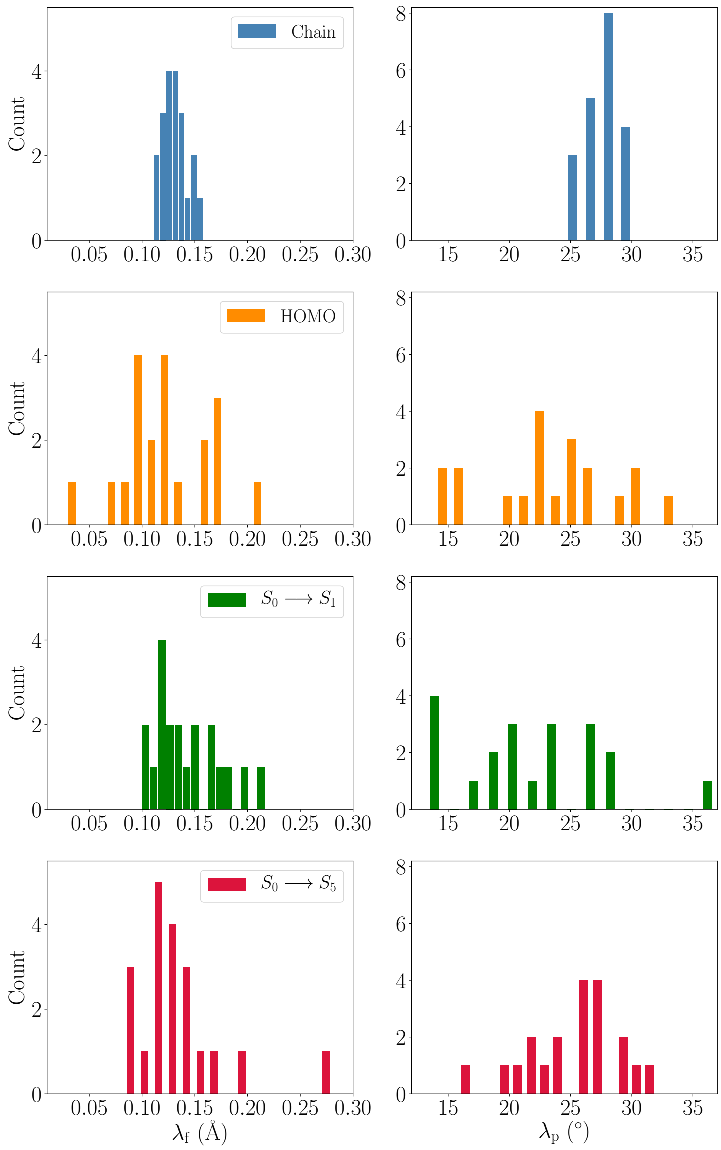

Figure 5.12: Distributions of chain folding (left panels) and nonplanarity (right panels) of the 20ch_20mers system. Blue bars are the distribution of the average chain folding ($\lambda_f^{\mathrm{chain}}$) and nonplanarity ($\lambda_p^{\mathrm{chain}}$) per chain. Orange bars are the distribution of the HOMO (per monomer) weighted average chain folding ($\lambda_f^{\mathrm{HOMO}}$) and nonplanarity ($\lambda_p^{\mathrm{HOMO}}$). Green bars are the distribution of the $\mathrm{S}_0 \rightarrow \mathrm{S}_1$ transition density ($P_k^{\mathrm{S}_0 \rightarrow \mathrm{S}_1}$) weighted average chain folding ($\lambda_f^{\mathrm{S}_0 \rightarrow \mathrm{S}_1}$) and nonplanarity ($\lambda_p^{\mathrm{S}_0 \rightarrow \mathrm{S}_1}$). Red bars are the distribution of the $\mathrm{S}_0 \rightarrow \mathrm{S}_5$ transition density ($P_k^{\mathrm{S}_0 \rightarrow \mathrm{S}_5}$) weighted average chain folding ($\lambda_f^{\mathrm{S}_0 \rightarrow \mathrm{S}_5}$) and nonplanarity ($\lambda_p^{\mathrm{S}_0 \rightarrow \mathrm{S}_5}$).

they are often found spreading over defects. On the other hand, distribution of the nonplanarity of the $\mathrm{S}_0 \rightarrow \mathrm{S}_5$ transition overlaps quite well with $\lambda_p^{\mathrm{chain}}$, indicating a more delocalised character over nonplanar regions of the higher excited states.

A similar observation can also be made for the case of the folding parameters (Figure 5.12a). Although both HOMO and excitons try to stay away from the chain defects, they are also often found at the average folding locations of the chain. It was suggested that defects (folding and nonplanarity) break the polymer chain into fragments in which excitons are localised (Collini & Scholes 2009). However, our results confirm that pure geometric definition of a chromophore or exciton is not advisable for amorphous polymers. Definitions based on the electron density are crucial, and explicit quantum chemical calculations should be carried out before formulating exciton transport models.

Having confirmed that the inter-chain excitonic couplings are negligible, we focus on analysing the evolution of the exciton along the polymer chains. More specifically, we investigate the hole dynamics for different transitions on different chains. Figure 5.13 shows the monomer contributions to $S_0 \rightarrow S_1$ and $S_0 \rightarrow S_5$ transitions for two representative chains (2 and 20) of the 20ch_20mers system at different times. The nuclear trajectories are taken from a 200 ns equilibrium run, separated by 50 ns. Since the polymer is in its amorphous state under the studied conditions, the overall chain conformation does not change significantly over tens of nanoseconds. However, this is certainly not the case for the excited state properties for which the time-scale is much shorter.

Figure 5.13 shows that excitons of both $S_0 \rightarrow S_1$ and $S_0 \rightarrow S_5$ transitions can move freely back and forth along the polymer chains. The centroid positions of excitons change considerably with time. While the shape of the lowest excited state ($S_0 \rightarrow S_1$) remains almost unchanged, that of the higher transition ($S_0 \rightarrow S_5$) varies significantly with time. The modulation of the exciton's size and shape is partly due to the fluctuation of the torsion angles, which effectively manipulates the magnitude of the intra-chain excitonic couplings. In addition, we also observe a variation of the orbital localisation lengths (Figure C.5), which is the result of the change in the shape of the DOS and the

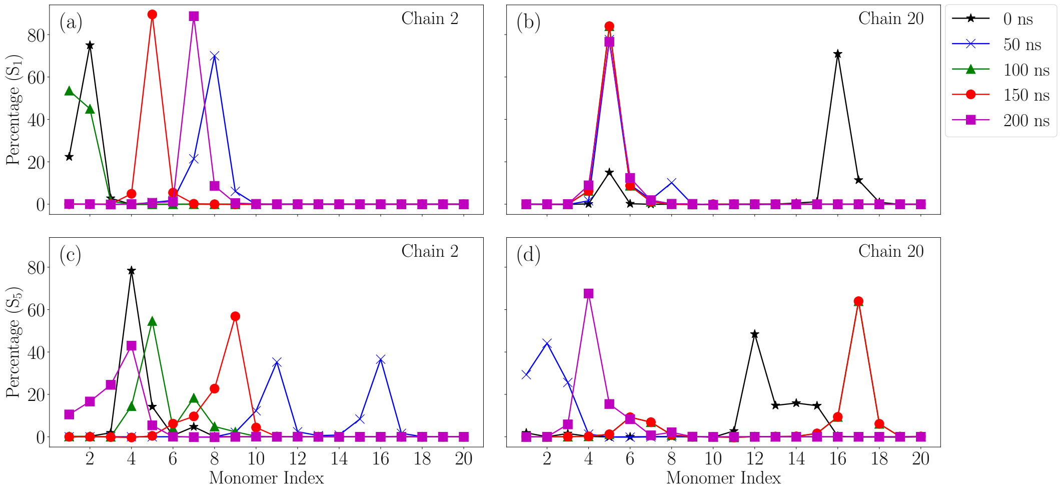

Figure 5.13: Exciton evolution along polymer chains at 0 ns (star black line), 50 ns (cross blue line), 100 ns (triangle green line), 150 ns (circle red line) and 200 ns (square magenta line). (a) S_1 hole of chain 2, (b) S_1 hole of chain 20, (c) S_5 hole of chain 2 and (d) S_5 hole of chain 20.

interchange of different molecular orbitals due to the evolution of the polymer chains. Thus, the conformational rearrangement of the polymer chain over time may alter the location, shape and energetic order of excited states but tends not to affect the nature of the low energy excitons (i.e. LEGS). Another critical point to note here is that the dynamics of the nuclei are much slower than that of the excitons; analysis based on a couple of snapshots is still sufficient to give a reliable picture of the excited states in amorphous polymers. Our results here for PDPPTT-T-10 are very similar to what was observed for MEH-PPV (Qin & Troisi 2013, Ma et al. 2014), which suggest these properties could be standard features for amorphous conjugated polymers.

5.5 Conclusion and Outlook

This chapter employs a range of computational tools to characterise the relationships between the morphology and electronic structure properties of amorphous conjugated PDPPTT-T-10 polymers. First of all, the force field parameters for these systems are carefully optimised to ensure that the classical potential energy surface and its gradients of the polymer are mapped onto the targeted *ab initio* ones. Then, MD simulation is utilised to generate amorphous polymer models, and the equilibrium trajectories are sampled. After that, large-scale TD-DFT calculations for the electronic excited states of the polymeric systems are performed to obtain the structure-property relationships. Given the size of the polymeric system, a balanced set of approximations is determined to provide the most accurate excited state calculations for the bulk PDPPTT-T-10 polymer models.

Our calculations reveal that the effects of the side-chain on the electronic structure properties of the polymer chain are minor, especially near the band edge. The electronic structure is chiefly determined by the conformational disorder of the chain backbone. Our polymer models are large enough to reproduce the electronic structure properties, such as the density of states and the localisation length, of the bulk system. We also confirm that the electronic couplings between polymer chains are negligibly small (mostly less than 5 meV), and the effect of electrostatic disorder is insignificant. This suggests that the exciton transport mechanism along the chain could be described by incoherent hopping. We observe that the excitons of PDPPTT-T-10 prefer to localise in regions that are relatively planar and less folded. However, exceptions are not rare, and these excitons can spread over defects. Thus, it is not possible to define a chromophore in this polymer purely based on geometric conjugation breaks. A rigorous definition can only be made based on evaluating the polymer excited state wave function. Hence, our results provide useful information for constructing more realistic models for the exciton dynamics study of this class of polymeric materials.

Chapter 6

Conclusions and Future Work

6.1 Conclusion

The main themes discussed in this thesis are exciton dynamics and structure-property relationships in organic semiconductors containing diketopyrrolopyrrole, thiophene and thienothiophene. To facilitate these studies, it is vital that the force fields used to describe the nuclear dynamics are accurate enough to capture the true molecular motion of the system. Thus, part of this thesis is dedicated to overcoming this challenge by employing our extension of the adaptive force-matching technique to parameterise accurate force fields for the studied molecular aggregates. Some of the fundamental theoretical aspects in these research fields are addressed with simplified models and various computational techniques.

Chapter 1 includes a review of the rapidly evolving field of organic electronics, emphasising its applications in sustainable energy and flexible electronic devices. It also gives an overview of the physical basis of organic semiconductors for a better understanding of the processes that affect the exciton dynamics and structure-property relationships in molecular aggregates. It then introduces a promising type of organic semiconductors containing DPP, TT and T that could be employed to achieve high-performance thin-film transistors and solar cell devices, followed by an overview of the methods most commonly used to describe exciton and charge transport in organic materials. The chapter ends by highlighting the current challenges for organic semiconductors and providing the thesis's aims and objectives. Chapter 2 describes the modelling of organic semiconductors, which involves using various computational tools and techniques. It gives an overview of the core methodologies employed to model electronic states and transport properties in organic semiconductors, including MD simulations, force field parameterisation and quantum chemical calculations.

It is not easy to find sufficiently accurate force fields for all applications where MD simulations are a preliminary step toward studying electronic structure properties. All single molecules, biological chromophores, and semiconducting polymers of interest display a complex chemical structure with extended π-conjugation that prevents the use of standard force fields. Most force fields have been designed mainly for biochemical systems, e.g. proteins or small organic molecules. Although these force fields contain transferable parameters to conjugated systems, many aspects require careful parameterisation due to the conjugation. Moreover, when one uses classical simulation methods as inputs for electronic structure calculations, it is desirable that the potential energy surfaces of the classical and quantum systems are as close as possible, i.e. the force field should be consistent with the electronic structure calculation that follows it. Thus, to mitigate the mismatch in the geometry, the classical potential energy surface and/or its gradients of the system of interest should be mapped onto the *ab initio* ones by optimising the force fields. Chapter 3 extends the adaptive force matching technique to rapidly parameterise force fields for complex conjugated systems. We develop a strategy for fragmenting the "larger" molecule into smaller segments, obtaining their parameters, and then assembling them to derive the force fields for the "larger" molecule. The thrust of our approach is to obtain parameters consistent with any pre-defined electronic structure calculation method. We employ our procedures to optimise parameters for systems investigated in Chapters 4 and 5.

Exciton transport in crystalline organic semiconductors is intrinsically limited by the presence of significant thermal molecular motions. These induce the localisation of the electronic wavefunction, which survives up to the typical time scales of the intermolecular vibration. Generally, these problems are challenging to solve using analytical theory due to the thermal fluctuations and spatial symmetry breaking in the crystal. Experimental data are invaluable for characterising the utility of materials for devices, but they often do not give detailed insight into the nature of the exciton transport. Thus, theoretical and computational approaches can be a crucial complement to experiments by providing direct access to microscopic and electronic properties of organic semiconductors and helping to guide their development. Chapter 4 investigates the exciton transport of the recently synthesised mono- and di-alkylated substituted TDPP molecular crystals utilising computational chemistry tools. We first propagate the dynamics of the systems using classical MD simulations to obtain the equilibrium trajectories (nuclear dynamics) for electronic structure calculations. Then, the excitonic couplings between all the relevant excited states in the molecular crystal pairs are computed, and their fluctuations due to thermal disorder are analysed. Finally, the exciton dynamics are studied using a Frenkel–Holstein like Hamiltonian with an appropriate theoretical approximation where the thermal excitonic coupling fluctuations (non-local exciton-phonon couplings) have been appropriately taken into account.

DPP-based conjugated polymers have emerged as desirable materials for thin-film transistors and solar cell devices. The electron-deficient nature of the DPP core has been exploited to synthesise extremely narrow bandgap donor-acceptor-type materials well suited for use in OPV with high power conversion efficiencies reported in both small molecules and polymers. Furthermore, the planarity of the DPP skeleton and its ability to accept hydrogen bonds result in copolymers that encourage $\pi - \pi$ stacking. DPP-based semiconducting polymers can achieve a surprisingly high mobility rate without having an overall crystalline structure. However, the detail of the relationship between the morphology and electronic structure properties of this class of conjugated polymers is still unclear, and a fundamental understanding is necessary for their design and development. Chapter 5 employs a range of computational tools to characterise the relationships between the morphology and electronic structure properties of amorphous conjugated PDPPTT-T-10 polymers. The force field parameters for these systems are carefully optimised to ensure that the classical potential energy surface and its gradients of the polymer are mapped onto the targeted *ab initio* ones. Then, MD simulation is utilised to sample the nuclear trajectories, followed by large-scale TD-DFT calculations for the electronic excited states of the polymeric systems to obtain the structure-property relationships. Given the size of the polymeric system, a balanced set of approximations is determined to provide the most accurate excited-state calculations for the bulk PDPPTT-T-10 polymer models.

Many technological applications envisioned for organic electronic materials involve the absorption and emission of light. The photophysical behaviour of these materials is governed by the structure and dynamics of their low-lying electronic states. These excited electronic states can be considered mobile quasi-particles that carry energy, collectively termed excitons. This area of research lies at the interface of chemistry and physics, and progress depends on the coordinated efforts of experiment and theory. This thesis embarks on a theoretical and computational approach to answering fundamental questions regarding charge and exciton transport in organic semiconducting materials. It also characterises the relationships between material morphology and electronic structure properties, which are crucial for designing new high-performance materials. Our studies provide a framework for a predictive structure-function understanding of excited states (or excitons) in organic solids. It is hoped that the work in this thesis helps facilitate the experimental advances needed to generate improved materials and usher in the era of organic electronics.

6.2 Major Contributions

The major contributions of this thesis are:

- New parameters for OPLS-style force fields for macromolecular assemblies containing DPP, T and TT.
- An extension of the adaptive force matching technique to rapidly parameterise force fields for complex conjugated systems by developing a strategy for fragmenting the “larger” molecule into smaller segments, obtaining their parameters, and then assembling them together to derive the force fields for the “larger” molecule.
- Characterising of the exciton transport of the recently synthesised mono- and di-alkylated substituted TDPP molecular crystals utilising computational chemistry tools.
- Providing insights into the electronic excited states of amorphous conjugated polymeric systems and their connections to the dynamical disorder of the nuclei.

6.3 Future Work

The transport of excitation energy (excitons) in aggregates of organic molecules is one of the most fundamental and challenging problems in organic photovoltaics. In order to convert to charge carriers after being prepared by photoabsorption, excitons need to diffuse into an interface between electron donor and acceptor materials before deactivating to the ground state. Therefore, a fundamental understanding of exciton diffusion dynamics is crucial for the design and development of future OPVs. However, it remains challenging to understand the relationship between the chemical structure and the exciton diffusion length in molecular aggregates, especially for amorphous systems in which exciton transport is 3D in nature. Moreover, the effect of conjugation length on exciton diffusion has not been appropriately addressed. The work presented in this thesis can be extended to characterise the dependence of exciton diffusion length on chemical structures. We will systematically investigate the transport mechanism of the excitons along the polymer chains and between chains. We will also elucidate the exciton transport regime in both ensembles of small organic molecules and polymers. Attention will be paid to the relationships between morphology and diffusion length.

To achieve this, we will employ machine learning to accelerate the parameterisation process of the empirical tight-binding model Hamiltonian. The scheme will encode details of a system's specific molecular morphology in the correlated distributions of model parameters by analysing many single-molecule excited-state electronic-structure calculations. We will start with the Frenkel model Hamiltonian, which comprises two parameters, the excitation energies of chromophores (sites) and the excitonic couplings between sites. Our approach is to train separate models based on the nuclear trajectories sampled from classical MD simulations using force fields parameterised against the predetermined level of theory of the quantum chemical calculations. The excitonic couplings between a pair of chromophores can be predicted directly from the bimolecular features. Alternatively, we can also predict a set of atom-centred transition charges using unimolecular features from which the coupling may be obtained.

Appendix A

Chapter 3: Force Field Development

A.1 Choosing Different Atom Types

The key idea in the selection of different atom types in our work is to maintain the alternation of single and double bonds along the backbone. This is crucial for conjugated molecules; especially for semiconducting polymers, which often display complex chemical structures with extended pi-conjugation that prevents the use of standard force fields . As such, we tend to have more atom-types than standard force fields . In addition, we also employ symmetry and chemical intuition to reduce the number of types of atoms where it is possible.

A.1.1 Single Chromophores

Referring to Figure A.1b, there are three atom types for carbon in the DPP molecule. First, we assign type TC1 to the two carbons in the middle of the molecule connected by a single bond. Then, TC2 is the carbon atom type that forms a double bond with TC1 type and at the same time bonds to a hydrogen atom. Finally, TC3 is the carbon type that forms a single bond with TC1 and also bonds to an oxygen atom. There is only one type for nitrogen and oxygen due to the symmetry of the DPP molecule. For hydrogen, we use two atom types one that bonds to carbon (TH0) and one that bonds to nitrogen (TN1).

Similarly, for TT molecule, we also have three atom types for carbon TC4, TC5 and TC6. These are also assigned using the same idea described above for DPP molecule. Due to symmetry there is only one atom type TS1 for sulfur. Here, we employ two atom types for hydrogen TH0 and TH1. Next, the choice for the atom types for T molecule is straight forward. We use the symmetry of the molecule to assign its atom types. For this molecule, we have two atom types for carbon (TC7 and TC8), one type for sulfur and two types for hydrogen.

A.1.2 Chromophore-pairs

For the chromophore-pairs, the atom types of the individual single chromophores are merged together. Referring to Figure A.2 and we take DPP-TT as an example. Since there are three carbon atom types in each single chromophore, there are now total six types of carbon atoms for DPP-TT. The atom types for nitrogen, oxygen and hydrogen remain the same as they were in the chromophore singles. A similar approach is applied to the other two chromophore-pairs DPP-T and TT-T. For TT-T, there are two atom types for sulfur S1 and S2; one is in T and the other one is in TT.

A.1.3 Chromophore-triple

For the chromophore-triple, three single chromophores DPP, TT and T are joined together. Thus, the number of carbon atom types becomes eight, while the number of atom types for oxygen and nitrogen remains the same. There are two atom types for sulfur TS1 and TS2, which is the same as the the case for TT-T.

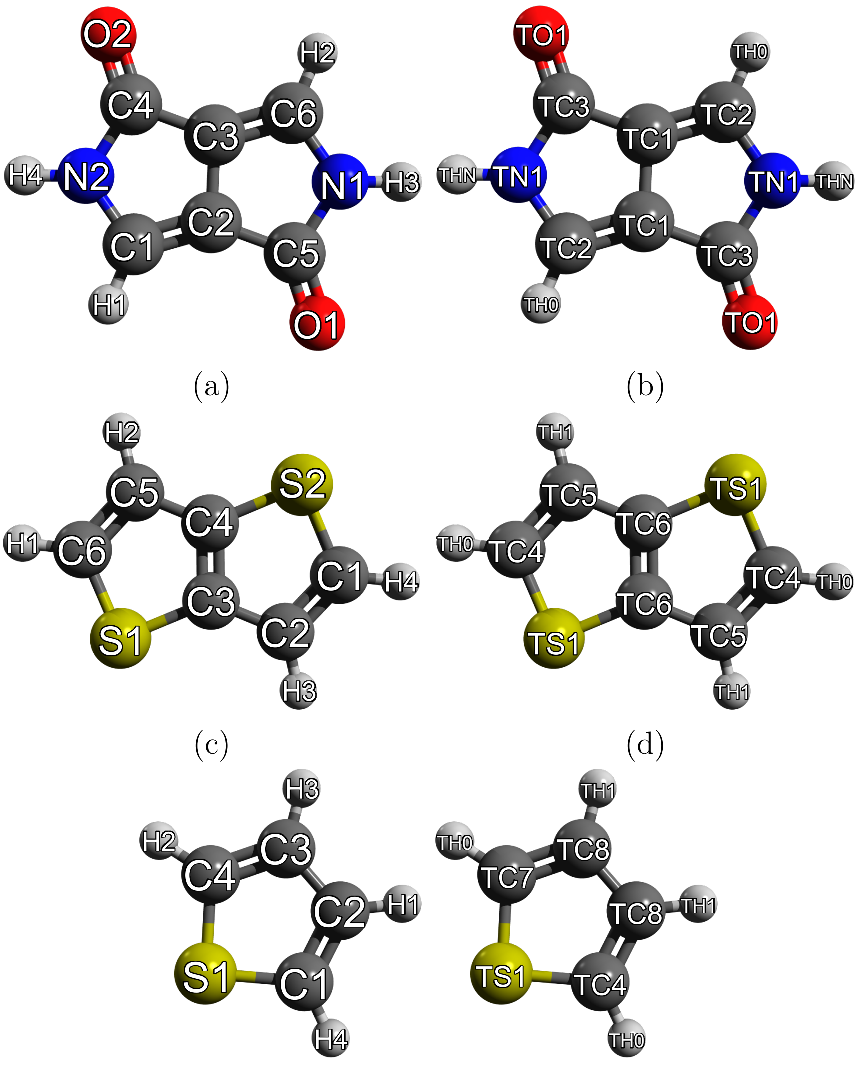

(a) (b)

(c) (d)

(e) (f)

Figure A.1: The structures of the DPP, TT and T molecules with (a) (c) (e) atom names and (b) (d) (f) atom types, respectively.

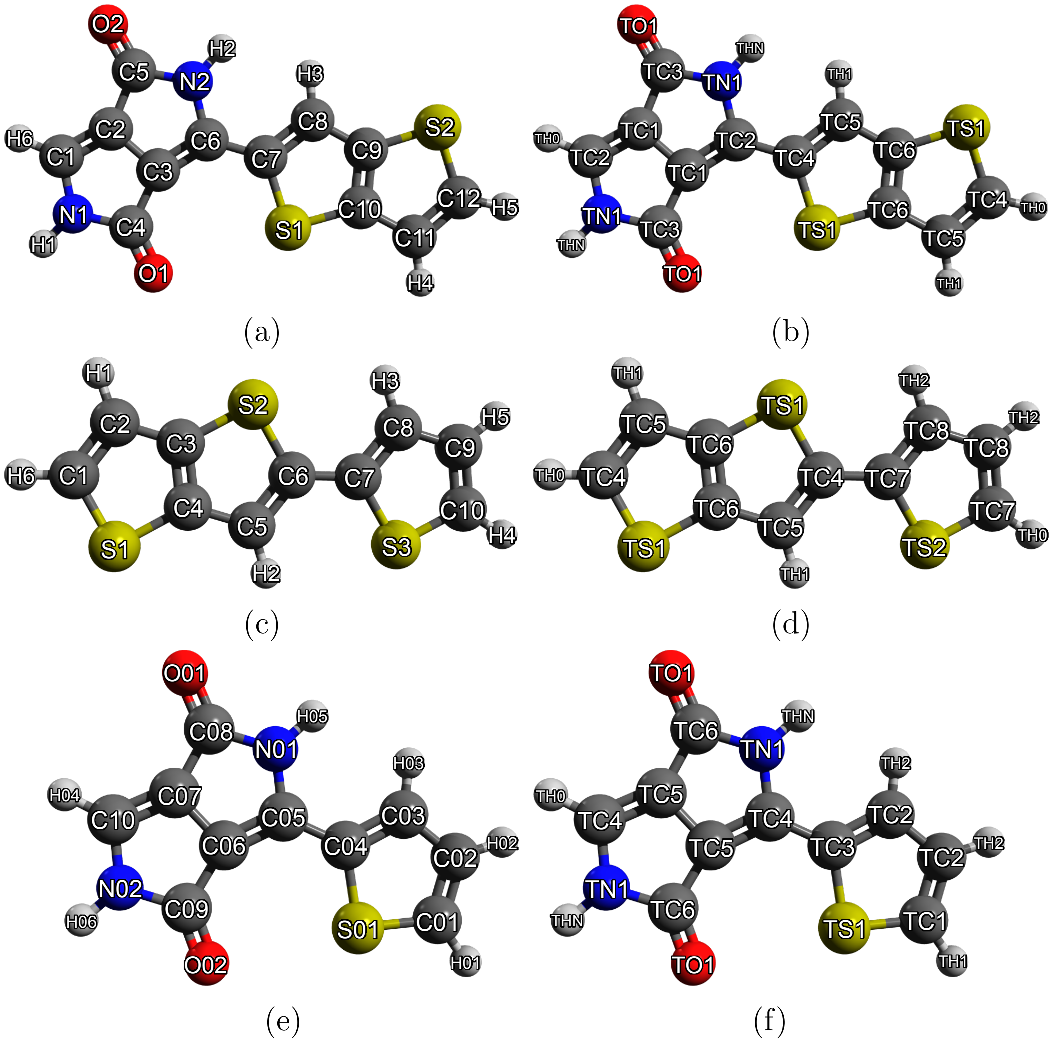

(a) (b)

(c) (d)

(e) (f)

Figure A.2: The structures of the DPP-TT, TT-T, and DPP-T molecules with (a) (c) (e) atom names and (b) (d) (f) atom types, respectively.

A.2 Choosing Different Atom Types

The single chromophores DPP, T and TT are the planar molecules that form the building blocks for constructing the force fields for macro-assemblies. Optimised parameters for DPP were reported previously (Do & Troisi 2015), while those for T and TT have not. Thus, for single chromophores, we shall utilise the existing parameters for DPP and optimise the parameters for T and TT. The atom-names and atom-types are shown in Figure A.1. For all molecules, we optimise their geometries at the B3LYP/6-31G* level of theory and use these optimised structures to compute the point charges. After setting up the initial "guessed" force fields , we perform MD simulations at 300 K in vacuum to collect the M uncorrelated structures as described in the Methods section. The minimum required numbers of structures for T and TT are 104 and 89, respectively. For all single chromophores we employ 150 structures for the optimisation processes. To verify these, we perform tests on these molecules and the results are described in Figure A.3 for DPP as an example. Figure A.3a shows that the minimised force RMSD for the DPP molecule starts to converge at about 85 structures. This is also consistent with previous study on this molecule (Do & Troisi 2015). Figure A.3b shows that for the DPP molecule three iterations are sufficient. Similar trends are also observed for the other molecules, and thus three iterations are employed for all three chromophores in this work.

Since the single chromophores are all planar molecules, their equilibrium dihedral angles, which contain two sp^2 atoms in the middle, are either 0° or 180°. For this reason, it is sufficient to employ only the second term in the OPLS expression $E_{\text{dihed}} = \frac{V_2}{2}[1 - \cos(2\phi - \delta)]$ to represent the torsion potentials for these angles. For planar and "rigid" molecules, it is best to fix the phases of the dihedral angles and optimise only the energy barriers (Do & Troisi 2015). Hence, δ is fixed at 180°. By fixing the phases, we substantially reduce the

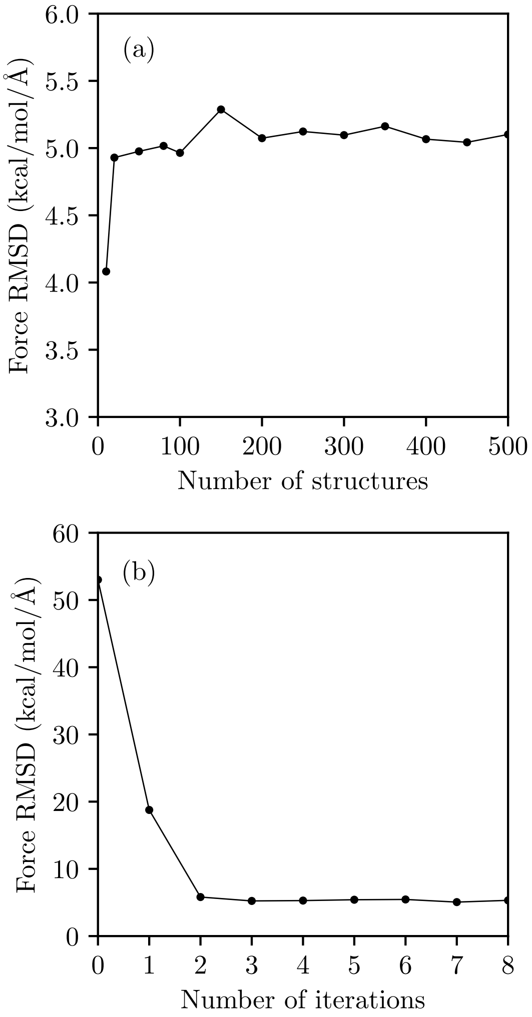

Figure A.3: (a) Root mean square differences of the optimised forces as a function of the number of the structures used for DPP. (b) Force RMSD versus the number of iterations for DPP molecule.

number of parameters to be optimised.

The whole optimisation process is considered to be converged if the RMSD of the forces computed for any arbitrary set of M structures is similar and the same as the minimised force RMSD. In general, this cannot be achieved from a single iteration, unless the initial "guessed" parameters coincide with the optimised parameters. This is rarely the case, and a few iterations are normally required to obtain good convergence. Three iterations are employed for all three chromophores in this work. Table A.1 compares the RMSD between the force fields and the B3LYP/6-31G* forces with the RMSD between the forces computed using other electronic structure methods and the reference B3LYP/6-31G* forces. These results are in the same range as those reported for DPP (Do & Troisi 2015).

Molecules	Method	Force RMSD (kcal mol^{-1} Å^{-1})	Energy RMSD (kcal mol^{-1})
TT	force field	4.16	0.95
	AM1	19.80	2.84
	HF/6-31G*	12.00	2.13
	B3LYP/3-21G*	3.32	0.59
T	force field	4.31	0.75
	AM1	13.70	1.70
	HF/6-31G*	10.02	1.75
	B3LYP/3-21G*	3.17	0.37

Table A.1: Force and energy RMSD between calculations at B3LYP/6-31G* levels and the optimised force field or other levels of theory, for 100 arbitrary geometries not used in the force field optimisation process.

To test our optimised force fields further, we compare the equilibrium structures predicted by our force fields with those optimised geometries computed at the B3LYP/6-31G* level of theory. Figure A.4 shows that the equilibrium structure predicted using our force fields agree very well with those obtained from DFT. The RMSD of the equilibrium bond lengths for DPP, T, and TT are about 0.002 Å, 0.003 Å and 0.006 Å, respectively. The RMSD of the equilibrium angles and dihedrals for all three chromophores are about the same order of magnitude and all less than 0.5°. These results suggest that the RMSD in the forces and energies shown in Table A.1 represent good force fields. Thus, it is reasonable to expect that the optimised force fields for all single chromophores are comparable with DFT "force fields" at the B3LYP/6-31G* level of theory. This is further confirmed by comparison of the excitation energies and oscillator strengths computed along both the classical and *ab initio* MD trajectories shown in Figures A.5 to A.10, respectively.

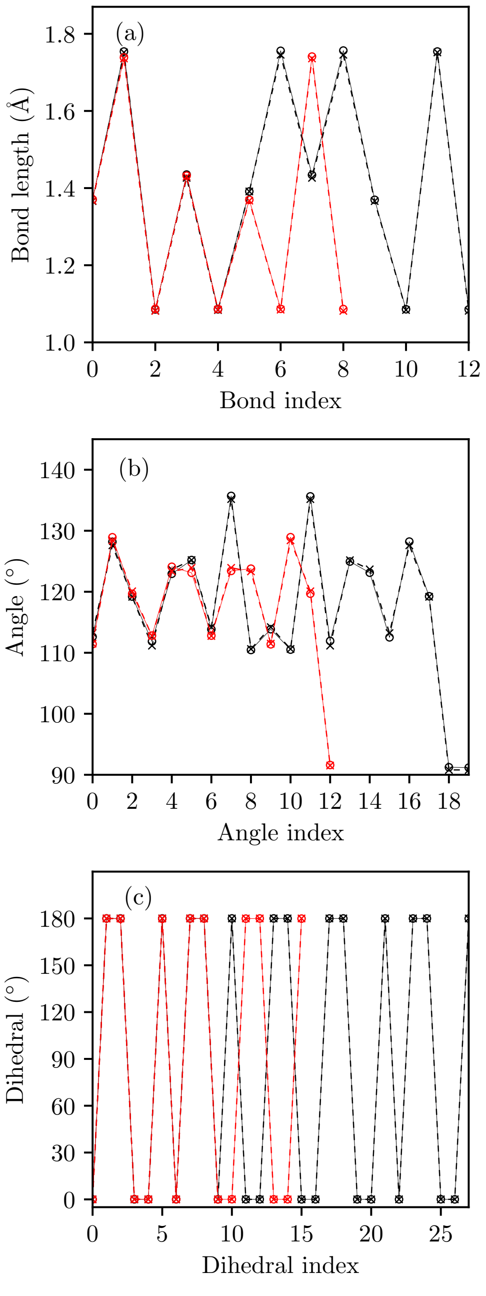

Figure A.4: Comparison of the equilibrium structures of T (red), TT (black) predicted by force fields (circled solid line) and computed at the B3LYP/6-31G* level of theory (crossed dash line): (a) Bond lengths, (b) Angles, and (c) Dihedrals. For dihedrals we use the absolute values.

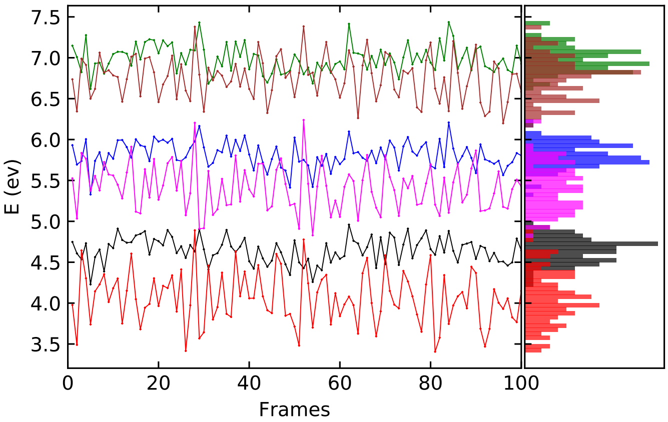

Figure A.5: Comparison of the transition energies of the lowest three excited states computed using trajectories from classical (black, blue and green) and *ab initio* (red, magenta and brown) MD simulations for chromophore T. All calculations are performed at the B3LYP/6-311G(d,p) level of theory. For greater legibility, the transition energies of the first and third excited states are offset by -1.0 eV and 1.0 eV, respectively.

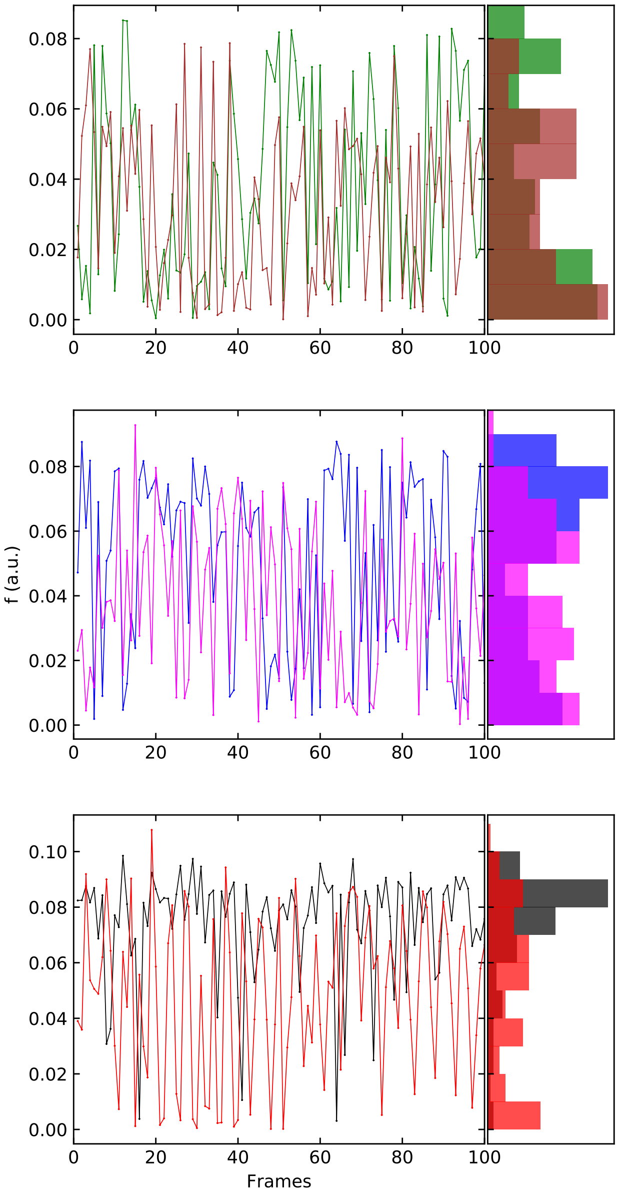

Figure A.6: Comparison of the oscillator strength (f) of the lowest three excited states computed using trajectories from classical (black, blue and green) and *ab initio* (red, magenta and brown) MD simulations for chromophore T. All calculations are performed at the B3LYP/6-311G(d,p) level of theory.

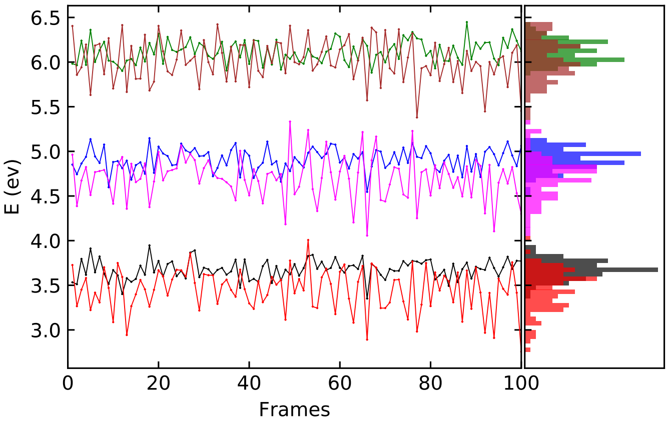

Figure A.7: Comparison of the transition energies of the lowest three excited states computed using trajectories from classical (black, blue and green) and *ab initio* (red, magenta and brown) MD simulations for chromophore TT. All calculations are performed at the B3LYP/6-311G(d,p) level of theory. For greater legibility, the transition energies of the first and third excited states are offset by -1.0 eV and 1.0 eV, respectively.

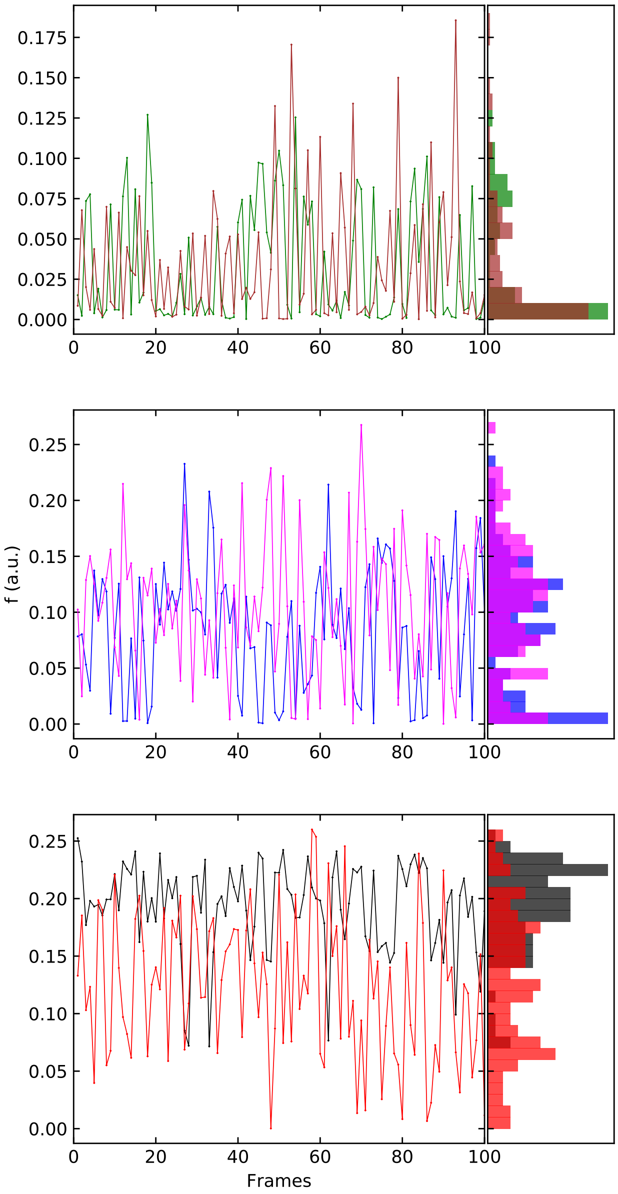

Figure A.8: Comparison of the oscillator strength (f) of the lowest three excited states computed using trajectories from classical (black, blue and green) and *ab initio* (red, magenta and brown) MD simulations for chromophore TT. All calculations are performed at the B3LYP/6-311G(d,p) level of theory.

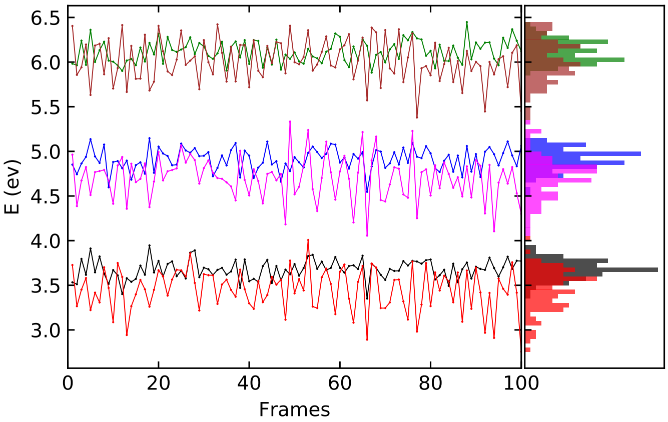

Figure A.9: Comparison of the transition energies of the lowest three excited states computed using trajectories from classical (black, blue and green) and *ab initio* (red, magenta and brown) MD simulations for chromophore DPP. All calculations are performed at the B3LYP/6-311G(d,p) level of theory. For greater legibility, the transition energies of the first and third excited states are offset by -1.0 eV and 1.0 eV, respectively.

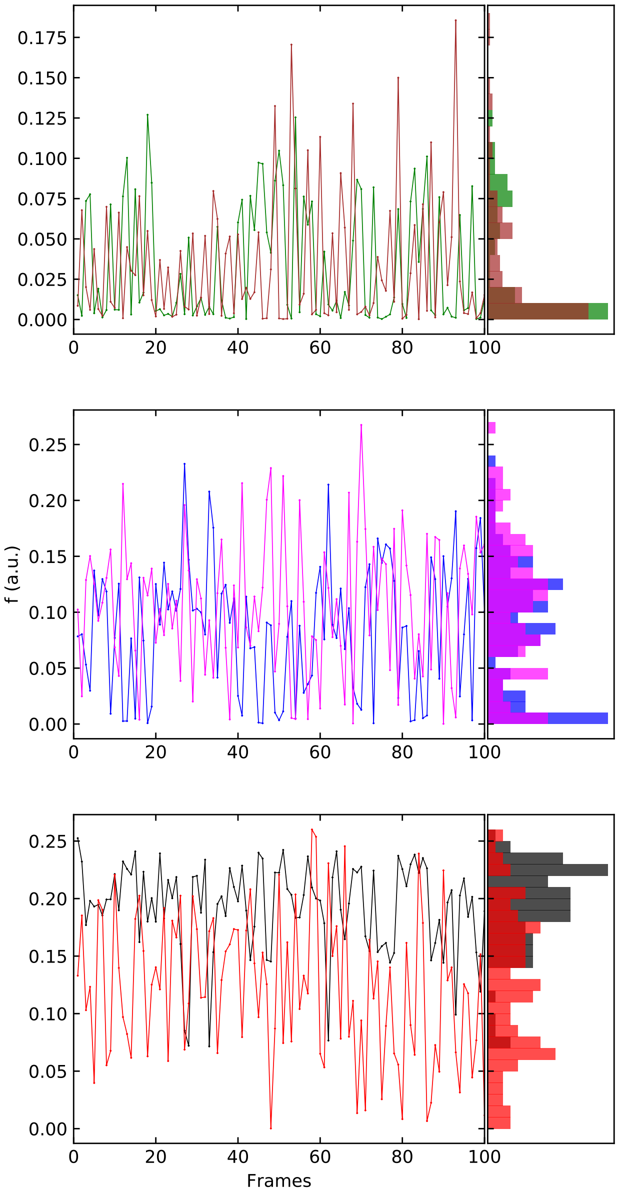

Figure A.10: Comparison of the oscillator strength (f) of the lowest three excited states computed using trajectories from classical (black, blue and green) and *ab initio* (red, magenta and brown) MD simulations for chromophore DPP. All calculations are performed at the B3LYP/6-311G(d,p) level of theory.

A.3 Force Field Development for Chromophore-pairs

The atom-names and atom-types for the chromophore-pairs (DPP-TT, DPP-T, TT-T) are shown in Figure A.2. For these molecules we follow the strategy of Do & Troisi (2015) and divide the optimisation process into two stages. In the first, we obtain all parameters apart from the soft dihedral that links the two fused rings together. And the second stage is to obtain the missing parameters for the flexible torsions. In the first stage, the flexible dihedral angles are fixed at either 0° or 180° (planar structures) to keep the forces of these torsions at zero. Then, the optimisation follows exactly the same procedure as those of chromophore singles described in the previous section. The initial "guessed" parameters are taken from the optimised parameters of the chromophore singles, *i.e.* DPP, TT and T. In addition, the combination of single chromophores introduces some missing parameters and the "guessed" parameters for these are taken from OPLS. For all three chromophore pairs, the optimisation processes converge in only two iterations. This is to be expected as the "guessed" parameters are quite close to the optimised ones by construction (using optimised parameters from single chromophores). The final optimised force RMSD for DPP-TT, DPP-T, and TT-T are 7.3, 7.2, 5.0 kcal mol^{-1} $\mathrm{\AA}^{-1}$, respectively.

In the second stage, we perform torsional scans to derive the parameters for the "soft" dihedral angles. We first carry out the scans at the B3LYP/6-31G* level of theory. Examples of the *ab initio* torsion potentials for the chromophore pairs are shown below. For each molecule, we perform separate scans using different dihedrals to check for consistency, and the results suggest that it is possible to use any one of the four dihedrals to construct the torsional potential (see for example Figures A.11 and A.12). This is followed by "classical" scans using the force fields derived from the first stage. Finally, the torsion potential is the difference between the potentials from the *ab initio* and the “classical” scans (Figures A.13, A.14, A.15). These data are fitted to a truncated cosine series to obtain the force fields parameters for the “soft” dihedrals (e.g. Figure A.16). To illustrate the idea, comparison between the “classical” (with “soft” dihedral parameters included) and *ab initio* scans for DPP-TT, DPP-T and TT-T are shown in Figures A.17 to A.19. In addition, a comparison of the RMSD between the force fields and the B3LYP/6-31G* forces and energies with the RMSD between the forces computed using other electronic structure methods and the reference B3LYP/6-31G* forces is shown in Table A.2.

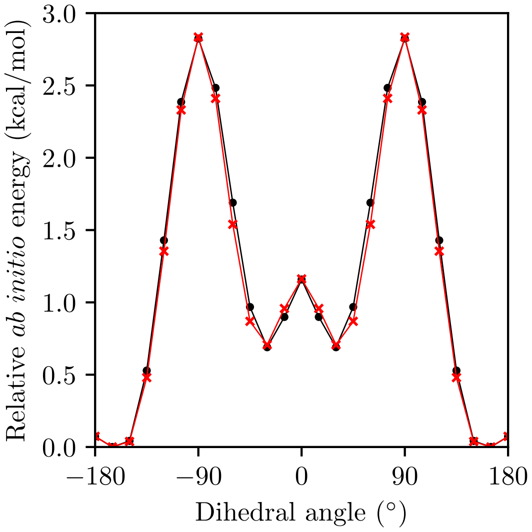

Figure A.11: *Ab initio* torsional scans of CCCC (black) and SCCS (red) soft dihedrals in TT-T. The energy is relative to the smallest one.

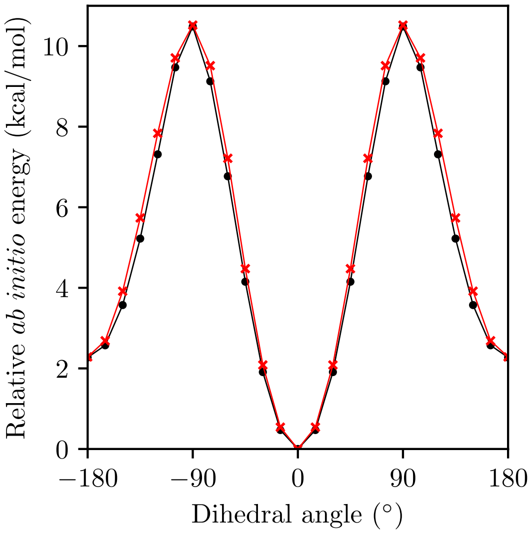

Figure A.12: *Ab initio* torsional scans of CCCC (black) and NCCS (red) soft dihedrals in DPP-TT. The energy is relative to the smallest one.

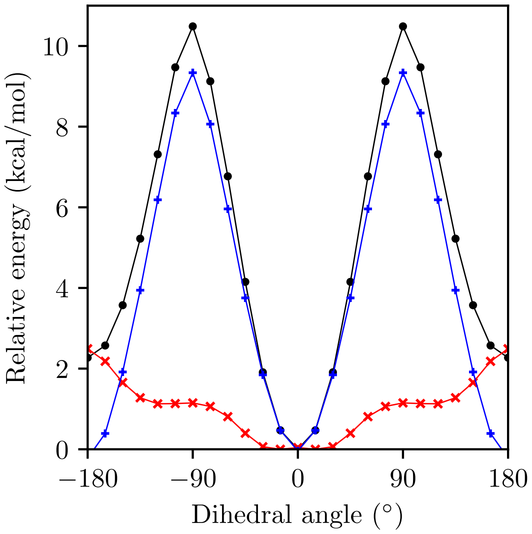

Figure A.13: Relative energy from *ab initio* scan (black), force fields scan (red) and their difference (blue) in DPP-TT.

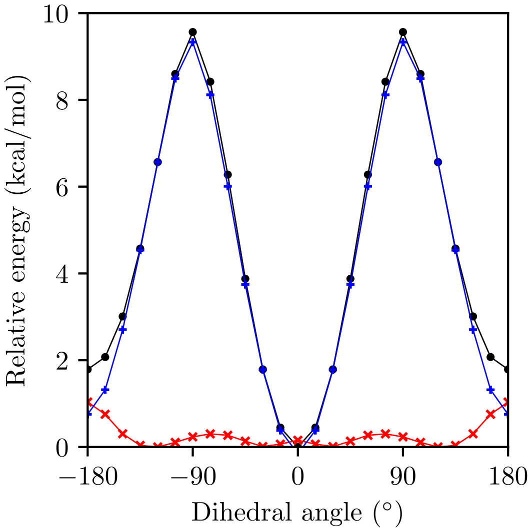

Figure A.14: Relative energy from *ab initio* scan (black), force fields scan (red) and their difference (blue) in DPP-T.

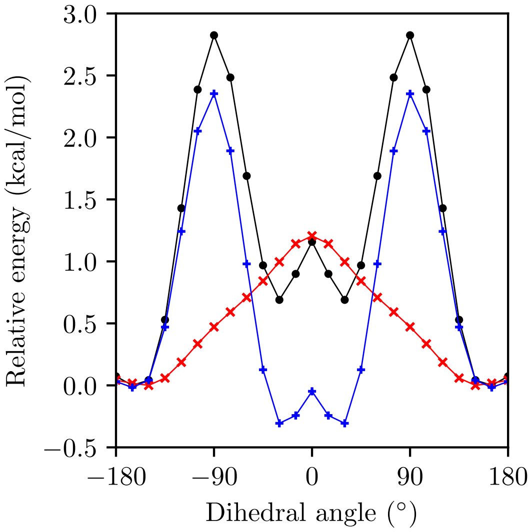

Figure A.15: Relative energy from *ab initio* scan (black), force fields scan (red) and their difference (blue) in TT-T.

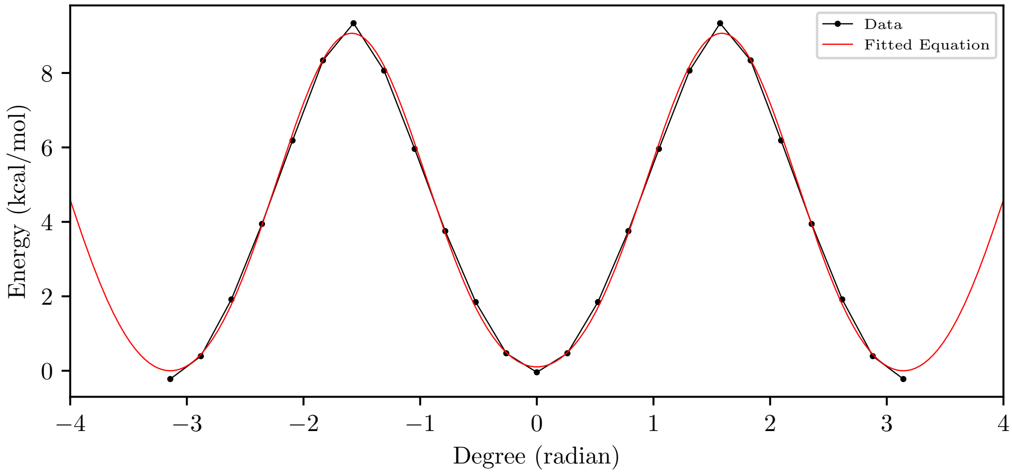

Figure A.16: An example of torsion fitting for DPP-TT torsion potential using a truncated cosine series

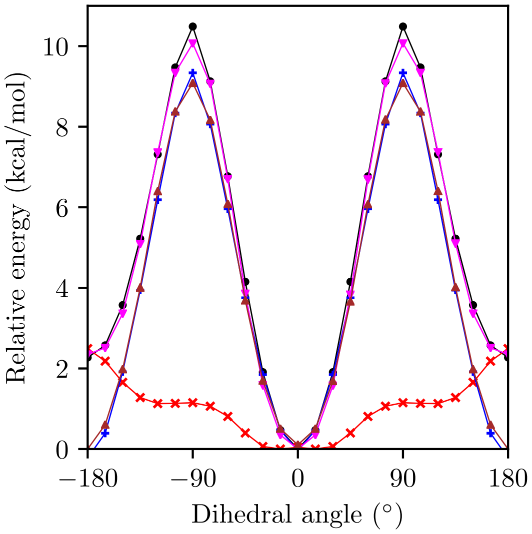

Figure A.17: Plots of torsional scan for the dihedral angle in DPP-TT. The energy is relative to the minimum energy. The black line is the *ab initio* scan, the red line is the force field scan, and the brown line is the torsion potential (the difference between *ab initio* and force field scans). The blue line is the fit of the torsion potential to a truncated cosine series and the purple line is the fitted torsion scan.

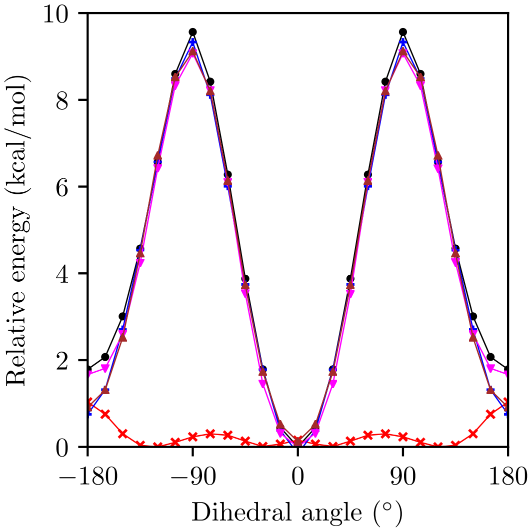

Figure A.18: Plots of torsional scan for the dihedral angle in DPP-T. The energy is relative to the minimum energy. The black line is the *ab initio* scan, the red line is the force field scan, and the brown line is the torsion potential (the difference between *ab initio* and force field scans). The blue line is the fit of the torsion potential to a truncated cosine series and the purple line is the fitted torsion scan.

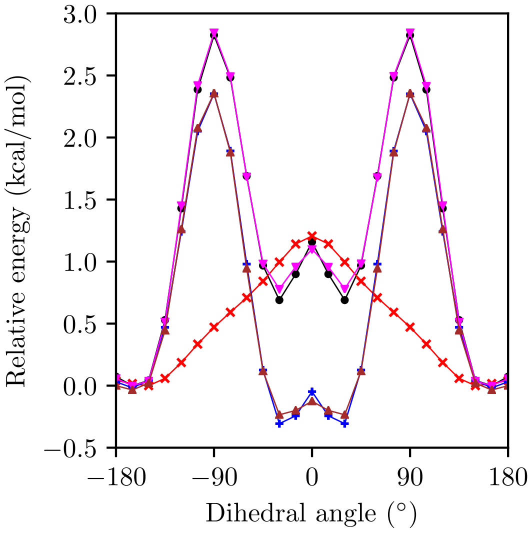

Figure A.19: Plots of torsional scan for the dihedral angle in TT-T. The energy is relative to the minimum energy. The black line is the *ab initio* scan, the red line is the force field scan, and the brown line is the torsion potential (the difference between *ab initio* and force field scans). The blue line is the fit of the torsion potential to a truncated cosine series and the purple line is the fitted torsion scan.

Molecules	Method	Force RMSD (kcal mol^{-1} $Å^{-1}$)	Energy RMSD (kcal mol^{-1})
DPP-TT	force field	7.34	2.49
	AM1	23.61	4.48
	HF/6-31G*	17.82	3.95
	B3LYP/3-21G*	7.03	2.26
DPP-T	force field	7.24	1.93
	AM1	22.72	4.64
	HF/6-31G*	17.76	3.60
	B3LYP/3-21G*	7.43	2.29
TT-T	force field	4.99	1.47
	AM1	17.62	3.01
	HF/6-31G*	13.53	2.91
	B3LYP/3-21G*	3.08	0.61

Table A.2: Force and energy RMSD between calculations at B3LYP/6-31G* levels and the optimised force field or other levels of theory, for 100 arbitrary geometries not used in the force field optimisation process

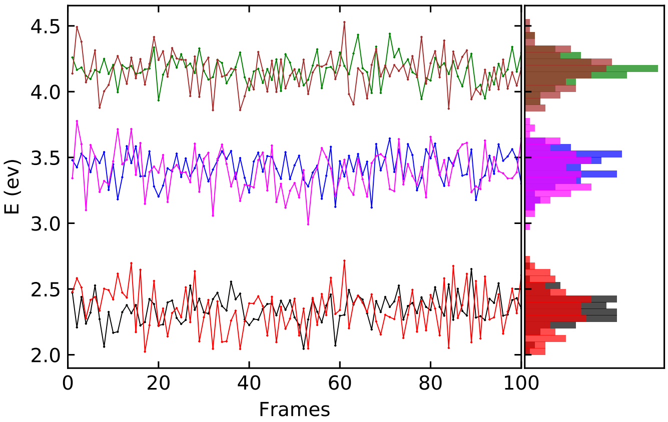

Figure A.20: Comparison of the transition energies of the lowest three excited states computed using trajectories from classical (black, blue and green) and *ab initio* (red, magenta and brown) MD simulations for chromophore DPP-T. All calculations are performed at the B3LYP/6-311G(d,p) level of theory. For greater legibility, the transition energies of the first and third excited states are offset by -0.5 eV and 0.5 eV, respectively.

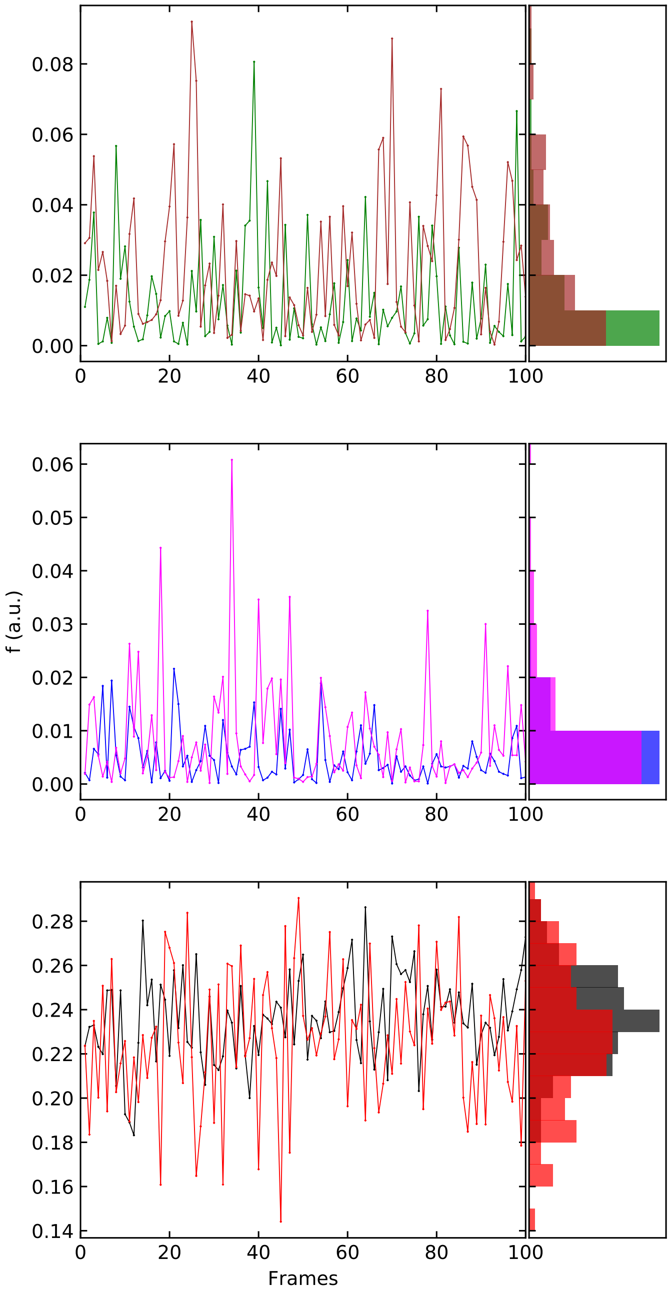

Figure A.21: Comparison of the oscillator strength (f) of the lowest three excited states computed using trajectories from classical (black, blue and green) and *ab initio* (red, magenta and brown) MD simulations for chromophore DPP-T. All calculations are performed at the B3LYP/6-311G(d,p) level of theory.

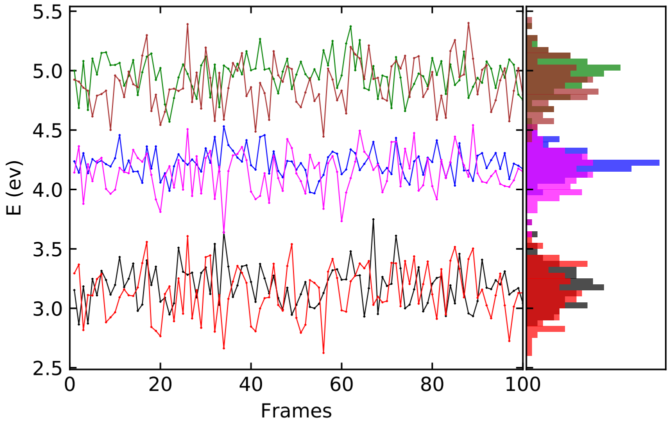

Figure A.22: Comparison of the transition energies of the lowest three excited states computed using trajectories from classical (black, blue and green) and *ab initio* (red, magenta and brown) MD simulations for chromophore TT-T. All calculations are performed at the B3LYP/6-311G(d,p) level of theory. For greater legibility, the transition energies of the first and third excited states are offset by -0.5 eV and 0.5 eV, respectively.

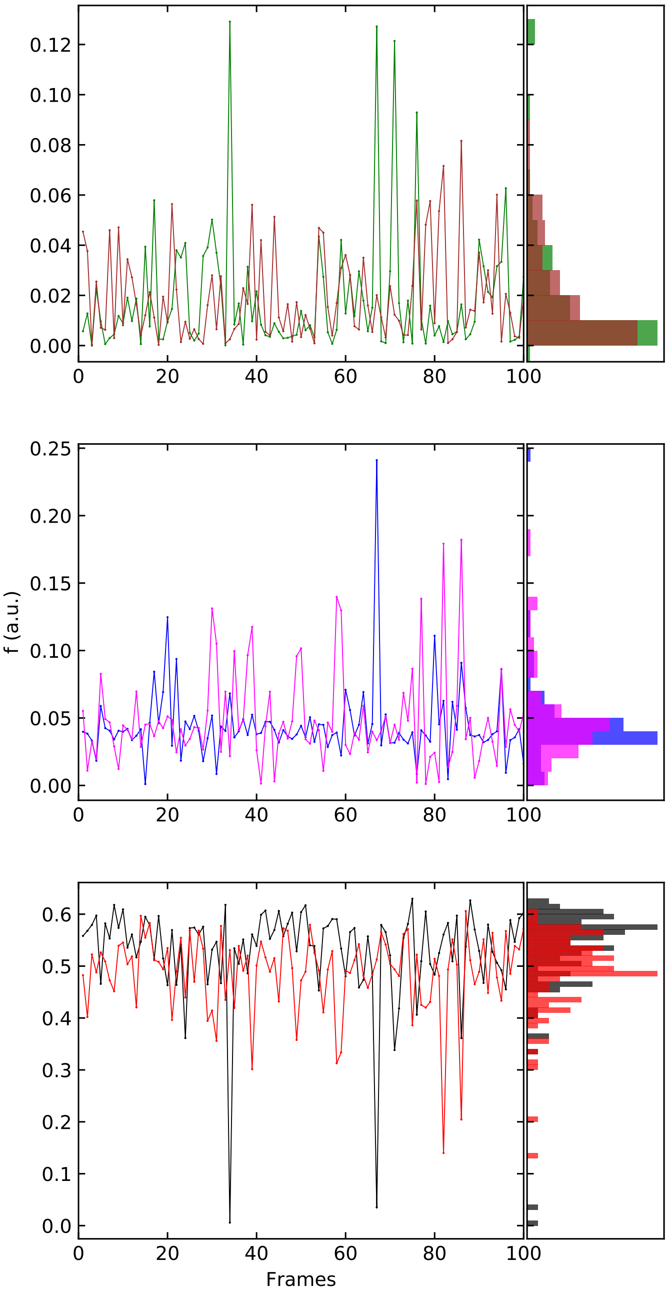

Figure A.23: Comparison of the oscillator strength (f) of the lowest three excited states computed using trajectories from classical (black, blue and green) and *ab initio* (red, magenta and brown) MD simulations for chromophore TT-T. All calculations are performed at the B3LYP/6-311G(d,p) level of theory.

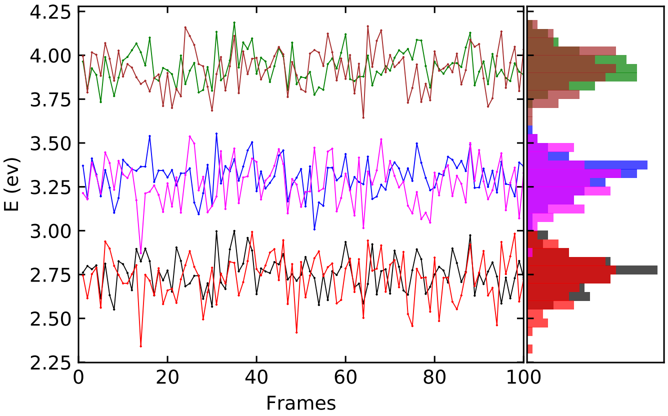

Figure A.24: Comparison of the transition energies of the lowest three excited states computed using trajectories from classical (black, blue and green) and *ab initio* (red, magenta and brown) MD simulations for chromophore DPP-TT. All calculations are performed at the B3LYP/6-311G(d,p) level of theory. For greater legibility, the transition energies of the third excited states are offset by 0.5 eV.

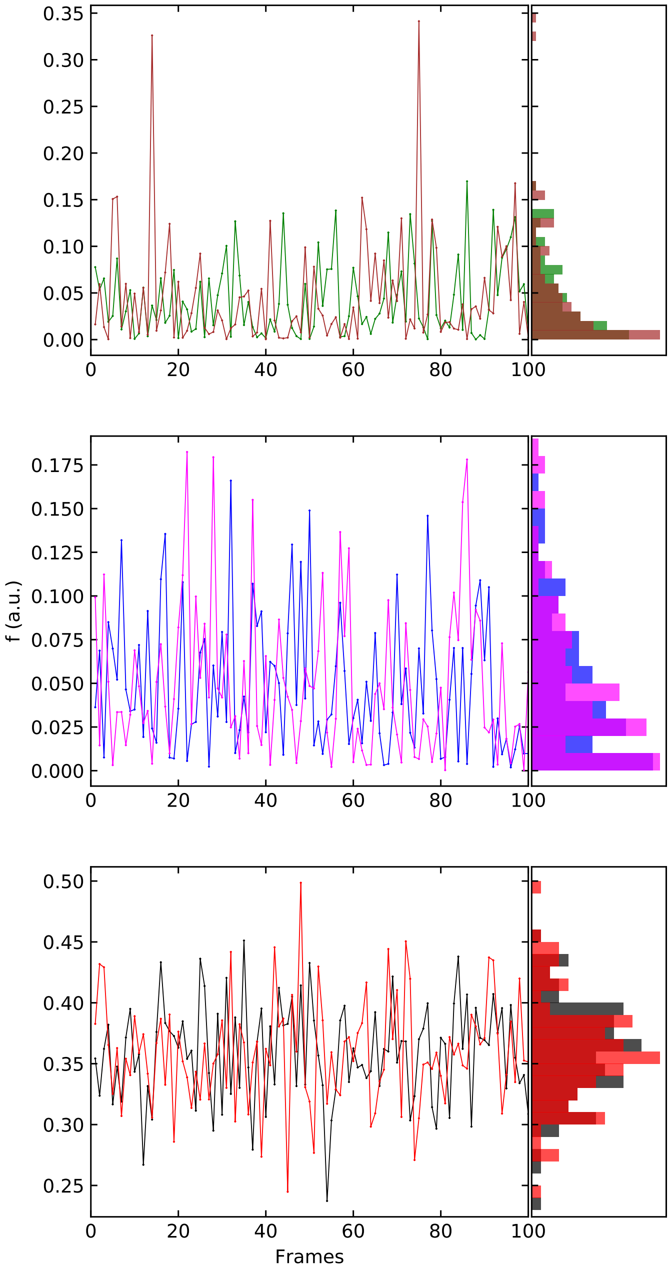

Figure A.25: Comparison of the oscillator strength (f) of the lowest three excited states computed using trajectories from classical (black, blue and green) and *ab initio* (red, magenta and brown) MD simulations for chromophore DPP-TT. All calculations are performed at the B3LYP/6-311G(d,p) level of theory.

A.4 Additional Properties of the Polymer and Molecular Crystal

The root mean squared displacement of the polymer (Figure A.26) allows us to characterise the molecular mobility. Here, the root mean squared displacement is used to quantify a comparison between the structures of the polymers with their initial amorphous structure (i.e. the starting amorphous structure is used as the reference structure). Figure A.26 shows that after ∼30 ns the system reaches equilibrium and the root mean squared displacement fluctuates at ∼6.5 Å. This indicates that the polymeric system undergoes a structural change under the studied conditions.

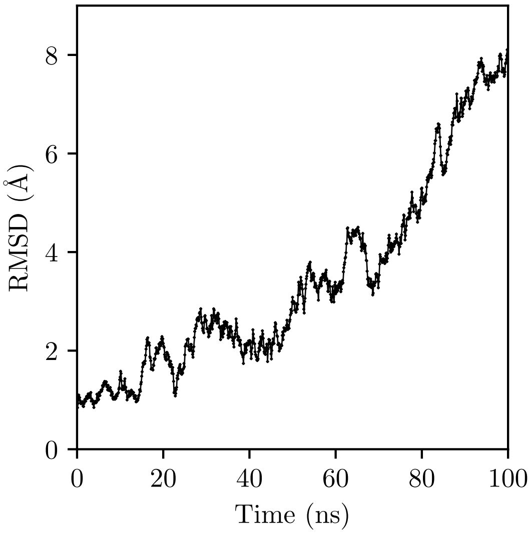

Figure A.26: Backbone root mean square deviation of the polymer.

The root mean squared displacement of UBEQOK molecular crystal is shown in Figure A.27. Since, the simulations are performed under ambient conditions, we can observe that the molecules do not move very far from the original crystal structure (∼0.9 Å) i.e. there is no melting and they vibrate about their lattice points.

We inspect the radius of gyration of the polymer under ambient conditions.

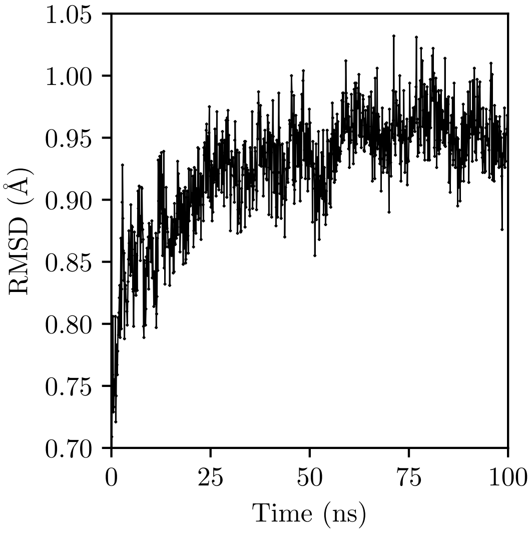

Figure A.27: Backbone root mean square displacement of the molecular crystal.

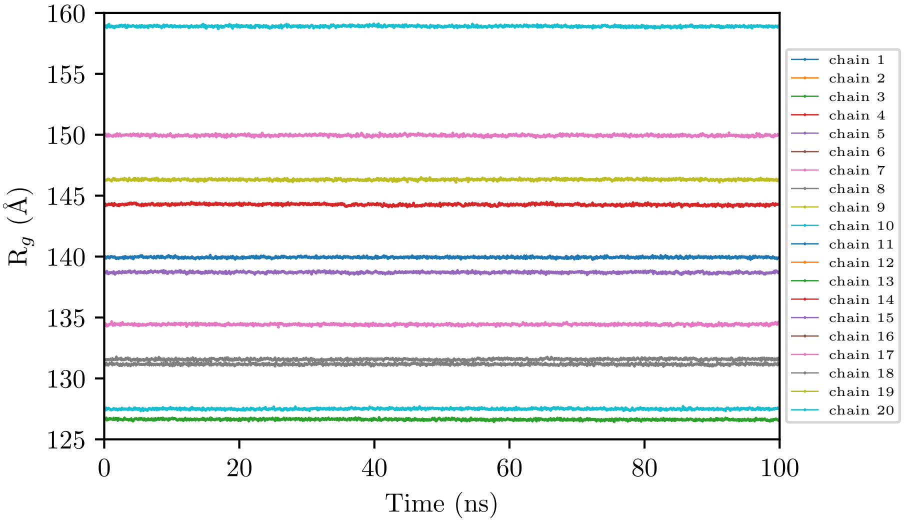

Figure A.28: Radius of gyration for the 20 individual chains of the 40-mer system at 300 K.

The range of gyration radii (Figure A.28) is between 125 to 160 Å, which indicates these chains are rather elongated. This property of the polymers very quickly reaches equilibrium and remains essentially unchanged during the course of the simulations at 300 K. This behaviour has been observed previously for other conducting polymers (Qin & Troisi 2013).

The velocity autocorrelation function (VAF) allows us to probe the dynamics of the system. For example, the intensity of the peaks in a power spectrum is inversely proportional to the reduced mass calculated from the velocity autocorrelation in an MD simulation (Thomas et al. 2013). This would also be useful in analyzing vibronic coupling (Loco & Cupellini 2019) and effective normal modes (Martinez et al. 2006). Figure A.29a shows the VAF for the amorphous PTPPTT-T polymer at 300 K. The plot is typical for a solid with negative correlations observed. However, the fluctuation of the VAF at equilibrium is rather small, which reflects the low density of the polymer.

The VAF of the UBEQOK molecules (Figure A.29b) compared to that of the

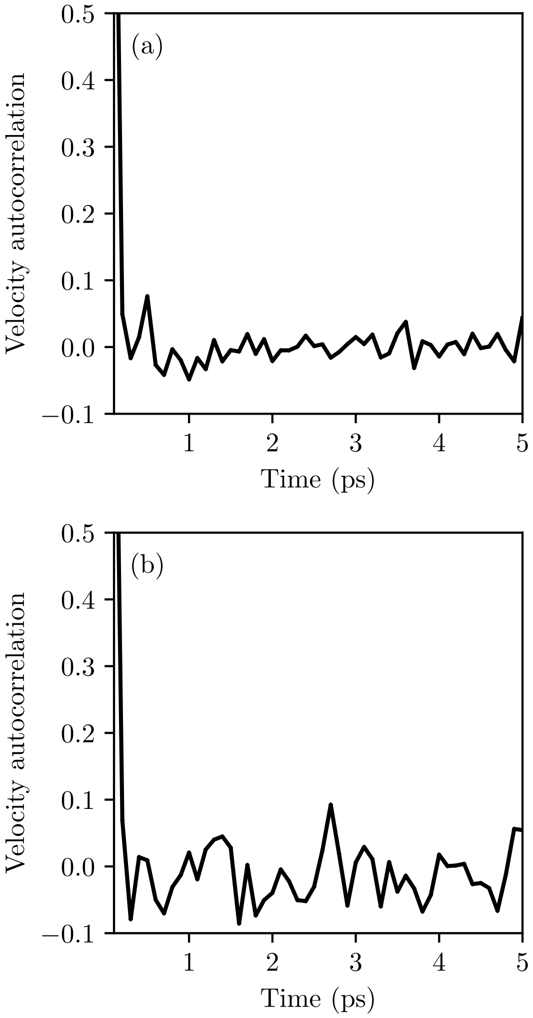

Figure A.29: Velocity autocorrelation function of (a) polymer taken from a 100 ns NVT simulation and (b) molecular crystal taken from a 100 ns NPT simulation.

amorphous PTPPTT-T polymer under the same conditions is more oscillatory. The oscillation here is due to the molecules in the crystal structure being confined to their lattice points (under the studied temperature). The molecules vibrate backwards and forwards, reversing their velocities (from positive to negative values and back again periodically). This is also in agreement with the root mean squared displacement.

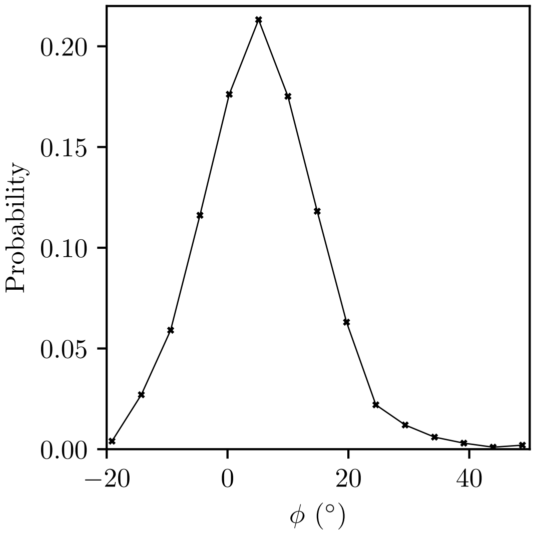

Figure A.30: Distribution of dihedrals of the molecular crystal during a 100 ns NPT simulation.

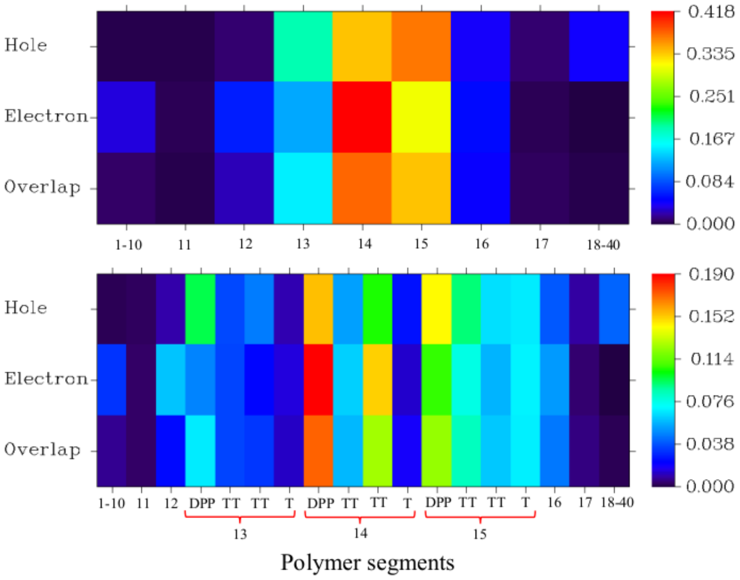

Figure A.31: Heat map of fragment contributions to hole and electron for the $S_0 \rightarrow S_2$ transition. The numeric ticks in the x-axis denote the monomer sequence while the letters indicate the chromophore within the monomers.

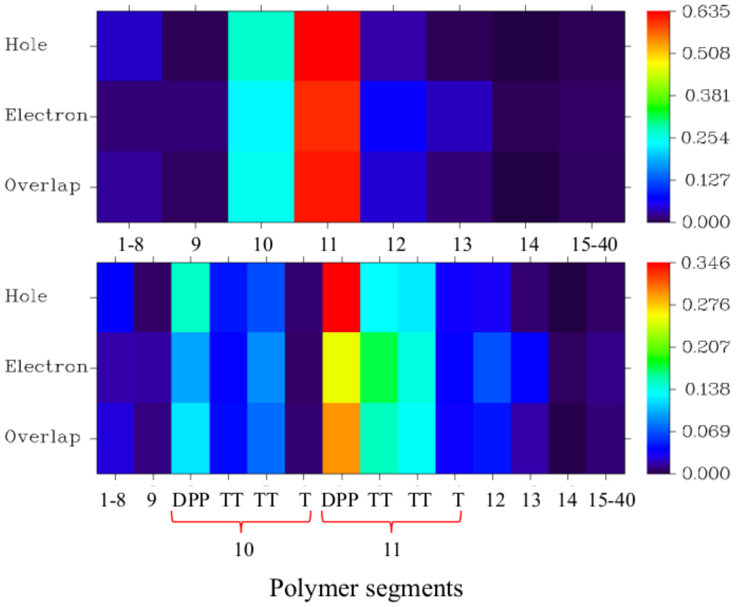

Figure A.32: Heat map of fragment contributions to hole and electron for the $S_0 \rightarrow S_3$ transition. The numeric ticks in the x-axis denote the monomer sequence while the letters indicate the chromophore within the monomers.

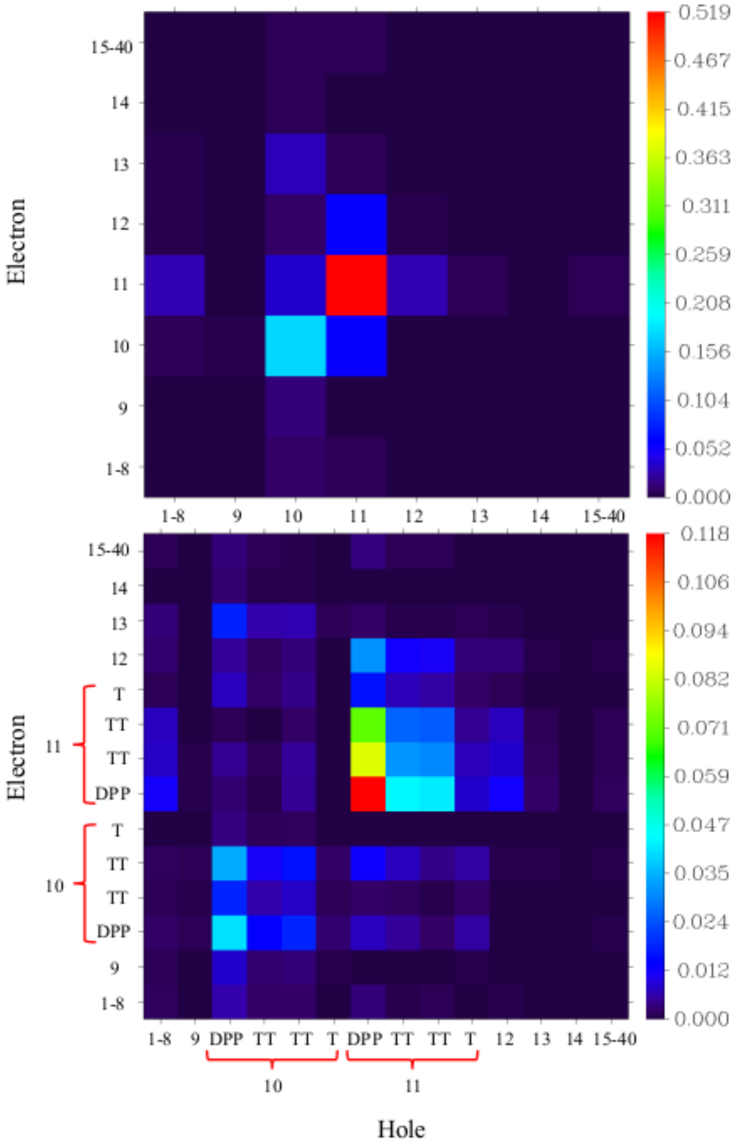

Figure A.33: Heat map of fragment transition density matrix for the $S_0 \rightarrow S_3$ transition. The numeric ticks in the x-axis denote the monomer sequence while the letters indicate the chromophore within the monomers.

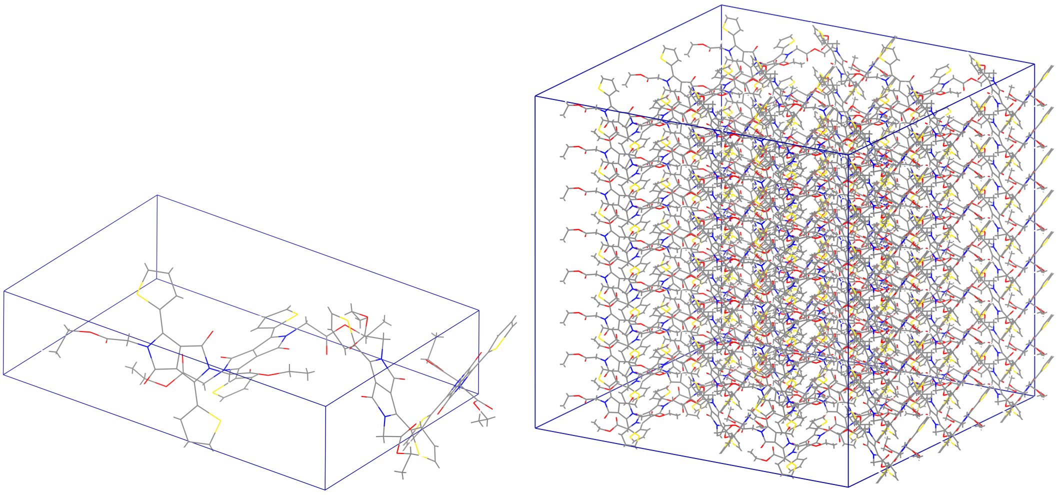
(a) (b)

Figure A.34: Initial structure of UBEQOK: (a) Unitcell (15.4 Å× 5.7 Å× 24.0 Å).(b) Supercell (46.0 Å× 45.5 Å× 48.0 Å).

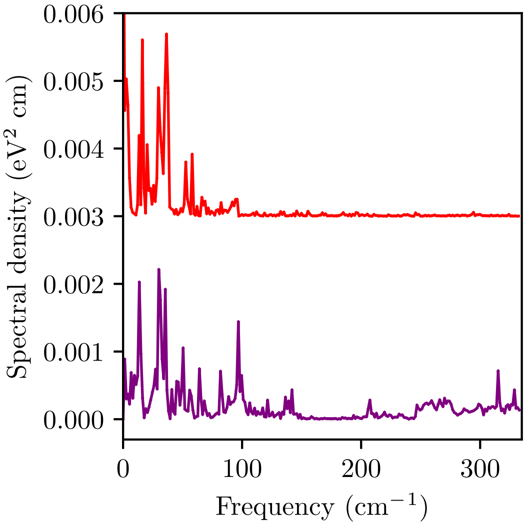

Figure A.35: Fourier transformation of the autocorrelation function of the negative excitonic couplings computed at 300 K for the dimers A (purple) and B (red). The spectral density for dimer B is shifted upward by 0.003 eV^2cm.

Appendix B

Chapter 4: Dynamic Disorder Drives Exciton Dynamics in Molecular Crystals

B.1 Chemical Names and Structures of Molecular Crystals

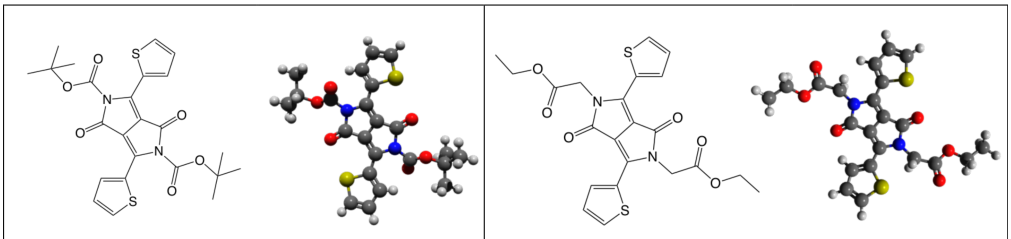

UBEQIE: di-t-butyl 1,4-dioxo-3,6-bis(2-thienyl)pyrrolo[3,4-c]pyrrole-2,5(1H,4H)-dicarboxylate

UBEQOK: diethyl 2,2'-(1,4-dioxo-3,6-bis(2-thienyl)pyrrolo[3,4-c]pyrrole-2,5(1H,4H)-diyl)diacetate

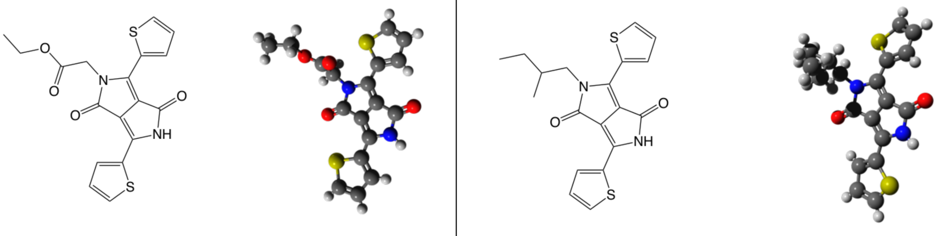

UBEQUQ: ethyl (1,4-dioxo-3,6-bis(2-thienyl)-4,5-dihydropyrrolo[3,4-c]pyrrol-2(1H)-yl)acetate

UBERAX: 2-(2-methylbutyl)-3,6-bis(2-thienyl)-2,5-dihydropyrrolo[3,4-c]pyrrole-1,4-dione

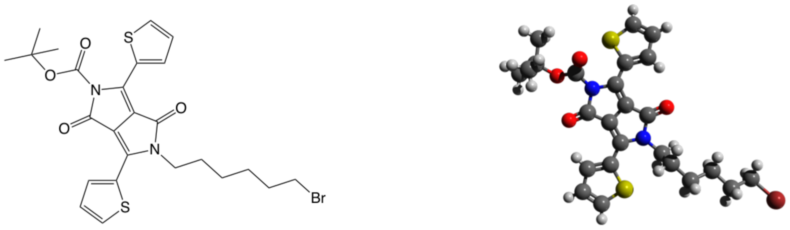

UBEREB: t-butyl 5-(6-bromohexyl)-1,4-dioxo-3,6-bis(2-thienyl)-4,5-dihydropyrrolo[3,4-c]pyrrole-2(1H)-carboxylate

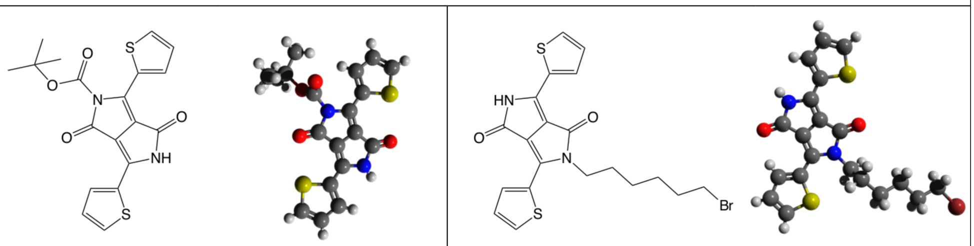

UBERIF: t-butyl 1,4-dioxo-3,6-bis(thiophen-2-yl)-4,5-dihydropyrrolo[3,4-c]pyrrole-2(1H)-carboxylate

UBEROL: 2-(6-bromohexyl)-3,6-bis(2-thienyl)-2,5-dihydropyrrolo[3,4-c]pyrrole-1,4-dione

Figure B.1: Chemical structures, Cambridge Structural Database codes and names of the studied molecular crystals.

B.2 Structure of the Supercell

An example of the supercell of the studied molecular crystals is shown in Figure B.2.

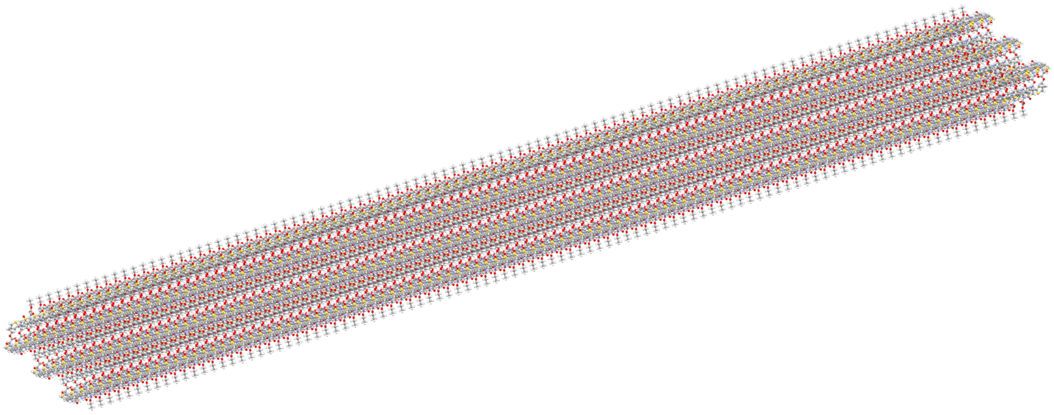

Figure B.2: A 3 × 100 × 1 supercell of UBEQUQ.

B.3 Orbital Localisation

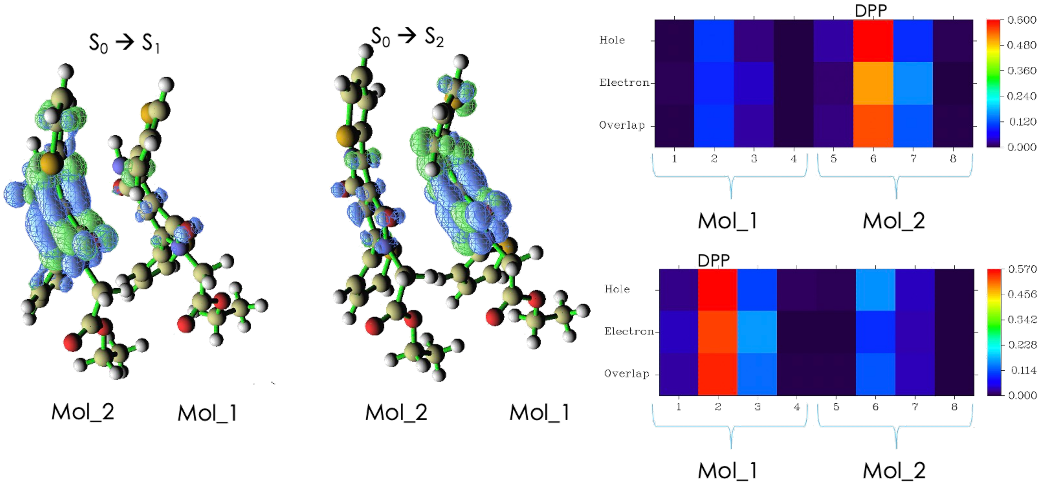

Figure B.3: Transformation of the canonical molecular orbitals to the localised form for the two lowest transition S_1 and S_2 of a UBEQUQ dimer in the parallel π-stacking. The nature of the lowest-energy excitations is Frenkel type. The exciton localised only the DPP segment, as depicted by the left panel's electron (green) and hole (blue) distributions. The right panel shows the distributions of the electrons, holes and their overlap as heat maps quantitatively.

B.4 Excitonic Coupling Calculations with Different Approaches

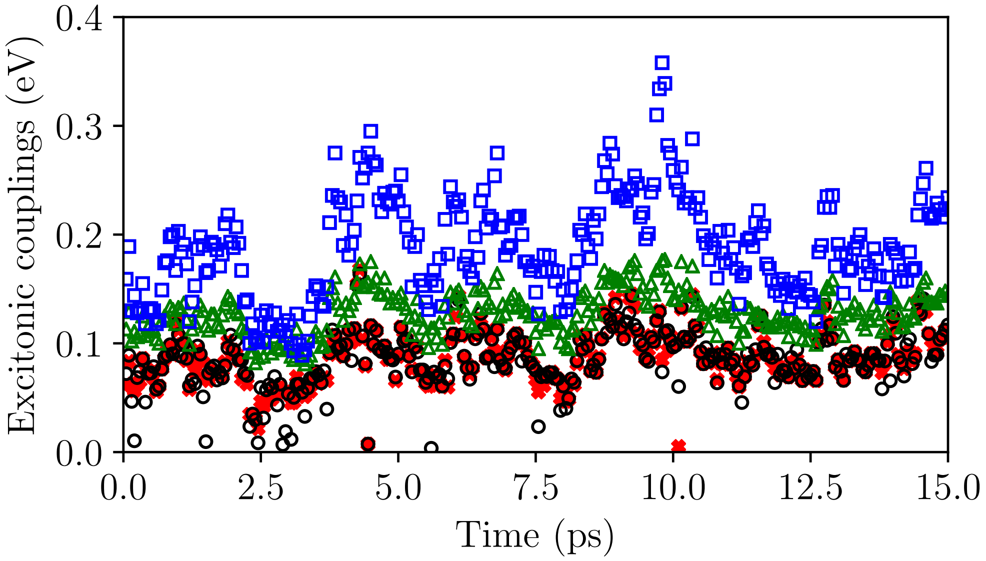

Figure B.4: Time evolution of the excitonic coupling for the parallel π-π stacking of UBEQUQ computed using point dipole approximation (blue squares), Coulomb approximation using ATC (green triangles), diabatisation scheme in conjunction with transition dipole moment (red crosses) and diabatisation scheme in conjunction with ATC (black circles).

B.5 Root Mean Square Displacement of the Nuclear Coordinates

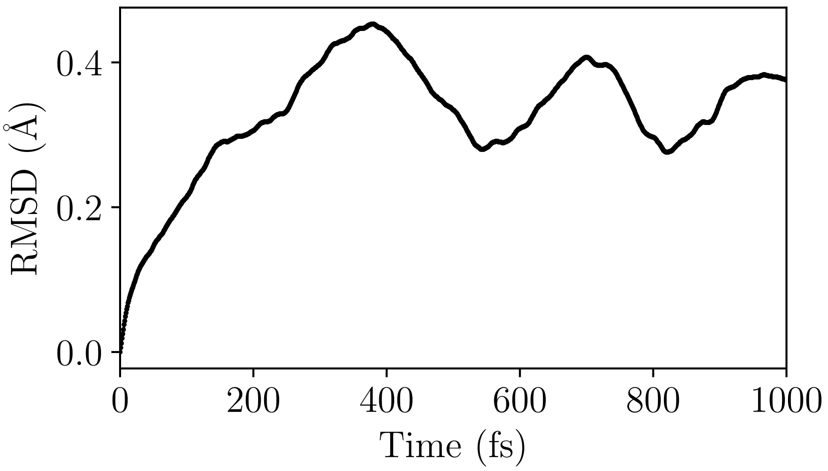

Figure B.5: Root mean square displacement of a molecule in the UBEQUQ molecular crystal.

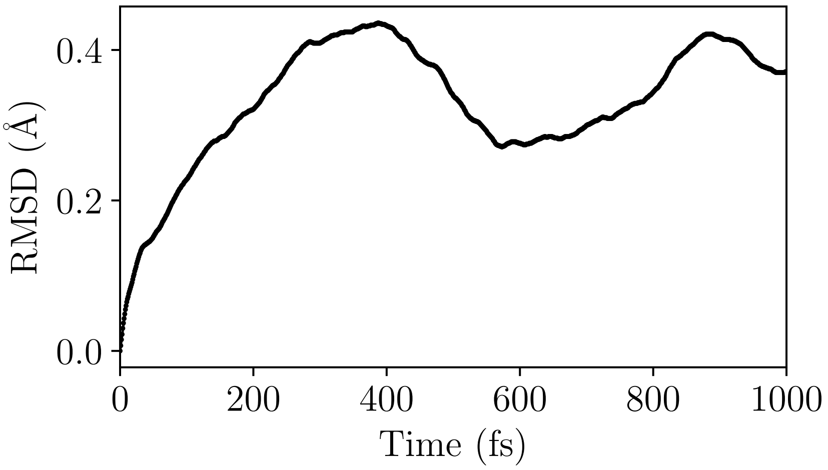

Figure B.6: Root mean square displacement of a molecule in the UBEQOK molecular crystal.

B.6 Fluctuation of the Excitonic Couplings

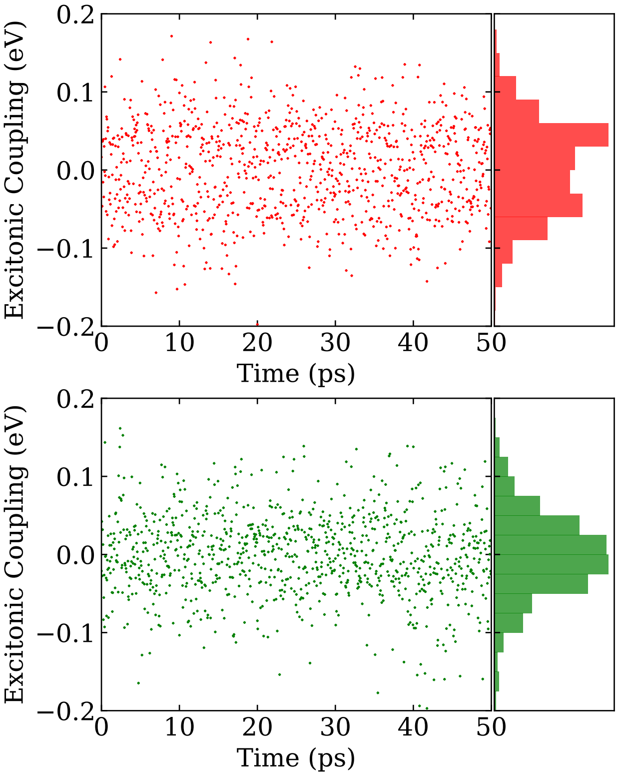

Figure B.7: Time evolution and distribution of the excitonic couplings of UBEQIE computed at 300 K for dimers A and B.

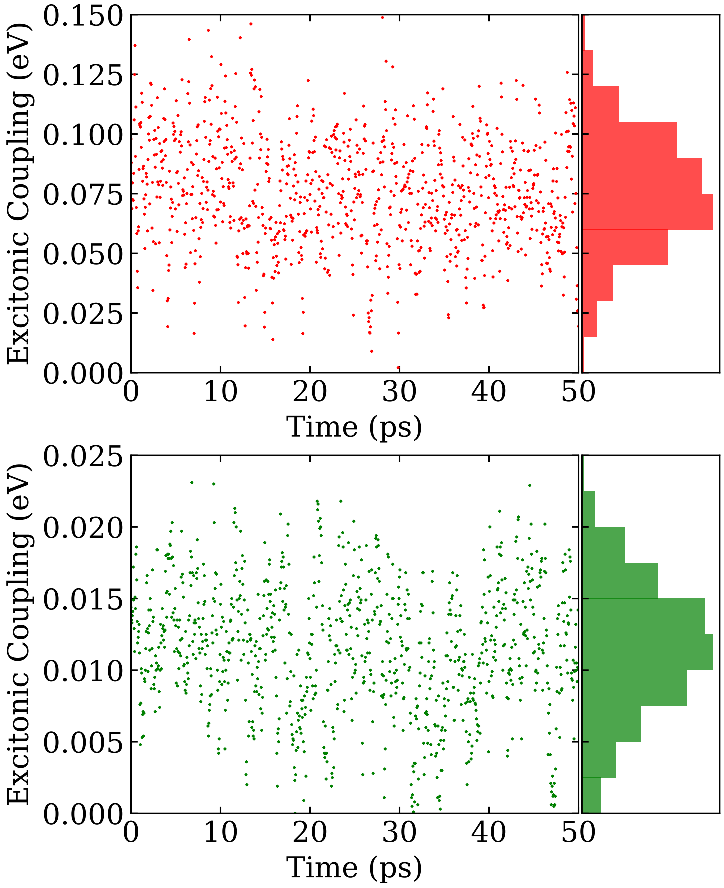

Figure B.8: Time evolution and distribution of the excitonic couplings of UBEQOK computed at 300 K for dimer A.

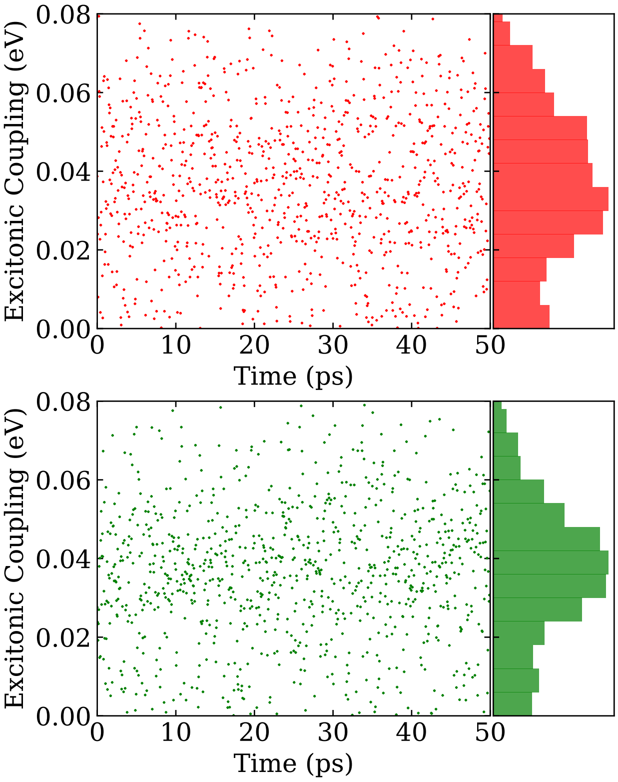

Figure B.9: Time evolution and distribution of the excitonic couplings of UBERAX computed at 300 K for dimers A and B.

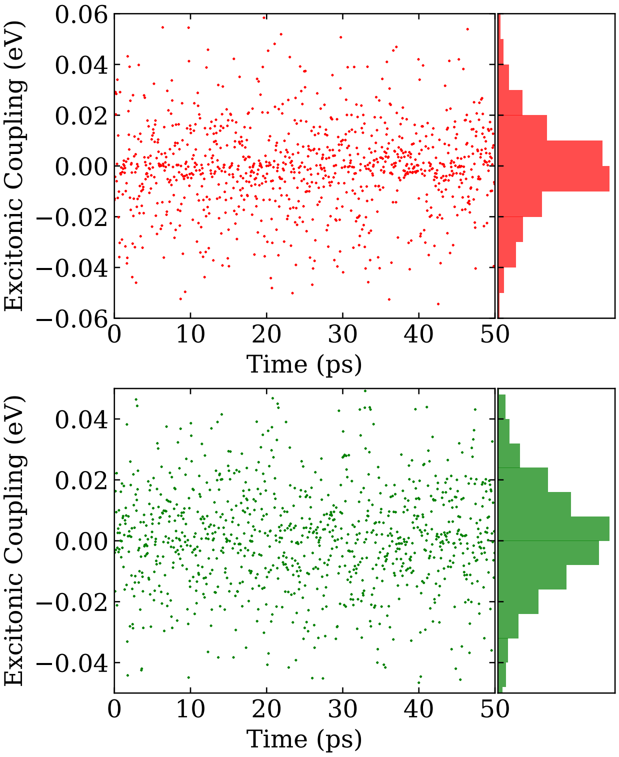

Figure B.10: Time evolution and distribution of the excitonic couplings of UBEREB computed at 300 K for dimers A and B.

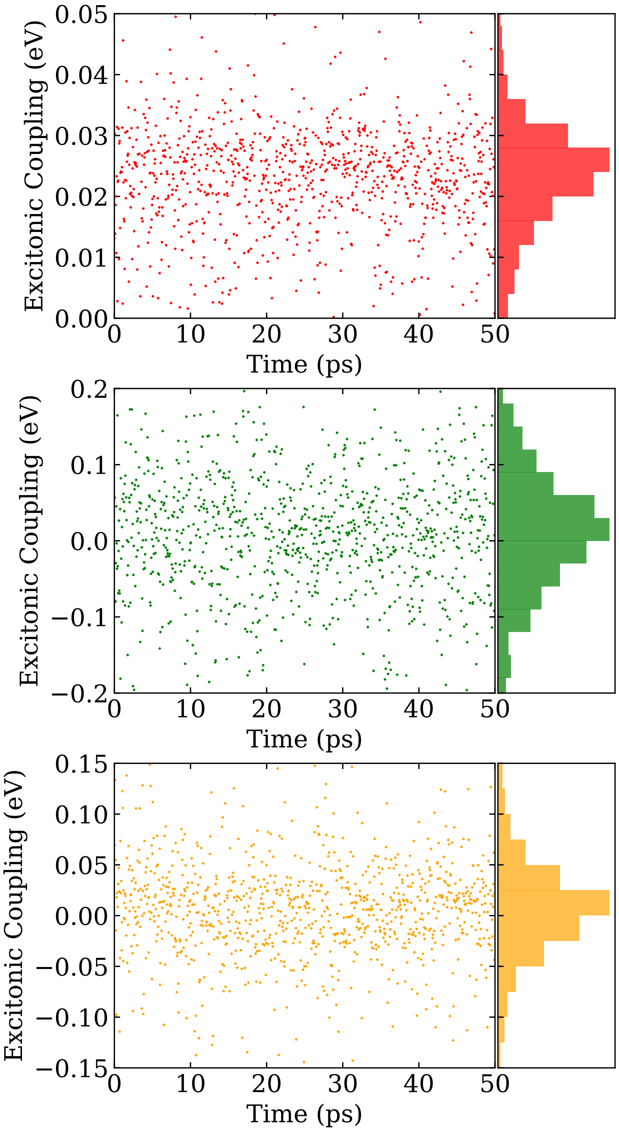

Figure B.11: Time evolution and distribution of the excitonic couplings of UBERIF computed at 300 K for dimers A, B and C.

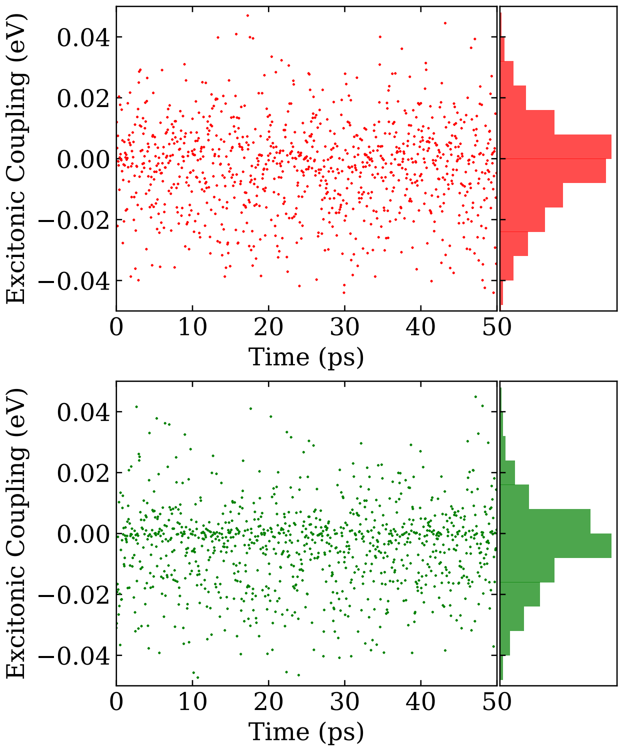

Figure B.12: Time evolution and distribution of the excitonic couplings of UBEROL computed at 300 K for dimers A and B.

B.7 Reorganisation Energy and Huang-Rhys Factor Calculations

For completeness, we describe the background theory relating to reorganisation energy and Huang-Rhys factors (Malagoli et al. 2004, Kwon et al. 2004) and give specific details as they pertain to the molecular systems of interest in our study.

B.7.1 Reorganisation Energy

An example of the potential energy surfaces of the ground state (S_0) and the first excited state (S_1) of any dimer involved in an excitation energy transfer process is demonstrated in Figure B.13. Here, the nuclear potentials are assumed to be harmonic. Each potential is parabolic, i.e., $V(Q) = \frac{1}{2}kQ^2$, where k is the force constant. We consider the lower potential energy surface is the ground state and the upper one is the first excited state of the two molecules in a dimer involved in the exciton transfer process. The x-axis Q represents the motion along a symmetric mode. ΔQ_0 is the relative displacement along normal mode 0 between the equilibrium positions of the two potentials.

In general, organic aggregates show a strong electron-phonon coupling which indicates their relative "softness" compared with inorganic materials. The phonons originate from the intramolecular vibrations. Some symmetric modes are typically related to the optical transitions. However, the strongest one is the high frequency vinyl stretching mode, ω_0, which causes a strong electron-vibration coupling shown in the vibronic progressions in Figure B.13. Generally, this is often observed in conjugated molecules in between 1200 and 1600 cm^{-1}. Another collection of modes at low frequency in the range of 100 to 200 cm^{-1} is also present due to the torsional motions of the molecules. However, these low frequency modes are usually neglected as they do not contribute sig-

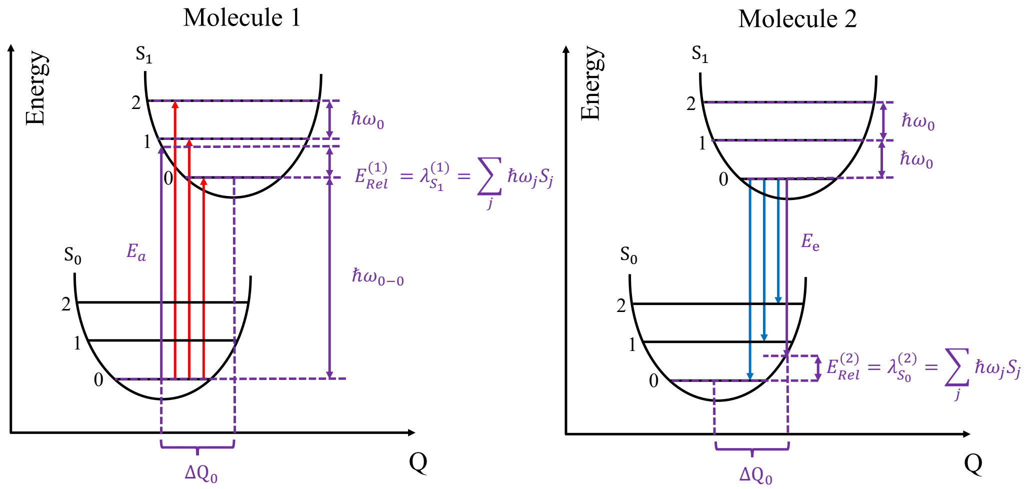

Figure B.13: A schematic presentation of the potential energy surfaces of the ground state S_0 and the first excited state S_1 for two molecules involved in an excitation energy transfer process. Several vibrational levels are shown. The red and blue arrows show typical excitation and de-excitation transition, respectively. $\lambda^{(1)}_{S_1}$ and $\lambda^{(2)}_{S_0}$ are the two contributions to the total reorganisation energy λ.

nificantly to the electron-phonon coupling. For convenience, the high frequency modes are often represented by a single effective mode (the vinyl stretching mode ω_0) and is is normally set to ~1400 cm^{-1} (~0.17 eV).

The red arrows in Figure B.13 show molecule 1 is electronically excited from the ground state (S_0) with zero vibrational quanta to different vibrational levels on the first excited state potential (S_1). The excitation energy, $\hbar\omega_{0-0}$, is the energy for a transition from the ground state surface (S_0) with zero vibrational quanta to the same vibrational energy level in the upper well. The purple arrow in the diagram of molecule 1 indicates the vertical excitation energy (E_a) from the minimum structure of the ground state surface (S_0) to the first excited state (S_1). After excitation, molecule 1 "reorganizes" its geometry instantly to relax to the minimum energy of the first excited state well (with zero vibrational quanta) and releases a relaxation energy ($E^{(1)}_{\text{rel}}$).

The blue arrows indicate that molecule 2 undergoes a relaxation from the first electronic excited state surface (S_1) (with zero vibrational quanta) to different vibrational levels on the ground state (S_0) surface. The purple arrow in the diagram of molecule 2 shows the "de-excitation" (E_e) from its optimised structure (in the zero vibrational level) on the first electronic excited state (S_1) to the ground state potential (S_0). After de-excitation, molecule 2 rapidly adjust its geometry to get to the equilibrium position on the ground state potential energy surface (and ground vibrational level). This process also releases a relaxation energy and is called ($E_{\text{rel}}^{(2)}$).

The intramolecular reorganisation energy (λ_{int}) has two relaxation parts. $\lambda_{S_1}^{(1)}$ is defined for the excited part, representing the geometry relaxation energies of molecule 1 going from the fully relaxed ground state (S_0) to the first electronic excited state (S_1). The de-excited part $\lambda_{S_0}^{(2)}$ is the relaxation energies of molecule 2 from the fully relaxed first excited state (S_1) to the ground state (S_0). The following three equations summarise the reorganisation processes for molecule 1 (M1) on surface S_1 and molecule 2 (M2) on surface S_0:

$$\lambda \approx \lambda_{\text{int}} = \lambda_{S_1}^{(1)} + \lambda_{S_0}^{(2)} \approx 2\lambda_{S_1}^{(1)} \approx 2\lambda_{S_0}^{(2)} \tag{B.1}$$

$$\lambda_{S_1}^{(1)} = E^{(S_1)}(\text{M1}) - E^{(S_1)}(\text{M1}^*) \tag{B.2}$$

$$\lambda_{S_0}^{(2)} = E^{(S_0)}(\text{M2}^*) - E^{(S_0)}(\text{M2}) \tag{B.3}$$

Here, the intramolecular reorganisation energy for the exciton transfer process is approximately $2\lambda_{S_1}^{(1)}$ or $2\lambda_{S_0}^{(2)}$ (Eq. B.1), as the magnitudes of $\lambda_{S_1}^{(1)}$ and $\lambda_{S_0}^{(2)}$ are more or less the same (due to energy conservation). $E^{(S_1)}(\text{M1})$ is the vertical excitation energy E_a of M1 and $E^{(S_1)}(\text{M1}^*)$ is the optimised energy of M1 in its first excited state (i.e. on the S_1 potential). $E^{(S_0)}(\text{M2}^*)$ is the energy released when molecule M2 transits from its optimised structure on its S_1 surface to the same vibrational level on the S_0 curve and $E^{S_0}(M2)$ is the optimised energy of M2 in its ground state.

In this work, the reorganisation energies are computed for all the studied molecular crystals at the ωB97XD/6-31G** level of theory. To find the reorganisation energy on the S_1 potential ($\lambda^{(1)}_{S_1}$), molecule 1 is first optimised in its ground electronic state S_0, followed by a vertical excitation to the first excited state (S_1) to obtain the vertical excitation energy $E^{(S_1)}(M1)$. After that, $E^{(S_1)}(M1^*)$ is calculated by optimise the geometry of M1 in its first excited state S_1. On the other hand, to compute $\lambda^{(2)}_{S_0}$, we first optimise molecule 2 in its excited state S_1 to get the optimised geometry $M2^*$, which is then utilised to perform a single point energy calculation on the S_0 potential to obtain $E^{(S_0)}$ $(M2^*)$. Finally, we relax this geometry on the S_0 potential energy surface of M2 to get the minimum energy $E^{S_0}(M2)$. The reorganisation energies for all studied molecular crystals are summarised in Table B.1.

Molecular Crystal	$\lambda^{(1)}_{S_1}$ (eV)	$\lambda^{(2)}_{S_0}$ (eV)
UBEQOK	0.183	0.174
UBEQUQ	0.188	0.178

Table B.1: Calculated reorganisation energies for the studied molecular crystals at the ωB97XD/6-31G** level of theory.

B.7.2 Huang-Rhys Factor

The Huang-Rhys factor (S_j) is a unitless number representing the relative shift between two potentials (e.g. S_0 and S_1), typically ranging from 0.6 to 1.2 for molecular aggregates. The reorganisation energy can also be defined in terms of the Huang-Rhys factor and the vibrational modes as:

$$\lambda^{(1)}_{S_1} = \lambda^{(2)}_{S_0} = \sum_j \lambda_j = \sum_j \hbar\omega_j S_j \tag{B.4}$$

where

$$\lambda_j = \frac{k_j}{2}\Delta Q_j^2 \tag{B.5}$$

and

$$S_j = \frac{\lambda_j}{\hbar\omega_j} \tag{B.6}$$

where j is the index of a normal mode, λ_j is the reorganisation energy contributed by the normal mode j, ω_j is the vibrational frequency, S_j is the Huang-Rhys factor, k_j is the force constants, and ΔQ_j is the displacement along the normal mode j between the equilibrium positions of the two electronic states of interest. Equation B.4 defines the reorganisation energy in terms of the Huang-Rhys factors and the vibrational frequencies of all normal modes j. On the other hand, Equation B.5 shows that the reorganisation energy contributed by each normal mode j can be calculated by the force constant of each vibrational normal mode j and the displacement along the normal mode. Finally, equation B.6 represents the corresponding Huang-Rhys factors in terms the ratio of the relaxation energy λ_j and the vibrational energy $\hbar\omega_j$.

The numerical procedure to compute the Huang-Rhys factor consists of three steps: (i) determine the normal-mode coordinates and the force constants, (ii) project the displacements onto the normal-mode vectors to obtain the normal mode displacements $\Delta Q_{1(2)}$, and (iii) obtain the reorganisation energy and the Huang-Rhys factors by substituting the calculated quantities in steps (i) and (ii) into Equation B.5 and B.6. The normal modes of the ground and the first excited states, Q_1 and Q_2 are related by a transformation consisting of multidimensional rotation and translation,

$$Q_1 = \mathbf{J}Q_2 + \Delta Q \tag{B.7}$$

where **J** is the Duschinsky matrix describing the mixing of the normal coordinates of the two states. For each molecular crystal, the ground and the first excited state geometry optimsation processes are performed using the ωB97XD functional and the 6-31G** basis set. Other electronic structure properties are also computed at the same level of theory. The transformation of the normal mode coordinates (Eq. B.7) is obtained by using the Duschin program (Reimers 2001). The output from this code contains the normal mode displacements, the Duschinsky matrix and the contributions to displacement and also the reorganisation energy in each normal mode.

In general, the total reorganisation energy (λ) for an excitation energy transfer includes both a classical (λ_{c}) and a quantum (λ_{q}) contributions. The quantum reorganisation energy (λ_{q}) can be associated with a single effective normal mode by

$$\lambda^{(1)}_{\mathrm{S}_{1,\mathrm{q}}} = S^{\mathrm{eff}}\hbar\omega^{\mathrm{eff}} \tag{B.8}$$

where $\hbar\omega^{\mathrm{eff}}$ is often set to coincide with that of the mode with the highest Huang-Rhys factor.

Figures B.14 and B.15 show that the contributions to the total reorganisation energies for both the $\mathrm{S}_0 \rightarrow \mathrm{S}_1$ and $\mathrm{S}_1 \rightarrow \mathrm{S}_0$ transitions for UBEQUQ are mainly from those high-frequency modes that are concentrated around 1500 cm^{-1}. This is in agreement with what is commonly observed for conjugated systems, in which the high-frequency modes are attributed to the vinyl stretching mode (between 1200 and 1600 $\mathrm{cm}^{-}1$).

Figure B.16 shows the Huang-Rhys factors computed at the ωB97XD/6-31G** level of theory for an isolated UBEQUQ molecule. The contribution to the reorganisation energy $\lambda^{(2)}_{S_0}$ of the three high-frequency normal modes with the

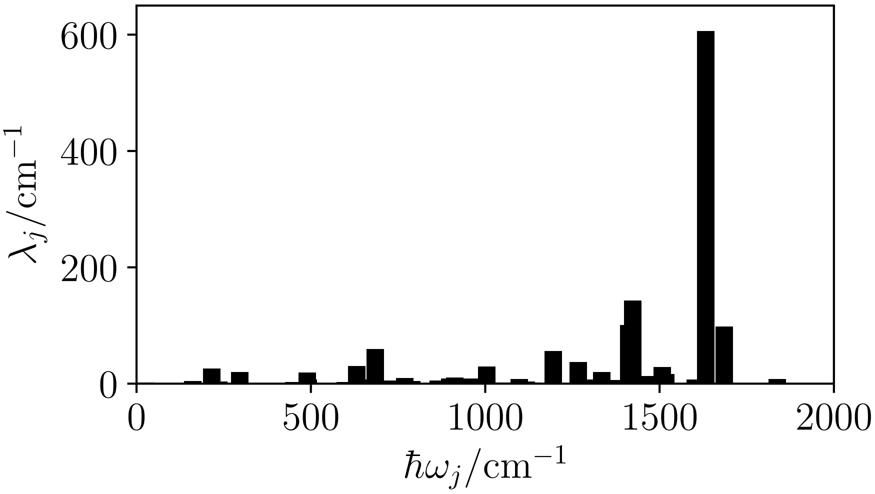

Figure B.14: Contribution of the individual reorganisation energies (from different vibrational states) to the total reorganisation energy ($\lambda_{S_1}^{(1)}$) for the S_0 → S_1 transition for UBEQUQ.

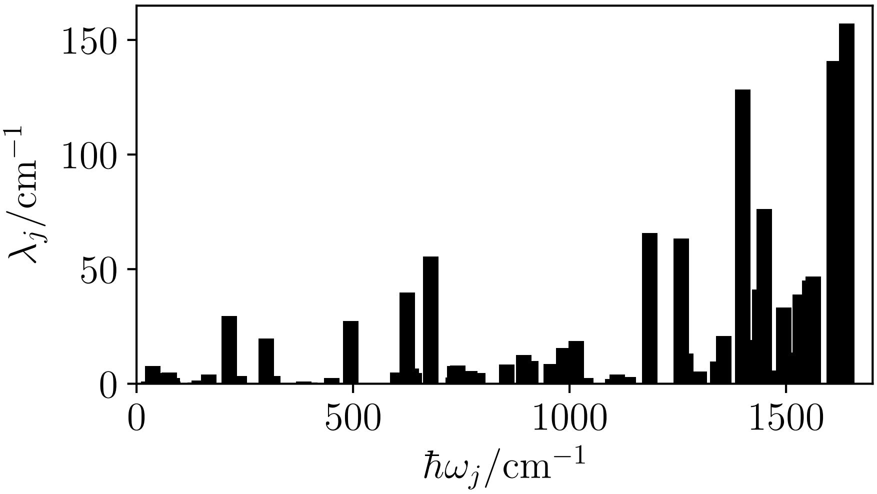

Figure B.15: Contribution of the individual reorganisation energies (from different vibrational states) to the total reorganisation energy ($\lambda_{S_0}^{(2)}$) for the S_1 → S_0 transition for UBEQUQ.

strongest Huang-Rhys factors (modes at 1632, 1423 and 1412 cm^{-1}) is included as a quantum contribution, which represents 56% of $\lambda_{S_1}^{(1)}$. This quantum reorganisation energy can be associated with a single effective normal mode as shown in Equation B.8. $\hbar\omega^{eff}$ is set to coincide with that of the mode with the highest S_j value (i.e. S_j = 1632 cm^{-1}) and the effective Huang-Rhys factor can be calculated as

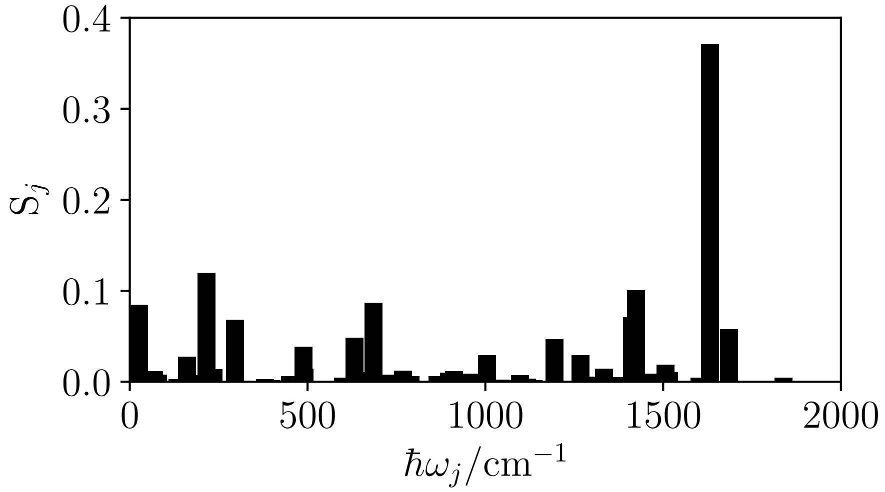

Figure B.16: Huang-Rhys factor as a function of the normal modes for the $S_0 \rightarrow S_1$ transition for UBEQUQ.

$$S^{\mathrm{eff}} = \frac{\lambda^{(1)}_{S_{1,q}}}{\hbar\omega^{\mathrm{eff}}} = \frac{0.188\mathrm{eV}}{1632\ \mathrm{cm}^{-1}} = \frac{1513\ \mathrm{cm}^{-1}}{1632\ \mathrm{cm}^{-1}} = 0.927 \tag{B.9}$$

The remaining contribution to $\lambda^{(1)}_{S_1}$ is included as a classical contribution $\lambda^{(1)}_{S_{1,c}}$. The total reorganisation energy for the exciton transfer process is approximately $2\lambda^{(1)}_{S_1}$. Therefore, the total quantum λ_q and classical λ_c contributions for UBEQUQ are $2\lambda^{(1)}_{S_{1,q}}$ (0.212 eV) and $2\lambda^{(1)}_{S_{1,c}}$ (0.164 eV), respectively.

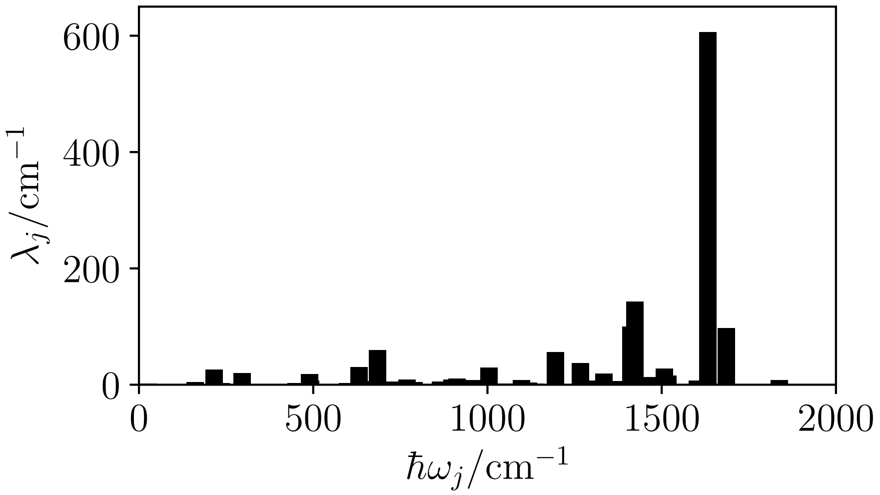

Figure B.17: Contribution of the individual reorganisation energies (from different vibrational states) to the total reorganisation energy ($\lambda^{(1)}_{S_0}$) for the $S_0 \rightarrow S_1$ transition for UBEQOK.

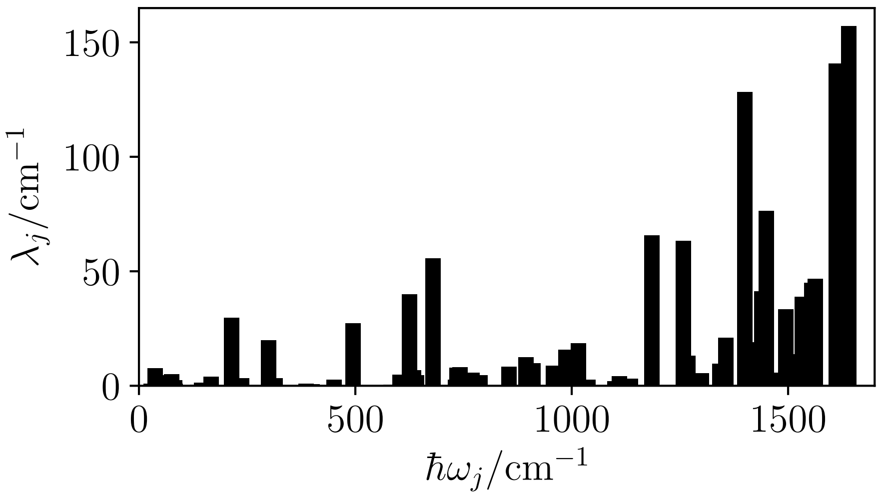

Figure B.18: Contribution of the individual reorganisation energies (from different vibrational states) to the total reorganisation energy ($\lambda_{S_0}^{(2)}$) for the S_1 → S_0 transition for UBEQOK.

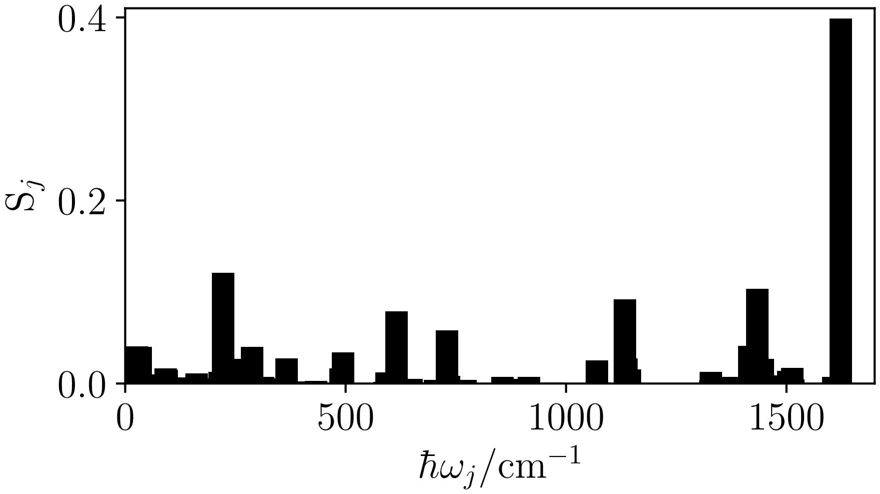

Figure B.19: Huang-Rhys factor as a function of the normal modes for the S_0 → S_1 transition for UBEQOK.

B.8 Exciton Dynamics

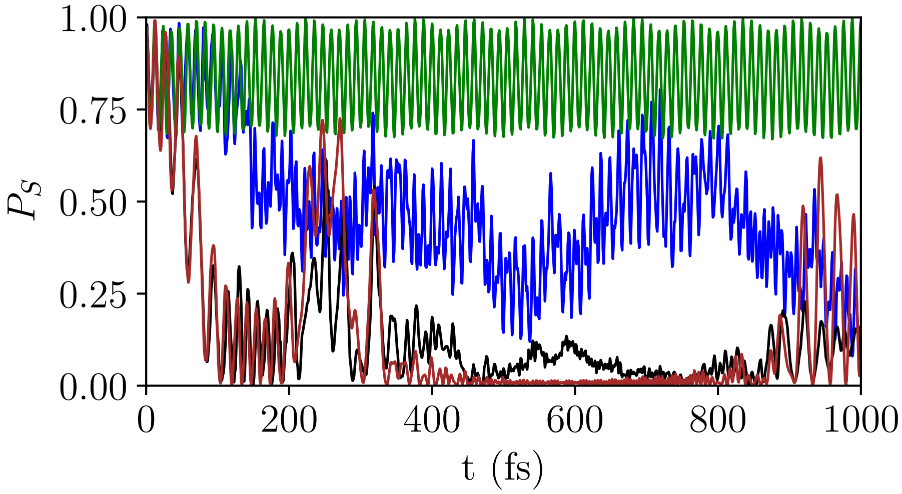

Figure B.20: Survival probability P_S of the initial state of UBEQOK in the case of the time-dependent Hamiltonian $H(t)$ (black solid line), static Hamiltonian H_1 (green solid line), constant coupling J (brown solid line) and constant nuclear displacement (blue solid line).

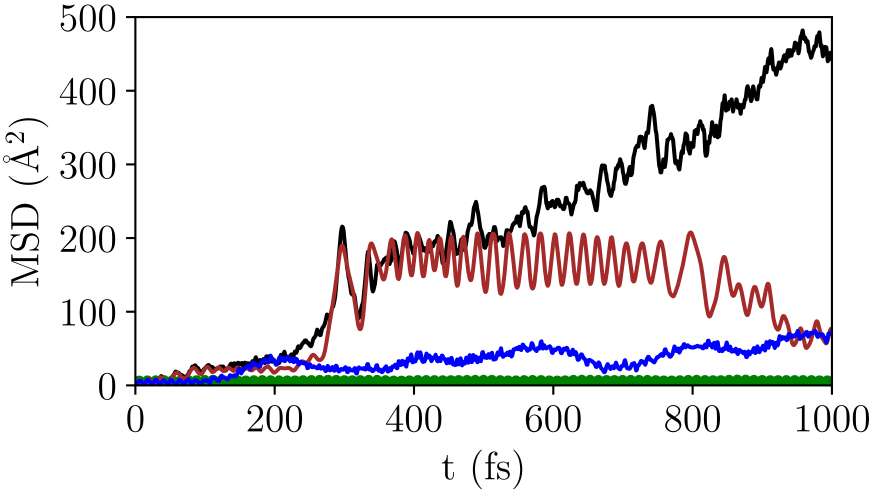

Figure B.21: Time evolution of the mean-square-displacement of the centre of the exciton of UBEQOK in four different cases: time-dependent Hamiltonian $H(t)$ (black solid line), static Hamiltonian H_1 (green solid line), constant coupling J (brown solid line) and constant nuclear displacement (blue solid line).

Appendix C

Chapter 5: Structure-Property Relationships in Amorphous Polymers

C.1 Force Field Development Procedure

For the chromophores, the initial “guessed” parameters are taken from the optimised parameters of DPP, TT, T, DPP-TT, DPP-T and TT-T in our previous work (Jiang et al. 2020). For the side chains, we use parameters from the OPLS force field (Dodda et al. 2017) and keep these fixed during the optimisation scheme, i.e. we only optimise the parameters for the chromophores and utilise the OPLS parameters for the side chains. We follow the same procedures as our previous work (Jiang et al. 2020) to obtain a new set of optimised parameters for DPP, TT, T, DPP-TT, DPP-T and TT-T at the ωB97XD/6-31G* level of theory, as this is the target functional used in subsequent quantum chemical calculations. Previously, these parameters were optimised at the B3LYP/6-31G* level of theory. Finally, we further optimise the whole monomer, including the side chains, to obtain better sets of parameters. By construction, the new parameters are capable of reproducing the potential energy surface of the targeted level of quantum chemical theory, i.e., ωB97XD/6-31G* (Jiang et al. 2020).

C.2 Molecular Dynamics Simulation Details

For both models, the system energies are first minimised using 100000 steepest descent steps followed by 10 ns initial equilibration at 1000 K. They are then slowly cooled down to 300 K using simulated annealing in 100 ns. After that, the NPT ensemble at 300 K and 1 atm is employed for over 2 μs to equilibriate the system. Finally, a further 200 ns is simulated in the NVT ensemble for calculating ensemble average properties. The Langevin thermostat (Hoover et al. 1982) with a damping coefficient equal to 1 ps^{-1} is employed to keep the temperature constant. The period and decay parameters of the Langevin piston are set to 100 and 50 fs, respectively, to maintain the pressure. A time step of 1 fs for integration of the equations of motion is used throughout the simulations. A cutoff of 12 Å is used for nonbonded interactions. The particle mesh Ewald algorithm (Herce et al. 2007) is used to calculate long-range electrostatic interactions.

C.3 P_k^m - The Weight of the Molecular Orbital m on a Given Monomer k

To partition the molecular density, $\rho_{\text{mol}}(\mathbf{r})$, into atomic contributions, we can define a weight function, $w_A(\mathbf{r})$, for every atom A in the molecule. The atomic density is then defined as $\rho_A(\mathbf{r}) = w_A(\mathbf{r})\rho_{\text{mol}}(\mathbf{r})$. The weight functions must satisfy the condition, $\sum_{A=1}^{N} w_A(\mathbf{r}) = 1, \forall \mathbf{r} \in \mathbf{R}^3$, where N is the number of atoms, to guarantee that the sum of the atomic densities gives back the molecular density. It is common practice to introduce for each atom a so-called pro-atomic function, $\rho_A^{\text{pro}}(\mathbf{r})$, as an auxiliary tool to define the actual weight functions. The weight functions are derived from the pro-atomic functions as $w_A(\mathbf{r}) = \rho_A^{\text{pro}}(\mathbf{r}) / \sum_{B=1}^{N} \rho_B^{\text{pro}}(\mathbf{r})$. We employ the Hirshfeld partitioning scheme (Hirshfeld 1977) to compute the atomic weight functions $w_A(\mathbf{r})$. In this approach, the pro-atomic densities are derived from computations on neutral atoms by simply averaging the atomic density ρ_A^{atom} over the angular degrees of freedom as $\rho_A^{\text{pro}}(|\mathbf{r} - \mathbf{r}_A|) = \rho_A^{\text{pro}}(r) = \int \rho_A^{\text{atom}}(r, \Omega)\mathrm{d}\Omega$, where Ω represents the angular degrees of freedom. Thus, the composition of an atom A in the molecular orbital m is defined as $\int \phi_m^2(\mathbf{r}) w_A(\mathbf{r})\mathrm{d}\mathbf{r}$, where $\phi_m(\mathbf{r})$ is the electron density in molecular orbital m. Finally, the weight of the molecular orbital m on a given monomer k, P_k^m, is simply the sum of the contributions of the atoms that belong to the monomer.

C.4 $P_k^{S_0\to S_n}$ - The Weight of the Transition Density from Monomer k to an Excited State S$_n$

The TDM is another valuable tool for analysing and interpreting electronic excitation processes in molecular systems. For any transition between two eigenstates of a many-body system, the TDM provides a characteristic spatial map that indicates the distribution of the associated electron–hole pairs and allows one to identify their delocalisation and coherence lengths. This is particularly useful for characterising charge-transfer excitations in large molecular chains. The TDM between ground and an excited state is defined as (de-excitation transitions are omitted for simplicity)

$$\mathbf{P}_{\mu\nu}^{\text{tran}} = \sum_i^{\text{occ}} \sum_a^{\text{vir}} w_i^a C_{\mu i} C_{\nu a} \tag{C.1}$$

where $C_{\mu i}$ is the expansion coefficient of basis function μ in molecular orbital i and w_i^a is the weight of the corresponding $i \to a$ orbital pair transition. The matrix is symmetrised as $\mathbf{P}_{\mu\nu}^{\text{tran}} = (\mathbf{P}_{\mu\nu}^{\text{tran}} + \mathbf{P}_{\nu\mu}^{\text{tran}})/\sqrt{2}$. To obtain the correlated e-h probability matrix (Zojer et al. 2000, Köse et al. 2007), we contract the TDM from the basis form to the atomic form as $\mathbf{P}_{AB}^{\text{tran}} = \sum_{\mu\in A}\sum_{\nu\in B}(P_{\mu\nu}^{\text{tran}})^2$. The element, e.g. (A, B), of this matrix, is essentially the probability of simultaneously finding a hole on atom A and an electron on atom B. The fragment (monomer) based form of the TDM can be obtained by simply summing over the contributions of the atoms that belong to the monomer k, i.e., $\mathbf{P}_{kl}^{\text{tran}} = \sum_{A\in k}\sum_{B\in l} P_{AB}^{\text{tran}}$. Finally, the weight of the transition density from monomer k to an excited state S$_n$, $P_k^{S_0\to S_n}$, is calculated as $P_k^{S_0\to S_n} = \sum_l P_{kl}^{S_0\to S_n}$.

C.5 Electronic Excitation Indices for Individual Chain

Transition	PI	H (Å)	E_{coul} (eV)	Δr-index (Å)
$S_0 \rightarrow S_1$	3	11.05	1.40	9.55
$S_0 \rightarrow S_2$	1	8.29	1.73	10.05
$S_0 \rightarrow S_3$	5	20.39	0.60	18.50
$S_0 \rightarrow S_4$	4	24.84	0.43	17.00
$S_0 \rightarrow S_5$	6	24.08	0.44	14.41

Table C.1: Electronic excitation indices for the five lowest singlet excited states for chain 1.

Transition	PI	H (Å)	E_{coul} (eV)	Δr-index (Å)
$S_0 \rightarrow S_1$	2	9.59	1.50	11.53
$S_0 \rightarrow S_2$	4	17.52	0.83	13.33
$S_0 \rightarrow S_3$	3	20.11	0.75	13.48
$S_0 \rightarrow S_4$	4	16.48	0.97	8.68
$S_0 \rightarrow S_5$	5	14.57	0.99	9.31

Table C.2: Electronic excitation indices for the five lowest singlet excited states for chain 2.

Transition	PI	H (Å)	E_{coul} (eV)	Δr-index (Å)
$S_0 \rightarrow S_1$	2	10.96	1.33	7.00
$S_0 \rightarrow S_2$	4	13.63	1.04	11.88
$S_0 \rightarrow S_3$	3	11.62	1.31	14.89
$S_0 \rightarrow S_4$	3	15.99	0.84	11.31
$S_0 \rightarrow S_5$	3	14.16	0.93	12.66

Table C.3: Electronic excitation indices for the five lowest singlet excited states for chain 3.

Transition	PI	H (Å)	E_{coul} (eV)	Δr-index (Å)
$S_0 \rightarrow S_1$	2	11.58	1.35	14.55
$S_0 \rightarrow S_2$	4	12.18	1.06	13.23
$S_0 \rightarrow S_3$	4	20.06	0.70	16.23
$S_0 \rightarrow S_4$	4	19.08	0.80	13.02
$S_0 \rightarrow S_5$	4	13.19	1.13	11.29

Table C.4: Electronic excitation indices for the five lowest singlet excited states for chain 4.

Transition	PI	H (Å)	E_{coul} (eV)	Δr-index (Å)
$S_0 \rightarrow S_1$	2	12.35	1.29	6.17
$S_0 \rightarrow S_2$	2	13.54	1.09	6.97
$S_0 \rightarrow S_3$	3	9.67	1.61	13.91
$S_0 \rightarrow S_4$	3	7.85	1.90	10.05
$S_0 \rightarrow S_5$	4	17.91	0.83	7.92

Table C.5: Electronic excitation indices for the five lowest singlet excited states for chain 5.

Transition	PI	H (Å)	E_{coul} (eV)	Δr-index (Å)
$S_0 \rightarrow S_1$	1	3.14	4.52	5.60
$S_0 \rightarrow S_2$	5	3.00	4.95	6.15
$S_0 \rightarrow S_3$	5	8.81	1.57	7.23
$S_0 \rightarrow S_4$	3	9.20	1.51	9.45
$S_0 \rightarrow S_5$	5	14.80	0.93	8.62

Table C.6: Electronic excitation indices for the five lowest singlet excited states for chain 6.

Transition	PI	H (Å)	E_{coul} (eV)	Δr-index (Å)
$S_0 \rightarrow S_1$	2	10.25	1.47	11.80
$S_0 \rightarrow S_2$	4	13.99	1.02	12.55
$S_0 \rightarrow S_3$	3	14.55	0.99	11.47
$S_0 \rightarrow S_4$	7	20.40	0.67	7.99
$S_0 \rightarrow S_5$	4	13.41	1.18	8.21

Table C.7: Electronic excitation indices for the five lowest singlet excited states for chain 7.

Transition	PI	H (Å)	E_{coul} (eV)	Δr-index (Å)
$S_0 \rightarrow S_1$	2	9.02	1.67	11.09
$S_0 \rightarrow S_2$	3	15.09	0.93	11.83
$S_0 \rightarrow S_3$	4	17.73	0.73	12.78
$S_0 \rightarrow S_4$	4	12.45	1.06	11.47
$S_0 \rightarrow S_5$	5	17.74	0.71	11.07

Table C.8: Electronic excitation indices for the five lowest singlet excited states for chain 8.

Transition	PI	H (Å)	E_{coul} (eV)	Δr-index (Å)
$S_0 \rightarrow S_1$	2	8.81	1.58	7.03
$S_0 \rightarrow S_2$	1	7.69	1.90	9.66
$S_0 \rightarrow S_3$	2	11.15	1.39	13.35
$S_0 \rightarrow S_4$	3	14.91	1.01	18.62
$S_0 \rightarrow S_5$	2	13.63	1.07	7.80

Table C.9: Electronic excitation indices for the five lowest singlet excited states for chain 9.

Transition	PI	H (Å)	E_{coul} (eV)	Δr-index (Å)
$S_0 \rightarrow S_1$	3	9.64	1.49	7.62
$S_0 \rightarrow S_2$	2	9.63	1.81	7.31
$S_0 \rightarrow S_3$	3	12.15	1.20	7.23
$S_0 \rightarrow S_4$	4	16.47	0.85	13.75
$S_0 \rightarrow S_5$	5	18.49	0.69	10.92

Table C.10: Electronic excitation indices for the five lowest singlet excited states for chain 10.

Transition	PI	H (Å)	E_{coul} (eV)	Δr-index (Å)
$S_0 \rightarrow S_1$	2	8.20	1.81	4.83
$S_0 \rightarrow S_2$	2	10.20	1.35	12.72
$S_0 \rightarrow S_3$	2	9.65	1.56	15.20
$S_0 \rightarrow S_4$	2	10.79	1.30	6.35
$S_0 \rightarrow S_5$	4	16.26	0.81	9.22

Table C.11: Electronic excitation indices for the five lowest singlet excited states for chain 11.

Transition	PI	H (Å)	E_{coul} (eV)	Δr-index (Å)
$S_0 \rightarrow S_1$	3	13.29	1.11	15.53
$S_0 \rightarrow S_2$	3	12.40	1.14	10.21
$S_0 \rightarrow S_3$	4	19.76	0.72	8.24
$S_0 \rightarrow S_4$	5	16.20	0.74	7.71
$S_0 \rightarrow S_5$	4	15.93	0.95	16.43

Table C.12: Electronic excitation indices for the five lowest singlet excited states for chain 12.

Transition	PI	H (Å)	E_{coul} (eV)	Δr-index (Å)
$S_0 \rightarrow S_1$	3	9.45	1.61	8.21
$S_0 \rightarrow S_2$	4	11.10	1.42	9.69
$S_0 \rightarrow S_3$	3	13.49	1.22	9.98
$S_0 \rightarrow S_4$	3	14.06	1.09	10.30
$S_0 \rightarrow S_5$	2	15.23	1.00	10.45

Table C.13: Electronic excitation indices for the five lowest singlet excited states for chain 13.

Transition	PI	H (Å)	E_{coul} (eV)	Δr-index (Å)
$S_0 \rightarrow S_1$	2	11.03	1.34	10.55
$S_0 \rightarrow S_2$	3	13.77	1.03	7.86
$S_0 \rightarrow S_3$	4	17.52	0.82	14.70
$S_0 \rightarrow S_4$	2	11.80	1.21	13.90
$S_0 \rightarrow S_5$	3	15.67	0.94	13.98

Table C.14: Electronic excitation indices for the five lowest singlet excited states for chain 14.

Transition	PI	H (Å)	E_{coul} (eV)	Δr-index (Å)
$S_0 \rightarrow S_1$	2	10.37	1.46	13.30
$S_0 \rightarrow S_2$	2	10.48	1.35	15.53
$S_0 \rightarrow S_3$	3	12.98	1.26	9.48
$S_0 \rightarrow S_4$	1	7.23	1.95	1.65
$S_0 \rightarrow S_5$	2	16.00	0.86	10.25

Table C.15: Electronic excitation indices for the five lowest singlet excited states for chain 15.

Transition	PI	H (Å)	E_{coul} (eV)	Δr-index (Å)
$S_0 \rightarrow S_1$	5	17.33	0.71	12.52
$S_0 \rightarrow S_2$	5	18.00	0.76	10.66
$S_0 \rightarrow S_3$	5	12.43	1.08	7.75
$S_0 \rightarrow S_4$	2	14.77	1.00	11.90
$S_0 \rightarrow S_5$	5	18.34	0.66	12.50

Table C.16: Electronic excitation indices for the five lowest singlet excited states for chain 16.

Transition	PI	H (Å)	E_{coul} (eV)	Δr-index (Å)
$S_0 \rightarrow S_1$	1	7.08	2.13	2.87
$S_0 \rightarrow S_2$	2	12.01	1.39	10.50
$S_0 \rightarrow S_3$	2	13.53	1.21	12.14
$S_0 \rightarrow S_4$	3	17.42	0.94	17.29
$S_0 \rightarrow S_5$	4	12.25	1.22	10.21

Table C.17: Electronic excitation indices for the five lowest singlet excited states for chain 17.

Transition	PI	H (Å)	E_{coul} (eV)	Δr-index (Å)
$S_0 \rightarrow S_1$	2	10.64	1.25	7.24
$S_0 \rightarrow S_2$	3	11.17	1.27	7.49
$S_0 \rightarrow S_3$	3	18.91	0.79	16.10
$S_0 \rightarrow S_4$	2	13.66	1.17	7.73
$S_0 \rightarrow S_5$	3	20.56	0.75	12.60

Table C.18: Electronic excitation indices for the five lowest singlet excited states for chain 18.

Transition	PI	H (Å)	E_{coul} (eV)	Δr-index (Å)
$S_0 \rightarrow S_1$	3	12.78	1.22	10.73
$S_0 \rightarrow S_2$	3	10.82	1.33	9.00
$S_0 \rightarrow S_3$	3	14.03	1.19	12.14
$S_0 \rightarrow S_4$	2	12.25	1.48	12.74
$S_0 \rightarrow S_5$	3	11.53	1.24	7.12

Table C.19: Electronic excitation indices for the five lowest singlet excited states for chain 19.

Transition	PI	H (Å)	E_{coul} (eV)	Δr-index (Å)
$S_0 \rightarrow S_1$	3	10.36	1.31	13.13
$S_0 \rightarrow S_2$	2	9.60	1.50	7.48
$S_0 \rightarrow S_3$	3	13.78	0.99	8.93
$S_0 \rightarrow S_4$	4	14.66	0.93	10.02
$S_0 \rightarrow S_5$	4	12.51	1.05	10.85

Table C.20: Electronic excitation indices for the five lowest singlet excited states for chain 20.

C.6 Extra Figures

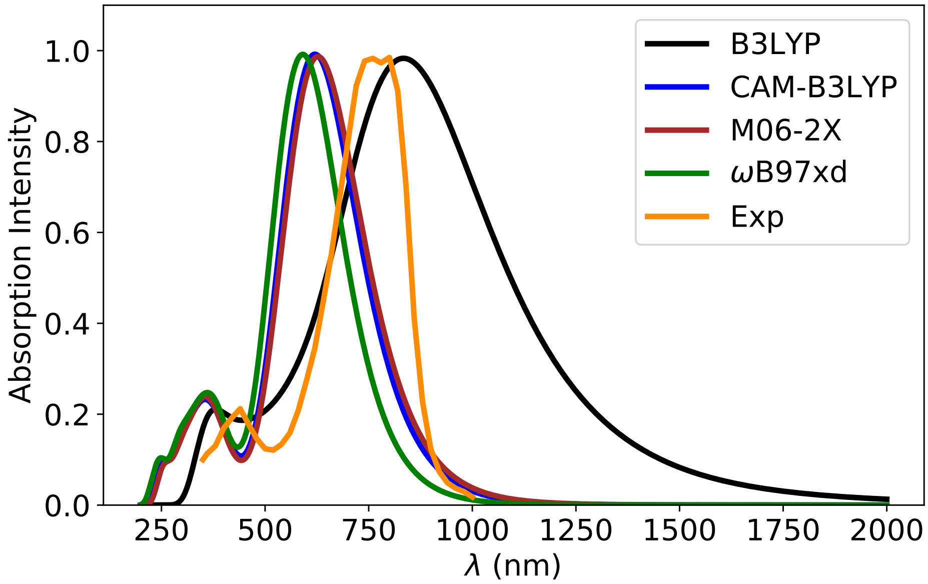

Figure C.1: Absorption spectra for a 4mers π-stacked assembly computed using the B3LYP (black line), CAM-B3LYP (blue line), M06-2X (red line) and ωB97XD (green line) functionals. All systems use the 3-21G* basis set. 100 lowest singlet excitations are included in the absorption spectra calculation of each chain. Experimentally measured spectra for thin film polymer (Bronstein et al. 2011) is also included (orange line).

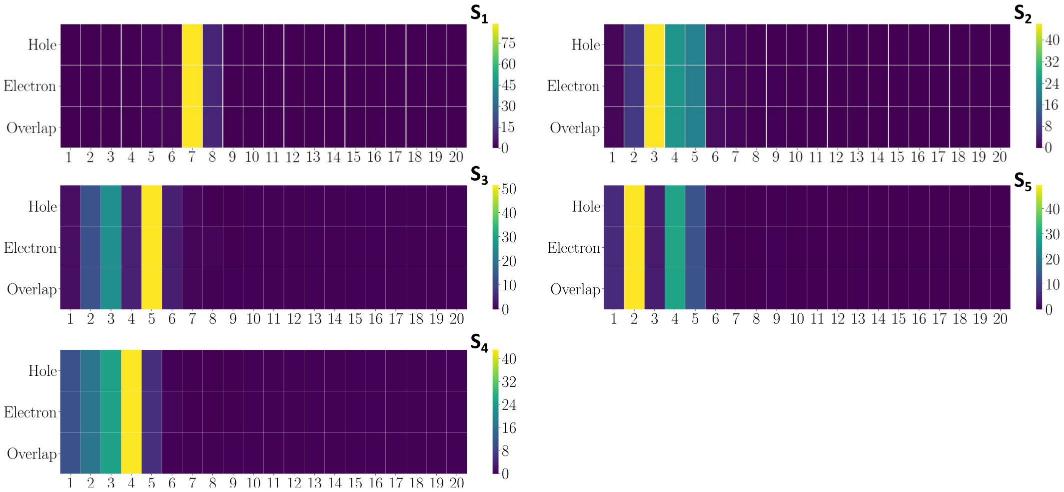

Figure C.2: Heat map of the monomer contributions to the hole and electron for the lowest five excited states of chain number 2.

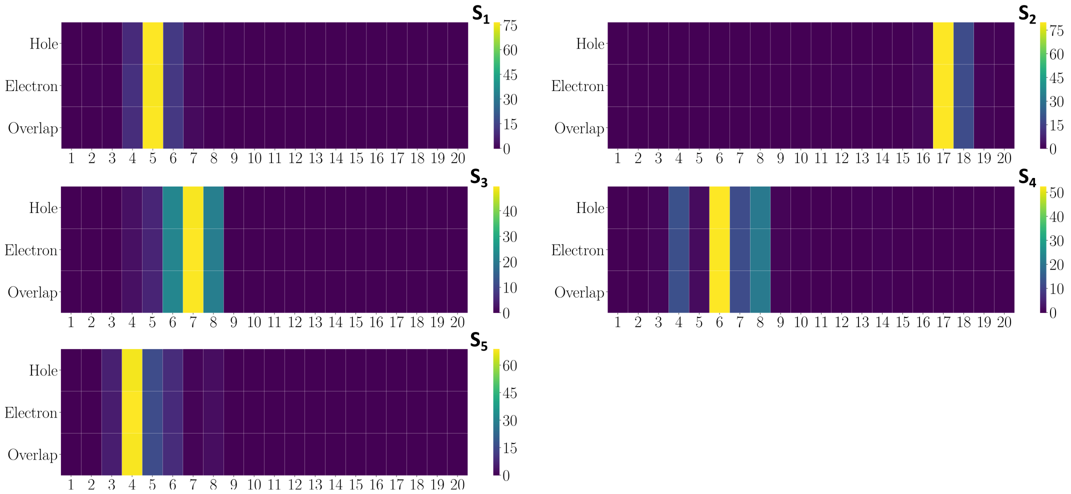

Figure C.3: Heat map of the monomer contributions to the hole and electron for the lowest five excited states of chain number 20.

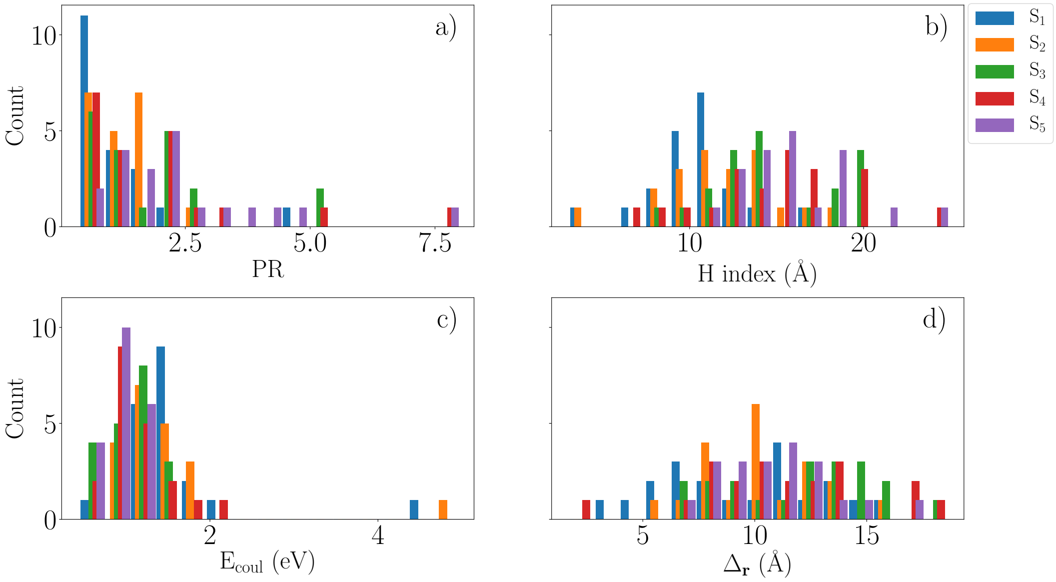

Figure C.4: Histogram distribution of (a) the participation index PI, (b) the e-h spatial overlap H-index, (c) the exciton binding energy E_{coul} and (d) the e-h distance $\mathbf{\Delta r}$-index for the lowest five excited states of the 20ch_20mers system at 200 ns in the NVT ensemble.

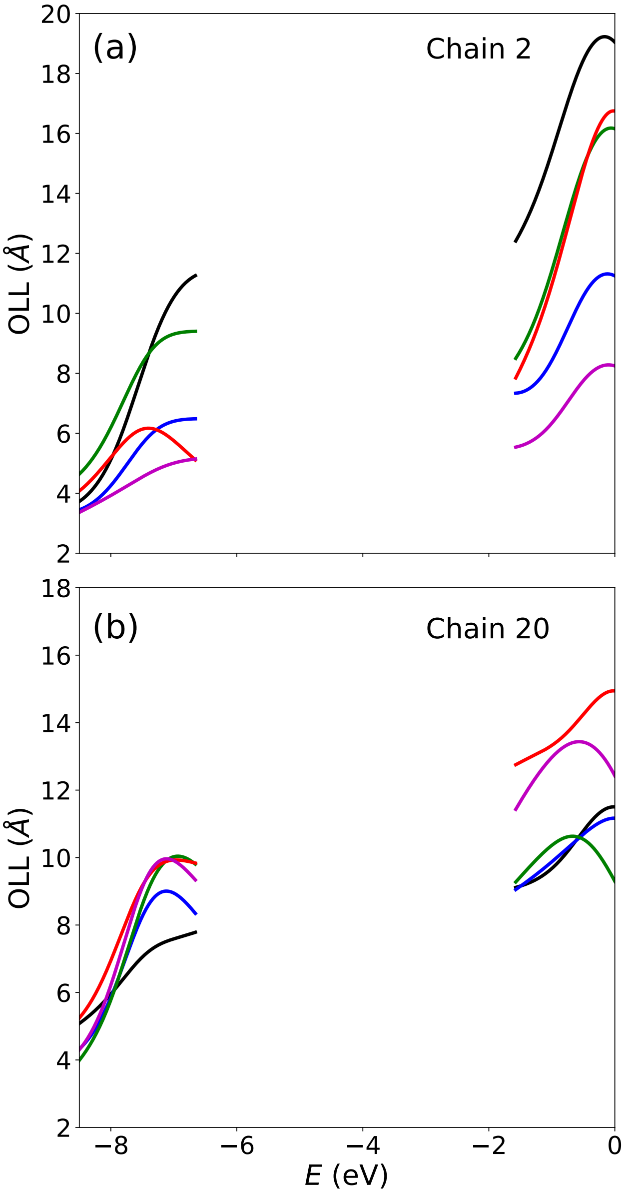

Figure C.5: Evolution of the orbital localisation length of chains (a) 2 and (b) 20 at 0 ns (black line), 50 ns (blue line), 100 ns (green line), 150 ns (red line) and 200 ns (magenta line).

Bibliography

Abramavicius, D., Jiang, J., Bulheller, B. M., Hirst, J. D. & Mukamel, S. (2010), 'Simulation Study of Chiral Two-Dimensional Ultraviolet Spectroscopy of the Protein Backbone', *Journal of the American Chemical Society* **132**(22), 7769–7775.

Adamo, C. & Jacquemin, D. (2013), 'The calculations of excited-state properties with time-dependent density functional theory', *Chemical Society Reviews* **42**(3), 845–856.

Aghtar, M., Kleinekathöfer, U., Curutchet, C. & Mennucci, B. (2017), 'Impact of Electronic Fluctuations and Their Description on the Exciton Dynamics in the Light-Harvesting Complex PE545', *The Journal of Physical Chemistry B* **121**(6), 1330–1339.

Akamatu, H., Inokuchi, H. & Matsunaga, Y. (1954), 'Electrical conductivity of the perylene–bromine complex', *Nature* **173**(4395), 168–169.

Akin-Ojo, O., Song, Y. & Wang, F. (2008), 'Developing ab initio quality force fields from condensed phase quantum-mechanics/molecular-mechanics calculations through the adaptive force matching method', *The Journal of Chemical Physics* **129**(6), 064108.

Alberga, D., Mangiatordi, G. F., Torsi, L. & Lattanzi, G. (2014), 'Effects of annealing and residual solvents on amorphous P3HT and PBTTT films', *The Journal of Physical Chemistry C* **118**(16), 8641–8655.

Andreussi, O., Prandi, I. G., Campetella, M., Prampolini, G. & Mennucci, B. (2017), 'Classical Force Fields Tailored for QM Applications: Is It Really a Feasible Strategy?', *Journal of Chemical Theory and Computation* **13**(10), 4636–4648.

Aragó, J. & Troisi, A. (2015*a*), 'Dynamics of the excitonic coupling in organic crystals', *Physical Review Letters* **114**(2), 026402.

Aragó, J. & Troisi, A. (2015*b*), 'Excitonic couplings between molecular crystal pairs by a multistate approximation', *The Journal of Chemical Physics* **142**(16), 164107.

Aragó, J. & Troisi, A. (2016), 'Regimes of exciton transport in molecular crystals in the presence of dynamic disorder', *Advanced Functional Materials* **26**(14), 2316–2325.

Aragó, J., Viruela, P. M., Gierschner, J., Ortí, E. & Milián-Medina, B. (2011), 'Oligothienoacenes versus oligothiophenes: impact of ring fusion on the optical properties', *Physical Chemistry Chemical Physics* **13**(4), 1457–1465.

Archer, M. D. & Green, M. A. (2014), *Clean electricity from photovoltaics*, Vol. 4, World Scientific.

Ashraf, R. S., Chen, Z., Leem, D. S., Bronstein, H., Zhang, W., Schroeder, B., Geerts, Y., Smith, J., Watkins, S., Anthopoulos, T. D. et al. (2011), 'Silaindacenodithiophene semiconducting polymers for efficient solar cells and high-mobility ambipolar transistors', *Chemistry of Materials* **23**(3), 768–770.

Baldo, M. A., O'Brien, D. F., You, Y., Shoustikov, A., Sibley, S., Thompson, M. E. & Forrest, S. R. (1998), 'Highly efficient phosphorescent emission from organic electroluminescent devices', *Nature* **395**(6698), 151–154.

Bao, Z., Dodabalapur, A. & Lovinger, A. J. (1996), 'Soluble and processable regioregular poly (3-hexylthiophene) for thin film field-effect transistor applications with high mobility', *Applied Physics Letters* **69**(26), 4108–4110.

Barford, W. (2013), 'Excitons in conjugated polymers: A tale of two particles', *The Journal of Physical Chemistry A* **117**(13), 2665–2671.

Barford, W. & Mannouch, J. R. (2018), 'Torsionally induced exciton localization and decoherence in π-conjugated polymers', *The Journal of Chemical Physics* **149**(21), 214107.

Bernanose, A. (1955), 'Electroluminescence of organic compounds', *British Journal of Applied Physics* **6**(S4), S54.

Bhatta, R. S. & Tsige, M. (2014), 'Chain length and torsional dependence of exciton binding energies in P3HT and PTB7 conjugated polymers: A first-principles study', *Polymer* **55**(11), 2667–2672.

Bijleveld, J. C., Zoombelt, A. P., Mathijssen, S. G., Wienk, M. M., Turbiez, M., de Leeuw, D. M. & Janssen, R. A. (2009), 'Poly (diketopyrrolopyrrole-terthiophene) for ambipolar logic and photovoltaics', *Journal of the American Chemical Society* **131**(46), 16616–16617.

Bondarenko, A. S., Knoester, J. & Jansen, T. L. (2020), 'Comparison of methods to study excitation energy transfer in molecular multichromophoric systems', *Chemical Physics* **529**, 110478.

Brédas, J.-L., Calbert, J. P., da Silva Filho, D. & Cornil, J. (2002), 'Organic semiconductors: A theoretical characterization of the basic parameters governing charge transport', *Proceedings of the National Academy of Sciences* **99**(9), 5804–5809.

Bronstein, H., Chen, Z., Ashraf, R. S., Zhang, W., Du, J., Durrant, J. R., Shakya Tuladhar, P., Song, K., Watkins, S. E., Geerts, Y. et al. (2011), 'Thieno [3, 2-*b*] thiophene-diketopyrrolopyrrole-containing polymers for high-performance organic field-effect transistors and organic photovoltaic devices', *Journal of the American Chemical Society* **133**(10), 3272–3275.

Bronstein, H., Collado-Fregoso, E., Hadipour, A., Soon, Y. W., Huang, Z., Dimitrov, S. D., Ashraf, R. S., Rand, B. P., Watkins, S. E., Tuladhar, P. S. et al. (2013), 'Thieno [3, 2-*b*] thiophene-diketopyrrolopyrrole containing polymers for inverted solar cells devices with high short circuit currents', *Advanced Functional Materials* **23**(45), 5647–5654.

Brunner, K., Van Dijken, A., Börner, H., Bastiaansen, J. J. A. M., Kiggen, N. M. M. & Langeveld, B. M. W. (2004), 'Carbazole Compounds as Host Materials for Triplet Emitters in Organic Light-Emitting Diodes: Tuning the HOMO Level without Influencing the Triplet Energy in Small Molecules', *Journal of the American Chemical Society* **126**(19), 6035–6042.

Burroughes, J., Jones, C. & Friend, R. (1988), 'New semiconductor device physics in polymer diodes and transistors', *Nature* **335**(6186), 137–141.

Callaway, C. P., Bombile, J. H., Mask, W., Ryno, S. M. & Risko, C. (2022), 'Thermomechanical enhancement of DPP-4T through purposeful π-conjugation disruption', *Journal of Polymer Science* **60**(3), 559–568.

Chai, J.-D. & Head-Gordon, M. (2008), 'Long-range corrected hybrid density functionals with damped atom–atom dispersion corrections', *Physical Chemistry Chemical Physics* **10**(44), 6615–6620.

Chan, W. K., Chen, Y., Peng, Z. & Yu, L. (1993), 'Rational designs of multifunctional polymers', *Journal of the American Chemical Society* **115**(25), 11735–11743.

Chandran, D. & Lee, K.-S. (2013), 'Diketopyrrolopyrrole: A versatile building block for organic photovoltaic materials', *Macromolecular Research* **21**(3), 272–283.

Chandrasekaran, S., Aghtar, M., Valleau, S., Aspuru-Guzik, A. & Kleinekathöfer, U. (2015), 'Influence of Force Fields and Quantum Chemistry Approach on Spectral Densities of BChl a in Solution and in FMO Proteins', *The Journal of Physical Chemistry B* **119**(31), 9995–10004.

Chang, J. C. (1977), 'Monopole effects on electronic excitation interactions between large molecules. i. application to energy transfer in chlorophylls', *The Journal of Chemical Physics* **67**(9), 3901–3909.

Chen, S., Li, Z., Qiao, Y. & Song, Y. (2021), 'Solution-processed organic semiconductor crystals for field-effect transistors: from crystallization mechanism towards morphology control', *Journal of Materials Chemistry C* **9**(4), 1126–1149.

Chenu, A. & Scholes, G. D. (2015), 'Coherence in energy transfer and photosynthesis', *Annual Review of Physical Chemistry* **66**, 69–96.

Cheung, D. L., McMahon, D. P. & Troisi, A. (2009*a*), 'A realistic description of the charge carrier wave function in microcrystalline polymer semiconductors', *Journal of the American Chemical Society* **131**(31), 11179–11186.

Cheung, D. L., Mcmahon, D. P. & Troisi, A. (2009*b*), ‘Computational study of the structure and charge-transfer parameters in low-molecular-mass P3HT’, *The Journal of Physical Chemistry B* **113**(28), 9393–9401.

Cheung, D. L. & Troisi, A. (2008), ‘Modelling charge transport in organic semiconductors: From quantum dynamics to soft matter’, *Physical Chemistry Chemical Physics* **10**(39), 5941–5952.

Cheung, D. L. & Troisi, A. (2010), ‘Theoretical Study of the Organic Photovoltaic Electron Acceptor PCBM: Morphology, Electronic Structure, and Charge Localization’, *The Journal of Physical Chemistry C* **114**(48), 20479–20488.

Chu, M., Fan, J.-X., Yang, S., Liu, D., Ng, C. F., Dong, H., Ren, A.-M. & Miao, Q. (2018), ‘Halogenated tetraazapentacenes with electron mobility as high as 27.8 cm2 v- 1 s- 1 in solution-processed n-channel organic thin-film transistors’, *Advanced Materials* **30**(38), 1803467.

Claridge, K. & Troisi, A. (2019), ‘Developing Consistent Molecular Dynamics Force Fields for Biological Chromophores via Force Matching’, *The Journal of Physical Chemistry B* **123**(2), 428–438.

Collini, E. & Scholes, G. D. (2009), ‘Coherent intrachain energy migration in a conjugated polymer at room temperature’, *Science* **323**(5912), 369–373.

Cornell, W. D., Cieplak, P., Bayly, C. I. & Kollman, P. A. (1993), ‘Application of RESP charges to calculate conformational energies, hydrogen bond energies and free energies of solvation’, *Journal of the American Chemical Society* **115**, 9620–9631.

Dantanarayana, V., Nematiaram, T., Vong, D., Anthony, J. E., Troisi, A., Nguyen Cong, K., Goldman, N., Faller, R. & Moulé, A. J. (2020), ‘Predictive Model of Charge Mobilities in Organic Semiconductor Small Molecules with Force-Matched Potentials’, *Journal of Chemical Theory and Computation* **16**(6), 3494–3503.

David, J., Weiter, M., Vala, M., Vyňuchal, J. & Kučerík, J. (2011), ‘Stability and structural aspects of diketopyrrolopyrrole pigment and its n-alkyl derivatives’, *Dyes and Pigments* **89**(2), 137–143.

d’Avino, G., Olivier, Y., Muccioli, L. & Beljonne, D. (2016), ‘Do charges delocalize over multiple molecules in fullerene derivatives?’, *Journal of Materials Chemistry C* **4**(17), 3747–3756.

DeLongchamp, D. M., Kline, R. J., Lin, E. K., Fischer, D. A., Richter, L. J., Lucas, L. A., Heeney, M., McCulloch, I. & Northrup, J. E. (2007), ‘High carrier mobility polythiophene thin films: structure determination by experiment and theory’, *Advanced Materials* **19**(6), 833–837.

Dexter, D. L. (1953), ‘A theory of sensitized luminescence in solids’, *The Journal of Chemical Physics* **21**(5), 836–850.

Dhar, J., Karothu, D. P. & Patil, S. (2015), 'Herringbone to cofacial solid state packing via H-bonding in diketopyrrolopyrrole (DPP) based molecular crystals: Influence on charge transport', *Chemical Communications* **51**(1), 97–100.

Do, H. & Troisi, A. (2015), 'Developing accurate molecular mechanics force fields for conjugated molecular systems', *Physical Chemistry Chemical Physics* **17**(38), 25123–25132.

Dodda, L. S., De Vaca, I. C., Tirado-Rives, J. & Jorgensen, W. L. (2017), 'LigParGen web server: An automatic OPLS-AA parameter generator for organic ligands', *Nucleic Acids Research* **45**(W1), W331–W336.

Dostál, J., Fennel, F., Koch, F., Herbst, S., Würthner, F. & Brixner, T. (2018), 'Direct observation of exciton–exciton interactions', *Nature Communications* **9**(1), 1–8.

Dou, L., You, J., Hong, Z., Xu, Z., Li, G., Street, R. A. & Yang, Y. (2013), '25th anniversary article: a decade of organic/polymeric photovoltaic research', *Advanced Materials* **25**(46), 6642–6671.

DuBay, K. H., Hall, M. L., Hughes, T. F., Wu, C., Reichman, D. R. & Friesner, R. A. (2012), 'Accurate force field development for modeling conjugated polymers', *Journal of Chemical Theory and Computation* **8**(11), 4556–4569.

Ebisawa, F., Kurokawa, T. & Nara, S. (1983), 'Electrical properties of polyacetylene/polysiloxane interface', *Journal of Applied Physics* **54**(6), 3255–3259.

Eggeman, A. S., Illig, S., Troisi, A., Sirringhaus, H. & Midgley, P. A. (2013), 'Measurement of molecular motion in organic semiconductors by thermal diffuse electron scattering', *Nature Materials* **12**(11), 1045–1049.

Eley, D. D. (1948), 'Phthalocyanines as semiconductors', *Nature* **162**(4125), 819–819.

Eley, D. & Parfitt, G. (1955), 'The semiconductivity of organic substances. part 2', *Transactions of the Faraday Society* **51**, 1529–1539.

Eley, D., Parfitt, G., Perry, M. & Taysum, D. (1953), 'The semiconductivity of organic substances. part 1', *Transactions of the Faraday Society* **49**, 79–86.

Ercolessi, F. & Adams, J. B. (1994), 'Interatomic potentials from first-principles calculations: the force-matching method', *Europhysics Letters* **26**(8), 583–588.

Farnum, D. G., Mehta, G., Moore, G. G. & Siegal, F. P. (1974), 'Attempted reformatskii reaction of benzonitrile, 1, 4-diketo-3, 6-diphenylpyrrolo [3,4-*c*] pyrrole. a lactam analogue of pentalene.', *Tetrahedron Letters* **15**(29), 2549–2552.

Fassioli, F., Dinshaw, R., Arpin, P. C. & Scholes, G. D. (2014), 'Photosynthetic light harvesting: excitons and coherence', *Journal of the Royal Society Interface* **11**(92), 20130901.

Feller, S. E., Zhang, Y., Pastor, R. W. & Brooks, B. R. (1995), 'Constant pressure molecular dynamics simulation: The langevin piston method', *The Journal of Chemical Physics* **103**(11), 4613–4621.

Finnis, M. (2003), *Interatomic forces in condensed matter*, Vol. 1, Oxford Series on Materials Mod.

Fornari, R. P., Aragó, J. & Troisi, A. (2016), 'Exciton dynamics in phthalocyanine molecular crystals', *The Journal of Physical Chemistry C* **120**(15), 7987–7996.

Forrest, S. R. (2004), 'The path to ubiquitous and low-cost organic electronic appliances on plastic', *Nature* **428**(6986), 911–918.

Förster, T. (1948), 'Zwischenmolekulare energiewanderung und fluoreszenz', *Annalen der Physik* **437**(1-2), 55–75.

Fratini, S., Mayou, D. & Ciuchi, S. (2016), 'The transient localization scenario for charge transport in crystalline organic materials', *Advanced Functional Materials* **26**(14), 2292–2315.

Fratini, S., Nikolka, M., Salleo, A., Schweicher, G. & Sirringhaus, H. (2020), 'Charge transport in high-mobility conjugated polymers and molecular semiconductors', *Nature Materials* **19**(5), 491–502.

Frenkel, J. (1931), 'On the transformation of light into heat in solids. i', *Physical Review* **37**(1), 17.

Frisch, M. J., Trucks, G. W., Schlegel, H. B., Scuseria, G. E., Robb, M. A., Cheeseman, J. R., Scalmani, G., Barone, V., Petersson, G. A., Nakatsuji, H., Li, X., Caricato, M., Marenich, A. V., Bloino, J., Janesko, B. G., Gomperts, R., Mennucci, B., Hratchian, H. P., Ortiz, J. V., Izmaylov, A. F., Sonnenberg, J. L., Williams-Young, D., Ding, F., Lipparini, F., Egidi, F., Goings, J., Peng, B., Petrone, A., Henderson, T., Ranasinghe, D., Zakrzewski, V. G., Gao, J., Rega, N., Zheng, G., Liang, W., Hada, M., Ehara, M., Toyota, K., Fukuda, R., Hasegawa, J., Ishida, M., Nakajima, T., Honda, Y., Kitao, O., Nakai, H., Vreven, T., Throssell, K., Montgomery, Jr., J. A., Peralta, J. E., Ogliaro, F., Bearpark, M. J., Heyd, J. J., Brothers, E. N., Kudin, K. N., Staroverov, V. N., Keith, T. A., Kobayashi, R., Normand, J., Raghavachari, K., Rendell, A. P., Burant, J. C., Iyengar, S. S., Tomasi, J., Cossi, M., Millam, J. M., Klene, M., Adamo, C., Cammi, R., Ochterski, J. W., Martin, R. L., Morokuma, K., Farkas, O., Foresman, J. B. & Fox, D. J. (2016), 'Gaussian˜16 Revision C.01'. Gaussian Inc. Wallingford CT.

Gabrieli, A., Sant, M., Demontis, P. & Suffritti, G. B. (2014), 'Fast and efficient optimization of Molecular Dynamics force fields for microporous materials: Bonded interactions via force matching', *Microporous Mesoporous Materials* **197**, 339–347.

Gartner III, T. E. & Jayaraman, A. (2019), 'Modeling and simulations of polymers: a roadmap', *Macromolecules* **52**(3), 755–786.

Ghosh, R. & Spano, F. C. (2020), 'Excitons and polarons in organic materials', *Accounts of Chemical Research* **53**(10), 2201–2211.

Granadino-Roldán, J., Vukmirović, N., Fernández-Gómez, M. & Wang, L.-W. (2011), 'The role of disorder on the electronic structure of conjugated polymers. the case of poly-2, 5-bis (phenylethynyl)-1, 3, 4-thiadiazole', *Physical Chemistry Chemical Physics* **13**(32), 14500–14509.

Granström, M., Petritsch, K., Arias, A., Lux, A., Andersson, M. R. & Friend, R. (1998), 'Laminated fabrication of polymeric photovoltaic diodes', *Nature* **395**(6699), 257–260.

Guido, C. A., Cortona, P., Mennucci, B. & Adamo, C. (2013), 'On the metric of charge transfer molecular excitations: a simple chemical descriptor', *Journal of Chemical Theory and Computation* **9**(7), 3118–3126.

Guo, X., Baumgarten, M. & Müllen, K. (2013), 'Designing π-conjugated polymers for organic electronics', *Progress in Polymer Science* **38**(12), 1832–1908.

Hamai, T., Arai, S. & Hasegawa, T. (2018), 'Effects of tunneling-based access resistance in layered single-crystalline organic transistors', *Journal of Materials Research* **33**(16), 2350–2363.

Handley, C. M. & Deeth, R. J. (2012), 'A multi-objective approach to force field optimization: Structures and spin state energetics of d 6 Fe(II) complexes', *Journal of Chemical Theory and Computation* **8**(1), 194–202.

Harcourt, R. D., Scholes, G. D. & Ghiggino, K. P. (1994), 'Rate expressions for excitation transfer. ii. electronic considerations of direct and through–configuration exciton resonance interactions', *The Journal of Chemical Physics* **101**(12), 10521–10525.

Hartnett, P. E., Margulies, E. A., Mauck, C. M., Miller, S. A., Wu, Y., Wu, Y.-L., Marks, T. J. & Wasielewski, M. R. (2016), 'Effects of crystal morphology on singlet exciton fission in diketopyrrolopyrrole thin films', *The Journal of Physical Chemistry B* **120**(7), 1357–1366.

Herce, H. D., Garcia, A. E. & Darden, T. (2007), 'The electrostatic surface term: (I) Periodic systems', *The Journal of Chemical Physics* **126**, 124106.

Hertwig, R. H. & Koch, W. (1997), 'On the parameterization of the local correlation functional. What is Becke-3-LYP?', *Chemical Physics Letters* **268**(5-6), 345–351.

Hestand, N. J., Kazantsev, R. V., Weingarten, A. S., Palmer, L. C., Stupp, S. I. & Spano, F. C. (2016), 'Extended-charge-transfer excitons in crystalline supramolecular photocatalytic scaffolds', *Journal of the American Chemical Society* **138**(36), 11762–11774.

Hestand, N. J., Tempelaar, R., Knoester, J., Jansen, T. L. & Spano, F. C. (2015), 'Exciton mobility control through sub-Å packing modifications in molecular crystals', *Physical Review B* **91**(19), 1–7.

Himmelberger, S. & Salleo, A. (2015), 'Engineering semiconducting polymers for efficient charge transport', *MRS Communications* **5**(3), 383–395.

Hirshfeld, F. L. (1977), 'Bonded-atom fragments for describing molecular charge densities', *Theoretical Chemistry Accounts* **44**(2), 129–138.

Hohenberg, P. & Kohn, W. (1964), 'Inhomogeneous electron gas', *Physical Review* **136**(3B), B864.

Hoover, W. G., Ladd, A. J. C. & Moran, B. (1982), 'High-strain-rate plastic flow studied via nonequilibrium molecular dynamics', *Physical Review Letters* **48**, 1818–1820.

Hoppe, H. & Sariciftci, N. S. (2004), 'Organic solar cells: An overview', *Journal of Materials Research* **19**(7), 1924–1945.

Horowitz, G., Fichou, D., Peng, X., Xu, Z. & Garnier, F. (1989), 'A field-effect transistor based on conjugated alpha-sexithienyl', *Solid State Communications* **72**(4), 381–384.

Hsu, C. P., You, Z. Q. & Chen, H. C. (2008), 'Characterization of the short-range couplings in excitation energy transfer', *The Journal of Physical Chemistry C* **112**(4), 1204–1212.

Huang, D. M., Mauger, S. A., Friedrich, S., George, S. J., Dumitriu-LaGrange, D., Yoon, S. & Moulé, A. J. (2011), 'The consequences of interface mixing on organic photovoltaic device characteristics', *Advanced Functional Materials* **21**(9), 1657–1665.

Huang, L. & Roux, B. (2013), 'Automated force field parameterization for nonpolarizable and polarizable atomic models based on ab initio target data', *Journal of Chemical Theory and Computation* **9**(8), 3543–3556.

Huang, X., Sheng, P., Tu, Z., Zhang, F., Wang, J., Geng, H., Zou, Y., Di, C.-a., Yi, Y., Sun, Y. et al. (2015), 'A two-dimensional π–d conjugated coordination polymer with extremely high electrical conductivity and ambipolar transport behaviour', *Nature Communications* **6**(1), 1–8.

Huijser, A., Savenije, T. J., Meskers, S. C., Vermeulen, M. J. & Siebbeles, L. D. (2008), 'The mechanism of long-range exciton diffusion in a nematically organized porphyrin layer', *Journal of the American Chemical Society* **130**(37), 12496–12500.

Hummer, K. & Ambrosch-Draxl, C. (2005), 'Oligoacene exciton binding energies: Their dependence on molecular size', *Physical Review B* **71**(8), 081202.

Inal, S., Rivnay, J., Suiu, A.-O., Malliaras, G. G. & McCulloch, I. (2018), 'Conjugated polymers in bioelectronics', *Accounts of Chemical Research* **51**(6), 1368–1376.

Iyengar, S. S., Schlegel, H. B., Millam, J. M., A. Voth, G., Scuseria, G. E. & Frisch, M. J. (2001), 'Ab initio molecular dynamics: Propagating the density matrix with Gaussian orbitals. II. Generalizations based on mass-weighting, idempotency, energy conservation and choice of initial conditions', *The Journal of Chemical Physics* **115**(22), 10291.

Jiang, L., Rogers, D. M., Hirst, J. D. & Do, H. (2020), 'Force fields for macromolecular assemblies containing diketopyrrolopyrrole and thiophene', *Journal of Chemical Theory and Computation* **16**(8), 5150–5162.

Johansson, J., Nation, P. & Nori, F. (2013), 'Qutip 2: A python framework for the dynamics of open quantum systems', *Computer Physics Communications* **184**(4), 1234–1240.

Johansson, J. R., Nation, P. D. & Nori, F. (2012), 'Qutip: An open-source python framework for the dynamics of open quantum systems', *Computer Physics Communications* **183**(8), 1760–1772.

Jorgensen, W. L., Maxwell, D. S. & Tirado-Rives, J. (1996), 'Development and Testing of the OPLS All-Atom Force Field on Conformational Energetics and Properties of Organic Liquids', *Journal of the American Chemical Society* **118**(45), 11225–11236.

Jorgensen, W. L. & Tirado-Rives, J. (1988), 'The OPLS [optimized potentials for liquid simulations] potential functions for proteins, energy minimizations for crystals of cyclic peptides and crambin', *Journal of the American Chemical Society* **110**(6), 1657–1666.

Jou, J.-H., Kumar, S., Agrawal, A., Li, T.-H. & Sahoo, S. (2015), 'Approaches for fabricating high efficiency organic light emitting diodes', *Journal of Materials Chemistry C* **3**(13), 2974–3002.

Kanibolotsky, A. L., Findlay, N. J. & Skabara, P. J. (2015), 'Polythiophene and oligothiophene systems modified by TTF electroactive units for organic electronics', *Beilstein Journal of Organic Chemistry* **11**, 1749–1766.

Kaur, M. & Choi, D. H. (2015), 'Diketopyrrolopyrrole: brilliant red pigment dye-based fluorescent probes and their applications', *Chemical Society Reviews* **44**(1), 58–77.

Kawanabe, Y., Moulé, A. J. & Faller, R. (2014), 'Molecular dynamics study of the local structure of photovoltaic polymer PCDTBT', *Journal of Chemical & Engineering Data* **59**(10), 2982–2986.

Kim, C. W., Park, J. W. & Rhee, Y. M. (2015), 'Effect of chromophore potential model on the description of exciton-phonon interactions', *The Journal of Physical Chemistry Letters* **6**(15), 2875–2880.

Kippelen, B. & Brédas, J.-L. (2009), 'Organic photovoltaics', *Energy & Environmental Science* **2**(3), 251–261.

Kline, R. J. & McGehee, M. D. (2006), 'Morphology and charge transport in conjugated polymers', *Polymer Reviews* **46**(1), 27–45.

Knupfer, M. (2003), 'Exciton binding energies in organic semiconductors', *Applied Physics A* **77**(5), 623–626.

Koezuka, H., Tsumura, A. & Ando, T. (1987), 'Field-effect transistor with polythiophene thin film', *Synthetic Metals* **18**(1-3), 699–704.

Kohn, W. & Sham, L. J. (1965), 'Self-consistent equations including exchange and correlation effects', *Physical review* **140**(4A), A1133.

Köse, M. E., Mitchell, W. J., Kopidakis, N., Chang, C. H., Shaheen, S. E., Kim, K. & Rumbles, G. (2007), 'Theoretical studies on conjugated phenyl-cored thiophene dendrimers for photovoltaic applications', *Journal of the American Chemical Society* **129**(46), 14257–14270.

Koziol, L., Fried, L. E. & Goldman, N. (2017), 'Using force matching to determine reactive force fields for water under extreme thermodynamic conditions', *Journal of Chemical Theory and Computation* **13**(1), 135–146.

Krämer, M., Dohmen, P. M., Xie, W., Holub, D., Christensen, A. S. & Elstner, M. (2020), 'Charge and exciton transfer simulations using machine-learned hamiltonians', *Journal of Chemical Theory and Computation* **16**(7), 4061–4070.

Krausko, J., Malongwe, J. K., Bičanová, G., Klán, P., Nachtigallová, D. & Heger, D. (2015), 'Spectroscopic properties of naphthalene on the surface of ice grains revisited: A combined experimental-computational approach', *The Journal of Physical Chemistry A* **119**(32), 8565–8578.

Kreisbeck, C. & Kramer, T. (2012), 'Long-lived electronic coherence in dissipative exciton dynamics of light-harvesting complexes', *The Journal of Physical Chemistry Letters* **3**(19), 2828–2833.

Kriete, B., Lüttig, J., Kunsel, T., Malỳ, P., Jansen, T. L., Knoester, J., Brixner, T. & Pshenichnikov, M. S. (2019), 'Interplay between structural hierarchy and exciton diffusion in artificial light harvesting', *Nature Communications* **10**(1), 1–11.

Kubo, T., Häusermann, R., Tsurumi, J., Soeda, J., Okada, Y., Yamashita, Y., Akamatsu, N., Shishido, A., Mitsui, C., Okamoto, T. et al. (2016), 'Suppressing molecular vibrations in organic semiconductors by inducing strain', *Nature Communications* **7**(1), 1–7.

Kunsel, T., Jansen, T. & Knoester, J. (2021), 'Scaling relations of exciton diffusion in linear aggregates with static and dynamic disorder', *The Journal of Chemical Physics* **155**(13), 134305.

Kwon, O., Coropceanu, V., Gruhn, N., Durivage, J., Laquindanum, J., Katz, H., Cornil, J. & Brédas, J.-L. (2004), 'Characterization of the molecular parameters determining charge transport in anthradithiophene', *The Journal of Chemical Physics* **120**(17), 8186–8194.

Köhler, A., Hoffmann, S. T. & Bässler, H. (2012), 'An order–disorder transition in the conjugated polymer MEH-PPV', *Journal of the American Chemical Society* **134**(28), 11594–11601.

Le Bahers, T., Adamo, C. & Ciofini, I. (2011), 'A qualitative index of spatial extent in charge-transfer excitations', *Journal of Chemical Theory and Computation* **7**(8), 2498–2506.

Lee, C., Yang, W. & Parr, R. G. (1988), 'Development of the colle-salvetti correlation-energy formula into a functional of the electron density', *Physical review B* **37**(2), 785.

Lee, J. S., Son, S. K., Song, S., Kim, H., Lee, D. R., Kim, K., Ko, M. J., Choi, D. H., Kim, B. & Cho, J. H. (2012), 'Importance of solubilizing group and backbone planarity in low band gap polymers for high performance ambipolar field-effect transistors', *Chemistry of Materials* **24**(7), 1316–1323.

Lei, T., Cao, Y., Fan, Y., Liu, C. J., Yuan, S. C. & Pei, J. (2011), 'High-performance air-stable organic field-effect transistors: Isoindigo-based conjugated polymers', *Journal of the American Chemical Society* **133**(16), 6099–6101.

Li, J. & Wang, F. (2017), 'Water graphene contact surface investigated by pairwise potentials from force-matching PAW-PBE with dispersion correction', *The Journal of Chemical Physics* **146**(5), 054702.

Li, X., Buda, F., De Groot, H. J. & Sevink, G. J. (2020), 'Dynamic disorder drives exciton transfer in tubular chlorosomal assemblies', *The Journal of Physical Chemistry B* **124**(20), 4026–4035.

Li, Y., Guo, X., Peng, Z., Qu, B., Yan, H., Ade, H., Zhang, M. & Forrest, S. R. (2020), 'Color-neutral, semitransparent organic photovoltaics for power window applications', *Proceedings of the National Academy of Sciences of the United States of America* **117**(35), 21147–21154.

Li, Y., Huang, X., Ding, K., Sheriff, H. K., Ye, L., Liu, H., Li, C.-Z., Ade, H. & Forrest, S. R. (2021), 'Non-fullerene acceptor organic photovoltaics with intrinsic operational lifetimes over 30 years', *Nature Communications* **12**(1), 1–9.

Li, Y., Singh, S. P. & Sonar, P. (2010), 'A high mobility P-type DPP-thieno [3,2-*b*] thiophene copolymer for organic thin-film transistors', *Advanced Materials* **22**(43), 4862–4866.

Li, Y., Sonar, P., Murphy, L. & Hong, W. (2013), 'High mobility diketopyrrolopyrrole (DPP)-based organic semiconductor materials for organic thin film transistors and photovoltaics', *Energy & Environmental Science* **6**(6), 1684–1710.

Li, Y., Sun, B., Sonar, P. & Singh, S. P. (2012), 'Solution processable poly(2, 5-dialkyl-2, 5-dihydro-3, 6-di-2-thienyl-pyrrolo [3,4-*c*] pyrrole-1,4-dione) for ambipolar organic thin film transistors', *Organic Electronics* **13**(9), 1606–1613.

Li, Y., Yi, Y., Coropceanu, V. & Brédas, J.-L. (2014), 'Optical conductivity and optical effective mass in a high-mobility organic semiconductor: Implications for the nature of charge transport', *Physical Review B* **90**(24), 245112.

Lin, P. & Yan, F. (2012), ‘Organic thin-film transistors for chemical and biological sensing’, *Advanced Materials* **24**(1), 34–51.

Lin, Y., Zhao, F., He, Q., Huo, L., Wu, Y., Parker, T. C., Ma, W., Sun, Y., Wang, C., Zhu, D. et al. (2016), ‘High-performance electron acceptor with thienyl side chains for organic photovoltaics’, *Journal of the American Chemical Society* **138**(14), 4955–4961.

Lindsey, R. K., Fried, L. E. & Goldman, N. (2017), ‘ChIMES: A force matched potential with explicit three-body interactions for molten carbon’, *Journal of Chemical Theory and Computation* **13**(12), 6222–6229.

Lindsey, R. K., Fried, L. E. & Goldman, N. (2019), ‘Application of the ChIMES force field to nonreactive molecular systems: Water at ambient conditions’, *Journal of Chemical Theory and Computation* **15**(1), 436–447.

Liu, Q., Bottle, S. E. & Sonar, P. (2020), ‘Developments of diketopyrrolopyrrole-dye-based organic semiconductors for a wide range of applications in electronics’, *Advanced Materials* **32**(4), 1903882.

Liu, T. & Troisi, A. (2014), ‘Understanding the microscopic origin of the very high charge mobility in PBTTT: Tolerance of thermal disorder’, *Advanced Functional Materials* **24**(7), 925–933.

Liu, Y., Chen, C.-C., Hong, Z., Gao, J., Yang, Y. M., Zhou, H., Dou, L., Li, G. & Yang, Y. (2013), ‘Solution-processed small-molecule solar cells: breaking the 10% power conversion efficiency’, *Sci. Rep.* **3**(1), 1–8.

Liu, Z., Lu, T. & Chen, Q. (2020), ‘An sp-hybridized all-carboatomic ring, cyclo[18]carbon: Electronic structure, electronic spectrum, and optical nonlinearity’, *Carbon* **165**, 461–467.

Loco, D. & Cupellini, L. (2019), ‘Modeling the absorption lineshape of embedded systems from molecular dynamics: A tutorial review’, *International Journal of Quantum Chemistry* **119**(1), e25726.

Lu, T. & Chen, F. (2012), ‘Multiwfn: A multifunctional wavefunction analyzer’, *Journal of Computational Chemistry* **33**(5), 580–592.

Ma, H., Qin, T. & Troisi, A. (2014), ‘Electronic excited states in amorphous MEH-PPV polymers from large-scale first principles calculations’, *Journal of Chemical Theory and Computation* **10**(3), 1272–1282.

Makhov, D. V. & Barford, W. (2010), ‘Local exciton ground states in disordered polymers’, *Physical Review B* **81**(16), 165201.

Malagoli, M., Coropceanu, V., da Silva Filho, D. A. & Brédas, J.-L. (2004), ‘A multimode analysis of the gas-phase photoelectron spectra in oligoacenes’, *The Journal of Chemical Physics* **120**(16), 7490–7496.

Marsh, H. S., Jankowski, E. & Jayaraman, A. (2014), ‘Controlling the morphology of model conjugated thiophene oligomers through alkyl side chain length, placement, and interactions’, *Macromolecules* **47**(8), 2736–2747.

Martinez, M., Gaigeot, M.-P., Borgis, D. & Vuilleumier, R. (2006), ‘Extracting effective normal modes from equilibrium dynamics at finite temperature’, *The Journal of Chemical Physics* **125**(14), 144106.

Martyna, G. J., Tobias, D. J. & Klein, M. L. (1994), ‘Constant pressure molecular dynamics algorithms’, *The Journal of Chemical Physics* **101**(5), 4177–4189.

Matsushima, T., Bencheikh, F., Komino, T., Leyden, M. R., Sandanayaka, A. S., Qin, C. & Adachi, C. (2019), ‘High performance from extraordinarily thick organic light-emitting diodes’, *Nature* **572**(7770), 502–506.

Matta, M., Pezzella, A. & Troisi, A. (2020), ‘Relation between local structure, electric dipole, and charge carrier dynamics in DHICA melanin: A model for biocompatible semiconductors’, *The Journal of Physical Chemistry Letters* **11**(3), 1045–1051.

McCulloch, I., Heeney, M., Bailey, C., Genevicius, K., MacDonald, I., Shkunov, M., Sparrowe, D., Tierney, S., Wagner, R., Zhang, W. et al. (2006), ‘Liquid-crystalline semiconducting polymers with high charge-carrier mobility’, *Nature Materials* **5**(4), 328–333.

McMahon, D. P., Cheung, D. L., Goris, L., Dacuna, J., Salleo, A. & Troisi, A. (2011), ‘Relation between microstructure and charge transport in polymers of different regioregularity’, *The Journal of Physical Chemistry C* **115**(39), 19386–19393.

McNeill, R., Siudak, R., Wardlaw, J. & Weiss, D. (1963), ‘Electronic conduction in polymers. i. the chemical structure of polypyrrole’, *Australian Journal of Chemistry* **16**(6), 1056–1075.

Meager, I., Ashraf, R. S., Rossbauer, S., Bronstein, H., Donaghey, J. E., Marshall, J., Schroeder, B. C., Heeney, M., Anthopoulos, T. D. & McCulloch, I. (2013), ‘Alkyl chain extension as a route to novel thieno[3, 2-*b*]thiophene flanked diketopyrrolopyrrole polymers for use in organic solar cells and field effect transistors’, *Macromolecules* **46**(15), 5961–5967.

Menke, S. M. & Holmes, R. J. (2014), ‘Exciton diffusion in organic photovoltaic cells’, *Energy & Environmental Science* **7**(2), 499–512.

Meredith, P. & Armin, A. (2018), ‘Scaling of next generation solution processed organic and perovskite solar cells’, *Nature Communications* **9**(1), 8–11.

Mizuguchi, J. & Homma, S. (1989), ‘Intermolecular charge transfer in 1, 4-dithioketo-3, 6-diphenyl-pyrrolo-[3, 4-*c*]-pyrrole’, *Journal of Applied Physics* **66**(7), 3104–3110.

Mollinger, S. A., Krajina, B. A., Noriega, R., Salleo, A. & Spakowitz, A. J. (2015), ‘Percolation, Tie-Molecules, and the Microstructural Determinants of Charge Transport in Semicrystalline Conjugated Polymers’, *ACS Macro Letters* **4**(7), 708–712.

Moorthy, S. B. K. (2015), *Thin film structures in energy applications*, Springer, Cham.

Muccini, M. (2006), 'A bright future for organic field-effect transistors', *Nature Materials* **5**(8), 605–613.

Naik, M. A. & Patil, S. (2013), 'Diketopyrrolopyrrole-based conjugated polymers and small molecules for organic ambipolar transistors and solar cells', *Journal of Polymer Science Part A: Polymer Chemistry* **51**(20), 4241–4260.

Naik, M. A., Venkatramaiah, N., Kanimozhi, C. & Patil, S. (2012), 'Influence of side-chain on structural order and photophysical properties in thiophene based diketopyrrolopyrroles: A systematic study', *The Journal of Physical Chemistry C* **116**(50), 26128–26137.

Nayyar, I. H., Batista, E. R., Tretiak, S., Saxena, A., Smith, D. L. & Martin, R. L. (2013), 'Role of geometric distortion and polarization in localizing electronic excitations in conjugated polymers', *Journal of Chemical Theory and Computation* **9**(2), 1144–1154.

Nelson, T. L., Young, T. M., Liu, J., Mishra, S. P., Belot, J. A., Balliet, C. L., Javier, A. E., Kowalewski, T. & McCullough, R. D. (2010), 'Transistor paint: high mobilities in small bandgap polymer semiconductor based on the strong acceptor, diketopyrrolopyrrole and strong donor, dithienopyrrole', *Advanced Materials* **22**(41), 4617–4621.

Nematiaram, T., Padula, D. & Troisi, A. (2021), 'Bright Frenkel excitons in molecular crystals: A survey', *Chemistry of Materials* **33**(9), 3368–3378.

Nielsen, C. B., Turbiez, M. & McCulloch, I. (2013), 'Recent advances in the development of semiconducting DPP-containing polymers for transistor applications', *Advanced Materials* **25**(13), 1859–1880.

Noriega, R., Rivnay, J., Vandewal, K., Koch, F. P., Stingelin, N., Smith, P., Toney, M. F. & Salleo, A. (2013a), 'A general relationship between disorder, aggregation and charge transport in conjugated polymers', *The Journal of Physical Chemistry C* **12**(11), 1038–1044.

Noriega, R., Salleo, A. & Spakowitz, A. J. (2013b), 'Chain conformations dictate multiscale charge transport phenomena in disordered semiconducting polymers', *Proceedings of the National Academy of Sciences of the United States of America* **110**(41), 16315–16320.

Ong, B. S., Wu, Y., Liu, P. & Gardner, S. (2004), 'High-performance semiconducting polythiophenes for organic thin-film transistors', *Journal of the American Chemical Society* **126**(11), 3378–3379.

Panda, A. N., Plasser, F., Aquino, A. J., Burghardt, I. & Lischka, H. (2013), 'Electronically excited states in poly(p-phenylenevinylene): Vertical excitations and torsional potentials from high-level ab initio calculations', *The Journal of Physical Chemistry A* **117**(10), 2181–2189.

Patel, B. B. & Diao, Y. (2017), ‘Multiscale assembly of solution-processed organic electronics: the critical roles of confinement, fluid flow, and interfaces’, *Nanotechnology* **29**(4), 044004.

Peach, M. J., Benfield, P., Helgaker, T. & Tozer, D. J. (2008), ‘Excitation energies in density functional theory: An evaluation and a diagnostic test’, *The Journal of Chemical Physics* **128**(4), 044118.

Peach, M. J., Le Sueur, C. R., Ruud, K., Guillaume, M. & Tozer, D. J. (2009), ‘TDDFT diagnostic testing and functional assessment for triazene chromophores’, *Physical Chemistry Chemical Physics* **11**(22), 4465–4470.

Perdew, J. P., Burke, K. & Ernzerhof, M. (1996), ‘Generalized gradient approximation made simple’, *Physical review letters* **77**(18), 3865.

Perdew, J. P., Burke, K. & Wang, Y. (1996), ‘Generalized gradient approximation for the exchange-correlation hole of a many-electron system’, *Physical review B* **54**(23), 16533.

Peumans, P., Uchida, S. & Forrest, S. R. (2003), ‘Efficient bulk heterojunction photovoltaic cells using small-molecular-weight organic thin films’, *Nature* **425**(6954), 158–162.

Phillips, J. C., Braun, R., Wang, W., Gumbart, J., Tajkhorshid, E., Villa, E., Chipot, C., Skeel, R. D., Kalé, L. & Schulten, K. (2005), ‘Scalable molecular dynamics with NAMD’, *Journal of Computational Chemistry* **26**(16), 1781–1802.

Podzorov, V., Pudalov, V. & Gershenson, M. (2003), ‘Field-effect transistors on rubrene single crystals with parylene gate insulator’, *Applied Physics Letters* **82**(11), 1739–1741.

Poelking, C., Cho, E., Malafeev, A., Ivanov, V., Kremer, K., Risko, C., Brédas, J.-L. & Andrienko, D. (2013), ‘Characterization of charge-carrier transport in semicrystalline polymers: electronic couplings, site energies, and charge-carrier dynamics in poly (bithiophene-alt-thienothiophene)[PBTTT]’, *The Journal of Physical Chemistry C* **117**(4), 1633–1640.

Pop, F., Lewis, W. & Amabilino, D. B. (2016), ‘Solid state supramolecular structure of diketopyrrolopyrrole chromophores: correlating stacking geometry with visible light absorption’, *CrystEngComm* **18**(46), 8933–8943.

Pope, M., Swenberg, C. E. et al. (1999), *Electronic processes in organic crystals and polymers*, Vol. 56, Oxford University Press on Demand.

Prandi, I. G., Viani, L., Andreussi, O. & Mennucci, B. (2016), ‘Combining classical molecular dynamics and quantum mechanical methods for the description of electronic excitations: The case of carotenoids’, *Journal of Computational Chemistry* **37**(11), 981–991.

Prins, P., Grozema, F. & Siebbeles, L. (2006), ‘Charge transport along phenylenevinylene molecular wires’, *Molecular Simulation* **32**(9), 695–705.

Probert, M. (2011), ‘Electronic structure: Basic theory and practical methods, by richard m. martin: Scope: graduate level textbook. level: theoretical materials scientists/condensed matter physicists/computational chemists’.

Qin, T. & Troisi, A. (2013), ‘Relation between structure and electronic properties of amorphous MEH-PPV polymers’, *Journal of the American Chemical Society* **135**(30), 11247–11256.

Reimers, J. R. (2001), ‘A practical method for the use of curvilinear coordinates in calculations of normal-mode-projected displacements and duschinsky rotation matrices for large molecules’, *The Journal of Chemical Physics* **115**(20), 9103–9109.

Reisjalali, M., Burgos-Mármol, J. J., Manurung, R. & Troisi, A. (2021), ‘Local structuring of diketopyrrolopyrrole (DPP)-based oligomers from molecular dynamics simulations’, *Physical Chemistry Chemical Physics* **23**(35), 19693–19707.

Renaud, N. & Grozema, F. C. (2015), ‘Intermolecular vibrational modes speed up singlet fission in perylenediimide crystals’, *The Journal of Physical Chemistry Letters* **6**(3), 360–365.

Reyes-Reyes, M., Kim, K., Dewald, J., López-Sandoval, R., Avadhanula, A., Curran, S. & Carroll, D. L. (2005), ‘Meso-structure formation for enhanced organic photovoltaic cells’, *Organic Letters* **7**(26), 5749–5752.

Rispens, M. T., Meetsma, A., Rittberger, R., Brabec, C. J., Sariciftci, N. S. & Hummelen, J. C. (2003), ‘Influence of the solvent on the crystal structure of PCBM and the efficiency of MDMO-PPV: PCBM ‘plastic’solar cells’, *Chemical Communications* pp. 2116–2118.

Rivnay, J., Mannsfeld, S. C., Miller, C. E., Salleo, A. & Toney, M. F. (2012), ‘Quantitative determination of organic semiconductor microstructure from the molecular to device scale’, *Chemical Reviews* **112**(10), 5488–5519.

Robertson, M. J., Qian, Y., Robinson, M. C., Tirado-Rives, J. & Jorgensen, W. L. (2019), ‘Development and Testing of the OPLS-AA/M Force Field for RNA’, *Journal of Chemical Theory and Computation* **15**(4), 2734–2742.

Robertson, M. J., Tirado-Rives, J. & Jorgensen, W. L. (2015), ‘Improved Peptide and Protein Torsional Energetics with the OPLS-AA Force Field’, *Journal of Chemical Theory and Computation* **11**(7), 3499–3509.

Robinson, D. & Besley, N. A. (2010), ‘Modelling the spectroscopy and dynamics of plastocyanin’, *Physical Chemistry Chemical Physics* **12**(33), 9667–9676.

Rogers, D. M., Jasim, S. B., Dyer, N. T., Auvray, F., Réfrégiers, M. & Hirst, J. D. (2019), ‘Electronic circular dichroism spectroscopy of proteins’, *Chem* **5**(11), 2751–2774.

Roseli, R. B., Tapping, P. C. & Kee, T. W. (2017), ‘Origin of the excited-state absorption spectrum of polythiophene’, *The Journal of Physical Chemistry Letters* **8**(13), 2806–2811.

Roy, P., Bressan, G., Gretton, J., Cammidge, A. N. & Meech, S. R. (2021), 'Ultrafast excimer formation and solvent controlled symmetry breaking charge separation in the excitonically coupled subphthalocyanine dimer', *Angewandte Chemie International Edition* **60**(19), 10568–10572.

Sala, J., Guàrdia, E. & Masia, M. (2011), 'Improving the force matching algorithm: Application to a simple point charge flexible model of water', *Computer Physics Communications* **182**(9), 1954–1957.

Schlegel, H. B., Iyengar, S. S., Li, X., Millam, J. M., Voth, G. A., Scuseria, G. E. & Frisch, M. J. (2002), 'Ab initio molecular dynamics: Propagating the density matrix with Gaussian orbitals. III. Comparison with Born–Oppenheimer dynamics', *The Journal of Chemical Physics* **117**(19), 8694–8704.

Schlegel, H. B., Millam, J. M., Iyengar, S. S., Voth, G. A., Daniels, A. D., Scuseria, G. E. & Frisch, M. J. (2001), 'Ab initio molecular dynamics: Propagating the density matrix with Gaussian orbitals', *The Journal of Chemical Physics* **114**(22), 9758–9763.

Scholes, G. D. & Ghiggino, K. P. (1994), 'Electronic interactions and interchromophore excitation transfer', *The Journal of Physical Chemistry* **98**(17), 4580–4590.

Schön, J. H., Meng, H. & Bao, Z. (2001), 'Self-assembled monolayer organic field-effect transistors', *Nature* **413**(6857), 713–716.

Schott, S., Gann, E., Thomsen, L., Jung, S.-H., Lee, J.-K., McNeill, C. R. & Sirringhaus, H. (2015), 'Charge-transport anisotropy in a uniaxially aligned diketopyrrolopyrrole-based copolymer', *Advanced Materials* **27**(45), 7356–7364.

Schweicher, G., Garbay, G., Jouclas, R., Vibert, F., Devaux, F. & Geerts, Y. H. (2020), 'Molecular semiconductors for logic operations: Dead-end or bright future?', *Advanced Materials* **32**(10), 1905909.

Seitz, M., Magdaleno, A. J., Alcázar-Cano, N., Meléndez, M., Lubbers, T. J., Walraven, S. W., Pakdel, S., Prada, E., Delgado-Buscalioni, R. & Prins, F. (2020), 'Exciton diffusion in two-dimensional metal-halide perovskites', *Nature Communications* **11**(1), 1–8.

Sekitani, T. (2021), 'A photocurable bioelectronics–tissue interface', *Nature Materials* **20**(11), 1460–1461.

Senthilkumar, K., Grozema, F. C., Guerra, C. F., Bickelhaupt, F. M., Lewis, F. D., Berlin, Y. A., Ratner, M. A. & Siebbeles, L. D. (2005), 'Absolute rates of hole transfer in DNA', *Journal of the American Chemical Society* **127**(42), 14894–14903.

Shi, L. & Willard, A. P. (2018), 'Modeling the effects of molecular disorder on the properties of Frenkel excitons in organic molecular semiconductors', *The Journal of Chemical Physics* **149**(9), 094110.

Shin, J., Park, G. E., Lee, D. H., Um, H. A., Lee, T. W., Cho, M. J. & Choi, D. H. (2015), 'Bis (thienothiophenyl) diketopyrrolopyrrole-based conjugated polymers with various branched alkyl side chains and their applications in thin-film transistors and polymer solar cells', *ACS Applied Materials & Interfaces* **7**(5), 3280–3288.

Siepmann, J. I. & Frenkel, D. (1992), 'Configurational bias Monte Carlo: a new sampling scheme for flexible chains', *Molecular Physics* **75**(1), 59–70.

Simine, L. & Rossky, P. J. (2017), 'Relating chromophoric and structural disorder in conjugated polymers', *The Journal of Physical Chemistry Letters* **8**(8), 1752–1756.

Sirringhaus, H. (2014), '25th anniversary article: Organic field-effect transistors: The path beyond amorphous silicon', *Advanced Materials* **26**(9), 1319–1335.

Strong, S. E. & Hestand, N. J. (2020), 'Modeling nonlocal electron–phonon coupling in organic crystals using interpolative maps: the spectroscopy of crystalline pentacene and 7, 8, 15, 16-tetraazaterrylene', *The Journal of Chemical Physics* **153**(12), 124113.

Sundar, V. C., Zaumseil, J., Podzorov, V., Menard, E., Willett, R. L., Someya, T., Gershenson, M. E. & Rogers, J. A. (2004), 'Elastomeric transistor stamps: reversible probing of charge transport in organic crystals', *Science* **303**(5664), 1644–1646.

Sutton, A. P., Finnis, M. W., Pettifor, D. G. & Ohta, Y. (1988), 'The tight-binding bond model', *Journal of Physics C: Solid State Physics* **21**(1), 35.

Sweetnam, S., Vandewal, K., Cho, E., Risko, C., Coropceanu, V., Salleo, A., Brédas, J. L. & McGehee, M. D. (2016), 'Characterizing the polymer: Fullerene intermolecular interactions', *Chemistry of Materials* **28**(5), 1446–1452.

Takeda, Y., Hayasaka, K., Shiwaku, R., Yokosawa, K., Shiba, T., Mamada, M., Kumaki, D., Fukuda, K. & Tokito, S. (2016), 'Fabrication of ultra-thin printed organic tft cmos logic circuits optimized for low-voltage wearable sensor applications', *Scientific Reports* **6**(1), 1–9.

Tang, C. W. & VanSlyke, S. A. (1987), 'Organic electroluminescent diodes', *Applied Physics Letters* **51**(12), 913–915.

Tao, J., Perdew, J. P., Staroverov, V. N. & Scuseria, G. E. (2003), 'Climbing the density functional ladder: Nonempirical meta–generalized gradient approximation designed for molecules and solids', *Physical Review Letters* **91**(14), 146401.

Tessler, N., Preezant, Y., Rappaport, N. & Roichman, Y. (2009), 'Charge transport in disordered organic materials and its relevance to thin-film devices: a tutorial review', *Advanced Materials* **21**(27), 2741–2761.

Thomas, M., Brehm, M., Fligg, R., Vöhringer, P. & Kirchner, B. (2013), ‘Computing vibrational spectra from ab initio molecular dynamics’, *Physical Chemistry Chemical Physics* **15**(18), 6608.

Troisi, A. (2007), ‘Prediction of the absolute charge mobility of molecular semiconductors: the case of rubrene’, *Advanced Materials* **19**(15), 2000–2004.

Troisi, A. & Orlandi, G. (2006*a*), ‘Charge-transport regime of crystalline organic semiconductors: Diffusion limited by thermal off-diagonal electronic disorder’, *Physical Review Letters* **96**(8), 086601.

Troisi, A. & Orlandi, G. (2006*b*), ‘Dynamics of the intermolecular transfer integral in crystalline organic semiconductors’, *The Journal of Physical Chemistry A* **110**(11), 4065–4070.

Tsumura, A., Koezuka, H. & Ando, T. (1986), ‘Macromolecular electronic device: Field-effect transistor with a polythiophene thin film’, *Applied Physics Letters* **49**(18), 1210–1212.

Turkoglu, G., Cinar, M. E. & Ozturk, T. (2019), ‘Thiophene-based organic semiconductors’, *Sulfur Chemistry* pp. 79–123.

Van der Horst, J.-W., Bobbert, P. A., Michels, M. A. & Bässler, H. (2001), ‘Calculation of excitonic properties of conjugated polymers using the bethe–salpeter equation’, *The Journal of Chemical Physics* **114**(15), 6950–6957.

Vanommeslaeghe, K., Hatcher, E., Acharya, C., Kundu, S., Zhong, S., Shim, J., Darian, E., Guvench, O., Lopes, P., Vorobyov, I. & Mackerell Jr., A. D. (2010), ‘CHARMM General Force Field’, *Journal of Computational Chemistry* **31**, 671–690.

Venkateshvaran, D., Nikolka, M., Sadhanala, A., Lemaur, V., Zelazny, M., Kepa, M., Hurhangee, M., Kronemeijer, A. J., Pecunia, V., Nasrallah, I. et al. (2014), ‘Approaching disorder-free transport in high-mobility conjugated polymers’, *Nature* **515**(7527), 384–388.

Verlet, L. (1967), ‘Computer ”experiments” on classical fluids. i. thermodynamical properties of lennard-jones molecules’, *Physical Review* **159**(1), 98.

Vukmirovic, N. & Wang, L.-W. (2011), ‘Density of states and wave function localization in disordered conjugated polymers: a large scale computational study’, *The Journal of Physical Chemistry B* **115**(8), 1792–1797.

Wang, J., Wolf, R. M., Caldwell, J. W., Kollman, P. A. & Case, D. A. (2004), ‘Development and testing of a general Amber force field’, *Journal of Computational Chemistry* **25**(9), 1157–1174.

Wang, Y., Sun, L., Wang, C., Yang, F., Ren, X., Zhang, X., Dong, H. & Hu, W. (2019), ‘Organic crystalline materials in flexible electronics’, *Chemical Society Reviews* **48**(6), 1492–1530.

Wegner, G., Klaus, M. et al. (2008), ‘Electronic materials: the oligomer approach’.

Wei, D., Song, Y. & Wang, F. (2011), 'A simple molecular mechanics potential for μm scale graphene simulations from the adaptive force matching method', *The Journal of Chemical Physics* **134**(18), 184704.

Wessels, M. G. & Jayaraman, A. (2019), 'Molecular dynamics simulation study of linear, bottlebrush, and star-like amphiphilic block polymer assembly in solution', *Soft Matter* **15**(19), 3987–3998.

Wienk, M. M., Turbiez, M., Gilot, J. & Janssen, R. A. (2008), 'Narrow-bandgap diketo-pyrrolo-pyrrole polymer solar cells: the effect of processing on the performance', *Advanced Materials* **20**(13), 2556–2560.

Wildman, J., Repiščák, P., Paterson, M. J. & Galbraith, I. (2016), 'General force-field parametrization scheme for molecular dynamics simulations of conjugated materials in solution', *Journal of Chemical Theory and Computation* **12**(8), 3813–3824.

Woody, R. W. (2012), 'Electronic circular dichroism of proteins', *Comprehensive Chiroptical Spectroscopy* **2**, 475–497.

Wright, L. B., Rodger, P. M. & Walsh, T. R. (2013), 'Aqueous citrate: A first-principles and force-field molecular dynamics study', *RSC Advances* **3**(37), 16399–16409.

Wu, R., Lu, Z., Cao, Z. & Zhang, Y. (2011), 'A transferable nonbonded pairwise force field to model zinc interactions in metalloproteins', *Journal of Chemical Theory and Computation* **7**(2), 433–443.

Xu, Y., Sun, H., Li, W., Lin, Y.-F., Balestra, F., Ghibaudo, G. & Noh, Y.-Y. (2017), 'Exploring the charge transport in conjugated polymers', *Advanced Materials* **29**(41), 1702729.

Yamagata, H., Maxwell, D. S., Fan, J., Kittilstved, K. R., Briseno, A. L., Barnes, M. D. & Spano, F. C. (2014), 'HJ-aggregate behavior of crystalline 7,8,15,16-tetraazaterrylene: Introducing a new design paradigm for organic materials', *The Journal of Physical Chemistry C* **118**(49), 28842–28854.

Yamagata, H., Norton, J., Hontz, E., Olivier, Y., Beljonne, D., Brédas, J.-L., Silbey, R. & Spano, F. (2011), 'The nature of singlet excitons in oligoacene molecular crystals', *The Journal of Chemical Physics* **134**(20), 204703.

Yanai, T., Tew, D. P. & Handy, N. C. (2004*a*), 'A new hybrid exchange–correlation functional using the coulomb-attenuating method (cam-b3lyp)', *Chemical physics letters* **393**(1-3), 51–57.

Yanai, T., Tew, D. P. & Handy, N. C. (2004*b*), 'A new hybrid exchange–correlation functional using the Coulomb-attenuating method (CAM-B3LYP)', *Chemical Physics Letters* **393**(1-3), 51–57.

Yu, L., Chan, W. K., Peng, Z. & Gharavi, A. (1996), 'Multifunctional polymers exhibiting photorefractive effects', *Accounts of Chemical Research* **29**(1), 13–21.

Zhang, Z., Jiang, L., Cheng, C., Zhen, Y., Zhao, G., Geng, H., Yi, Y., Li, L., Dong, H., Shuai, Z. et al. (2016), 'The impact of interlayer electronic coupling on charge transport in organic semiconductors: a case study on titanylphthalocyanine single crystals', *Angewandte Chemie* **128**(17), 5292–5295.

Zhao, Y. & Truhlar, D. G. (2010), 'Density functional calculations of e2 and sn2 reactions: effects of the choice of density functional, basis set, and self-consistent iterations', *Journal of Chemical Theory and Computation* **6**(4), 1104–1108.

Zhu, J., Zhang, Z., Lv, Y., Lan, A., Lu, H., Do, H. & Chen, F. (2022), 'Organic solar cells based on non-fullerene acceptors containing thiophene [3,2-*b*] pyrrole', *Organic Electronics* **103**, 106461.

Zhu, L., Yi, Y., Li, Y., Kim, E.-G., Coropceanu, V. & Brédas, J.-L. (2012), 'Prediction of remarkable ambipolar charge-transport characteristics in organic mixed-stack charge-transfer crystals', *Journal of the American Chemical Society* **134**(4), 2340–2347.

Zhu, S., Dorh, N., Zhang, J., Vegesna, G., Li, H., Luo, F.-T., Tiwari, A. & Liu, H. (2012), 'Highly water-soluble neutral near-infrared emissive bodipy polymeric dyes', *Journal of Materials Chemistry* **22**(6), 2781–2790.

Zojer, E., Buchacher, P., Wudl, F., Cornil, J., Calbert, J. P., Brédas, J.-L. & Leising, G. (2000), 'Excited state localization in organic molecules consisting of conjugated and nonconjugated segments', *The Journal of Chemical Physics* **113**(22), 10002–10012.

Zoombelt, A. P., Mathijssen, S. G., Turbiez, M. G., Wienk, M. M. & Janssen, R. A. (2010), 'Small band gap polymers based on diketopyrrolopyrrole', *Journal of Materials Chemistry* **20**(11), 2240–2246.

Zou, S.-J., Shen, Y., Xie, F.-M., Chen, J.-D., Li, Y.-Q. & Tang, J.-X. (2020), 'Recent advances in organic light-emitting diodes: toward smart lighting and displays', *Materials Chemistry Frontiers* **4**(3), 788–820.